UNIVERSITÉ DE LIÈGE

Faculté des sciences

Ab-initio calculation of spin dependent transport quantities in disordered materials

Défense de Thèse pour l'obtention du titre de Docteur en Sciences

par

Marco DI GENNARO

Membres du jury:

Prof. Matthieu Verstraete, promoteur
Prof. Philppe Ghosez, président
Prof. Gustav Bihlmayer
Prof. Jean-Yves Raty
Prof. Georg Madsen
Prof. Françoise Remacle

Septembre 2015

Ab-initio calculation of spin dependent transport quantities in disordered materials

Défense de Thèse pour l'obtention du titre de Docteur en Sciences

par

Marco DI GENNARO

Membres du jury:

Prof. Matthieu Verstraete, promoteur
Prof. Philppe Ghosez, président
Prof. Gustav Bihlmayer
Prof. Jean-Yves Raty
Prof. Georg Madsen
Prof. Françoise Remacle

Septembre 2015

Acknowledgements

Mentioning all the people that directly or indirectly contributed to this Thesis is a difficult task, if not impossible.
The Highest Place of Honor in this acknowledgements is dedicated to my supervisor, and very good friend, Matthieu Verstraete. Train a fresh Ph.D. student must not be an easy task. Matthieu's coaching has been attentive and dedicated, regardless of the time I put to understand what he was trying to explain. I consider myself extremely lucky to have met him in the first place since our relationship has spread way beyond the limits of scientific research, beside the fact that he was there all the times I needed. His generosity in time is equal only to its youthful energy. He also left me extreme freedom of action and strategy, which were probably not always successful, but I certainly acquired a sense of facing unknown questions, keeping always things cool.
I would like to thanks all the people which materially helped me with careful reading of the manuscript or with this or that software, sometimes with various iteration, until some convergence has been reached: Bin, Cyril, Brahim, Micael, Antoine, Jordan, Zeila, Fabio.
My scientific curiosity has certainly been stimulated throughout these four years by the interaction with all the scientists involved in the Nanomat, PhyThema and Spin group at the University of Liège, almost all from different nationalities. Thus many thanks to: Philippe, Jean Yves, Eric, Momar, Theodoros, Srian, Baris, Daniel, Julien, Nick, Hania, and Gabriele. I spent this time with many other students, some of them received their Ph.D. in the meanwhile: Jinzhu, Henu, Alina, Denis, Safari, Wilfredo, Naihua, Begüm, Can, Safari, Alain, Sébastien, Hanen, Camilo, Misha and Henrique.
I wish to thanks all the ETSF research network, the young fellas in particular, for making some scientific meeting and discussion extremly fruitful from the amusement point of view. Many of them also belong the *Abinit* network, which provided the main tool of investigation I used.
A special thank goes to the people oversea: Aldo and Alonso which played with us on the magnetic exchange game table.
This Thesis has been polarized by my stay in Austin (TX), where I had the chance

to know a complementary way of doing research. I would like to thanks Allen MacDonalds in particular for the time he spent discussing and explaining extremely interesting physics, without forgetting all the members of his group (which is too large to mention everybody).
My thesis would not have been the same without the people I met in Liège, which gave me some unforgettable moments. I can proudly say that I have met some extraordinary people in Liège, and I am happy to have them as friends. My flatmates: Bertrand (aka Thoss), Martina, Alicia, Henrique (aka Jesus), Simon (aka Dr. Simon), Alejandro, Rasih, Charles, Chiara, Meri, Giada, Mathieu, Claire. My Ouftimateamates: Yvan (aka ya moyen), Damien (aka Coach), Manu (aka the ouftivan guy), Renaud (aka Ren's), Damien (aka Leon), Annette, Steve (aka kiwy), Kevin, Arnaud, Guillaume, Aurore, Lyne, toute la tribu des Roubaix, RJ, Lorelle, Xavier, Arthur, Tom, Maïté and Olivier etc.
Moreover, a number of which people does not enter in any of the category mentioned so far helped facing the hardest weeks of work with some robust week end backup of happiness and crazyness. To mention only a few: Chandra (aka James), Marina, Mirco , Renato, Vincent , Marie A., Marie B., all the Chileans.
I finally acknowledge The University of Liège and the FNRS for financial support throughout 7 months and 4 years respectively. I thanks the Federation Wallonie Bruxelles for the grant provided to visit the University of Texas at Austin. I would like to thanks computer support: CECI (especially David Colignon) and PRACE, and all the administrative stuff of the Physics department, of the Faculty of Science and of F.N.R.S for their kindness.
Un'ultima frase per permettere ai miei genitori, Nicola e Rosa, di capire qualcosa in tutto questo bla bla, e ringraziarli, insieme a Vale e al resto della mia famiglia, per avermi cresciuto e istruito al meglio, e spinto a ragionare sempre con la mia testa. Sembra che alla fine, qualcosa di buono sia riuscito.

Liège, July 31^{th}, 2015

Abstract

The study of mutual interaction between microscopic excitations in Solid State Physics opened the way to an impressive technology development. Over the time lapse of a couple of decades, scientists managed to improve the efficiency and capacity of spin-based electronic devices to a level able to overcome Moore's law for traditional electronics. Often, these acheivements have been predicted theoretically before their experimental establishment.
In this Thesis, I present a theoretical method to calculate macroscopic transport quantities systematically from first principles. We use *ab-initio* Density Functional Theory to calculate electronic ground state properties. We consider vibrational excitation within perturbation theory and we include anharmonic terms within quasi harmonic approximation. We consider the special cases of spin-polarized materials, spin-orbit coupled materials and disordered materials.
A theory to introduce temperature corrections to the calculation of magnetic exchange interactions is also presented. Magnetic ground state properties are studied within the *ab-initio* Korringa-Kohn-Rostoker method, and magnon-phonon coupling is estimated within a frozen-phonon, frozen-magnon approach. This correction gives an estimation of the weight of magnon-phonon coupling effect which is normally neglected in well established first-principle methods for the calculation of magnetic properites of materials such as Mean Field Approximation and Atomistic Spin Dynamics. Results for a set of materials which are interesting for Spintronics and Spin-Caloritronics applications are presented.
The physics of the interface between a spin-polarized material and a heavy-metal is also analyzed, and the magnetic proximity effects arising in this kind of systems due to the Dzyaloshinskii-Moriya interaction are qualitatively presented.

Résumé

En physique de la matière condensée, l'étude des interactions entre excitations microscopiques a ouvert la voie à d'impressionnants développements technologiques. Durant ces quelques dernières décennies, les chercheurs sont parvenus à améliorer l'efficacité des dispositifs électroniques basés sur le spin. Ces découvertes ont permis à l'industrie de l'électronique de countorner la loi de Moore qui prédisait l'évolution des performances de nos ordinateurs. Les découvertes qui ont permis ces améliorations ont souvent été prédites théoriquement avant d'avoir putre réalisées expérimentalement. Dans cette thèse, Je présente une méthode théorique permettant de calculer les propriétés de transport macroscopique à partir des premiers principes. Nous utilisons la théorie de la fonctionnelle densité au niveau ab-initio pour calculer les propriétés électroniques de l'état fondamental des cristaux étudiés lors de cette thèse. Les propriétés des excitations vibrationnelles harmoniques sont établies grâce à la théorie de la perturbation et la partie anharmonique de l'excitation a été déterminée sur base de l'approximation quasi harmonique. Les structures considérées ici sont des matériaux polarisés en spin, des matériaux comprenant un couplage spin-orbit et des matériaux désordonnés. Ici sera également présenté une théorie permettant d'introduire les effets de la température au calcul des interactions d'échanges magnétiques sous forme de corrections. Les propriétés magnétiques de l'état fondamental sont étudiées avec la méthode ab-inition Korringa-Kohn-Rostoker, et le couplage magnon-phonon est déterminé en se basant sur une approche de frozen-phonon et frozen-magnon. Cette approche permet d'estimer l'importance de ce couplage qui est habituellement négligé dans les méthodes habituelles telles que Mean Field Approximation et Atomistic spin dynamics. Les résultats présentés ici concernent des matériaux aux propriétés très interessantes pour des applications en spintronic et spin-caloritronic. Les propriétés physiques de l'interface entre un matériau polarisé en spin et un métal lourd sont aussi analysées, et une analyse qualitative des effets de proximité magnétique apparaissant dans ce type de système et relative à l'intéraction Dzyaloshinskii-Moriya a également été réalisée.

Contents

Preface

In this Thesis I present the results I have achieved throughout my Ph.D. at the University of Liège which I started on March 15^{th}, 2011.
Two main research lines have been developed throughout the past four years. The first one regards the role dynamical stability of the high pressure phases of Calcium within the Density Functional Theory methods and the effect that finite temperature has on phonon frequencies. My results on were published on *Physical Review Letters* **111**, 025503, 2013 [52] and will not be treated in this Thesis.
This Thesis is entirely devoted to the results I obtained regarding the F.N.R.S.-F.R.I.A. project "Ab initio study of the Spin Seebeck Effect in metallic alloys" which I presented in October 21^{st}, 2011, to the Education Ministry of the Belgian French community and which was approved on December 15^{th}, 2011.
The Spin Seebeck Effect is a physical effect discovered in 2008, which attracted the curiasity of the Solid State Physics community due to its asthonishing properties. The interest of the scientific community for the Spin Seebeck effect was initially so large that an entirely new research field has been introduced after it, i.e. the Spin-Caloritronics, whose aim is the study of the mutual interactions of magnetic and temperature excitations in solids. Actually the Spin Seebeck Effect revealed to be so complicated that at this stage, a microscopic theory is still missing.
The Thesis is organized as follows. A short and colloquial introduction is given. Chapter one presents three field of research in Solid State Physics: Thermoelectrics, Spintronics and Spin-Caloritronics. Each of them studies the coupling of different excitations (electronic charge and thermal excitations, electronic charge and electronic spin, electronic spin and thermal excitations respectively) and how these coupling influences or generates new physical properties. The three subjects are huge subjects if taken alone, so I tried to mention only theit most important features, in function of what is done in the rest of the Thesis.
Chapter two introduces the theoretical workhorses and basis formalism and lexicon for the rest of the Thesis: Electronic Structure, Density Functional Theory, Empirical Magnetic Models, Atomistic Spin Dynamics, Phonons, Magnons etc.
In Chapter three, the Semiclassical Theory of Transport is briefly introduced and the Lowest Order Variational Approximation to the Boltzmann transport equation

as introduced by P.B. Allen in the 70's. The Relaxation Time Approximation to the Boltzmann equation is introduced as well. Explicit relations for resistivity, Seebeck coefficient and thermal conductivity are derived and calculated for Copper. In chapter four, I apply systematically this method to a set of chosen materials which are interesting for Spintronics and Spin-Caloritronics applications. I show the virtues and the limits of the Lowest Order Variational Approximation compared to the Relaxation Time Approximation.
Chapter five presents a quantitative *ab-initio* calculation of temperature dependent exchange integrals in spin polarized materials commonly used in Spintronics and Spin-Caloritronics devices. Ground state exchange integrals calculations and *ab-initio* thermal vibration of atoms in the lattice are considered, and the temperature dependent exchange are derived within a frozen-phonon frozen-magnon approach. Modifications to the theoretical Curie termperature calculations from Mean Field Approximation and Magnon Band Structure are presented.
Finally, Chapter 6 contains a discussion of the proximity magnetic effects which can arise at the Ferromagnetic-Heavy metal interfaces, which present peculiar physical properties and represent the base of many Spintronics and Spin-Caloritronics devices.
All the results presented in this Thesis are original and carried out mainly in the Nanomat group of the Physics Department of the University of Liège.

List of Figures

List of Tables

List of Abbreviations

aka	also known as
AFM	Anti Ferromagnet/ Anti Ferromagnetic
arb.un.	Arbitrary units
at.un.	Atomic units
BZ	Brillouin Zone
CPA	Coherent Potential Approximation
DFPT	Density functional Perturbation theory
DFT	Density functional theory
EBS	Electronic Band Structure
ECP	Electrochemical potential
EDOS	Electronic Density of States
eg	*exempli gratia*
EPC	Electron-Phonon Coupling
Exc	Exchange-Correlation Functional
FHI	Fritz Haber Institute
FM	Ferromagnet/Ferrmagnetic
FSF	Fermi Surface
GGA	Generalized Gradient Approximation
GF	Green Functions
GS	Ground State
Gsm	Gaussian Smearing in EPC calculations
HM	Heavy Metal

ie	*id est*
IFC	Interatomic Force Constant
ISHE	Inverse Spin Hall Effect
KKR	Korringa, Kohn and Rostocker
kpt	points in the irreducible BZ for DFT calculations
LDA	Local Density Approximation
LSDA	Local Spin Density Approximation
MBS	Magnon Band Structure
MPC	Magnon-Phonon Coupling
NLSV	Non Local Spin Valve
NM	Normal Metal
NN	Nearest Neighbor
PBS	Phonon Band Structure
PDOS	Phonon Density of States
PM	Paramagnet/Paramagnetic
PP	Pseudo-potential
QHA	Quasi-Harmonic Approximation
qpt	points in the irreducible BZ for DFPT calculations
SCF	Self Consistent Field
SDFT	Spin Density functional theory
SDSE	Spin Dependent Seebeck Effect
SE	Seebeck Effect
SHE	Spin Hall Effect
SSE	Spin Seebeck Effect

List of Symbols

$\mathring{A}$	Angsrom
a_0	Bohr radius
$\alpha^2F(\omega)$	Spectral functions
ΔS	Spin Dependent Seebeck coefficient
ϵ_F	Fermi energy
$F(\omega)$	Phonon density of states
$g_{\boldsymbol{kk'}}$	Electron-Phonon coupling matrix element
$\hbar$	Reduced Plank constant
κ	Electronic thermal conductivity
m	meter
μ	Electrochemical potential (EPC)
μ_B	Bohr magneton
ρ	Electrical resistiviy
S	Seebeck coefficient
$< S >$	Seebeck coefficient for ferromagnets
ω	Phonon frequency
s	second

Introduction

Why we study materials?

Scrolling down the history of science, one of the oldest and most recursive question is "what" composes the stuff which surrounds us and "why" they are so different. The chair on which we sit, the sheet of paper we touch, the blood which brings oxygen to our brain are "just" different kind of materials.
The atomistic theory is at least as old as the history of philosophy, and we can say that only recently we understood "why" wood is different from steel, water and oxygen and so on. The question which bumps up immediately after in everybody's head would probably be "how" we can realize something which is better, or cheaper, or which just fits better to a specific scope.
Physicist, chemists and material scientists will be more interested in answering the "why" question, and sleep soundly after realizing that an interaction simply exists. Material engineers would probably be just interested in the "how" question, and be happy with a new material, with some amazing property that the market has been long waiting for. Whether you belong to the first or to the second group, you have one thing in common: rarely the answer can be find with bare hand and naked eyes, and research on materials involves advanced theoretical methods and ultimately complicated experimental set-ups.

The third way

A typical example of (extremely successful) research on materials is the one which brought to the invention of the incandescent light bulb which we all know. Many scientists contributed to the development of this device, and many different materials were tested over a time laps of more than a century, before the "correct" answer was found (a tungsten wire into argon or nitrogen atmosphere or vacuum). Today, thanks to the invention of computer, we can study materials properties into a "gray zone" between theory and experiment, which is simulation. The afore mentioned testing procedure to find that tungsten is the best material for light

bulb could probably be done by a not so bad student on a not so bad commercial machine in a few hours running some simulation programs.
The list of techniques and methods which one could use is extremely large, and any material for any kind of applications could in principle be simulated nowadays. The discussion on whether simulations are to be considered theoretical or experimental techniques is of academic concern only, and probably interests only purists of the two fields (none of whom would probably ever accept simulation as a investigation method belonging to its field). Unfortunately for them, the die is cast. Scientist, engineers and all sorts of analysts widely uses simulations for the most variegated purposes.
The only real epistemological problem we have with simulations is that, at a certain point, some approximations always enter into the game (as it always happens in physics nonetheless). Thus, having an amazing result from a simulation does not mean that it is true, and, as the evergreen Galileo teaches, only experiment will discern between what is true and what is not. But experience also tells us that good simulations give an indication, which is true within a 10% of error.
Only the stupid scientist would take the results of his simulations for granted. But one thing is clear and accepted by all, simulations are making things much faster and cheaper.

One day we will probably dispose of materials so smart that we could collect all the energy we need from green sources, and we will no more worry about energy waste, and we could finally think to something else. Until then, surely simulation will be an useful aid.

Chapter 1

Heat, Charge and Spin

In the present chapter I introduce most of the concepts developed in the rest of the Thesis. I try to follow a phenomenological approach with a description of experiments first and a perspective on the theoretical development. Several of the concepts here presented are still objects of research, so what is presented here is the state of the art in 2015.
Thermoelectric effects and their generalization to ferromagnets are presented in Sec. 1.1 and Sec. 1.3 respectively. Fundamental concepts of Spintronics are presented in Sec. 1.2. Finally, Sec 1.5 is entirely devoted to the Spin Seebeck effect, which is considered to be the starting point of Spin-Caloritronics, a new sub-field of Solid State Physics which is founded on the coupling between electronic spin and thermal excitations.

1.1 Thermoelectric phenomena

Thermoelectric phenomena relate a thermal gradient to an electrical voltage. They happen in conductors or semiconductors and have been discovered during the XIX century, long before the discovery of electrons or quantum mechanics. The effort made to understand thermoelectricity pushed forward the theory of Solid State Physics. The **Seebeck** effect (SE) was discovered in the 1820s by T.J. Seebeck [200, 201] and is the generation of a electrical potential difference when a conductor or a doped semiconductor is subject to a gradient of temperature. The SE is the basic thermoelectric effect. The **Peltier** effect (PE) is the change in temperature that occurs at the edge of a thermocouple when an electrical current passes through the junction. The two effects are related to each other by an Onsager relation:

$$\begin{pmatrix} \boldsymbol{j}_c \\ \boldsymbol{j}_Q \end{pmatrix} = \sigma \begin{pmatrix} 1 & S \\ \Pi & \kappa/\sigma \end{pmatrix} \begin{pmatrix} \boldsymbol{E} \\ -\boldsymbol{\nabla} T \end{pmatrix} , \tag{1.1}$$

where $\boldsymbol{j}_c$ and $\boldsymbol{j}_Q$ are respectively the electric and heat currents, S and Π are the Seebeck and the Peltier coefficients, σ and κ are the electrical and thermal conductivities and $\boldsymbol{E}$ and $\boldsymbol{\nabla} T$ are the external electric field and temperature gradient.

1.1.1 Macroscopic transport coefficients

Electrical and thermal currents are to a good approximation linear functions of electric field and temperature:

$$\begin{cases} \boldsymbol{j}_e = L_{EE}\boldsymbol{E} + L_{ET}\nabla T\,, \\ \boldsymbol{j}_Q = L_{TE}\boldsymbol{E} + L_{TT}\nabla T\,. \end{cases} \tag{1.2}$$

Strictly speaking, these coefficients are tensors, but this complication is avoided in isotropic geometry. These coefficient can be determined for any material experimentally:

i) Electrical conductivity σ:
An electric field $\boldsymbol{E}$ is applied to a metal at uniform temperature ($\nabla T = 0$). Since $\boldsymbol{j}_e = \sigma\boldsymbol{E}$, it follows that $\sigma = L_{EE}$.

ii) Thermal conductivity κ:
A metallic sample is submitted to a thermal gradient ∇T and electrically insulated $\left(\boldsymbol{j}_e = 0 \Rightarrow \boldsymbol{E} = -\frac{L_{ET}}{L_{EE}}\nabla T\right)$.
Eq.(1.2) gives:

$$\boldsymbol{j}_Q = \left(-\frac{L_{ET}}{L_{EE}}L_{TE} + L_{TT}\right)\nabla T = -\kappa\nabla T\,, \tag{1.3}$$

whence:

$$\kappa = L_{TT} - \frac{L_{ET}}{L_{EE}}L_{TE}\,. \tag{1.4}$$

iii) Thermopower or Seebeck coefficient S:
A thermal gradient applied to an electrically insulated metallic sample produces an electric field in the metal. This is expressed by:

$$\boldsymbol{E} = S\nabla T\,. \tag{1.5}$$

And, being $\boldsymbol{j}_e = 0$, $S = -\frac{L_{ET}}{L_{EE}}$. The Seebeck effect is presented in Sec. 1.1.2.

iv) Peltier coefficient Π:
In the same experimental condition as for the measurement of σ, i.e. $\nabla T = 0$, Eq.(1.2) yields:

$$\boldsymbol{j}_Q = \frac{L_{TE}}{L_{EE}}\boldsymbol{j}_e, \quad \Pi \equiv \frac{L_{TE}}{L_{EE}}\,. \tag{1.6}$$

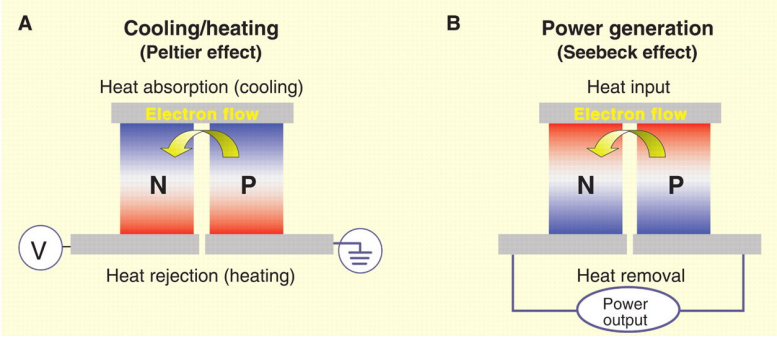

Figure 1.1: Representation of a thermocouple composed by a N-type and a P-type conductor. Left: Peltier effect, an electronic voltage produces a difference in temperature. This can be used to cooling or heating purposes. Right: Seebeck effect, a difference in temperature can generate an electronic voltage difference between the hot and the cold side. Figure 1 from Ref. [20].

1.1.2 Seebeck effect

In practice it is difficult to measure directly the S of a material and what is possible to measure is the difference of thermopower between two materials. A **thermocouple** is used for this purpose, i.e. a circuit of two different materials, say A and B, whose junctions are kept at a different temperatures, say T_1 and T_2, as shown in Figure 1.1. One of the two materials is then broken to allow the voltage measurement. The voltage across the gap is then equal to:

$$V_{AB} = -\int \boldsymbol{E} \cdot d\boldsymbol{r} = -\int S\frac{\partial T}{\partial r} d\boldsymbol{r} = \int_{T_1}^{T_2} (S_A - S_B) dT = (S_A - S_B)\Delta T\,. \quad (1.7)$$

The temperature gradient is supposed to be constant in this equation. If this is not the case then the **Thomson** effect arises. The SE may be easily explained using macroscopic transport formalism. The electrical current between two contacts 1 and 2 is:

$$I = \frac{1}{q}\int D(\epsilon)(f_1(\epsilon) - f_2(\epsilon))d\epsilon\,, \quad (1.8)$$

with q, $D(\epsilon)$ and $f(\epsilon)$ being the electrical charge, electronic density of state (DOS) and Fermi-Distribution function. The Fermi-Dirac distribution $f(\epsilon)$ is more "smeared" around the Fermi energy (ϵ_F) for the "hot" side while it is more "abrupt" approaching from 1 to 0 on the "cold" side (Fig. 1.2 top, left). Assuming f_1 (f_2) to be hotter (colder), the difference in Eq. (1.8) is then positive above the Fermi energy and negative below the Fermi energy (Fig. 1.2 top, right). The sign of the current depends on the shape of the DOS $D(\epsilon)$. For a material with more available states above the Fermi energy, there will be more electrons on the hot side, which

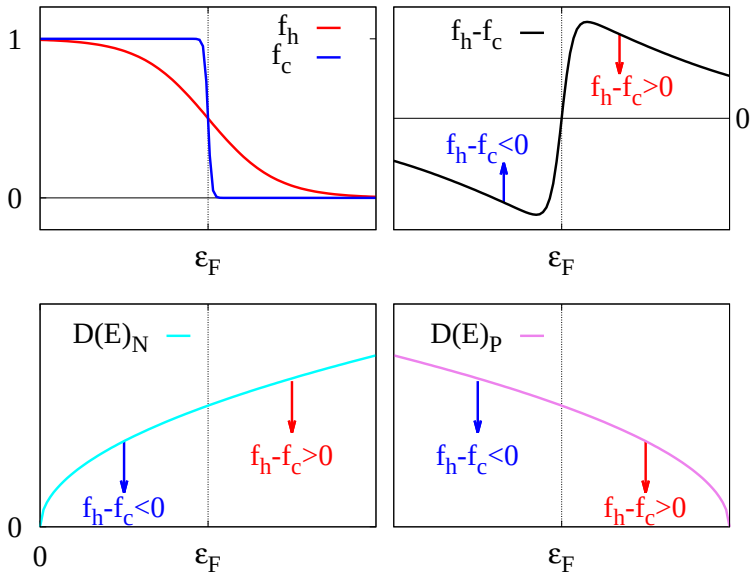

Figure 1.2: Qualitative picture of the Seebeck effect. Top left: Fermi-Dirac distribution functions for "hot" and "cold" materials. Top right: difference between "hot" and "cold" distribution functions. Bottom: Density of states for N-type materials (left) and P-type materials (right).

will diffuse towards the cold side as shown in Fig. 1.2. Electrons will travel in the other direction for materials with a density of states which has more available states for energies below the Fermi energy ϵ_F.

This is actually an alternative way of defining N and P type materials. N (P) type materials are those in which, under a thermal gradient, electrons travel from the hot (cold) to the cold (hot) side. Note that while under an electric field electrons always go from the higher potential to the lower potential, under a thermal gradient this difference depends on the density of states of the specific material.

Figure of merit

An empirical formula to estimate the Seebeck coefficient is Mott's relation [15]:

$$S = \frac{\pi}{3}\frac{k_B}{q}k_B T\left(\frac{d[ln(\sigma(\epsilon))]}{d\epsilon}\right)_{\epsilon=\epsilon_F}, \tag{1.9}$$

where $\sigma(\epsilon) = D(\epsilon)e\mu(\epsilon)$ is the spectral conductivity derived in terms of density of states $D(\epsilon)$, the electrical charge e and the charge mobility $\mu(\epsilon)$. The Seebeck

coefficient is of central importance in the figure of merit for thermoelectric materials:

$$ZT = \frac{\sigma S^2}{\kappa_{el} + \kappa_{latt}}, \tag{1.10}$$

where σ is the electrical conductivity and the κ are the thermal conductivity of electrons and lattice respectively. Modern thermoelectric research's goal is to increase the generated power by engineering nanoscaled materials.

1.2 Concepts of Spintronics

Spintronics [108, 268] has made its appearance over 30 years ago and spin based nanoelectronics is today a reality. The first observation of spin dependent transport dates back to 1985, when Johnson and Silsbee observed charge-spin coupling at the interface between a ferromanget (FM) and a normal metal (NM) [117].
The discovery of the Giant Magneto Resistance (GMR) by Fert et al. [16] and Grünberg et al. [23] represents a milestone in the field of nanoelectronics *The Nobel Prize in Physics 2007 was awarded jointly to Albert Fert and Peter Grünberg "for the discovery of Giant Magnetoresistance"*[1]. GMR is exploited in magnetic field sensors which are applied to read data in hard disk drives, biosensors, micro-electromechanical systems and other devices. GMR multilayers are also used in magnetoresistive random-access memory as storage for the information.
Spintronics research spans from the control of a single localized electronic spin to use as a spin qbit in solid state quantum computers to the transport in macroscopic systems with coupling between a spin and its dynamics.
Spintronics has proven the validity of the theoretical approach towards a rapid development of user-end technology (the time between theory formulation and practical applications is of the order of the decade) and raised at the same time a number of fundamental questions.

1.2.1 Spin current

A **spin current** is a flow of angular momentum [182, 268, 108, 214, 113, 227, 121]. It is the pivotal concept in Spintronics. The debate on what is the correct definition for a spin current is still open [204, 168, 186, 224, 12] since, contrary to the electrical charge, spin is not a conserved quantity in spin-coupled systems. We will skip this discussion since it goes far beyond the scope of this thesis.
We adopt the following definition for the spin current carried by an excitation

[1] www.nobelprize.org

moving with velocity $\boldsymbol{v}_k$ [3]:

$$\boldsymbol{j}_s = \sum_k s_k^z \boldsymbol{v}_k \,, \tag{1.11}$$

where s_k^z is the z-component of the spin density s_k (the z axis has been chosen in the spin-quantization direction). From definition (1.11) two kinds of spin currents (i.e. free from charge current) can be derived: a conduction-electron pure spin current and a **magnon** pure spin current (Figs. 1.3b and 1.3a). The decay lengths of these two currents is extremely different, a few nm for electronic [227] and up to a few millimetres for magnonic spin currents [121].
A spin current can be detected with the method of **nonlocal spin injection** by using a magnetic conductor [114, 115] or a magnetic insulator [122]. In both cases, the **Spin Hall effect** and its inverse are exploited. These effects are presented in Sec. 1.4.2.
An electrical current through a thick magnetic layer becomes **spin-polarized**. Two macroscopic currents can be defined and measured in ferromagnets: the electrical current and the spin current. The **electrical current** is a flux of electronic charge through the sample and is the sum of the contributions from the two spin channels since the electronic spin direction is irrelevant. The **spin current** [182, 268, 108, 214, 113, 227, 121] is a flux of angular momentum in the sample. In a ferromagnet, spin direction is always collinear and there are only two possible directions allowed, so the only possible flux of angular momentum is the one in which electrons with different spins are pushed in different directions. Thus it is natural to define the spin current as the difference between the two spin channels contributions:

$$\mathbf{j}_c = \mathbf{j}_\uparrow + \mathbf{j}_\downarrow \,, \tag{1.12a}$$

$$\mathbf{j}_s = \mathbf{j}_\uparrow - \mathbf{j}_\downarrow \,. \tag{1.12b}$$

1.2.2 Collinear effects

Giant Magneto-Resistance

GMR is an effect of "filtering" spin in a polarized current when this passes through a **Spin valve**. A spin valve (Fig. 1.4, top) is a multilayer device composed by at least three different layers: a FM called "pinned" since the direction of its internal magnetization is fixed, a second NM layer and a third FM layer called "free layer" since the direction of its internal magnetization can be varied externally. The total resistance of the whole structure depends on the mutual direction of the magnetization in the ferromagnetic layers: the resistivity is lower when the ferromagnets are aligned in the same direction and lower when they are antiparallel.

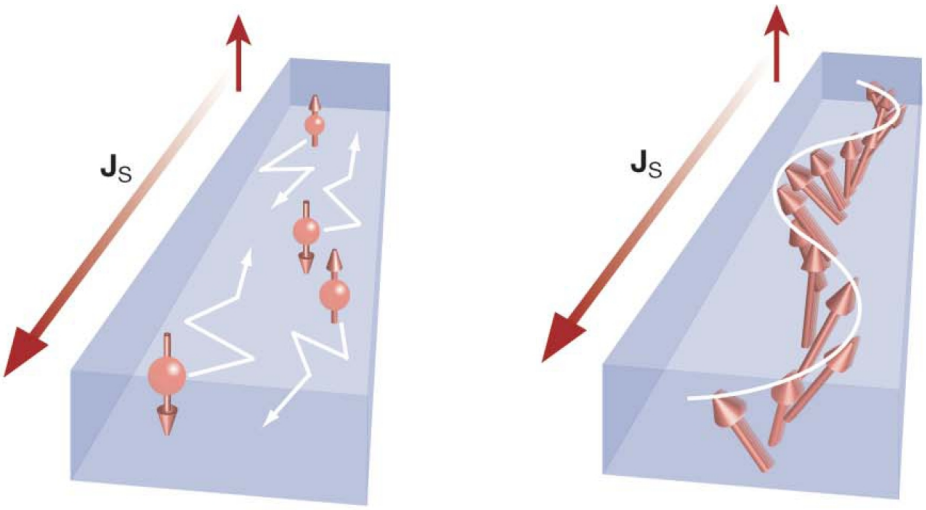

(a) Conduction electron spin current **(b)** Spin-wave spin current

Figure 1.3: Cartoons representing the two kind of spin currents introduced in Sec.1.2.1. From Ref. [191].

The difference in current can be as large as 100% . This can be easily explained in classical terms through the concept of spin dependent scattering. Electronic spin can assume only two discrete values and according to this value the scattering rate at the FM-NM interface is different. In the resistor model [68, 69, 253], the resistance across the interface is higher for non-aligned spin directions than for aligned spin direction (Fig. 1.4, bottom).
Similarly to the tunnel effect, if the nonmagnetic metal is substituted by a thin insulator, the phenomena of **Tunnel Magnetoresistance** can arise, and electrons can tunnel the barrier with a rate which is proportional to the relative alignment of the two ferromagnetic layers.

Valet-Fert model

In 1993 T.Valet and A.Fert calculated transport properties for a current perpendicular to plane (CPP) multilayer with the Boltzmann equation. The current density flowing in the $\hat{\boldsymbol{z}}$ direction in a non magnetic material can be written in terms of the electro-chemical potential (ECP) μ:

$$\boldsymbol{j}_c = -\frac{\sigma}{e}\frac{d\mu}{dz}\,, \tag{1.13}$$

and in stationary state: $\frac{d\boldsymbol{j}_e}{dz} = 0$ implies $\frac{d^2\mu}{d^2z} = 0$ for a constant σ.
If the spin diffusion length l_{sf} is much larger than the electronic mean free path

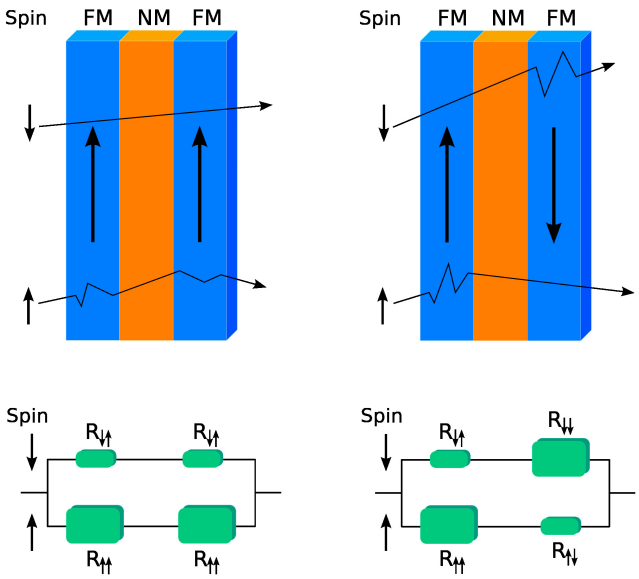

Figure 1.4: Top: representation of a spin valve composed by a non-magnetic material sandwiched between two ferromagnets. Bottom: circuit resistor model for parallel and antiparallel orientation of the magnetisation in the two FM layers. From Ref. [267]

λ, the spin flip can be neglected, and two independent diffusion equations can be written down for spin up and spin down spin electronic currents $\boldsymbol{j}_\uparrow$ and $\boldsymbol{j}_\downarrow$ by introducing $\mu_\uparrow, \mu_\downarrow$

$$\boldsymbol{j}_\uparrow = -\frac{\sigma}{2e}\frac{d\mu_\uparrow}{dz}\,, \tag{1.14a}$$

$$\boldsymbol{j}_\downarrow = -\frac{\sigma}{2e}\frac{d\mu_\downarrow}{dz}\,, \tag{1.14b}$$

where the factor two has been introduced at the denominator since for NM we have $\sigma_\uparrow = \sigma_\downarrow = \sigma/2$ and in a steady state the derivative of both equals to zero.
If the assumpion $l_{sf} >> \lambda$ is dropped, the spin flip must be considered and different spin reservoirs come in contact. The steady state condition must be satisfied for the sum of the two currents but not for the two channels separately:

$$\frac{d\boldsymbol{j}_\uparrow}{dz} + \frac{\boldsymbol{j}_\downarrow}{dz} = 0\,. \tag{1.15}$$

Assuming now that one spin channel is much more populated than the other ($\mu_\uparrow >> \mu_\downarrow$), it makes sense to assume that many spin up are flipped to down, while the other proces is negligible. The variation of current up would be proportional

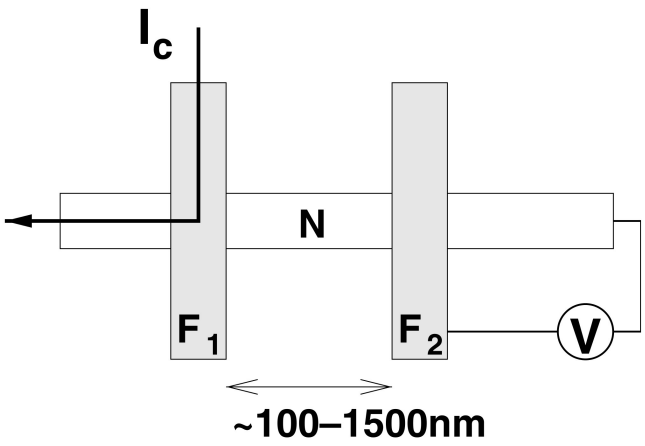

Figure 1.5: NLSV scheme: An electrical current is injected from a FM into a NM. After passing through FM the electrical current is spin polarized. Spin diffuse through the NM and then is injected into a second FM at some hundreds of nm. Figure 1 from Ref [3].

to the difference $\mu_S \equiv \mu_\uparrow - \mu_\downarrow$ and one can write:

$$\frac{d^2}{dz^2}\left(\mu_\uparrow - \mu_\downarrow\right) = \frac{\left(\mu_\uparrow - \mu_\downarrow\right)}{l_{sf}^2}\,, \tag{1.16a}$$

$$\frac{d^2}{dz^2}\left(\mu_\uparrow + \mu_\downarrow\right) = 0\,. \tag{1.16b}$$

Thus, in the CPP configuration, the spin dynamics is described by a pretty simple diffusion equation. When the current flows in plane (CIP) the derivation of a similar expression is more elaborated [177].

Non Local Spin Valve method

An electrical current $\boldsymbol{j}_c$ (I_c in Fig. 1.5) is sent through a ferromagnet (F1) and a normal metal (N). The current is spin polarized in the F1 by exchange interaction and at the F-N interface a spin potential μ_S builds up at the interface. Electrons can diffuse into it the right part of N. The number of states available for minority spins is similar across the interface ($D_{\downarrow,NM}(\epsilon) \approx D_{\downarrow,FM}(\epsilon)$), while the available number of states decreases drastically for majority spin electrons ($D_{\uparrow,NM}(\epsilon) \ll D_{\uparrow,FM}(\epsilon)$), which are more likely to diffuse into N. In this way a current of majority spin electrons is pumped into the N metal. Spin-flip occurs over a length of a few nanometers into the NM, then μ_S decays exponentially according to the Valet-Fert equation 1.16. For Cu for example l_{sf} is $1\mu m$ at 4.2K and $350nm$

at room temperature [114]. μ_S can be measured to within a few interatomic layers by introducing a second FM.
NLSV can also be used to estimate the local heating at the nanoscale [210, 17]. Heating at the FM-NM interface has a linear (Peltier) and a quadratic (Joule) contribution. The heat current is continuous across the interface, and this generates a further, thermally induced, spin injection. It adds to the electrically induced pumping but its sign depends on the direction of flow of the electrical current, and is opposite if the current flows from the FM to the NM or the other way around. This effect allows to quantify the SDSE introduced in Sec 1.3.1.

1.2.3 Non collinear effects

Bulk magnetization dynamics

The magnetization dynamics of a bulk ferromagnet can be described by the phenomelological **Landau-Lifshitz-Gilbert** equation:

$$\frac{d\boldsymbol{m}}{dt} = \gamma\mu_0 \boldsymbol{m} \times \boldsymbol{H}_{\text{eff}} + \alpha \left(\boldsymbol{m} \times \frac{d\boldsymbol{m}}{dt} \right) , \tag{1.17}$$

in which $\boldsymbol{m}$ is the magnetization direction, γ is the gyromagnetic ratio, $\boldsymbol{H}_{\text{eff}}$ is the effective field including exteral, demagnetization and crystal anisotropy fields. The second term in the right hand side of (1.17) is the Gilbert contribution [83, 141]. When $\boldsymbol{H}_{\text{eff}}$ is constant and $\alpha = 0$, there is no dissipation of energy and $\boldsymbol{m}$ precesses around $\boldsymbol{H}_{\text{eff}}$ with frequency $\omega = \gamma \boldsymbol{H}_{\text{eff}}$. When the damping is activated ($\alpha > 0$), the magnetization direction $\boldsymbol{m}$ is pushed towards the $\boldsymbol{H}_{\text{eff}}$ direction with a chacacteristic time of $1/\alpha\omega$ (Fig1.6).

Spin torques

When a non-polarized current passes through a spin-polarized material, it becomes spin polarized due to the exchange interaction (Sec. 2.5.1) between the electronic spin and the internal magnetization of the FM.
This is normally a one way process in which the magnetization of the spin-polarized material does not experience any change. Nevertheless, when the size of the system shrinks to the nanoscale, the opposite phenomenon is possible, i.e. a spin polarized current affects the local magnetic order of a FM while passing through it, according to the conservation law of angular momentum. This effect is known as **Spin-transfer torque** [213, 21] and, if strong enough, the torque can lead to coherent magnetization precession and even magnetization reversal.
This effect has initiated a new research field in which is possible to control magnetic structure (domain walls, skyrmions) through magnetic nanostructures. Spin torques

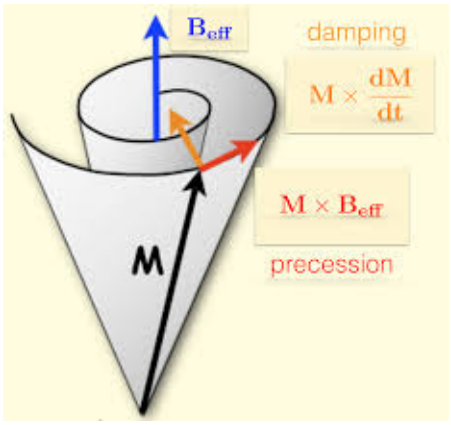

Figure 1.6: Schematic representation of magnetization dynamics. The magnetization $\boldsymbol{M}$ precesses under the effect of the effective field $\boldsymbol{B}_{\text{eff}}$ and spirals down towards the effective field under the effect of the dissipative damping. Fi.7 from Ref. [67].

can be driven by spin-polarized currents [156], thermal currents [99, 274] or optical excitations [167]. Nowadays, current as low as a few tens of μA can switch magnetization at room temperature in metal-oxide semiconductors [78].
A picture of all the torques present into a spin valve is given in Fig. 1.7. $\boldsymbol{T}_{\text{damping}}$ is the damping torque from Eq. (1.17), aready shown in Fig.1.6, $\boldsymbol{T}_{\text{IP}}$ is an in-plane contribution. These two contribution are dissipative, and their sum characterizes the damping process. $\boldsymbol{T}_{\text{OOP}}$ and $\boldsymbol{T}_{\text{field}}$ are non dissipative torques. Their sum characterizes the precession frequency.

Spin pumping

Spin pumping [235, 195, 122, 251, 48] is a basic method of generating a spin current at a NM-FM interface. It can be seen as the analogue of a battery in traditional electronics. When a NM material is attached to a FM with a precessessing magnetization $\boldsymbol{m}(t)$, a spin current "leaks" from the FM to the NM. This spin current exerts a torque on the magnetic moments of the NM. This can be formulated in terms of scattering formalism [235]:

$$\boldsymbol{j}_s = \frac{\hbar}{4\pi}\left(g_r \boldsymbol{m}(t) \times \frac{d\boldsymbol{m}(t)}{dt}\right), \tag{1.18}$$

where g_r is the real part of the mixing conductance $g = g_r + ig_i = \sum(1 - r_\uparrow r*_\downarrow)$ [38, 260] and r_σ is the reflection coefficient for the spin channel $\sigma = \{\uparrow, \downarrow\}$ at the FM-NM interface.

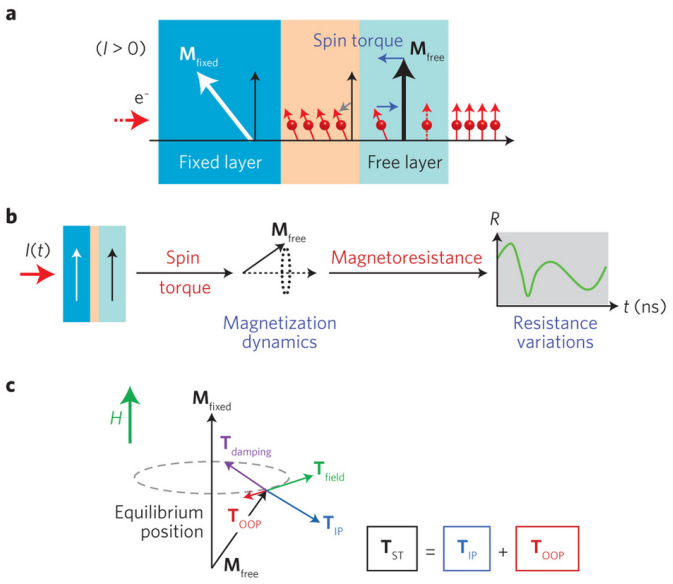

Figure 1.7: **a**: An unpolarized current I enters a spin valve and is polarized by the pinned magnetization $\boldsymbol{M}_{\text{fixed}}$. In the free layer it induces a torque on the magnetization direction. **b**: The current I in **a** can be modulated to get a time dependent spin torque on the free layer. The resistivity of the whole system varies accordingly. **c**: representation of the torques acting on the free layer magnetization $\boldsymbol{M}_{\text{free}}$. Fig 1 from Ref. [147]

1.3 Spin dependent thermoelectric effects

When spin polarisation is considered, the electronic bands and the density of states split in two. Spin-up ($\uparrow$) and spin-down ($\downarrow$) conduction electrons have different scattering rates according to the orientation of their spin. If no spin-mixing mechanism is present, the number of spins up and down are conserved, and we can model the system as two parallel sub-parts. Transport is independent for each of the two channels, so that transport coefficients can be defined for both channels. Thermoelectric transport phenomena presented in Sec. 1.1 have spin-polarized counterparts, the spin dependent Seebeck effect [210, 65, 98, 171, 118] (SDSE) and the spin dependent Peltier effect [74] (SDPE).
Specifically, when a temperature gradient is applied to a spin-polarized metal, spin-up and spin-down electrons "feel" the temperature gradient differently. Eq.(1.1) can be generalized as follows:

$$\begin{pmatrix} \mathbf{j}_\uparrow \\ \mathbf{j}_\downarrow \\ \mathbf{j}_Q \end{pmatrix} = - \begin{pmatrix} \sigma_\uparrow & 0 & \sigma_\uparrow S_\uparrow \\ 0 & \sigma_\downarrow & \sigma_\downarrow S_\downarrow \\ \sigma_\uparrow \Pi_\uparrow & \sigma_\downarrow \Pi_\downarrow & \kappa \end{pmatrix} \begin{pmatrix} \nabla \mu_\uparrow / e \\ \nabla \mu_\downarrow / e \\ \nabla T \end{pmatrix} . \tag{1.19}$$

In Eq. (1.19) $\mathbf{j}_{\uparrow(\downarrow)}$ represent the density of electronic current in the $\uparrow$ ($\downarrow$) spin channel, $\mu_{\uparrow(\downarrow)}$ is the chemical potential for the $\uparrow$ ($\downarrow$) spin channel. $\sigma_{\uparrow(\downarrow)}$, $S_{\uparrow(\downarrow)}$ and $\Pi_{\uparrow(\downarrow)}$ represent the electrical conductivity, Seebeck and Peltier coefficient for the two channels [238, 18].

1.3.1 Spin dependent Seebeck effects

The current densities in the two channels read:

$$\mathbf{j}_{\uparrow,\downarrow} = -\sigma_{\uparrow,\downarrow}\Big(\frac{1}{e}\nabla\mu_{\uparrow,\downarrow} + S_{\uparrow,\downarrow}\nabla T\Big)\,. \tag{1.20}$$

The Seebeck coefficient for ferromagnets is the average of the two Seebeck coefficient S over the electrical conductivity σ for each channel [18]:

$$\langle S\rangle_\sigma = \frac{\sigma_\uparrow S_\uparrow + \sigma_\downarrow S_\downarrow}{\sigma_\uparrow + \sigma_\downarrow}\,. \tag{1.21}$$

This quantity can be measured in the same way as the Seebeck coefficient for non spin-polarized materials.
To measure a spin current on the other side, the new method of non local spin valve (NLSV) has been introduced [114, 115], which is explained in Sec. 1.2.2 and is sketched in Fig. 1.5. This methods exploits the phenomena of **spin pumping** at the ferromagnetic-paramagnetic interface [235, 195, 122].
When a temperature gradient ∇T is applied through a ferromagnet in the absence of an electrical current a spin current is driven by the SDSE [118, 210]:

$$\mathbf{j}_s = -\sigma_F(1-P^2)\Delta S\frac{\nabla T}{2}\,, \tag{1.22}$$

where $\sigma_F = \sigma_\uparrow + \sigma_\downarrow$, P is its polarisation $(\sigma_\uparrow - \sigma_\downarrow)/(\sigma_\uparrow + \sigma_\downarrow)$ and the spin dependent Seebeck coefficient is:

$$\Delta S = S_\uparrow - S_\downarrow\,. \tag{1.23}$$

Experimental results relative to the SDSE are limited to room temperature. Further, no direct measurement of thermal gradients was performed. Experiments are rather complex since the superposition of thermal and electrical contributions to the effective spin injection is difficult to control in such a small devices. The phenomenology of the SDSE remains in the "realm" of electronic diffusion.
Results from extensive calculations are presented for the Seebeck coefficient and the spin dependent Seebeck coefficients in Chapter 4.

1.4 Spin-Caloritronics

Spin Caloritronics [191, 32] studies the mutual interaction of spin and temperature excitations. Spin Caloritronics is an active research field. Both theoretical and experimental aspects are under continuous modification.
The interaction between charge currents and magnetisation dynamic can in general be described by means of general Onsager reciprocity formalism [37].
Conventionally [191], the label "spin" is used to indicate those effects which appear in NMs because of spin (Spin Hall effect, spin Nernst effect) while "anomalous" and "planar" refer to effects happening in FMs when the current is either perpendicular (Anomalous Hall effect, anomalous Nernst effect) or in plane with respect to the flux of current (Planar Hall effect, Planar Nernst effect).
Thermoelectric effects, Anomalous effects and Spin dependent effects are summarized in Tab.1.1.

1.4.1 Intrinsic magnetization dependent effects

The internal magnetization affects transport properties of materials. Traditional transport effects like the Hall effect or thermoelectric effects like the Nernst effect have an anomalous counterpart in ferromagnets.

Anomalous Hall Effect

The Hall effect is the appearance of a transverse electric field when an electric current passes through a normal metal subject to an external magnetic field [93]. The Anomalous Hall Effect [94, 164] (AHE) was discovered soon after the Hall Effect and is the appearance of a transverse electric field in a ferromagnet subject to an electric current flow. In the case of Nickel, the Anomalous Hall resistivity is one hundred times more elevated than the Hall resistivity close to the Curie temperature, while they are similar at low temperature [123]. Today we explain the AHE as a consequence of two microscopic contributions: from disorder related to spin-dependent scattering (called extrinsic) or from an intrinsic contribution due to the Berry phase effect in the k-space [164].

Anomalous Nernst Effects

The **Nernst effect** is the appearance of a transverse electrical field in a NM subjected to an external magnetic field and a temperature gradient perpendicular to each others [211, 183, 158].
Conversely, the **Ettingshausen effect** is a thermal gradient which appears along a conductor subjected to an external magnetic field and an electric current. The

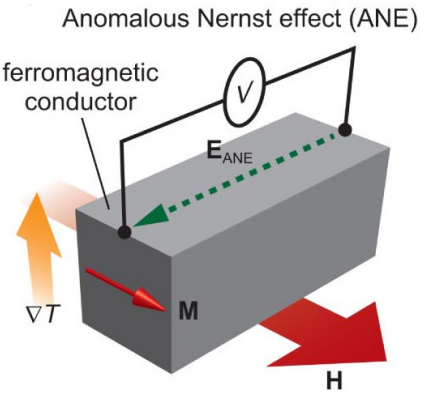

Figure 1.8: Fig 1(b) from Ref. [242]. Schematic representation of the Anomalous Nernst Effect: an electric field $\boldsymbol{E}_{ANE}$ appears in a ferromanget when it is subject to a thermal gradient and an external magnetic field. The direction of $\boldsymbol{E}_{ANE}$ is given by $\boldsymbol{M} \times \boldsymbol{\nabla} T$

thermal gradient is perpendicular to the external fields.
The **Anomalous Nernst Effect** [158] (ANE) consists of the generation of an electrical field parallel to the $\boldsymbol{M} \times \boldsymbol{\nabla} T$ direction when a thermal gradient is applied to a ferromagnet.

1.4.2 Spin orbit coupling dependent effects

Spin orbit coupling (SOC) is a quantum mechanical phenomena with no classical equivalent. Several effects have been observed in materials with high SOC, i.e. heavy metals (HM), e.g. Platinum, Gold, Tantalum, which are absent in lighter materials, with low SOC (e.g. Copper).

Spin Hall Effect

In systems with strong SOC, electrons are scattered according to the direction of their spin. A spin up electron will be scattered by atoms in opposite direction with respect to a spin down electron. This effect is called Spin Hall Effect [104] (SHE, Fig1.9 (**a**)) and was predicted over 40 years ago [57, 58]. It offers a valuable means to generate a spin current from an electrical current and has been extensively investigated [104, 163, 208, 124, 126, 59, 227, 104].
The inverse of the SHE, the **Inverse Spin Hall Effect** [192, 252, 127] (ISHE, Fig1.9 (**b**)) transforms a spin current into a electrical current and is of great experimental importance, since it allows the detection of a spin current through traditional experimental methods.

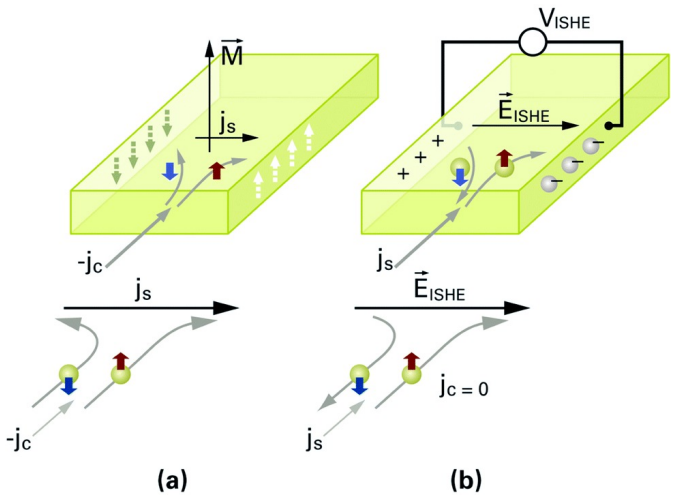

Figure 1.9: Schematic representation of SHE (left) and ISHE (right). A spin current and an electric current can be transformed into each other if SOC is present.

Macroscopically, the SHE and the ISHE efficiency depends on the orientation beween the spin $\boldsymbol{\sigma}$ and the incident current, and on the spin Hall angle θ_H [227, 277, 64, 234]:

$$\boldsymbol{j}_s = \theta_H \boldsymbol{\sigma} \times \boldsymbol{j}_c \text{ (SHE)}\,, \tag{1.24a}$$
$$\boldsymbol{j}_c = \theta_H \boldsymbol{\sigma} \times \boldsymbol{j}_s \text{ (ISHE)}\,. \tag{1.24b}$$

For Pt, $\theta_{Pt} = 0.0037$ [127].

1.5 The Spin Seebeck Effect

The Spin Seebeck effect (SSE) transforms a heat current into a spin voltage [248, 246, 250, 111]. It has been revealed in a large variety of magnetic materials (including magnetic insulators) and in different configurations. It also raised numerous questions for theoreticians, some of which are still debated.

1.5.1 Experimental set-ups

The SSE has been observed in metallic films $Ni_{81}Fe_{19}$ [248], ferromagnetic semiconductors GaMnAs [111, 112], ferromagnetic insulators: $Y_3Fe_5O_{12}$[240], $LaY_2Fe_5O_{12}$[250] and (Mn,Zn)Fe_2O_4 [243], ferrimagnetic insulator La:YIG [245] and the half-metallic Heusler compound Co_2MnSi [34]. This variety establishes that the SSE is a general property of magnetic materials.
A HM strip (generally Platinum) is used as spin current detector thanks to the

Name	Material			Applied Field			Measured Field			
	PM	FM	SOC	$\boldsymbol{E}$	$\boldsymbol{\nabla} T$	$\boldsymbol{H}$	$\boldsymbol{E}_T$	$\boldsymbol{E}_L$	$\boldsymbol{\nabla} T$	$\boldsymbol{\nabla} \mu$
SE	✓				✓			✓		
PE	✓			✓					✓	
HE	✓			✓		✓	✓			
NE	✓				✓		✓			
EE	✓			✓					✓	
AHE		✓	✓	✓			✓			
AHE	✓		✓	✓		✓	✓			
ANE		✓			✓		✓			
SHE	✓		✓	✓						✓
SNE	✓				✓					✓
SSE		✓			✓					✓
SPE		✓				✓			✓	

Table 1.1: Representation of thermoelectrics, anomalous and spin dependent effects.

ISHE. Two main experimental configurations have been proposed to detect the spin current.

Transverse configuration

In the transverse configuration (TSSE) [248, 246, 250, 111, 112, 34, 240] spin current flows perpendicularly to the thermal gradient direction. It is represented in Fig. 1.10 and is the first geometry in which the SSE was observed.
A Permalloy ferromagnetic strip a few millimetres long (along the $\hat{\boldsymbol{x}}$ direction) and 20 nm thick is deposited on a sapphire substrate. Two strips of Pt (10 nm of thickness) are sputtered at the edges of the FM strip ($\hat{\boldsymbol{y}}$ direction).
An external magnetic field $\boldsymbol{H}$ is applied along the $\hat{\boldsymbol{x}}$ direction to overcome the coercive force H_c and align the internal magnetization $\boldsymbol{\sigma}$ (H_c is of about 15 Oe for Py at room temperature [248]). The temperature gradient $\boldsymbol{\nabla} T$ is applied along the $\hat{\boldsymbol{x}}$ direction as well. Experimental data extracted from Ref [248] are reported in Fig. 1.11.

The characteristic length of the SSE signal is surprisingly of the order of a few mm. The characteristic intensity of the voltage measured across the HM is of a few μV for a $\Delta T \approx 20K$. Its output is proportional to the length of the sample.
If the HM is removed or replaced by a lighter paramagnet (Cu) the SSE disappears [248] indicating that the electrical signal obtained comes from ISHE. The voltage produced in the HM is proportional to ΔT and signal measured in the two Pt contacts at the cold (300K) and hot side (300K+ΔT) flows in opposite directions (Fig. 1.11a) [248, 246, 250, 111, 112, 34]. Due to the properties of ISHE (Eq. (1.24)) it is easy to conclude that the spin current at the two opposite edges of the FM flows upward and downward along the $\hat{\boldsymbol{z}}$ direction. Removing the thermal gradient ∇T also deletes the effect.
Another characteristic of TSSE signal can be observed by varying the relative orientation of the thermal gradient and the external magnetization field. The external magnetic field is $H = 100Oe$ and the results are shown in Fig. 1.11b. Inverting the external magnetic field $\boldsymbol{H}$, the SSE signal follows a hysteresis cycle.
The **spatial dependence** of the TSSE signal is studied by varying the position of the HM strip over the FM. A hyperbolic sine profile was found for the SSE $\Delta V/T \propto \sinh(x/\lambda)$ with decay length λ_{SSE} and x being the position of the Pt strip in the La:YIG experiment [247, 245]. λ_{SSE} varies on the scale of a few mm with a minimum at about 100 K up to 8 mm at room temperature. This is shown in Fig. 1.11c.
The **temperature distribution** must be carefully taken into account as well the substrate choice [34]. Infact, the thermal conductivity mismatch between the substrate and the FM film can generate an uncontrolled temperature gradient in the $\hat{\boldsymbol{z}}$ direction when measuring the SSE and this can lead to parasitic contributions from the ANE in the Pt strip[107, 34].

Longitudinal configuration

In the **longitudinal** configuration [240, 245, 244] the spin current $\boldsymbol{j}_s$ is generated parallel to the temperature gradient $\boldsymbol{\nabla} T \parallel \hat{\boldsymbol{z}}$ (Fig. 1.12). The FM is entirely covered with a HM film and an external magnetic field is applied $\boldsymbol{H}$ to align electron spins in the $\hat{\boldsymbol{x}}$ direction. ISHE current is measured in the $\hat{\boldsymbol{y}}$ direction.
The longitudinal configuration is easier to set up and considered more suitable for future applications.
The ISHE in this configuration has some symmetry properties similar to the transverse configuration: it is proportional to ΔT and it is inverted if the thermal gradient points in the opposite direction. Moreover it goes to zero for $\boldsymbol{H} \parallel \hat{\boldsymbol{y}}$. It is clear only in insulating FM though, otherwise the SSE would be entangled to the ANE.
Another important difference is that in the LSSE configuration the sign of the spin

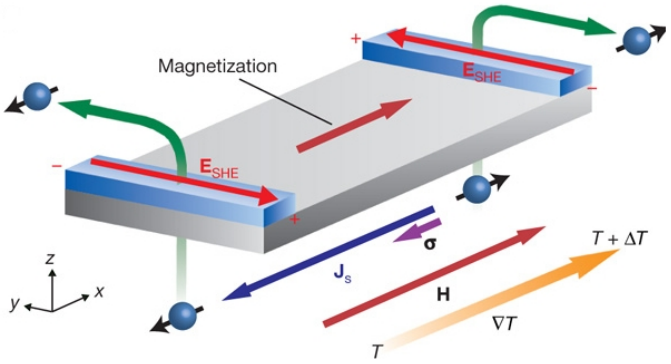

Figure 1.10: Illustration of the Spin Seebeck experimental setup. The effect is induced by a temperature gradient $\boldsymbol{\nabla} T$ into a Py film and consequently a ISHE signal is induced into Pt strip attached on top of the Py. Here $\boldsymbol{J}_s$ represents the spin current, $\boldsymbol{\sigma}$ is the spin polarization vector and $\boldsymbol{H}$ the external magnetic field. From Ref. [248]

injection results to be opposite respect to the TSSE [2, 3, 212] since in the LSSE the electron in the HM contact feels an effective temperature which is above that of the magnons in FM (Sec. 1.5.4).

1.5.2 Thermal gradient and spin current detection

A few comments are in order, to describe the experimental process in its globality. The thermal gradient, for example, is not applied directly to the FM strip, but is applied to the substrate. At the same time, the spin current cannot be measured directly and its detection depends on the spin pumping efficiency through the FM-NM interface. Thus the effective SSE can be quenched by spurious effects.

Role of Pt

Before the SSE discovery, the SHE was the only way of generating a spin current. The ISHE is the most widely used method to detect a spin current in experiments. Platinum has been indispensable to establish the presence of spin current in numerous investigations, e.g. for spin-pumping experiments [192]. It is characterized by a strong SOC, which yields a high value of Spin Hall angle θ_{Pt} (Eq. (1.24)).
Nevertheless, strong magnetic proximity effects have been shown in Pt thin films [106]. It turns out that SHE is entangled to AHE in Pt and that SSE in its longitudinal configuration is strongly entangled to the ANE. This is because Pt is close to the Stoner instability, and its transport properties change if it is close

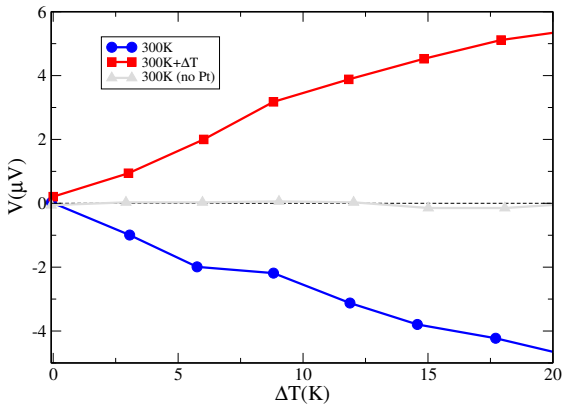

(a) Dependence of the SSE signal measured on the Pt contact on the temperature difference. Filled blue circle: cold side, filled red square hot side. Filled up triangles: measurement directly on the Py strip on the hot side.

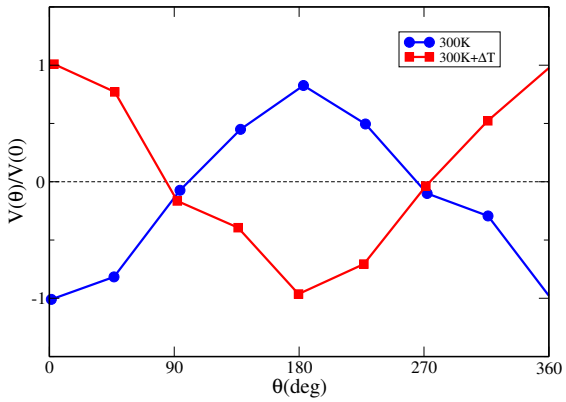

(b) SSE signal as a function of the angle θ between the thermal gradient $\boldsymbol{\nabla} T$ and the magnetization field $\boldsymbol{H}$. The two curves represent the two ends of the FM.

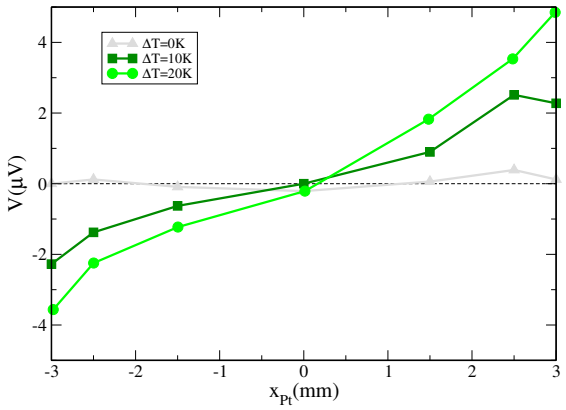

(c) SSE signal as the position of the Platinum strip is changed on the FM. The three lines represent three different values of the total temperature difference between the hot and the cold side of FM.

Figure 1.11: Experimental data for TSSE. Data from Ref. [248].

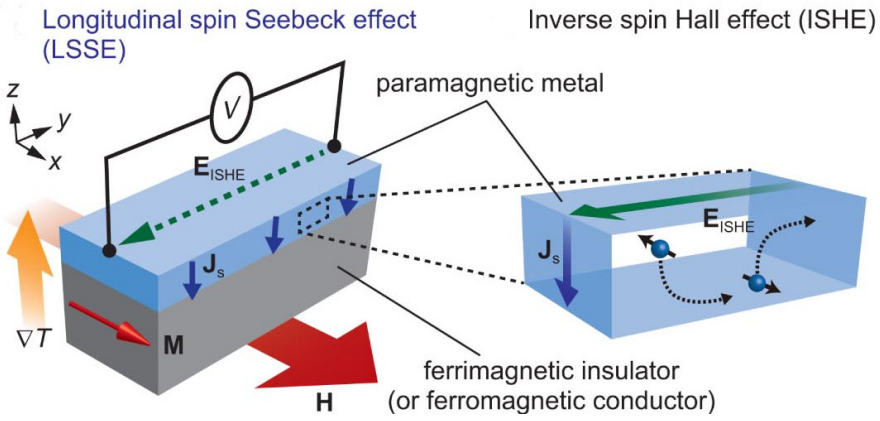

Figure 1.12: Illustration of longitudinal SSE: the spin current is produced parallel to the temperature gradient (z direction). This configuration is clear only for ferromagnetic insulators otherwise ANE would arise. Figure 1 (c-d) from Ref. [242].

to a FM or to a NM.
This contribution has been found to be negligible [125] though, and can be avoided using a heavy metal different from Pt, like Gold or Tantalum.

Role of the substrate

Experimental evidence showed that the substrate plays a fundamental role in the SSE. As first shown in Ref. [111], the SSE signal does not change before and after a part of the ferromagnetic GaMnAs layer in polished away. This experiment underlined that the SSE signal can travel through the substrate (Fig. 1.13a).
In a modified transverse geometry the magnetic $Ni_{81}Fe_{19}$ strip was substituted by a magnetic wire [239, 245] (Fig. 1.13b). A bi-metal wire with 20-nm thick $Ni_{81}Fe_{19}$/10-nm thick Pt bilayer was placed on top of single-crystalline sapphire substrate, which is magnetically and electrically insulating (Fig. 1.13b). Owing to this structure, only acoustic vibrations (phonons), can propagate through the sapphire. A clear SSE was observed, having characteristic symmetry with respect to the direction of $\boldsymbol{H}$ and $\boldsymbol{\nabla} T$, while the SSE disappears if the substrate is changed to a glass one, where phonon lifetimes are much smaller.

A monochromatic sound wave was also directly injected from a piezoelectric generator into a hybrid FM/HM structure (Fig. 1.14). This shows that the phonons in the substrate are important for the SSE to take place (Sec. 1.5.3).

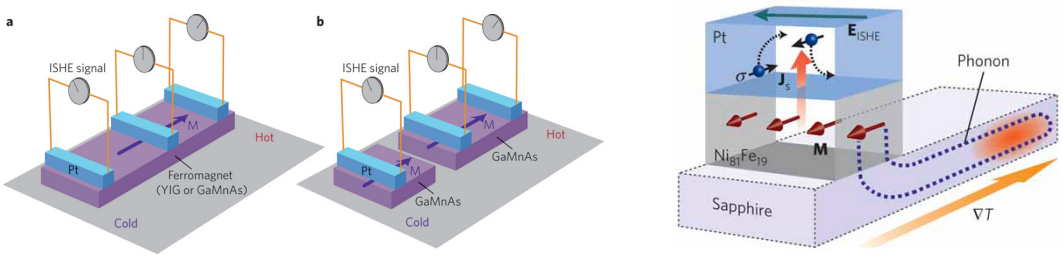

(a) Figure from Ref. [207]. **(b)** Figure from Ref. [239].

Figure 1.13: Illustration of the SSE in two modified transverse configuration. Left: a small part of the FM film is polished away to forbid electric diffusion through the FM. Right: the FM is shrank to the same size as the HM strip.

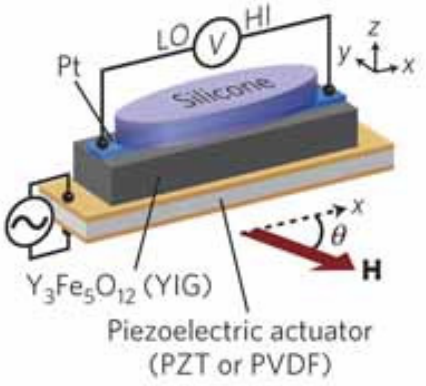

Figure 1.14: Illustration of the acoustic SSE. A monochromatic wave is generated by a piezoelectric actuator and sent into a YIG slab. Figure 4 a from Ref. [239].

Low temperature enhancement

A low temperature enhancement of a few mV/K is observed at around 40-50 K, independently in YIG [4, 245, 245], GaMnAs [112] and Py [245]. The peak corresponds to the increase of the phonon lifetime in the substrate, and to its thermal conductivity [232, 212]. Also in the semiconductor GaMnAs on GaAs, the amplitude of the SSE scales with the thermal conductivity of the GaAs substrate and with the phonon drag of the electrons [112]. At low temperature (< 200 K) the thermal conductivity of materials is increased due to the suppression of inelastic phonon-phonon scattering process. This phenomena gives rise to phonon-electron drag (PED) [26, 145] and its contribution to thermopower [139] is a well known effect.
In Ref. [245] a peak in the SSE signal is observed in single-crystalline YIG but not in polycrystalline YIG. The peak corresponds to the maximum of the thermal conductivity of the single-cristalline YIG due to the increase of the phonon lifetime. This underlines the role of the phonons of the magnetic material for the SSE [4, 276, 239].

1.5.3 Theoretical explanation attempts

The SSE has attracted a lot of interest in the scientific community. The experimental data have grown exponentially and the theoretical explanations did not keep up. A real theory which could reconcile the many different results is difficult.
Several models [269, 112, 1, 3, 230] have been proposed.
What we know from experiments is that both magnons in the FM and phonons in the substrate are necessary for the effect to be measured, besides the electrons in the Pt strips. What we don't know is how magnons and phonons couple to each other and how they produce such a long range effect. An indication about the degree of coupling is the effective temperature of excitations and how this is distributed along the sample.
In this Section I present different theoretical explanations which have been proposed, with an historical perspective, and whether we should or should not discard them.

Entropy contribution picture

The first explaination given was in a diffusive picture for metals [248], with spin up and spin down electrons in the FM pushed in opposite directions. Even taking into account entropy correction [249], this cannot be responsible for all the experimental results, especially for the characteristic length, which is of the order of the millimiter.

Moreover the discovery of the SSE in ferromagnetic insulators [250] definitely excluded this hypothesis. It is worth to point out that this initial misunderstanding coined the expression Spin Seebeck Effect in the first place. This kind of physics is the physics correctly describing the SDSE instead.

Phonon driven SSE

The low temperature enhancement was first observed in [112]. This peak would follow the phonon distribution in the substrate. Moreover, if a substrate with no phonons is used (e.g. glass), the SSE disappears [239]. Moreover not all the phonons have the same importance for SSE as demonstrated in [4]. The phonon-driven SSE was then proposed as a mechanism in [112, 4].

Magnon driven SSE

Experiments have shown that magnons (Sec. 2.5) are ideal candidates for the propagation of spin currents [269, 1, 250, 172]. Linear response calculations [269, 250, 1, 172, 50] showed that an inbalance in temperature between the phonon and the magnon reservoir can induce a spin pumping at the FM-NM interface. This is the leading theory for SSE and will be explained in Sec.1.5.4. This theory underestimates the length scale as well, probably due to incorrect estimation of the relaxation time in the magnon-phonon coupling. It is not clear if the difference in temperature between magnons and phonons exists, if it has local origin, or if it has non-local origin.
Magnon diffusion together with phonon drag gives a good fit of the experimental data [4] and reconciles most of the experimental evidence.
What exactly happens at the interface has not been treated yet. The signal should be proportional to the phonon lifetime in the substrate and a parameter reflecting the acoustic-impedance-matching [138] between the substrate and the ferromagnet.

1.5.4 Thermal fluctuations and spin currents

Microscopic theories have been proposed by Xiao *et al.* [269] (scattering) and by Adachi *et al.*[4, 1, 239] (linear response).
The current understanding of the SSE [191, 3, 245] relies on a mechanism where a heat current induces an out-of equilibrium situation at the interface between the FM and the PM, leading to an imbalance between a fluctuating thermal spin-pumping current [236] $\boldsymbol{j}_{sp}$ from FM to HM and spin torques [185] $\boldsymbol{j}_{fl}$ in the other direction. Following Ref. [245], the magnon states in the FM can be described by means of an effective temperature T_m^*. The electron in the HM can be described by T_e^*. At the interface there are several fluctuations, which are excited by a random magnetic

field $\boldsymbol{h}$ which is the sum over different sources of dissipation: lattice, contacts etc... If we denote j the dissipative source, then $\boldsymbol{h}^{(j)}$, $T^{(j)}$ and $\alpha^{(j)}$ are respectively the random magnetic field, temperature and damping due to source j, then the following Langevin equation must be satisfied:

$$\langle h_i^{(j)}(t) h_{i'}^{(j')}(t') \rangle = \Big(\frac{2k_B T^{(j)} \alpha^{(j)}}{\gamma M_s V_a} \Big) \delta_{jj'} \delta_{ii'} \delta(t - t') \,, \tag{1.25}$$

with $i, i' = x, y, z$ Cartesian components. Here the effective magnon temperature is given by $T_m^* = \frac{\alpha^{(0)} T^{(0)} + \alpha^{(1)} T^{(1)} + \dots}{\alpha}$. If the only two dissipative sources are the lattice and the electrons in the HM then, say for $j = 0$, $T^{(0)}$ and $\alpha^{(0)}$ are the bulk temperature and Gilbert damping parameter (Eq. (1.17)) and for $j = 1$, $T^{(1)} = T_e^*$ is the electron effective temperature and $\alpha^{(1)} = \gamma \hbar g_r / 4\pi M_s V_a$ is the damping enhancement due to the spin pumping with g_r being the real part of the mixing conductance at the FM/HM interface [41, 116, 36, 215]. M_s is the saturation magnetization and V_{coh} is a magnetic coherence volume, a material dependent parameter of the order of (10 nm)^3 scaling as $\sqrt{T_F D^3}$, being D the spin-wave stiffness [269] described in Sec. 2.5.2.
The thermally excited FM attached to a HM would pump a net spin current into the HM $\boldsymbol{j}_{sp}$ proportional to T_m^*.
On the other side, in the HM thermal noise generates current fluctuations $\boldsymbol{j}_{fl}$ which are spin polarised and which generate spin transfer torques proportional to T_e^* [269, 270, 75]. These two contributions sum to zero on average, but out of equilibrium there is a net spin current:

$$\boldsymbol{j}_s = \boldsymbol{j}_{sp} + \boldsymbol{j}_{fl} = \frac{M_s V_a}{\gamma} [\alpha^{(1)} \boldsymbol{m} \times \dot{\boldsymbol{m}} + \gamma \boldsymbol{m} \times \boldsymbol{h}^{(1)}] \,. \tag{1.26}$$

The dc component along the magnetization equilibrium direction is finally:

$$j_s \equiv \langle \boldsymbol{j}_s \rangle = 2\alpha^{(1)} k_B (T_m^* - T_e^*) \,. \tag{1.27}$$

Phonon Drag contribution to the SSE

Phonons and electrons are normally strongly coupled in metals. They are at the same temperature, which is assumed to be the same as the electrons in the HM in the transverse SSE.
Linear response theory showed that also non equilibrium phonons can generate the temperature imbalance in eq.(1.27) [4, 239]. In the acoustic spin pumping, since only phonons with a long wavelength and small frequency are allowed to propagate

in the substrate, the expression of the spin current is derived by a magnon phonon exchange model and is found to be proportional to the power of the external sound wave [3].
When more phonons are allowed to propagate and to interact with magnons, then the phonon amplitude can be replaced with the deviation of the phonon distribution from its equilibrium value. The spin current due to the magnon-phonon interaction is proportional to the phonon lifetime τ_P.

Local vs. non-local pictures

Whether the spin accumulation is caused by a local or a non local mechanism is the object of debate [3].
If one assumes that the interaction happens on a length scale so small that any spatial variation can be neglected, the spin current obtained is proportional to the difference in local temperatures in the FM and in the PM: $\boldsymbol{j}_s = \boldsymbol{j}_{sp} + \boldsymbol{j}_{fl} \propto (T_F - T_N)$. Both phonon and magnon heat current contributions are present in this picture. If magnons are allowed to deviate from thermal equilibrium, then they can "exit" the local domain i^{th} in which $T_{N_i} = T_{F_i} = T_i$ and interact with a domain at temperature $T_j \neq T_i$ through long range interactions. In this non local picture, the spin current is proportional to the difference between domains $T_j - T_i$.
The effective magnon and phonon temperature was first discussed in Ref. [193]. Agrawal *et. al* [5, 239] showed that there is no difference in average temperature between phonons and magnons in the substrate, so that the the local theory is not enough, at least for the systems they tested.
The effect of magnon-phonon thermal relaxation was investigated in Ref. [193]. This works well at room temperature for YIG [269].

1.5.5 Seebeck, spin dependent Seebeck and spin Seebeck effects

The SSE was initially named after the ordinary Seebeck effect (Sec. 1.1) but the two effect have different origins. While the Seebeck effect can be explained in terms of electronic diffusion, the SSE cannot clearly be due to electron diffusion (even taking into account entropy corrections) for several reasons: i) its characteristic length is ∼1 mm, ii) it occurs independently of the electronic structure [111, 122], iii) it involves several excitations: long-wavelength phonons in the substrate, magnons in the sample and electrons in nonmagnetic strip [112, 269, 248, 241, 240], iv) its amplitude is of a few $\mu V/K$ while the SE and SDSE are about three orders of magnitude stronger, v) its amplitude scales with the thermal conductivity of the substrate [112], with a high intensity peak at low temperature suggesting strong

magnon-phonon coupling.
The choice of the name was unfortunate and justified by an initial misunderstanding of the underlying physics in terms of bulk spin accumulation (which is indeed the SDSE). Thus SSE must be carefully differentiated from the SE and SDSE.
The SSE has been extremely fruitful for the scientific community because it raised a number of fundamental questions on the mutual interactions of different excitations at the nanoscale. Understanding how a temperature gradient can excite spin currents, or if the SSE phenomenology can be explained in terms of known mechanisms is a challenge. In a few years, many characteristics have been highlighted by different groups even though experiments differ for the techniques used and for the results obtained, which makes an objective analysis difficult.

Giant spin Seebeck effect in InSb

The Giant spin Seebeck effect (GSSE) [110] is a signal with characteristics similar to the normal SSE, but with two main differences: it was detected in a non-magnetic semiconductor (InSb) and it is three orders of magnitude larger than the SSE (millivolts per kelvin). GSSE is supposed to be mediated by phonon-electron drag, which changes the electrons' momentum and directly modifies the spin-splitting energy through spin-orbit interactions. Owing to the simultaneously strong phonon-electron drag and spin-orbit coupling in InSb, the magnitude of the giant spin Seebeck voltage is comparable to the largest known classical thermopower values. A model for SDSE of InSb in a magnetic field was proposed in [179].

Chapter 2

Electronic and magnetic structures

In Chapter 1, I introduced a general framework to the research presented in this Thesis, *e.g.*, contributing to build a picture of how the electronic structure of materials can be modified by thermomagnetic excitations. Ideally, this picture should help in predicting new materials for Spintronics applications and their properties.
In this Chapter I shall introduce specific theoretical tools of analysis used throughout the rest of the Thesis. I have chosen to give a short overview of Many Electron Theory (Sec. 2.1), Density Functional Theory (Sec. 2.3) and Micromagnetic Models (Sec. 2.5.2) by introducing the basic lexicon. I try to cut down to the bone concepts which can be found in an enormous number of references: classical textbook references for Solid State Physics are [278, 15, 129] and for Electronic Structure [152]. References for Density Functional Theory can be found in [73, 259]. A classical textbook for magnetism is [265] while a more recent book on Spin Waves is [221]. Ref. [29] is a more recent text with the latest developments.
Three ingredients are considered in our recipe of thermally induced spin dynamics: electrons, phonons and magnons. These three excitations respond to different fields, electric, thermal and magnetic. The three reservoirs under consideration (Electrons, Spin and Lattice) can be seen with their own energy and angular momentum, and mutual exchange of energy must respect laws of conservation, angular momentum included. Experiment showed that the three excitations interact with each other with different characteristic times: for electron-lattice time $\tau_{el} \sim ps$, spin-lattice $\tau_{sl} \sim 100ps$ and finally electron-spin $\tau_{es} \sim 100fs$ [237, 82].
Other excitations are possible: optical, plasmonic, etc., which are not considered here.
Phonons and magnons are introduced and a short description of how to calculate their spectrum is given in Sec. 2.4 and Sec. 2.5 respectively. Copper and iron are

taken as examples.
Atomic units are used unless otherwise noted: electronic mass (m), elementary charge (e), reduced Plank's constant ($\hbar$) and Colulomb's constant ($1/4\pi\epsilon_0$) are all unity by definition:

$$m = e = \hbar = 1/4\pi\epsilon_0 \equiv 1\,. \tag{2.1}$$

The unit of length is the Bohr radius ($a_0 \simeq 0.529\mathring{A}$) and the energy unit is one Hartree ($\sim$27.21 eV).

2.1 Many electron system

The time independent physics of a quantum system is described by a wavefunction ψ and energy E obeying the **Schrödinger** :

$$\hat{\mathcal{H}}\psi = E\psi\,, \tag{2.2}$$

with $\hat{\mathcal{H}}$ the Hamiltonian of the system.
The many body Hamiltonian $\hat{\mathcal{H}}_{MB}$ reads:

$$\hat{\mathcal{H}}_{MP} = \hat{\mathcal{H}}_N(\boldsymbol{R}) + \hat{\mathcal{H}}_e(\boldsymbol{r}) + \mathcal{V}_{eN}(\boldsymbol{R},\boldsymbol{r})\,. \tag{2.3}$$

It describes N_e identical electrons of equal mass and charge and N_n nuclei with masses and charges M_I and Z_I. $\hat{\mathcal{H}}_{MB}$ contains a purely nuclear part $\hat{\mathcal{H}}_N(\boldsymbol{R})$ depending on the ionic coordinates $\boldsymbol{R} \equiv \{\boldsymbol{R}_I\}$, a purely electron part $\hat{\mathcal{H}}_e(\boldsymbol{r})$ depending on the electronic coordinates $\boldsymbol{r} \equiv \{\boldsymbol{r}_i\}$ only, and a term describing the ion-electron interaction $\mathcal{V}_{eN}(\boldsymbol{R},\boldsymbol{r})$.
Both $\hat{\mathcal{H}}_N(\boldsymbol{R})$ and $\hat{\mathcal{H}}_e(\boldsymbol{r})$ have a kinetic and an electrostatic component:

$$\hat{\mathcal{H}}_N(\boldsymbol{R}) = -\frac{1}{2}\sum_{I=1}^{N_n}\frac{\nabla_I^2}{M_I} + \frac{1}{2}\sum_{I\neq J}^{N_n}\frac{Z_I Z_J}{|\boldsymbol{R}_I - \boldsymbol{R}_J|}\,, \tag{2.4a}$$

$$\hat{\mathcal{H}}_e(\boldsymbol{r}) = -\frac{1}{2}\sum_{i=1}^{N_e}\nabla_i^2 + \frac{1}{2}\sum_{i\neq j}^{N}\frac{1}{|\boldsymbol{r}_i - \boldsymbol{r}_j|}\,, \tag{2.4b}$$

$$\mathcal{V}_{eN} = -\frac{1}{2}\sum_{i=1}^{N_e}\sum_{I=1}^{N_n}\frac{Z_I}{|\boldsymbol{R}_I - \boldsymbol{r}_i|}\,. \tag{2.4c}$$

Born and Oppenheimer introduced the **adiabatic approximation** [33] to simplify the problem. The ions are "frozen" into some configuration $\{\bar{\boldsymbol{R}}\}$ and the energy of the electrons $E_{\bar{\boldsymbol{R}}}$ depends on this configuration. The two terms containing ionic coordinates $\{\boldsymbol{R}\}$ in Eq. (2.4a) and (2.4c) can be written as an external potential

$\mathcal{V}_{ext}(\bar{\boldsymbol{R}}, \boldsymbol{r})$ which depends parametrically on the ionic positions. This potential represent the energy of electrons in the potential of fixed nucleii. $\hat{\mathcal{H}}_{MP}$ becomes:

$$\hat{\mathcal{H}}_{BO} = \hat{\mathcal{H}}_e(\boldsymbol{r}) + \mathcal{V}_{ext}(\bar{\boldsymbol{R}}, \boldsymbol{r}) \,, \tag{2.5}$$

The electronic and ionic coordinates are now decoupled and we assume that the function $\Phi_{\bar{\boldsymbol{R}}}(\boldsymbol{r})$ is the electronic wave function which parametrically depends on the ionic position $\{\boldsymbol{R}\}$ and solves the Schrödinger equation:

$$\hat{\mathcal{H}}_{BO}\Phi_{\bar{\boldsymbol{R}}}(\boldsymbol{r}) = E_{\bar{\boldsymbol{R}}}\Phi_{\bar{\boldsymbol{R}}}(\boldsymbol{r}) \,, \tag{2.6}$$

We further assume that the eigenfunctions of (2.3) have the form:

$$\Xi(\boldsymbol{R}_i, \boldsymbol{r}_i) = \Psi(\boldsymbol{R}_i)\Phi_{\bar{\boldsymbol{R}}}(\boldsymbol{r}) \,. \tag{2.7}$$

If $\Psi(\boldsymbol{R}_i)$ is chosen to satisfy:

$$\left(\hat{\mathcal{H}}_N(\boldsymbol{R}) + E_{\bar{\boldsymbol{R}}}\right)\Psi(\boldsymbol{R}_i) = E\Psi(\boldsymbol{R}_i) \,, \tag{2.8}$$

it can be shown that $\Xi(\boldsymbol{R}_i, \boldsymbol{r}_i)$ is a suitable eigenfunction of the whole system with total energy E [278]. This method is justified by the fact that the ionic mass is much larger then the electronic one ($M_I \gg m$) and then it makes sense to neglect ionic dynamics since it is much slower than the electronic one.
The Hamiltonian (2.5) can be split further between a set of N "one-body' Hamiltonians in the external potential $\mathcal{V}_{ext}$, plus a term of interaction between electrons $\mathcal{V}_{ee}$:

$$\hat{\mathcal{H}}_{BO} = \hat{\mathcal{H}}_0 + \mathcal{V}_{ee} = \sum_{i=1}^{N} h_i + \mathcal{V}_{ee} \,. \tag{2.9}$$

If the interaction term is neglected ($\mathcal{V}_{ee} = 0$) we get an **electron gas**, i.e. a set of non interacting particles obeying the Schrödinger equation:

$$\hat{\mathcal{H}}_0\Psi(\boldsymbol{r}_1...\boldsymbol{r}_N) = E\Psi(\boldsymbol{r}_1...\boldsymbol{r}_N) \,,$$

whose solution is the product of N_e independent wavefunctions:

$$\Psi(\boldsymbol{r}_1...\boldsymbol{r}_N) = \prod_{i=1}^{N}\psi(\boldsymbol{r}_i) \equiv \prod_{i=1}^{N}\psi_i \,,$$

each one satisfying the Schrödinger equation:

$$\hat{h}_i\psi_i = \epsilon_i\psi_i \,. \tag{2.10}$$

For fermionic systems, the **exchange** of any couple of electrons must be reflected in the wavefunction.
The Slater determinant can be introduced as ansatz for the solution to the non-interacting N-electrons problem:

$$\Psi_{Slater}(\boldsymbol{x}_1 ... \boldsymbol{x}_N) = \frac{1}{\sqrt{N_e!}} \sum_P \left((-1)^P P \left(\prod_{i=1}^{N} \psi(\boldsymbol{r}_i) \right) \right) , \tag{2.11}$$

where $\boldsymbol{x} = (\boldsymbol{r}, \sigma)$ is a combination of spatial and spin coordinates, P runs over all the possible permutations of coordinates $\boldsymbol{x}$, and the $(-1)^P$ is introduced to satisfy the Pauli principle.

2.2 First principles vs Empirical models

The accurate prediction of material properties is one of the main goals of modern computational solid state physics. A balance between the precision in describing relevant particulars of the quantum structure and the computational cost must be sought. In this perspective two kinds of approach can be differentiated, first principles and empirical models.
A **first principle** is a basic assumption which cannot be deduced from any other assumption. A theoretical calculation is called from first principles (or **ab-initio**) if there are no assumptions such as fitting parameters. Density Functional Theory (Sec. 2.3) is probably the most versatile and used model in solid state physics and quantum chemistry. *The Nobel Prize in Chemistry 1998 was divided equally between Walter Kohn "for his development of the density-functional theory" and John A. Pople "for his development of computational methods in quantum chemistry"*[1].
The Korringa, Kohn and Rostocker theory (Sec. 2.5.1) is an alternative *ab-initio* method built on Green's functions instead of wavefunctions.
Empirical models on the other hand are valid for specific cases, when a particular assumption can be made. The **Tight binding** model (TB), e.g., assumes that the ionic potential is so strong that the electrons are strongly bound to the ionic core and occasionally tunnel from one atomic site to the other. The electron-electron interaction is not considered explicitly, and the interaction of a single electron with the other electrons and the lattice is only considered on average.
In the **Micromagnetic Model of Magnetism** (Sec. 2.5.2), the *continuum approximation* is made, i.e., a coarse grained magnetization vector is introduced to describe the magnetization of a **domain**. The length scale is large enough to ignore the atomic structure (10^{-10} m) yet still small enough to resolve larger magnetic

[1] www.nobelprize.org

structure such as **domain walls**, **vortices**, or **skyrmions** (10^{-7} m). Similarly, the time scale, the size and the number of atoms involved in magnetic dynamics is enormous compared to standard *ab-initio* calculations. A representation of the length and time scale relative to some theoretical models is sketched in Fig. 2.1.

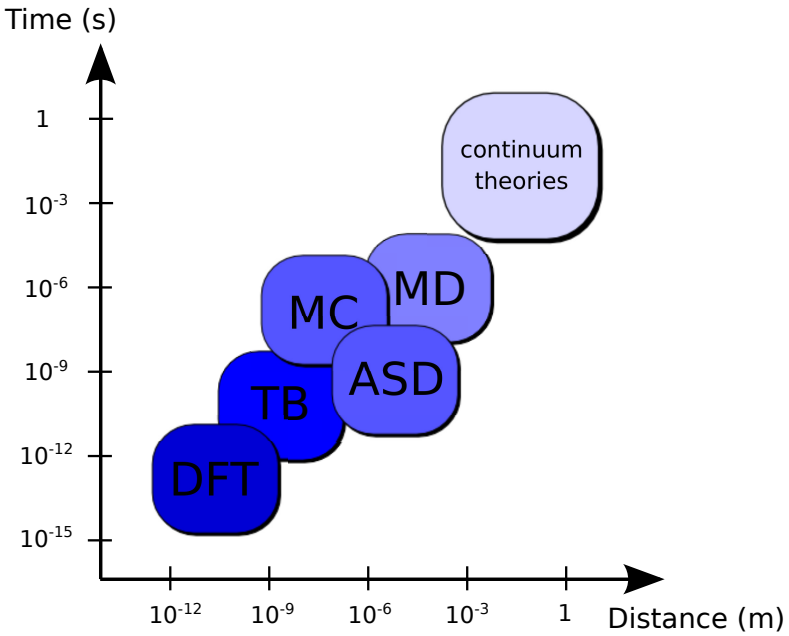

Figure 2.1: Characteristic time and length scales for different simulations techniques in Solid State Physics. The more suitable technique to analyze a specific problem depends on its size. For "large" systems, one should prefer Molecular Dynamics (MD), Monte Carlo (MC) or Atomistic dynamics (AD), while Tight Binding (TB) and DFT are purely quantistic and represent each atom individually, accessing timelength and energy scales which are unaccessible to empirical methods.

2.3 Density Functional Theory

The complete description of a solid can, in principle, be achieved by knowing its total energy. In practice, even after the Born-Oppenheimer approximation, it is impossible to deal with a system of $N \sim 10^{23}$ electrons and therefore further approximations are required.
Density functional theory (DFT) was established thanks to the works of Hohenberg and Kohn [105] and Kohn and Sham [134] and allows to calculate the single particle

total energy using the **electron density**:

$$n(\boldsymbol{r}) = \sum_{\nu=1}^{N} |\psi_\nu(\boldsymbol{r})|^2 \,, \tag{2.12}$$

where ν labels the occupied single-particle orbitals in an effective potential.
Two important theorems due to Hoenberg and Kohn are fundamental for DFT (for which we give no demonstration). The first one states that all physical properties of a system can be obtained knowing its ground state density.

Th 1. *For a given external potential $\mathcal{V}_{ee}(\boldsymbol{r})$, a* universal *functional $F[n(\boldsymbol{r})]$ exists such that the functional*

$$E[n(\boldsymbol{r})] = F[n(\boldsymbol{r})] + \int n(\boldsymbol{r}) v_{ext}(\boldsymbol{r}) \,, \tag{2.13}$$

is minimized by the electronic density of the ground state corresponding to the external potential $v_{ext}(\boldsymbol{r})$.

The second theorem states that the ground state energy can be obtained variationally.

Th 2. *The exact ground state density of the system minimises the energy functional $E[n(\boldsymbol{r})]$*

In a second step, Kohn and Sham managed to map this problem onto a non interacting one with an ansatz: i.e. that it exists a particle Ψ_ν with the same density of the many body system (2.12). They assumed that it is possible to express the unknown universal function as follows:

$$F[n(\boldsymbol{r})] = T[n(\boldsymbol{r})] + \frac{1}{2} \int\int \frac{n(\boldsymbol{r}) \cdot n(\boldsymbol{r'})}{|\boldsymbol{r} - \boldsymbol{r'}|} d\boldsymbol{r} d\boldsymbol{r'} + E_{xc}[n(\boldsymbol{r})] \,, \tag{2.14}$$

i.e., the sum of the one-particle kinetic energy T, the electrostatic electron-electron term (Hartree term), and the exchange-correlation functional E_{xc} which gathers the remaining many-body quantum effects.
Variation of Eq. (2.14) with respect to the electronic density (2.12), provided the number of particle is fixed, leads to the effective potential (called self-consistent field):

$$\mathcal{V}_{SCF}(\boldsymbol{r}) = v_{ext}(\boldsymbol{r}) + \int \frac{n(\boldsymbol{r'})}{|\boldsymbol{r'} - \boldsymbol{r}|} + \frac{\delta E_{xc}[n]}{\delta n(\boldsymbol{r})} \,. \tag{2.15}$$

The **ground state** is determined **self consistently** through the minimisation of the energy functional in eq. (2.14) under the condition that the wavefunctions are

orthonormal:

$$\Big(-\frac{\nabla^2}{2} + \mathcal{V}_{SCF}\Big)\psi_i = \epsilon_i \psi_i \,, \tag{2.16a}$$

$$\mathcal{V}_{SCF}(\boldsymbol{r}) = v_{ext}(\boldsymbol{r}) + \int \frac{n(\boldsymbol{r}')}{|\boldsymbol{r}' - \boldsymbol{r}|} + \frac{\delta E_{xc}[n]}{\delta n(\boldsymbol{r})} \,, \tag{2.16b}$$

$$n(\boldsymbol{r}) = \sum_{i}^{occ} \psi_i^*(\boldsymbol{r})\psi_i(\boldsymbol{r}) \,. \tag{2.16c}$$

A new electronic density is obtained after solving these equations and is compared to the old one. The iteration is repeated until two consecutive steps give results which agree up to a certain numerical precision.

Exchange-correlation functionals

An analytic expression for E_{xc} has not truly demonstrated to exist yet. Only for a few cases it can be calculated exactly, e.g., for an electron gas either in the low [81] or high density [266] limits. One can interpolate for any intermediate value of the density [45].
A number of approximations have been presented for the XCF and are used for practical calculations in DFT, for example Ref. [151].
In the **local density approximation** (LDA) the XCF depends only on the value of the electronic density at each point in space:

$$E_{xc}^{LDA}[n(\boldsymbol{r})] = \int \epsilon_{xc}[n(\boldsymbol{r})]n(\boldsymbol{r})d\boldsymbol{r} \,, \tag{2.17}$$

where $\epsilon_{xc}[n(\boldsymbol{r})]$ is the exchange correlation energy density.
To take into account spatial variations of the density, the **generalised gradient approximation** (GGA) is introduced, in which the parametrisation depends on the first spatial derivative of the density:

$$E_{xc}^{GGA}[n(\boldsymbol{r})] = \int f(n(\boldsymbol{r}), \nabla n(\boldsymbol{r}))d\boldsymbol{r} \,. \tag{2.18}$$

One of the most used forms of f was proposed by Perdew, Burke and Ernzerhof [176].

2.3.1 Practical ground state calculations in DFT

Practical calculations of physical quantities are possible thanks to numerical codes which implement DFT. The main tool I have used for my calculations is

Abinit[2][84, 87, 85].
In the next paragraphs I introduce some concepts relative to DFT calculations. The goal is not to provide a complete overview but only to introduce concepts which will be used in the rest of the Thesis.

Symmetries and Wavefunction

In a perfect periodic infinite crystal the **Bloch theorem** holds. The **translation symmetry** allows to write the wavefunction of an electron moving into a periodic potential in terms of **plane waves** times a periodic function $U(\boldsymbol{r})$ ($U(\boldsymbol{r}+\boldsymbol{R}) = U(\boldsymbol{r})$ for all vectors $\boldsymbol{R}$ of the **Bravais lattice** of the crystal):

$$\psi(\boldsymbol{r}) = U(\boldsymbol{r}) \exp\left(i\boldsymbol{k}\cdot\boldsymbol{r}\right), \tag{2.19}$$

where $\boldsymbol{k}$ is the electron wave vector and $\boldsymbol{r}$ its position. The Schrödinger equation for a single $\boldsymbol{k}$ vector for a single unit cell with periodic boundary conditions needs to be solved in this case.
Bloch functions (2.19) are decomposed in a **Fourier expansion**:

$$\psi_{n,\boldsymbol{k}}(\boldsymbol{r}) = \frac{1}{\sqrt{\Omega}} \sum_{\boldsymbol{G}} C_{n,\boldsymbol{k}}(\boldsymbol{G}) e^{i(\boldsymbol{k}+\boldsymbol{G})\cdot\boldsymbol{r}}, \tag{2.20}$$

where **G** is a vector of the reciprocal lattice and $C_{n,\boldsymbol{k}}$ are the coefficients of the expansion. This expansion is truncated in practical calculations to a finite set of plane waves. For example, one can request that the plane waves to consider are only those such that:

$$\frac{\hbar^2}{2m}|\boldsymbol{k}+\boldsymbol{G}|^2 < E_{\text{cut}}\,. \tag{2.21}$$

Once the wavefunction is calculated, the equations (2.16) can be solved iteratively until some imposed convergence criterion is satisfied. The calculation of the electronic density $n(\boldsymbol{r})$ implies the summation over all the occupied states, labeled ν in eq. (2.12). For periodic systems, the summation runs over the $\boldsymbol{k}$ values and the band index. The spin index should also be considered for magnetic systems (Sec. 2.3.2). The summation over $\boldsymbol{k}$ is actually an integration over the **Brillouin Zone** (BZ), but in practice only a finite set of $\boldsymbol{k}$s is taken into account. A sampling of the reciprocal space according to the symmetry of the system is due to H. J. Monkhorst and J. D. Pack [159] and only the **irreducible** BZ points are considered in the summation. This discretization in Eq. (2.20) can lead to unphysical results: in the case of metallic systems (which are the only kind of materials studied in

[2] *Abinit* is a common project of the Catholic University of Louvain, Corning Incorporated, the University of Liège, the Commissariat à l'Energie Atomique, Mitsubishi Chemical Corp., and the Ecole Polytechnique Palaiseau (`http://www.abinit.org`).

this Thesis), convergence problems arise due to the discontinuity in the occupation number, such that an extremely large number of **k**-points is necessary. Alternatively, the method of **smearing** of the Fermi-Dirac distribution can be used [155, 256].

Electronic band structure and density of states

The **electronic band structure** (EBS) describes the energy wave vector states that electrons in a solid may assume. The EBS is obtained plotting the eigenvalues $\epsilon(\boldsymbol{k})$ against the k-points along some high-symmetry path in the BZ. The EBS holds information about the nature of materials (metals, insulators, etc.), about many physical properties of solids (such as electrical resistivity and optical absorption) and for the description of solid-state devices (transistors, solar cells, etc.). Information about the **inversion symmetry**, **time reversal** and **spin** degrees of freedom of the system are contained as well.
The **density of states** (DOS) of a system $D(\epsilon)$ is the number of states per energy range at each available energy level. The DOS can be projected over electronic orbitals (*s, p, d, f, ...*).

All electron vs. pseudopotential calculations

The complete solution of eq. (2.14) can be separated into three contributions:

$$n(\boldsymbol{r}) = n_{val}(\boldsymbol{r}) + n_{sc}(\boldsymbol{r}) + n_{core}(\boldsymbol{r})\,, \tag{2.22}$$

which come from **valence**, **semi-core** and **core** orbitals. Valence electrons are the solution close to the Fermi Surface and are, in general, delocalized over several atoms. On the contrary, core states are much more localized close to the nucleii. Core states can be calculated by solving an atomic problem, while valence equations have to be calculated solving the Kohn-Sham equations in all space. Semi-core states can be included in the core-electrons problem or treated explicitly as valence equations.
In **all electron** calculations all the wave functions are considered and this implies dealing with the Coulomb singularity for $r \to 0$.
Core electrons are usually constrained near the nucleus and do not affect the macroscopic properties we are interested in (mechanical, electrical, chemical). They actually repel outer electronic shells, so they "screen" the nuclear potential felt by the valence electrons. Thus, it makes sense to replace the true potential of the specific species with a weaker potential, called **pseudo-potential** (PP), which includes core states. In a PP calculation the $1/r$ singularity is simply avoided and the number of plane waves needed in Eq. (2.20) is drastically reduced.

Fermi surface

The **ground state** (GS) is the lowest stable energy level of a system. In the case of a fermionic system, the GS is the configuration in which all the lowest energy states are occupied. At zero temperature, the highest energy value occupied is defined as the **Fermi enegy** (ϵ_F). Alternatively, the **electrochemical potential** μ of a body (ECP) is a thermodynamic quantity referring to the thermodynamic work required to add one electron to the body. The ECP is defined for any temperature, while ϵ_F is a GS property. The **Fermi surface** (FS) is a surface in the reciprocal space defined as the ensemble of points representing quasiparticles with infinite lifetime and energy equal to the Fermi energy ($\epsilon(\boldsymbol{k}) = \epsilon_F$) [152]. The complexity of the FS depends on the system symmetry. It is of special interest if one or more parts of the Fermi surface are parallel to each other, indicating the existence of a special reciprocal vector which connects many pairs of points. This possibility is defined as **nesting** of the Fermi surface and, in this case, the system is more sensitive to perturbations.

An example: Copper

Copper is a chemical element which presents a face-center-cubic symmetry at room conditions, and has a very high thermal and electrical conductivity. I show in some ground state properties calculated with *Abinit*. I employed a GGA pseudopotential generated with the *Fritz Haber Institute* (FHI) code [77, 96, 233, 88, 30]. The electronic configuration for Copper is: $[Ar]3d^{10}4s^1$ while the PP used to generate Fig. 2.3 contains only the 11 electrons of the outer shells ($3d^{10}4s^1$). The energy cutoff was set to 40 Ha. A grid of 24^3 points in the irreducible BZ (kpt) was employed for GS calculations. The smearing of the Fermi-Dirac distribution was set to 0.1 mHa and the WF was converged up to 10^{-9}. The FS of Copper in the first BZP is shown in Fig. 2.2: the white lines represent the boundary of the first BZP, the red surface is the highest occupied valence band. The "cuts" visible in the FS represent momentum directions along which electrons have higher momentum with respect to other directions in which electrons are bounded. The EBS and total DOS for Copper are shown in Fig. 2.3. The DOS shows that most of the valence electrons lie between -5 and 0 eV. The electronic DOS in Fig. 2.3 is enhanced close to the Fermi energy. This particularity is important for transport properties of Copper as will be explained in Chapter 3.

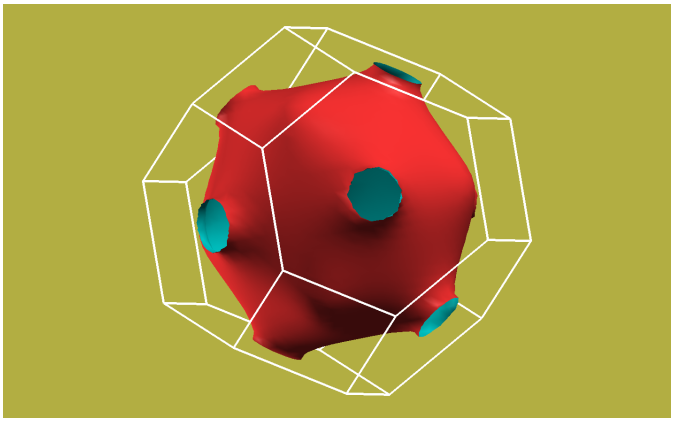

Figure 2.2: Copper Fermi surface (red) inside the first BZP (white lines).

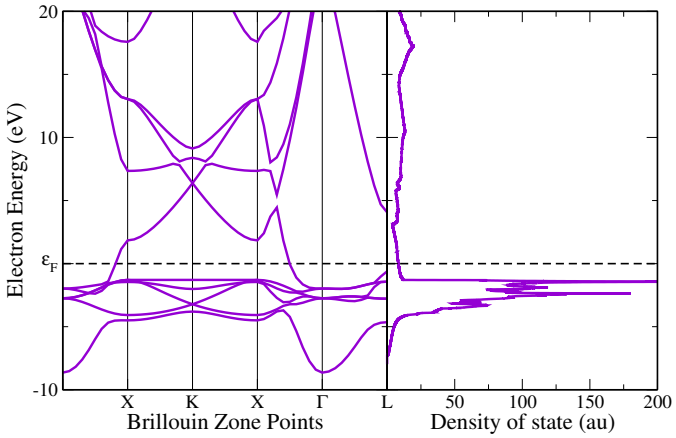

Figure 2.3: EBS (left) and electronic DOS (right) for Copper. The EBS is calculated over a grid of 24^3 irreducible $\boldsymbol{k}$ points in the BZP. The value of energy bands at any point is then interpolated between the values explicitly calculated.

2.3.2 Spin Density Functional Theory

So far, I have totally neglected the information relative to the magnetic order of materials. Spin polarized materials present a variety of phenomenological effects, some simply due to the split of the EBS and of the DOS at the GS level. While DFT is exact to calculate the GS energy of most systems, the spin polarization is not present in the Kohn-Sham formalism. Spin-collinear systems can be treated with Spin Density Functional Theory (SDFT), in which two wavefunctions are calculated for different spin. The two spin "channels" are treated independently and no spin dynamics is taken into account.

The local spin density approximation

The Local Spin Density Approximation (LSDA) is the generalization of LDA to a system of uncoupled, homogeneously polarized, electron gases. The total density of the system is the sum of the two densities for spin up and spin down electronic channels. The exchange correlation energy is:

$$E_{xc}^{LSDA}[\rho_\alpha, \rho_\beta] = \int \rho(\mathbf{r})\epsilon(\rho_\alpha, \rho_\beta)d\mathbf{r}\,, \tag{2.23}$$

with exchange energy given by [173]:

$$E_x[\rho_\alpha, \rho_\beta] = \frac{1}{2}\Big(E_x[2\rho_\alpha] + E_x[2\rho_\beta]\Big)\,, \tag{2.24}$$

and spin polarisation:

$$\zeta(\mathbf{r}) = \frac{\rho_\alpha(\mathbf{r}) - \rho_\beta(\mathbf{r})}{\rho_\alpha(\mathbf{r}) + \rho_\beta(\mathbf{r})}\,. \tag{2.25}$$

Iron

As an example, I report here GS calculations for iron. Iron is a transition metal and represents the most common element on Earth by mass. It is present at ambient condition with bcc symmetry. A similar FHI pseudopotential was used for calculations with a 32^3 grid of irreducible BZ points in the reciprocal space, and an energy cutoff of 50 Ha. In Fig. 2.5, the FS is shown for spin up and spin down electron separately. Spin up and down electrons have extremely different FS, which leads to extremely different transport properties (Sec. 4.1.1). In Fig. 2.4, EBS and DOS of Iron from LSDA are shown. The splitting of the bands is of the order of 1eV.

2.3.3 Density Functional Perturbation Theory

DFT allows the calculation of GS properties, such as EBS, magnetic moment, and so on. The application of **perturbation theory** on top of DFT allows the calculation of physical quantities as responses to external perturbations such as, for example: force, stress tensor, interatomic force constant, elastic constant, phonon-phonon interaction, anharmonic parameters and so on.
Here again, I give only a short overview. Exhaustive descriptions of Density Functional Perturbation Theory (DFPT) can be found in Refs. [29, 86, 19].
Let us consider a system described by the Hamiltonian $\mathcal{H}^{(0)}$ obeying the Schrödinger equation: $\mathcal{H}^{(0)}\,|\psi_i^{(0)}\rangle = \epsilon_i^{(0)}\,|\psi_i^{(0)}\rangle$ with normalized wavefunction $|\psi_i^{(0)}\rangle$ (the index i referring to the eigenvalues of $\mathcal{H}^{(0)}$). This "unperturbed" system undergoes the

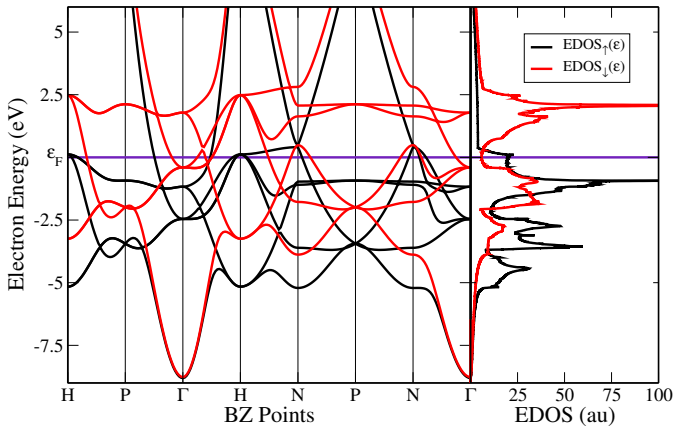

Figure 2.4: Electronic GS properties for Iron from DFT. Left: EBS. Right: EDOS. Black lines: spin up electrons. Red: spin down electrons. More details on the calculation are given in the main text.

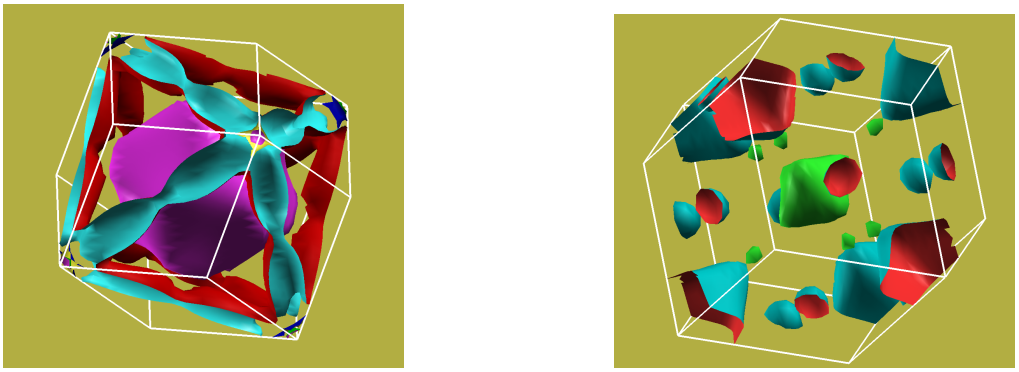

(a) Spin up Fermi surface

(b) Spin down Fermi surface

Figure 2.5: Iron Fermi surface for spin up (left) and spin down (right) inside the first BZ (white lines).

application of an external perturbation $\mathcal{V}_{ext}(\lambda)$ depending on a small parameter ($\lambda \ll 1$):

$$\mathcal{H}(\lambda) = \mathcal{H}^{(0)} + \mathcal{V}_{ext}(\lambda)\,. \tag{2.26}$$

The Schrödinger equation for the perturbed system reads:

$$\mathcal{H}(\lambda)\,|\psi_i(\lambda)\rangle = \epsilon_i(\lambda)\,|\psi_i(\lambda)\rangle\ , \tag{2.27}$$

with $|\psi_i(\lambda)\rangle$ being orthonormal set of wavefunctions ($\langle\psi_i(\lambda)\,|\,\psi_j(\lambda)\rangle = \delta_{ij}$). Assuming that a Taylor expansion is allowed for the Hamiltonian (2.26), its

wavefunction and eigenvalues in terms of the parameter λ are:

$$\begin{aligned}\mathcal{H}(\lambda) &= \mathcal{H}^{(0)} + \lambda\mathcal{H}^{(1)} + \lambda^2 H^{(2)} + \dots ,\\ \psi_i(\lambda) &= \psi_i^{(0)} + \lambda\psi_i^{(1)} + \lambda^2\psi_i^{(2)} + \dots ,\\ \epsilon_i(\lambda) &= \epsilon_i^{(0)} + \lambda\epsilon_i^{(1)} + \lambda^2\epsilon_i^{(2)} + \dots .\end{aligned} \tag{2.28}$$

At the first order in λ, the Schrödinger equation (2.27) becomes:

$$\mathcal{H}^{(0)}\left|\psi_i^{(1)}\right\rangle + \mathcal{H}^{(1)}\left|\psi_i^{(0)}\right\rangle = \epsilon_i^{(0)}\left|\psi_i^{(1)}\right\rangle + \epsilon_i^{(1)}\left|\psi_i^{(0)}\right\rangle , \tag{2.29}$$

which yields the so called **Sternheimer equation** [222]:

$$(\mathcal{H}^{(0)} - \epsilon_i^{(0)})\left|\psi_i^{(1)}\right\rangle = -(\mathcal{H}^{(1)} - \epsilon_i^{(1)})\left|\psi_i^{(0)}\right\rangle . \tag{2.30}$$

This cannot be solved for any random vector since the inversion would lead to a singularity, at $\epsilon_i^{(0)}$ eigenvalue of $\mathcal{H}^{(0)}$. Nevertheless, $|\psi_i^{(0)}\rangle$ is complete and orthonormal, thus we can expand $|\psi_i^{(1)}\rangle$ as follows:

$$\left|\psi_i^{(1)}\right\rangle = \sum_j c_{ij}^{(0)}\left|\psi_j^{(0)}\right\rangle . \tag{2.31}$$

The coefficients $c_{ij}^{(0)}$ can be found separating the space of solutions in two subsets: the space I of all wavefunctions corresponding to the eigenvector $\epsilon_i^{(0)}$ and its complement $I^\perp$:

$$\left|\psi_i^{(1)}\right\rangle = \sum_{j\in I^\perp} \frac{\left\langle\psi_j^{(0)}\right|\mathcal{H}^{(1)}\left|\psi_i^{(0)}\right\rangle}{\epsilon_i^{(0)} - \epsilon_j^{(0)}}\left|\psi_j^{(0)}\right\rangle . \tag{2.32}$$

The Sternheimer equation can then be written in terms of the projector onto the $I^\perp$ subspace $P_{I^\perp} = \sum_{j\in I^\perp}\left|\psi_j^{(0)}\right\rangle\left\langle\psi_j^{(0)}\right|$ as:

$$P_{I^\perp}\left(\mathcal{H}^{(0)} - \epsilon_i^{(0)}\right)P_{I^\perp}\left|\psi_i^{(1)}\right\rangle = -P_{I^\perp}\mathcal{H}^{(1)}\left|\psi_i^{(0)}\right\rangle . \tag{2.33}$$

The singularity has been removed and, hence, the Sternheimer equation can be solved for $|\psi_i^{(1)}\rangle$. Defining the Green's function in the subspace $I^\perp$ for a generic ϵ as:

$$G_{I^\perp}(\epsilon) = \left[P_{I^\perp}\left(\epsilon - \mathcal{H}^{(0)}\right)P_{I^\perp}\right]^{-1} , \tag{2.34}$$

equation (2.33) becomes:

$$P_{I^\perp}\left|\psi_i^{(1)}\right\rangle = G_{I^\perp}(\epsilon_i^{(0)})\mathcal{H}^{(1)}\left|\psi_i^{(0)}\right\rangle , \tag{2.35}$$

i.e., Green's function techniques can be used to solve the Sternheimer equation (2.30). The first-order correction to the energy eigenvalue can be obtained by multiplying Eq. (2.29) by $\langle\psi_i^{(0)}|$:

$$\epsilon_i^{(0)} = \langle\psi_i^{(0)}|\,\mathcal{H}^{(1)}\,|\psi_i^{(0)}\rangle\ . \tag{2.36}$$

The first order correction to the electronic energy can be computed from the 0^{th} order wavefunctions and the perturbing potential at the 1^{st} order (2.36):

$$\begin{aligned} E_{el}^{(1)} =& \sum_{i=1}^{N_e} \langle\psi_i^{(0)}|\,H^{(1)}\,|\psi_i^{(0)}\rangle = \\ =& \sum_{i=1}^{N_e} \langle\psi_i^{(0)}|\,(T+\mathcal{V}_{ext})^{(1)}\,|\psi_i^{(0)}\rangle + \left.\frac{dE_{xc}}{d\lambda}\right|_{\lambda=0}. \end{aligned} \tag{2.37}$$

Eq. (2.37) is equivalent to the **Hellmann-Feynman theorem** of quantum mechanics [102, 71], which states that the derivative of the total energy with respect to a parameter is the expectation value of the derivative of the Hamiltonian with respect to the same parameter.
Similar expressions can be found for higher-order corrections. It can be further shown that the knowledge of the derivatives of the wavefunctions at order n permits the computation of the derivatives of the energy up to order $2n+1$. This result is known as the **"$2n+1$" theorem**. The theorem follows from the variational principle and holds in DFT [89]. Higher order effects (such as anharmonic phonon line widths, Raman scattering cross sections, nonlinear optical response) can be accessed at the same computational cost as harmonic properties.

2.4 Phonons

Phonons are quasiparticles representing the quanta of lattice vibrations. They obey the Bose-Einstein distribution. Let us define $u_j(\boldsymbol{R})$ a small deviation of the atom j from its equilibrium position $\boldsymbol{R}$. The ionic potential undergoes a variation which respect to the equilibrium which can be expressed by a Taylor expansion. In the Born-Oppenheimer approximation (2.5), the external potential $\mathcal{V}_{ext}$ is:

$$\mathcal{V}_{ext}(\bar{\boldsymbol{R}},\boldsymbol{r}) = \mathcal{V}_{eq} + \frac{1}{2}\sum_{\bar{\boldsymbol{R}}\bar{\boldsymbol{R}}'jj'}\left[\frac{\partial^2\mathcal{V}}{\partial u_j(\bar{\boldsymbol{R}})\partial u_{j'}(\bar{\boldsymbol{R}}')}\right]_{eq} u_j(\bar{\boldsymbol{R}})u_{j'}(\bar{\boldsymbol{R}}') + \dots\ . \tag{2.38}$$

jj' label different atoms. The zeroth order term is constant and irrelevant for the dynamics of the system. The first order term vanishes since at equilibrium no

force is acting on the system. The Lagrangian of the system $\mathcal{L} = \mathcal{T} - \mathcal{V}$ obeys the Euler-Lagrange equation:

$$\frac{\partial \mathcal{L}}{\partial u_j(\boldsymbol{R})} = \frac{d}{dt}\frac{\partial \mathcal{L}}{\partial \dot{u}_j(\boldsymbol{R})}\,. \tag{2.39}$$

Solving this equation leads to:

$$m\ddot{u}_j(\boldsymbol{R}) = -\sum_{\boldsymbol{R'}j'} \mathcal{D}_{jj'}(\boldsymbol{R},\boldsymbol{R'})u_{j'}(\boldsymbol{R'})\,, \tag{2.40}$$

where the **dynamical matrix** has been defined as:

$$\mathcal{D}_{jj'}(\boldsymbol{R},\boldsymbol{R'}) \equiv \left[\frac{\partial^2 \mathcal{V}}{\partial u_j(\boldsymbol{R})\partial u_{j'}(\boldsymbol{R'})}\right]_{eq} \equiv \mathcal{C}_{jj'}(\boldsymbol{R},\boldsymbol{R'})/\left(m_j m_{j'}\right)^{\frac{1}{2}}\,, \tag{2.41}$$

where $\mathcal{C}_{jj'}(\boldsymbol{R},\boldsymbol{R'})$ are the Interatomic Force Constants (IFC) of the system. The practical way to analyse crystal vibrations is to calculate the forces between every pair of atoms in the crystal and construct the IFC matrix of the system. Two methods are mostly used for force calculations: **linear response** calculations within DFPT or the **frozen phonon** method within a supercell.

2.4.1 Linear response vs. Finite differences

In linear response, the dynamical matrix is calculated as the inverse dielectric matrix describing the response of the electronic density to a periodic lattice perturbation [203, 178, 19]. The dielectric matrix is nevertheless not always possible to calculate. In the frozen phonon approach [264, 273, 175, 46] the adiabatic approximation is exploited. This approach finds its physical justification in the different time scale which characterizes electron and phonon dynamics: electron relaxation time ($< 10^{-12}$sec) is shorter than phonon relaxation time ($\sim 10^{-12}$sec). So after a lattice perturbation, electrons relax to equilibrium much faster than the lattice itself [209]. A supercell must be built, and one atom is displaced from its equilibrium position by a finite displacement. The force that the displaced atom induces on other atoms in the supercell is calculated from finite differences in energy between the two configurations. These energies are always calculated with some DFT code through the Hellman-Feynman theorem.
The Phonon Dispersion Curves (PDC) for Copper is shown in Fig. 2.6.
Three phonon modes are present since the unit cell is composed of one atom. The linear response (Black line) and the frozen phonon (purple) calculations are compared to experimental data from [72]. Both theoretical curves were calculated on top of the DFT results for Copper GS presented in Sec. 2.3.1 and agree fairly

well with experiments. For DFPT calculations, the energies of the perturbed states (2.36) were calculated at a high symmetry wavevectors in the reciprocal space [202]. The interpolation of the discrete results is performed with two *Abinit* utilities: *mrgddb*, which merges the database containing the IFC for each high symmetry point, and *Anaddb*, which integrates the results.
Practical calculations for frozen phonons is carried out in *Phonopy*[3][231]. When a good convergence in the BZ space is reached, the two methods agree.

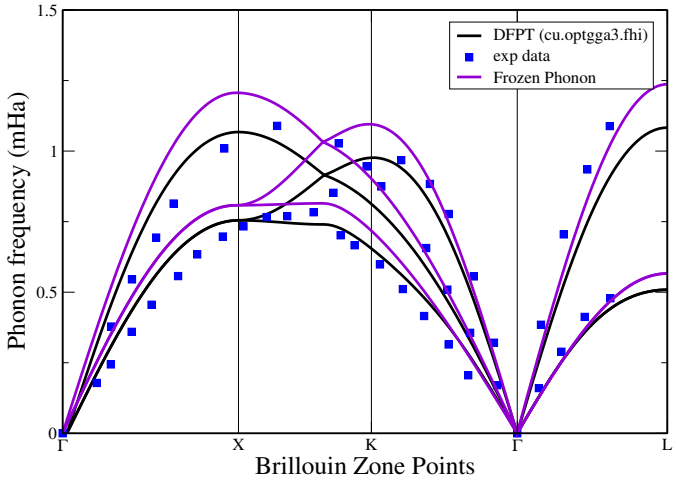

Figure 2.6: Copper PDC along high symmetry directions in the BZP. Full black lines: theoretical DFPT calculations on top of DFT. Full purple line: theoretical adiabatic calculations on top of DFT GS results. Blue full squares: experimental data from [72].

Thermal displacement

All atoms vibrate within a crystalline lattice. This happens also at zero temperature, an effect calles *zero point motion*, which is a purely quantum effect. At finite temperature, atoms vibrate because of thermal agitation. The amplitude of the vibration depends on the temperature, the phonon mode and the mass of the atom. From [261], the time dependent α Cartesian component of atomic displacement ($u_j(\boldsymbol{R})$ in Eq. (2.38)) for an atom of mass m_j at position $\boldsymbol{R}_{jl}$ in the jth atomic position of the lth unit cell is:

$$u_{jl}^{\alpha}(t) = \left(\frac{\hbar}{2Nm_j}\right)^{\frac{1}{2}} \sum_{\boldsymbol{q},\nu} \exp(i\boldsymbol{q}\cdot\boldsymbol{R}_{jl}) e_{\nu}^{\alpha}(j,\boldsymbol{q}) \left[\omega_{\nu}(\boldsymbol{q})\right]^{-\frac{1}{2}} \left[\hat{a}_{\nu}(\boldsymbol{q})\exp(-i\omega_{\nu}(\boldsymbol{q})t) + \hat{a}_{\nu}^{\dagger}(-\boldsymbol{q})\exp(i\omega_{\nu}(\boldsymbol{q})t)\right] , \tag{2.42}$$

[3]Copyright 2009, Atsushi Togo. `phonopy.sourceforge.net`

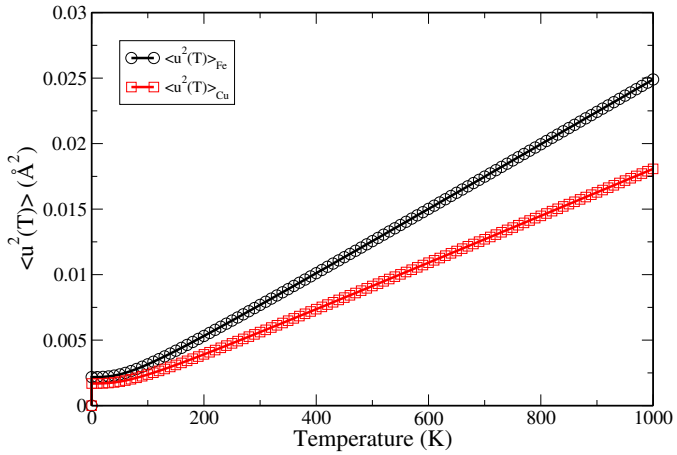

Figure 2.7: Expectation value of the squared atomic displacement vs. temperature. Black with open circles: Iron. Red with open squares: Copper. More calculation details are given in the main text.

with N number of unit cells, $\boldsymbol{q}$ is the wave vector, ν is the index of phonon mode and t is the time and ω is the phonon frequency, λ is the polarization vector of the atom jl and the band ν at $\boldsymbol{q}$. $\hat{a}^\dagger$ and $\hat{a}$ are the creation and annihilation operators of phonon in second quantization notation. The expectation value of the squared atomic displacement reads:

$$\left\langle |u(jl,t)|^2 \right\rangle = \frac{\hbar}{2Nm_j} \sum_{\boldsymbol{q},\nu} \omega_\nu(\boldsymbol{q})^{-1}(1+2n_\nu(\boldsymbol{q}))|\hat{\boldsymbol{n}} \cdot \boldsymbol{e}_\nu(j,\boldsymbol{q})|^2 \,, \tag{2.43}$$

with $n_\nu(\boldsymbol{q})$ being the phonon population given by Bose-Einstein distribution:

$$n_\nu(\boldsymbol{q}) = \frac{1}{\exp(\hbar\omega_\nu(\boldsymbol{q})/\mathrm{k_B}T) - 1} \,. \tag{2.44}$$

Thermal displacement calculations are shown in Fig. 2.7 for Copper and Iron. Being both systems cubic symmetric, the thermal displacement along the three Cartesian axes is the same.

2.5 Magnons

Materials can be traditionally classified according to their magnetic properties: **diamagnetic** materials do not posses a permanent magnetic moment and respond to an external magnetic field with an induced magnetic moment . **Paramagnetic** materials posses a magnetic moment which aligns with an external magnetic field.

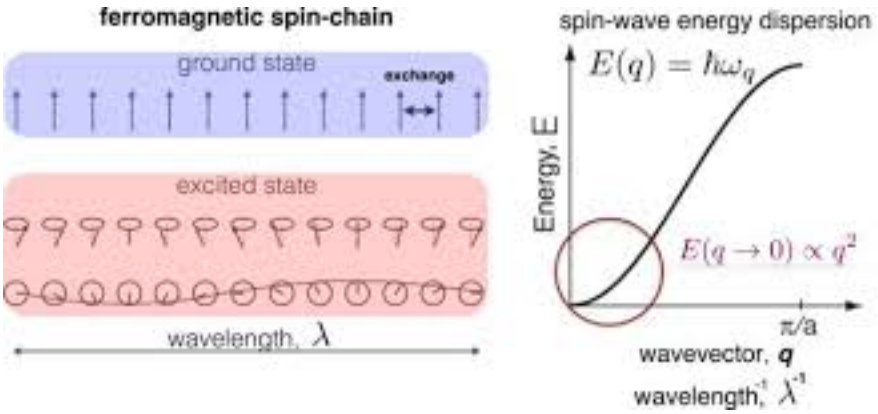

Figure 2.8: Cartoon representing ferromagnetic spin-chain ground state (left top) and a coherent excited state (or spin wave) with wavelength λ (left bottom). On the right the spin wave dispersion curve for a spin chain derived in Sec. 2.5 is shown. Figure 1 from Ref. [67].

Those which show long-range order are distinguished according the relative orientation of nearest neighbors: they align parallel into **ferromagnets** and antiparallel in **antiferromagnets** (with equal amplitude of antiparallel moments) and **ferrimagnet** (for different magnitude of antiparallel moments).
These are examples of magnetic systems with a **collinear** GS. With rising crystal complexity, non-collinear states become possible, such as **magnetic domains**, **magnetic vorteices** and **skyrmions**.
At non-zero temperature, thermal fluctuations compete with magnetic ordering. Magnetic excitations in a magnetic system are called Magnons. A coherent propagation of this excitation is called a **Spin Wave**.
When the fluctuations are large enough, a phase transition from a magnetically ordered configuration to a paramagnetic disordered configuration can happen. The transition temperature to the disordered state is called Curie temperature for ferromagnets and Néel temperature for antiferromagnets.

2.5.1 Magnetic Exchange interaction

Let us introduce the **Heisenberg Hamiltonian** [101]:

$$\mathcal{H} = -\frac{1}{2}\sum_{\langle i,j\rangle} \mathcal{J}_{ij}\boldsymbol{m}_i \cdot \boldsymbol{m}_j \,. \tag{2.45}$$

The $\langle\cdot,\cdot\rangle$ notation means that the two spin are on neighbour sites. Two spins located in two sites $\{i, j\}$ interact through the **exchange interaction**. The origin of the exchange interaction is purely quantum, and represents the difference in

energy of the state due to interchange of two spins.
The total exchange energy of the i^{th} spin interacting with its neighbors is:

$$E_i^{(ex)} = -\boldsymbol{m}_i \cdot {\sum_j}' \mathcal{J}_{i,j} \boldsymbol{m}_j \,. \tag{2.46}$$

The ${\sum}'$ indicates the sum over neighbors. Considering the magnetic moment $\boldsymbol{\mu} = -g\mu_B \boldsymbol{m}$ associated to the spin $\boldsymbol{m}$ (g and μ_B are the gyromagnetic ratio and the Bohr magneton) and the Zeeman relation between magnetic moment and applied magnetic field, we can introduce the **exchange field** as an effective magnetic field which interacts with the i^{th} moment:

$$\boldsymbol{H}_{ex} = -\frac{1}{g\mu_0\mu_B} {\sum_j}' \mathcal{J}_{i,j} \boldsymbol{m}_j \,, \tag{2.47}$$

wwhere μ_0 is the magnetic permeability. In the simple case of parallel spins with equal interaction ($\mathcal{J}_{i,j} = \mathcal{J}$), the exchange field can be written as:

$$\boldsymbol{H}_{ex} = -\frac{Z\mathcal{J}}{g\mu_0\mu_B} \boldsymbol{m} \,, \tag{2.48}$$

with Z numbers of first neighbors. The exchange parameter can be related to the Curie temperature as follows [221]:

$$\mathcal{J} = \frac{3k_B T_c}{ZJ(J+1)}, \tag{2.49}$$

where J is the total (orbital plus spin) angular momentum. Yet other possible interactions are possible for electrons in a conductor: the **superexchange interaction** arises when the electrons of two ions separated by a nonmagnetic ion mediate the magnetic interaction through the common nonmagnetic neighbour. **Indirect** and **itinerant** exchanges can also occur in the cases of rare earth metals, or when the exchange is among conduction electrons [15].

Exchange Integrals

The exchange interaction introduced in Eq. (2.45) can be calculated *ab-initio* with the Korringa, Kohn and Rostocker method [136, 133, 144] (KKR). The electronic structure properties of a system are obtained by means of its Green's functions (GF) by solving the Lippman-Schwinger equation for the Bloch states. The energy associated to the local rotation of magnetization is calculated through the magnetic-force theorem using the formulation of [143]. The exchange coupling parameters $\mathcal{J}_{ij}$ are:

$$\mathcal{J}_{ij} = \frac{1}{4\pi} \int^{\epsilon_F} d\epsilon \Im \left(\mathrm{Tr}_L \{ \Delta_i \hat{T}_\uparrow^{ij} \hat{T}_\downarrow^{ij} \} \right) \,, \tag{2.50}$$

were $\hat{T}$ are scattering operators for spin up and down electrons, Δ_i is the difference between the inverse of the single-site scattering matrices for spin up and down electrons at the site i and Tr_L is the trace respect to the electronic orbital L. The intensity of each exchange interaction with as many neighbors as needed can be calculated within this method.
Practical calculations can be performed with the *SPRKKR* package [4] [61] which implements a spin-polarized relativistic KKR method. In Fig. 2.9, the amplitude of the exchange integrals in a bcc-Fe structure is shown, as a function of the distance between the atomic sites. Two sets of atoms are considered: the atom in the primitive cell (red) and its replicas in adjacent cells and the replicas of the atom at the origin in the adjacent cells (blue). The exchange interaction quickly decades after a few unit cells.

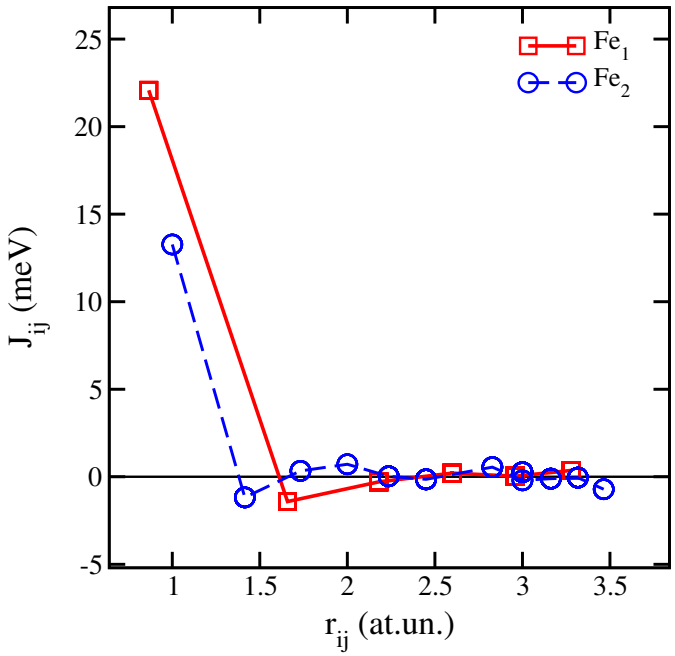

Figure 2.9: Exchange integrals $\mathcal{J}$ for bcc-Fe vs. distance between the atoms. Red full line: Exchange with the neighbor in the primitive cell and its replicas. Blue dashed line: exchange between the atom at the origin and its replicas in the adjacent cells. The first integral is FM and the second is slightly AFM in both cases. Higher order terms are FM but they quickly go to zero. The distance is given in units relative to the conventional cubic cell parameter.

[4] H. Ebert, The Munich SPRKKR package Version 5.4 (2005).

Dispersion relation

Magnon dispersions can be obtained from the Heisenberg Hamiltonian (2.45) for a spin chain. The ground state is the state with all spins aligned in the same direction (Fig. 2.8, top left). The lowest excited state is the system with only one spin flipped with respect to the others. The dispersion relation for a classical spin chain in which the n^{th} spin is flipped can be obtained solving the torque equation:

$$T = \frac{d\boldsymbol{m}_n}{dt} = \boldsymbol{m}_n \times \mathcal{J}\left(\boldsymbol{m}_{n-1} + \boldsymbol{m}_{n+1}\right) , \tag{2.51}$$

the x component of eq. (2.51) is:

$$\frac{dm_n^x}{dt} = \mathcal{J}\left[m_n^y\left(m_{n-1}^z + m_{n+1}^z\right) - m_n^z\left(m_{n-1}^y + m_{n+1}^y\right)\right] , \tag{2.52}$$

we assume that all the unperturbed spins are aligned in the $\hat{\boldsymbol{z}}$ direction and we consider only excitations with small amplitude. It makes sense to assume that $m_n^z \approx m$ and $m_n^{x(y)} \ll m$, with m being the magnitude of electronic spin:

$$\frac{dm_n^x}{dt} = m\mathcal{J}\left[2m_n^y - \left(m_{n-1}^y + m_{n+1}^y\right)\right] , \tag{2.53a}$$

$$\frac{dm_n^y}{dt} = -m\mathcal{J}\left[2m_n^x - \left(m_{n-1}^x + m_{n+1}^x\right)\right] , \tag{2.53b}$$

$$\frac{dm_n^z}{dt} = 0 . \tag{2.53c}$$

We suppose that the x component of a $\boldsymbol{m}_n$ has the form $m_n^x = Se^{i(nqa-\omega t)}$ (a is the spacing between spins and q wavevector), and plugging this into the secular matrix for eq. 2.53, one gets the dispersion curve for magnons:

$$\omega = \frac{2\mathcal{J}m}{\hbar}(1 - \cos qa) . \tag{2.54}$$

In the limit $aq << 1$ we can adopt the quadratic approximation :

$$\omega \simeq \frac{D}{\hbar}q^2 , \tag{2.55}$$

with $D = JSa^2$ defined as the **stiffness**. Second quantization bosonic operators can be introduced through the Holstein-Primakoff transformations [221]. We can than postulate the existence of a particle with effective mass:

$$m^* = \frac{\hbar^2}{2\mathcal{J}a^2} . \tag{2.56}$$

As an example, magnons were analysed in Ref. [205] and a stiffness of $D = 286meV\mathring{A}$ was found.

2.5.2 Micromagnetic model of magnetism

As stated in Sec. 2.2, to deal with the physics of the sub-micrometer scale it is often unnecessary to provide a local description of every electron. It is useful to define a continuous variable $\boldsymbol{M}(\boldsymbol{r})$ describing the average magnetization of a magnetic domain. If the temperature is below the Curie temperature, the modulus $|\boldsymbol{M}|$ of the magnetization is assumed to be everywhere equal to the saturation magnetization M_S. Let us introduce the macroscpin $\boldsymbol{m} = \frac{\boldsymbol{M}}{|M_S|}$. We can treat $\boldsymbol{m}$ as a classical spin.

Total energy

The static equilibrium configuration minimizes the total magnetic energy:

$$E = E_{ex} + E_{anis} + E_Z + E_{demag}\,, \tag{2.57}$$

subject to the constraint $|\boldsymbol{M}| = M_s$ or $|\boldsymbol{m}| = 1$. The different contributions are listed below. E_{ex} is the phenomenological exchange energy:

$$E_{ex} = D \int_V \sum_i (\nabla m_i)^2 dV\,, \tag{2.58}$$

D being the **stiffness** of the crystal (Eq. (2.55)). The magnetic anisotropy term can be written as

$$E_{anis} = -\int_V K m_z^2 dV\,, \tag{2.59}$$

with K being the **anisotropy constant** in the uniaxial anisotropy. When the shape of the electronic orbital is taken into account, the energy depends on the orientation of the orbital respect to the moment direction of the surrounding ions. The third term is the Zeeman energy described in Eq. (2.48):

$$E_Z = -\mu_0 \int_V \boldsymbol{M} \cdot \boldsymbol{H_{ext}} dV\,. \tag{2.60}$$

Finally, we can consider the energy due to the demagnetizing field $\boldsymbol{H}_d$

$$E_{demag} = -\frac{\mu_0}{2} \int_V \boldsymbol{M} \cdot \boldsymbol{H}_d dV\,. \tag{2.61}$$

Other terms can be added to this scheme, such as the magnetoelastic energy.

2.6 Linear response vs. Finite differences

The description of finite temperature magnetism *ab-initio* is a challenging problem. While the ground state of a large class of collinear [161, 40, 49] and non collinear materials [194, 137] have been successfully described by LSDA (Sec. 2.3.2), magnetic excitations even at low energy are difficult to describe.
As briefly explained in Sec. 2.4, vibrational and charge excitations can be decoupled within the adiabatic approximation. Two practical methods are in principle possible for magnons calculations, in analogy with phonons calculations: a linear response and a frozen magnon approaches. A rigorous linear response *ab-initio* theory has been presented for the calculation of spin fluctuations induced by an external magnetic field [197]. Within this method, a generalization of the Born-Oppenheimer approximation can be used to decouple spin and charges into a many body system [169] for a non-collinear configuration. This method was implemented into a constrained DFT scheme [80].
An alternative scheme has been developed in Ref. [92]. The adiabatic approach neglects the electron spin-flip for example, but yields a magnon stiffness with the same accuracy [92].

2.6.1 Mean Field Approximation

Within the Mean Field Approximation (MFA) it is possible to study the physics of one spin in the magnetic field produced by all the other spins [109, 154]. We modify the first neighbors Hamiltonian (2.45) introducing the sum over different sublattices μ, ν:

$$\mathcal{H}_{\text{eff}} = -\sum_{\mu,\nu} {\sum_{i,j}}' \mathcal{J}_{ij}^{\mu,\nu} \boldsymbol{m}_i^{\mu} \boldsymbol{m}_j^{\nu}. \tag{2.62}$$

In Eq. (2.62), i, j refer to the magnetic moments located at positions $\boldsymbol{R}_i^{\mu}$ and $\boldsymbol{R}'^{\nu}_j$ located within one of the sublattices. The primed sum indicates that the interaction of identical atoms in two different sublattices shall not be considered ($\boldsymbol{R}_i^{\mu} \neq \boldsymbol{R}'^{\nu}_j$). Let $\langle s^{\nu} \rangle$ be the average of the spin located at $\boldsymbol{R}_i^{\nu}$ in the $\hat{\boldsymbol{z}}$ direction. The Curie temperature (Eq. (2.49)) within the MFA can be calculated [13] by solving the system of coupled equation:

$$\langle s^{\mu} \rangle = \frac{2}{3k_B T} \sum_{\nu} J_0^{\mu,\nu} \langle s^{\nu} \rangle, \tag{2.63a}$$

$$(\Theta - T\boldsymbol{I})\, \boldsymbol{m} = 0, \tag{2.63b}$$

$$J_0^{\mu,\nu} = \sum_{\boldsymbol{R} \neq 0} J_{0\boldsymbol{R}}^{\mu,\nu}, \tag{2.63c}$$

with: $\Theta_{\mu\nu} = (2/3k_B)J_0^{\mu,\nu}$ and $\boldsymbol{m}$ being the vector of $\langle s^\nu \rangle$s.
The Curie temperature is the largest eigenvalue of Θ. Thus the knowledge of the exchange integrals allows in principle to calculate the Curie temperature.

2.6.2 Atomistic Spin Dynamics

The Magnon Band Structure (MBS) can also be obtained by Fourier transforming Eqs. (2.62) and (2.63c)

$$\mathcal{H} = -N \sum_{\boldsymbol{q}} \mathcal{J}(\boldsymbol{q}) \boldsymbol{m}(\boldsymbol{q}) \boldsymbol{m}(-\boldsymbol{q}) \,. \tag{2.64}$$

This approach neglects the thermal dependence of $\mathcal{J}$.
Dynamical properties of magnetic systems can be retrieved through the Atomistic Spin Dynamics method (ASD). We introduce the space-time correlation function:

$$C(\boldsymbol{r}', t') = \langle \boldsymbol{m}(\boldsymbol{r}, t) \cdot \boldsymbol{m}(\boldsymbol{r} + \boldsymbol{r}', t + t') \rangle \,. \tag{2.65}$$

Spin wave excitations can be calculated through the Fourier transform of the correlation function, also called dynamic structure function:

$$S(\boldsymbol{q}, \omega) = \int d\boldsymbol{r} e^{-i\boldsymbol{q}\cdot\boldsymbol{r}} \int dt e^{-i\omega t} C(\boldsymbol{r}', t') \,, \tag{2.66}$$

sharp peaks in this quantities represent excitations which are well defined, that correspond to magnons.

Chapter 3

Semiclassical Transport Theory

In this Chapter, I introduce the semiclassical transport theory based on the Boltzmann Transport Equation. Two possible approximations to solve this equation are presented: the Relaxation Time Approximation (Sec. 3.3.1) and the Variational Approach (Sec. 3.4). The Fermi Surface Harmonics basis set, Generalized Spectral Functions and the Lowest Order Variational Approximation formulated by P.B. Allen [9, 8] are introduced and fully described in Secs. 3.5 and 3.6.
The Boltzmann Transport Equation is solved in a closed form and macroscopic transport coefficients presented in Sec 1.1 are given in terms of Generalized Spectral Functions. The Elastic and Inelastic electron-phonon scattering cases are also discussed. More references on this approach can be find in two textbooks [11, 10]. Results for Copper are presented alongside.

3.1 Electron transport

The *Boltzmann Transport Equation* (BTE) was derived in 1872 and describes the statistical behaviour of a thermodynamic system out of equilibrium in the frame of kinetic theory for gases [31]. The theory was extended to the semiclassical case of electrons in materials thanks to P. Drude, H. Lorentz, A.Sommerfeld and F. Bloch [55, 54, 216, 217, 27]. Landau [140] introduced the idea of a single-particle electronic excitation or *quasiparticle* with charge $\pm|e|$, spin $\pm 1/2$, wavevector $\boldsymbol{k} \pm 1/l_{\boldsymbol{k}}$ and energy $\epsilon_{\boldsymbol{k}} \pm \hbar/\tau_{\boldsymbol{k}}$. $l_{\boldsymbol{k}} = v_{\boldsymbol{k}}\tau_{\boldsymbol{k}}$ is the mean free path and $\tau_{\boldsymbol{k}}$ is the statistical time before the excitation loses it sharp definition in energy or momentum. A distribution function $F(\boldsymbol{k}, \boldsymbol{r}, t)$ is introduced which measures the number of carriers with wavenumber $\boldsymbol{k}$ that are out of equilibrium in the neighborhood of the spatial vector $\boldsymbol{r}$ at the time t.
The BTE is valid in the *mesoscopic case*, e.g. when the system is large enough to neglect *quantum interference* effects and small enough to consider electrons

mean-free path much smaller than the size of the system. A complete introduction to the argument, and a proper discussion can be found in Ref. [229].

Current

The electronic current density per volume (V) is defined as:

$$\boldsymbol{j}_e = -\frac{e}{V}\sum_k \mathbf{v}_{\boldsymbol{k}} F(k). \tag{3.1}$$

k denotes the quasiparticle state and is shorthand for $(\boldsymbol{k}, n, \sigma)$, $F(k)$ is the distribution function of the state k with energy $\epsilon_{\boldsymbol{k}}$. $\mathbf{v}_{\boldsymbol{k}}$ is the group velocity $\mathbf{v}_{\boldsymbol{k}} = \boldsymbol{\nabla}_{\boldsymbol{k}}\epsilon_{\boldsymbol{k}}/\hbar$. An external electric field $\boldsymbol{E}$ accelerates electron wavepacket according to $\hbar\dot{\boldsymbol{k}} = -e\boldsymbol{E}$. After an infinitesimal time interval of δt, electrons are rigidly shifted in the reciprocal space of an infinitesimal quantity $\delta\boldsymbol{k} = +e\boldsymbol{E}\delta t/\hbar$. This is the *rigid shift* ansatz. Let us suppose [278] that the occupancy of the state $\boldsymbol{k} + \delta\boldsymbol{k}$ when the field is applied is the same as the unperturbed $\boldsymbol{k}$ state:

$$F(k) = f(k + \delta k) = f(k + e\boldsymbol{E}\delta t/\hbar), \tag{3.2}$$

where $f(k)$ is the distribution function of the unperturbed state. Empirically, it is possible to define the electrical conductivity σ (Sec. 1.1.1):

$$\boldsymbol{j}_e = \sigma\boldsymbol{E} = \frac{e^2}{m^*}\tau_{\mathrm{tr}}\boldsymbol{E}, \tag{3.3}$$

where τ_{tr} is the macroscopic relaxation time and m^* is the electron effective mass:

$$\left(\frac{1}{m^*}\right)_{\mathrm{eff},\alpha\beta} = \frac{\partial^2\epsilon_{\boldsymbol{k}}}{\hbar^2\partial k_\alpha \partial k_\beta}. \tag{3.4}$$

We define the generalized effective mass tensor:

$$\left(\frac{n}{m^*}\right)_{\mathrm{eff},\alpha\beta} \equiv \frac{1}{V}\sum_{\boldsymbol{k}} v_{\boldsymbol{k}\alpha} v_{\boldsymbol{k}\beta}\left(-\frac{\partial f_k}{\partial\epsilon_{\boldsymbol{k}}}\right) = \frac{1}{V}\sum_{\boldsymbol{k}}\left(\frac{1}{m^*}\right)_{\mathrm{eff},\alpha\beta} f(k), \tag{3.5}$$

where an integration by part has been carried out in the last equality.

Phenomenological resistivity

A phenomenological estimation of resistivity for metals is the Bloch-Grüneisen formula [27, 28, 91]:

$$\rho(T)_{BG} = \rho_0 + \frac{16\pi^2\lambda_{\mathrm{tr}}\omega_D}{4\pi(n/m)_{\mathrm{eff}}e^2}\left(\frac{2T}{\theta_D}\right)^5 \int_0^{\frac{\Theta_D}{2T}} \frac{x^5}{\sinh^2 x}dx, \tag{3.6}$$

where the temperature dependent part is separated from ρ_0 which is the residual resistivity due to scattering from defects. The resistivity is linear in the temperature for high temperatures while at low temperature it goes as $\rho \propto T^5$. $\Theta_D = \frac{h\omega_D}{k_B}$ is the Debye temperature, e.g. the temperature of a crystal's highest normal mode of vibration (which can be obtained from phonon DOS calculations or specific heat measurements) and the Debye frequency $\omega_D = \left(\frac{3N}{4\pi V}\right)^{1/3} v_s$ (v_s is the speed of sound in a solid).
$\lambda_{\mathrm{tr}}/\omega_p^2$ macroscopically characterizes the electron-phonon interaction.
$\omega_p^2 = 4\pi(n/m)_{\mathrm{eff}}e^2$ defines the Drude plasma frequency. λ_{tr} is the electron-phonon coupling constant and is closely related to the Eliashberg coefficient λ for superconducting materials [11, 7]. It is possible to extract ω_p and λ_{tr} separately from experiments. For quite a few metals, DFT produces reasonable results for ω_P [10]. This allows an empirical determination of λ_{tr}, provided that the resistivity is known. Actually, we present a *first principle* derivation of λ_{tr} in Sec. 3.7.

Scattering mechanisms

In kinetic theory [278], we postulate that the probability that a scattering event occurs in the infinitesimal time dt shall be $dt/\tau_{\boldsymbol{k}}$. The probability that a quasiparticle "lives" (e.g. that the system evolves back to equilibrium) decreases exponentially with characteristic time $\tau_{\boldsymbol{k}}$. The distribution function then obeys:

$$\delta F(k,t) = \delta F(k,t=0)e^{-t/\tau_{\boldsymbol{k}}}, \tag{3.7}$$

Various scattering mechanisms can affect the lifetime of quasiparticles in metals, each with its characteristic time: impurities, electron-phonon interaction, Coulomb interaction between electrons and holes, spin-flip scattering etc.
The full relaxation time is given by Matthiessen's rule [10] which sums up the contributions from various scattering sources when these events are independent:

$$\frac{1}{\tau_{\mathrm{tr}}} = \frac{1}{\tau_{\mathrm{imp}}} + \frac{1}{\tau_{\mathrm{ep}}} + \frac{1}{\tau_{eh}} + \frac{1}{\tau_{sf}} + \ldots, \tag{3.8}$$

Fermi's golden rule gives a simple estimation of lifetimes τ for the scattering event:

$$\hbar/\tau_{\mathrm{imp}} = 2\pi n_{\mathrm{imp}}|V_{\mathrm{imp}}|^2 N(0), \tag{3.9a}$$
$$\hbar/\tau_{\mathrm{ep}} = 2\pi n_{\mathrm{ph}}|V_{\mathrm{ep}}|^2 N(0), \tag{3.9b}$$
$$\hbar/\tau_C = 2\pi n_{\mathrm{pairs}}|V_C|^2 N(0), \tag{3.9c}$$

where n_{imp}, n_{ph}, n_{pairs} arethe density of impurities, the number of phonons or the number of electron-hole pairs respectively and V_{imp}, V_{ph} , and V_C are the scattering

matrix for various scattering events. $N(0)$ is the density of states at the Fermi level:

$$N(0) = \frac{V_{\text{cell}}}{(2\pi)^3} \int d^3\boldsymbol{k} \delta(\epsilon_{\boldsymbol{k}}) = \frac{V_{\text{cell}}}{(2\pi)^3} \int_{FS} \frac{ds_{\boldsymbol{k}}}{|\hbar \mathbf{v}_{\boldsymbol{k}}|}, \tag{3.10}$$

with V_{cell} being the cell volume and $ds_{\boldsymbol{k}}$ an element of Fermi surface.
The order of magnitude can be estimated as follows:

$$\hbar/\tau_{\text{imp}} \sim n_{\text{imp}} \epsilon_F, \tag{3.11a}$$

$$\hbar/\tau_{\text{ep}} \sim k_B T, \tag{3.11b}$$

$$\hbar/\tau_C \sim (k_B T)^2/\epsilon_F. \tag{3.11c}$$

The relative contributions depend on the temperature [10]. Usually Coulomb scattering dominates at high temperatures, impurity scattering dominates at low temperatures (except for clean materials) and in the intermediate range phonon scattering dominates [79].

3.2 Boltzmann Transport Equation

Assuming that a distribution function F_k which measures the number of carriers in the state $k = (\boldsymbol{k}, \boldsymbol{r}, t)$ exits, it can change in time according to three mechanisms [278]:

i) diffusion:

$$\left.\frac{\partial F_k}{\partial t}\right|_{\text{diff}} = -\mathbf{v}_{\boldsymbol{k}} \cdot \frac{\partial F_k}{\partial \boldsymbol{r}}, \tag{3.12}$$

ii) drift under external fields:

$$\left.\frac{\partial F_k}{\partial t}\right|_{\text{drift}} = -\frac{e}{\hbar}\Big(\boldsymbol{E} + \frac{1}{c}\mathbf{v}_{\boldsymbol{k}} \times \boldsymbol{H}\Big) \cdot \frac{\partial F_k}{\partial \boldsymbol{k}}, \tag{3.13}$$

iii) scattering.

The BTE reads [278]:

$$\frac{dF_k}{dt} = \left.\frac{\partial F_k}{\partial t}\right|_{\text{diff}} + \left.\frac{\partial F_k}{\partial t}\right|_{\text{drift}} + \left.\frac{\partial F_k}{\partial t}\right|_{\text{scatt}}. \tag{3.14}$$

In the *steady state*, the distribution function does not evolves, yielding the general form of the BTE:

$$-\mathbf{v}_{\boldsymbol{k}} \cdot \frac{\partial F_k}{\partial \boldsymbol{r}} - \frac{e}{\hbar}\Big(\boldsymbol{E} + \frac{1}{c}\mathbf{v}_{\boldsymbol{k}} \times \boldsymbol{H}\Big) \cdot \frac{\partial F_k}{\partial \boldsymbol{k}} = -\left.\frac{\partial F_k}{\partial t}\right|_{\text{scatt}}. \tag{3.15}$$

Further approximations can be made by assuming a uniform temperature gradient ∇T which produces a small deviation from the local equilibrium distribution function, so that the variation in space is given by:

$$\frac{\partial F_k}{\partial \boldsymbol{r}} \sim \frac{\partial F_k}{\partial T}\nabla T = \frac{\epsilon_{\boldsymbol{k}}}{T}\frac{\partial F_k}{\partial \epsilon_{\boldsymbol{k}}}\nabla T, \tag{3.16}$$

and, ignoring the magnetic field in the drift term, f_k depends now only on the energy $\epsilon_{\boldsymbol{k}}$:

$$\frac{\partial f_k}{\partial \boldsymbol{k}} = \frac{\partial f_k}{\partial \epsilon_{\boldsymbol{k}}}\frac{\partial \epsilon_{\boldsymbol{k}}}{\partial k} = \hbar\frac{\partial f_k}{\partial \epsilon_{\boldsymbol{k}}}\frac{\partial}{\partial k}(\epsilon_{\boldsymbol{k}}/\hbar) = \hbar\frac{\partial f_k}{\partial \epsilon_{\boldsymbol{k}}}\mathbf{v}_{\boldsymbol{k}}. \tag{3.17}$$

Eq. (3.15) becomes:

$$-\mathbf{v}_{\boldsymbol{k}}\cdot\left(e\boldsymbol{E} + \frac{\epsilon_{\boldsymbol{k}}}{T}\boldsymbol{\nabla}T\right)\frac{\partial f_k}{\partial \epsilon_{\boldsymbol{k}}} = -\left.\frac{\partial F_k}{\partial t}\right|_{\text{scatt}}. \tag{3.18}$$

3.2.1 Linearized Boltzmann Equation

At *equilibrium*, the distribution function is $F_k = f_k$ and there is no collision: $\partial F_k/\partial t|_{\text{scatt}} = 0$. In a *steady state* not far from *equilibrium* the BTE can be written by taking f_k instead of F_k on the left hand side of Eq. (3.15) and the lowest non vanishing power of $(F_k - f_k)$ for the scattering term.
In the case of *elastic* scattering, the intrinsic transition rate $\mathcal{Q}_{\boldsymbol{k}\boldsymbol{k}'}$ from the state $\boldsymbol{k}$ to $\boldsymbol{k}'$ is symmetric respect to the $\boldsymbol{k}$ index because of the *microscopical reversibility principle*: $\mathcal{Q}_{\boldsymbol{k}\boldsymbol{k}'} = \mathcal{Q}_{\boldsymbol{k}'\boldsymbol{k}}$. The transition probability is given by the intrinsic rate, times the probability that the state $\boldsymbol{k}$ is full (F_k), times probability that the state $\boldsymbol{k}'$ is empty $(1 - F_{k'})$. For $\boldsymbol{k}'$ in the interval $d\boldsymbol{k}'$:

$$\mathcal{P}_{\boldsymbol{k}\boldsymbol{k}'}d\boldsymbol{k}' = F_k(1 - F_{k'})\mathcal{Q}_{\boldsymbol{k}\boldsymbol{k}'}d\boldsymbol{k}\,. \tag{3.19}$$

The total scattering will be the sum of all the processes electrons from $\boldsymbol{k}'$ to $\boldsymbol{k}$, minus all the processes bringing carriers out from the state $\boldsymbol{k}$ to any other state $\boldsymbol{k}'$:

$$\begin{aligned}\left.\frac{\partial F_k}{\partial t}\right|_{\text{scatt}} &= \int\{F_{\boldsymbol{k}'}(1 - F_k) - F_k(1 - F_{\boldsymbol{k}'})\}\mathcal{Q}_{\boldsymbol{k}\boldsymbol{k}'}d\boldsymbol{k} \\ &= \int\{(F_{k'} - f_{k'}) - (F_k - f_{k'})\}\mathcal{Q}_{\boldsymbol{k}\boldsymbol{k}'}d\boldsymbol{k},\end{aligned} \tag{3.20}$$

where in the last equality F_k has been substituted by $F_k - f_k$ because of the assumption stated earlier.
The *Linerarized BTE* (LBTE) then reads:

$$-\mathbf{v}_{\boldsymbol{k}}\cdot\left(e\boldsymbol{E} + \frac{\epsilon_{\boldsymbol{k}}}{T}\boldsymbol{\nabla}T\right)\frac{\partial f_k}{\partial \epsilon_{\boldsymbol{k}}} = \int\{(F_{k'} - f_{k'}) - (F_k - f_k)\}\mathcal{Q}_{\boldsymbol{k}\boldsymbol{k}'}d\boldsymbol{k}'. \tag{3.21}$$

3.2.2 Constant Relaxation Time Approximation

In case the relaxation time introduced with Eq.(3.7) has a weak $\boldsymbol{k}$ dependence, the transport properties can be easily derived with a constant relaxation time ($\tau_{\boldsymbol{k}} = \tau$). An energy-dependent conductivity tensor can be defined as:

$$\sigma_{\alpha\beta}(\epsilon) = e^2\tau \sum_{\boldsymbol{k}} v_{\boldsymbol{k}\alpha} v_{\boldsymbol{k}\beta} \delta(\epsilon - \epsilon_{\boldsymbol{k}}), \tag{3.22}$$

where $\tau_{\boldsymbol{k}} \approx \tau$ has been supposed. The $\boldsymbol{k}$ dependence only resides in the electrical band structure. It can be shown [150] that electronic thermal conductivity and the Seebeck coefficient become:

$$\sigma_{\alpha\beta} = \frac{1}{V_{cell}} \int \sigma_{\alpha\beta}(\epsilon) \left(-\frac{\partial f_k}{\partial \epsilon}\right) d\epsilon, \tag{3.23a}$$

$$\kappa^0_{\alpha\beta} = \frac{1}{e^2 T V_{cell}} \int \sigma_{\alpha\beta}(\epsilon)(\epsilon - \mu)^2 \left(-\frac{\partial f_k}{\partial \epsilon}\right) d\epsilon, \tag{3.23b}$$

$$S_{\alpha\beta} = \frac{1}{eT} \frac{\int \sigma_{\alpha\beta}(\epsilon)(\epsilon - \mu)\left(-\frac{\partial f_k}{\partial \epsilon}\right) d\epsilon}{\int \sigma_{\alpha\beta}(\epsilon)\left(-\frac{\partial f_k}{\partial \epsilon}\right) d\epsilon}. \tag{3.23c}$$

This approach has been adopted in the *BolzTraP* code[150].

3.3 Electron Phonon Coupling

The electron-phonon coupling (EPC) is a pivotal concept in transport and superconducting theory [90]. Let us write the EPC hamiltonian:

$$\mathcal{H}_{\text{ep}} = \sum_{\boldsymbol{k}\boldsymbol{k}',\lambda,\sigma} g^{\lambda,\sigma}_{\boldsymbol{k}\boldsymbol{k}'} c^\dagger_{\boldsymbol{k}\sigma} c_{\boldsymbol{k}'\sigma} (a^\dagger_{-\boldsymbol{q}\lambda} + a_{\boldsymbol{q}\lambda}), \tag{3.24}$$

where $c^\dagger_{\boldsymbol{k}\sigma}$ and $c_{\boldsymbol{k}\sigma}$ are second quantization creation and annihilation operator for electrons of spin σ and wavevector $\boldsymbol{k}$, $a^\dagger_{\boldsymbol{q}\lambda}$ and $a_{\boldsymbol{q}\lambda}$ are operators for phonons and λ and $\boldsymbol{q}$ are the phonon mode and wavevector. $\boldsymbol{k'} = \boldsymbol{k} + \boldsymbol{q}$ because of momentum conservation.
The general form EPC coupling matrix element $g^\lambda_{\boldsymbol{k}\boldsymbol{k}'}$ is [44]:

$$g^\lambda_{\boldsymbol{k}\boldsymbol{k}'} = \boldsymbol{u}^\lambda(\boldsymbol{q}) \sqrt{\frac{\hbar}{2M\omega^\lambda_{\boldsymbol{q}}}} \langle \psi_{\boldsymbol{k}'} | \boldsymbol{\nabla} V | \psi_{\boldsymbol{k}} \rangle, \tag{3.25}$$

V being the distorted crystal potential, $\boldsymbol{u}^\lambda(\boldsymbol{q})$ the phonon eigenvector for the $\lambda, \boldsymbol{k}$ phonon mode and M is the ion mass. Eliashberg introduced the *spectral function*

$\alpha^2F(\boldsymbol{k},\boldsymbol{k'},\omega)$ in order to explain superconductivity:

$$\alpha^2F(\boldsymbol{k},\boldsymbol{k'},\omega) \equiv N_F \sum_{\lambda} |g^{\lambda}_{\boldsymbol{k}\boldsymbol{k'}}|^2 \delta(\omega - \omega_{\boldsymbol{k}-\boldsymbol{k'},\lambda}). \tag{3.26}$$

With N_F incorporating the cell volume and other constants:

$$N_F = \left(\frac{V_{\text{cell}}}{(2\pi)^3}\right)^2 \frac{1}{N(0)\hbar}, \tag{3.27}$$

$\alpha^2F(\boldsymbol{k},\boldsymbol{k'},\omega)$ represents the transition probability of a quasiparticle from(to) the state k after coupling to a phonon mode of frequency $\omega_{\boldsymbol{q}}$. All relevant quantities to EPC can be deduced once $\alpha^2F(\boldsymbol{k},\boldsymbol{k'},\omega)$ is known.

Elastic vs. Inelastic approach

In Eq.(3.26) the dependence on the two momenta can be averaged out by assuming that the scattering is elastic and that there is no difference between $\epsilon_{\boldsymbol{k}}$, $\epsilon_{\boldsymbol{k'}}$ and ϵ_F. By introducing two delta functions in Eq.(3.26) yields:

$$\alpha^2F(\boldsymbol{k},\omega) \equiv N_F \sum_{\lambda} \int d\boldsymbol{k'} |g^{\lambda}_{\boldsymbol{k}\boldsymbol{k'}}|^2 \delta(\omega - \omega_{\boldsymbol{k}-\boldsymbol{k'},\lambda}) \delta(\epsilon_{\boldsymbol{k'}}), \tag{3.28a}$$

$$\alpha^2F(\omega) \equiv N_F \sum_{\lambda} \int d\boldsymbol{k'} \int d\boldsymbol{k} |g^{\lambda}_{\boldsymbol{k}\boldsymbol{k'}}|^2 \delta(\omega - \omega_{\boldsymbol{k}-\boldsymbol{k'},\lambda}) \delta(\epsilon_{\boldsymbol{k}}) \delta(\epsilon_{\boldsymbol{k'}}). \tag{3.28b}$$

The two Dirac functions limit the momentum integration over the Fermi Surface and the Fermi energy is taken as reference. In the last formula, $F(\omega)$ is the phonon density of states (PDOS):

$$F(\omega) = \frac{1}{N} \sum_{\boldsymbol{k},\lambda} \delta(\omega - \omega_{\boldsymbol{k},\lambda}), \tag{3.29}$$

with N number of ions. The main difference between $F(\omega)$ and $\alpha^2F(\omega)$ is the weight given to each single phonon: one in the case of PDOS, $|g^{\lambda}_{\boldsymbol{k}\boldsymbol{k'}}|^2$ in the spectral function. The comparison between these two quantities is shown in Fig. 3.1 for Copper.
The coupling constant λ giving the mass enhancement due to EPC is:

$$\lambda = 2 \int_0^{\infty} d\omega \frac{\alpha^2F(\omega)}{\omega}. \tag{3.30}$$

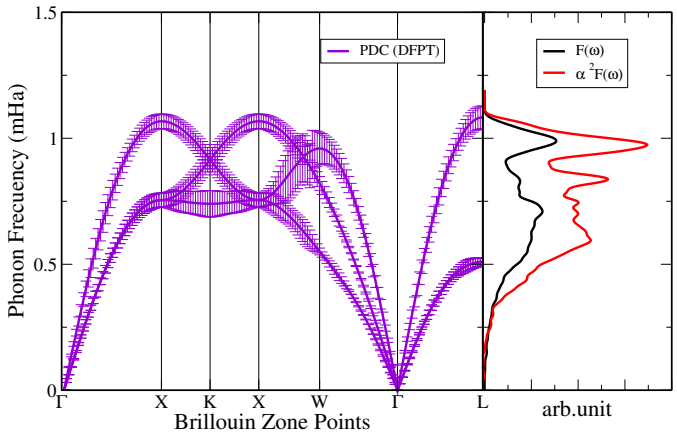

Figure 3.1: Left: Copper PDC from DFPT, the error bars represent the EPC linewidth, e.g. the strength of the interaction depending on the direction in the $\boldsymbol{k}$ space. Right: PDOS $F(\omega)$ (black) and Eliashberg spectral function $\alpha^2F(\omega)$ as defined in Eq. (3.28b) (red).

Electron-phonon scattering operators

Let us denote the phonon state $q = (\boldsymbol{q}, \lambda)$ and $N(q)$ the phonon distribution function out of equilibrium. The process of emission (absorption) of a phonon with wavevector $-\boldsymbol{q}$ ($\boldsymbol{q}$) is labeled by $-$ ($+$). The "out" ("in") superscript indicates the processes which depopulates (populates) the electronic state k:

$$P_{\pm}^{(out)} = -\frac{2\pi}{\hbar}\sum_{\pm}|g_{\boldsymbol{k},\boldsymbol{k}+\boldsymbol{q}}|^2\delta(\epsilon_{\boldsymbol{k}+\boldsymbol{q}} - \epsilon_{\boldsymbol{k}} \mp \hbar\omega_{\boldsymbol{q}}) \times \left[F_k(1-F_{k+q})\left(N(\pm q) + \frac{1}{2} \mp \frac{1}{2}\right)\right], \tag{3.31a}$$

$$P_{\pm}^{(in)} = -\frac{2\pi}{\hbar}\sum_{\pm}|g_{\boldsymbol{k}-\boldsymbol{q},\boldsymbol{k}}|^2\delta(\epsilon_{\boldsymbol{k}} - \epsilon_{\boldsymbol{k}-\boldsymbol{q}} \mp \hbar\omega_{\boldsymbol{q}}) \times \left[F_{k-q}(1-F_k)\left(N(\pm q) + \frac{1}{2} \mp \frac{1}{2}\right)\right]. \tag{3.31b}$$

$N(q)$ evolves in the process as well, but it can be approximated by the equilibrium Bose-Einstein distribution $n_{\mathrm{BE}}(\omega_{\boldsymbol{q}})$ since it is assumed that phonons are kept close to their equilibrium by anharmonic scattering (Except for the Phonon-drag case as treated in [148]).

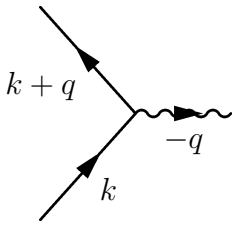

(a) "out" (-) process

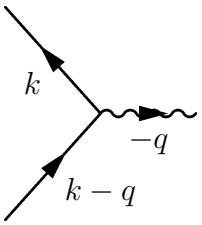

(b) "in" (-) process

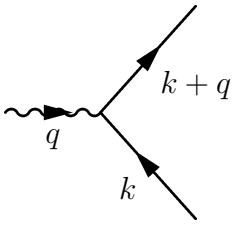

(c) "out" (+) process

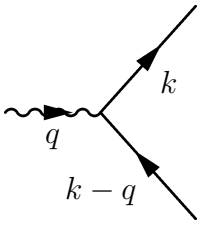

(d) "in" (+) proces

Figure 3.2: Feynman diagrams representing the four possible scattering events described by Eqs. (3.31).

3.3.1 Relaxation time approximation

For scatterings of electrons by phonons, $\tau_{\boldsymbol{k}}$ can be calculated *ab-initio* using [90]:

$$\frac{1}{\tau_{\boldsymbol{k},n}} = \frac{2\pi}{\hbar}\sum_{\boldsymbol{q}n'}|g_{\boldsymbol{k},\boldsymbol{k}+\boldsymbol{q}}|^2\Big\{\big[F(\epsilon_{\boldsymbol{k}+\boldsymbol{q},n})+n_{\boldsymbol{q}}\big]\delta(\epsilon_{\boldsymbol{k}n}-\epsilon_{\boldsymbol{k}+\boldsymbol{q}n'}+\hbar\omega_{\boldsymbol{q}})+ \\ \big[1+n_{\boldsymbol{q}}-F(\epsilon_{\boldsymbol{k}+\boldsymbol{q}n'})\big]\delta(\epsilon_{\boldsymbol{k}n}-\epsilon_{\boldsymbol{k}+\boldsymbol{q}n'}-\hbar\omega_{\boldsymbol{q}})\Big\}, \quad (3.32)$$

$g_{\boldsymbol{k},\boldsymbol{k}+\boldsymbol{q}}$ is shorthand for the electron-phonon coupling matrix (3.25), and $n_{\boldsymbol{q}} \equiv n_{\mathrm{BE}}(\omega_{\boldsymbol{q}})$ is the phonon occupation number from Bose-Einstein distribution function. The spin and phonon mode dependencies have been dropped in the previous equation.
Note that in this equation all directions are relevant. We will derive a more complex relations which keeps track of the position on the FS.

3.4 Variational approximation

Eq.(3.21) is an inhomogeneous linear integral equation, with a positive definite self-adjoint kernel. Following Ziman [278], the solution can be deduced from a

variational principle. A new function Φ can be introduced such that [131, 132, 218]:

$$F_k \equiv f_k - \Phi_{\boldsymbol{k}} \frac{\partial f_k}{\partial \epsilon_{\boldsymbol{k}}}. \tag{3.33}$$

For fermions, f_k assumes the for of the Fermi-Dirac distribution fucntion $f_{\mathrm{FD}}(\epsilon_{\boldsymbol{k}}) = (e^{-\beta\epsilon_{\boldsymbol{k}}} + 1)^{-1}$ and its derivative with respect to energy is:

$$\frac{\partial f(\epsilon_{\boldsymbol{k}})}{\partial \epsilon_{\boldsymbol{k}}} = -\frac{f(\epsilon_{\boldsymbol{k}})(1 - f(\epsilon_{\boldsymbol{k}}))}{k_B T}. \tag{3.34}$$

For bosons, a similar expression holds, with $n_{\mathrm{BE}}(\omega_{\boldsymbol{q}})$ instead of $f_{\mathrm{FD}}(\epsilon_{\boldsymbol{k}})$.
Eq. (3.2) for the *rigid shift* ansatz can be written as:

$$F_k \approx f_k + e\boldsymbol{E}\tau_{\boldsymbol{k}}/\hbar \frac{\partial f_k}{\partial k} = f_k + e\boldsymbol{E}\tau_{\boldsymbol{k}}\mathbf{v}_{\boldsymbol{k}} \frac{\partial f_k}{\partial \epsilon_{\boldsymbol{k}}}. \tag{3.35}$$

Plugging this equation into the definition of the current (3.1) and keeping only the perturbed term, yields the variational expression for the conductivity:

$$\sigma = \frac{e^2}{V} \sum_k \mathbf{v}_{\boldsymbol{k}}^2 \tau_{\boldsymbol{k}} \left(-\frac{\partial f_k}{\partial \epsilon_{\boldsymbol{k}}} \right), \tag{3.36}$$

in which the relaxation time $\tau_{\boldsymbol{k}}$ depends on the scattering details and need to be determinated.
Following Ziman [278], we rewrite the LBTE Eq. (3.21) as:

$$-\mathbf{v}_{\boldsymbol{k}} \cdot \left(e\boldsymbol{E} + \frac{\epsilon_{\boldsymbol{k}}}{T} \boldsymbol{\nabla} T \right) \frac{\partial f_k}{\partial \epsilon_{\boldsymbol{k}}} = \frac{1}{k_B T} \int (\Phi_{\boldsymbol{k}} - \Phi_{\boldsymbol{k}'}) \mathcal{P}_{\boldsymbol{k}\boldsymbol{k}'} d\boldsymbol{k}'. \tag{3.37}$$

This can be generalized to the integral equation:

$$X(k) = \int \left(\Phi(k) - \Phi(k')\right) P(k, k') dk' \Leftrightarrow X = P\Psi, \tag{3.38}$$

with the P operator which transforms the function Ψ into X by integration over k. A internal product can be defined by:

$$\langle \Phi, \Psi \rangle \equiv \int \Phi(k)\Psi(k) dk, \tag{3.39}$$

with $\Phi(k)$ being the solution of the problem. Several properties hold for the P operator:

- symmetric: $P(k, k') = P(k', k)$,

- positive definite: $\langle \Psi, P\Psi \rangle \geq 0$,
- the exact solution of the variational problem Φ minimizes the value of:

$$\frac{\langle \Psi, P\Psi \rangle}{\langle \Psi, X \rangle^2} \tag{3.40}$$

for any approximate solution X satisfying $\langle \Psi, P\Psi \rangle = \langle \Psi, X \rangle$.

Thanks to these properties, we can solve the problem (3.39) variationally by introducing a set of trial functions $\{\phi_i\}$ chosen carefully and constructing a function $\Phi(k)$ which is not the exact solution Φ but satisfies the variational problem (3.39):

$$\Phi(k) = \sum_i \eta_i \phi_i(k). \tag{3.41}$$

For any operator or matrix which satisfies relations as:

$$\langle \Phi, P\Phi \rangle = \sum_{ij} P_{ij} \eta_i \eta_j \quad \text{and} \quad \langle \Phi, X \rangle = \sum_i X_i \eta_i, \tag{3.42}$$

where $\{\eta_i\}$ is a basis set and the elements P_{ij} and X_i can be expressed in terms $\{\phi_i\}$:

$$P_{ij} \equiv \langle \phi_i, P\phi_j \rangle \quad \text{and} \quad X_i \equiv \langle \phi_i, X \rangle. \tag{3.43}$$

The variational principle tells us that the $\{\eta_i\}$ basis elements satisfy:

$$X_i = \sum_j P_{ij} \eta_j. \tag{3.44}$$

This general principle can be used to map complicated integrodifferential problems to more simplified problems, provided that a set of trial functions is available. Eq.(3.37) can be rewritten in operator form:

$$-\mathbf{v}_{\boldsymbol{k}} \cdot \left(e\boldsymbol{E} + \frac{\epsilon_{\boldsymbol{k}}}{T} \boldsymbol{\nabla} T \right) \frac{\partial f_k}{\partial \epsilon_{\boldsymbol{k}}} = \sum_{k'} Q_{kk'} \phi_{k'}, \tag{3.45}$$

with $\phi_{k'}$ being the elements of trial basis set and $Q_{kk'}$ scattering operators.

3.5 Fermi Surface Harmonics

The method of Fermi Surface Harmonics (FSH) was introduced by P.B. Allen [8, 9] in the 1970's as a general method to solve exactly the Boltzmann and Eliashberg functions for non-spherical problems. This theory is reviewed in this paragraph.

Let us generally consider a physical quantity $\mathcal{A}_k$ which depends on the electronic state labeled $k = (\boldsymbol{k}, n, \sigma)$ and with energy $\epsilon_{\boldsymbol{k}}$ (for example the quasiparticle scattering rate $1/\tau_{\boldsymbol{k}}$). In metal case, the electronic energy is of the order of 1 eV, while thermal excitations ($\sim k_B T$) or phonons energy ($\sim \hbar\omega$) occur on a much smaller scale. It is therefore worth to separate the $\mathcal{A}_k$ dependence on energy ϵ *near* the Fermi energy ("radial" part) and the dependence on $\boldsymbol{k}$ position *on* the Fermi Surface ("angular" part). This separation is desirable when one has to sum or integrate over $\boldsymbol{k}$, since the often complicated operations over the surface can left. Allen has chosen FSH proportional to the group velocity, a natural choice for a problem involving integration processes over the FS. For noble metals the Fermi surface is spherical and spherical harmonics $Y_{lm}(\hat{k})$ provide convenient coordinates to locate points on the Fermi surface. For materials which present a complex Fermi surface, a parametrization in spherical harmonics coordinates will not work the same way. The shape of the Fermi surface is a big obstacle for practical calculations in this case and FSH are a useful parametrization tool. Moreover spherical harmonics are complete but they are not orthonormal if integrated over the Fermi surface with a weight function. Another crucial point is that spherical harmonics are not cell periodic in reciprocal space, so this makes it difficult to use them to solve the BTE.

3.5.1 Definition

The FSH basis set (labeled $\psi_J(k)$) consists of all the orthonormal polynomials of order N constructed on the Cartesian components of the velocity $\mathbf{v}_{\boldsymbol{k}} = \boldsymbol{\nabla}_{\boldsymbol{k}}\epsilon_{\boldsymbol{k}}/\hbar$, e.g. all the functions of the form $(v_{\boldsymbol{k}x})^l(v_{\boldsymbol{k}y})^m(v_{\boldsymbol{k}z})^n$ such that $l+m+n = N$ (for l, m, n non negative) normalized according to:

$$\frac{\sum_{\boldsymbol{k}} \psi_J(k)\psi_{J'}(k)\delta(\epsilon_{\boldsymbol{k}} - \epsilon)}{\sum_{\boldsymbol{k}} \delta(\epsilon_{\boldsymbol{k}} - \epsilon)} = \delta_{JJ'}. \tag{3.46}$$

Here J represent a convenient set of labels. The number of functions $\psi_J(k)$ for index l, m, n depends on the number of sheets the Fermi surface is composed of (Fig.2.2) and so on...
The FSH can be chosen to transform as the irreducible representation for the point group of the crystal. Other properties such as completeness, periodicity and multiple sheet Fermi surfaces are discussed in [8].
Let us consider hereafter the special case of cubic symmetry systems with a single sheet Fermi surface. It is easy to construct low order polynomials (Table 3.1) they are just the spherical harmonics with velocities Cartesian components instead of wave vector components. For higher number of sheets or lower symmetry the

problem is in principle still solvable with the same method but with more tedious calculations [8]. In what follows we will consider only the x component of the FSH. The following relations hold:

Order	Label	Explicit form
$N=0$	ψ_0	1
$N=1$	ψ_x	$v_{\boldsymbol{k}x}/\langle v_x^2\rangle^{1/2}$
	ψ_y	$v_{\boldsymbol{k}y}/\langle v_y^2\rangle^{1/2}$
	ψ_z	$v_{\boldsymbol{k}z}/\langle v_z^2\rangle^{1/2}$

Table 3.1: Fermi surface harmonics for single sheet cubic system

$$\psi_x(k) = v_{\boldsymbol{k}x}/v(\epsilon), \tag{3.47a}$$

$$v^2(\epsilon) \equiv \langle v_x^2(\epsilon)\rangle = \frac{\sum_k v_{\boldsymbol{k}x}^2 \delta(\epsilon_{\boldsymbol{k}} - \epsilon)}{\sum_k \delta(\epsilon_{\boldsymbol{k}} - \epsilon)}, \tag{3.47b}$$

$$N(\epsilon) = \sum_k \delta(\epsilon_{\boldsymbol{k}} - \epsilon), \tag{3.47c}$$

$$N(\epsilon)v^2(\epsilon) = \sum_k v_{\boldsymbol{k}x}^2 \delta(\epsilon_{\boldsymbol{k}} - \epsilon) = \frac{1}{2}\left(\frac{n}{m}\right)_{\text{eff}}. \tag{3.47d}$$

General properties

Provided that FSH are a complete set, it is possible to pass from a function defined in the reciprocal space k to a FSH representation J:

$$h_k = \sum_J h_J(\epsilon)\psi_J(k), \tag{3.48a}$$

the inverse relation can be shown using the orthonormalization condition (3.46):

$$h_J(\epsilon) = \frac{\sum_k \delta(\epsilon_{\boldsymbol{k}} - \epsilon)\psi_J(k)h_k}{\sum_k \delta(\epsilon_{\boldsymbol{k}} - \epsilon)}, \tag{3.48b}$$

The same applies for tensors:

$$A_{kk'} = \sum_{JJ'} A_{JJ'}(\epsilon\epsilon')\psi_J(k)\psi_{L'}(k'), \tag{3.48c}$$

$$A_{JJ'}(\epsilon\epsilon') = \frac{\sum_{kk'} \delta(\epsilon_{\boldsymbol{k}} - \epsilon)\delta(\epsilon_{\boldsymbol{k'}} - \epsilon')\psi_J(k)\psi_{L'}(k')A_{kk'}}{\sum_{kk'} \delta(\epsilon_{\boldsymbol{k}} - \epsilon)\delta(\epsilon_{\boldsymbol{k'}} - \epsilon')}. \tag{3.48d}$$

Energy dependent part

Let us introduce the function $\sigma_n(\epsilon)$ which conveniently describe the purely energy dependent part of the problem:

$$\int d\epsilon \left(\frac{-\partial f_k}{\partial \epsilon_{\boldsymbol{k}}} \right) \sigma_n(\epsilon)\sigma_{n'}(\epsilon) = \delta_{nn'}. \tag{3.49}$$

The functions are specified by choosing $\sigma_0 = 1$ and $\sigma_n(\epsilon)$ orthonormal to all lower polynomials. A recursion relation to obtain higher order polynomials is the following:

$$\sigma_n(\epsilon) = (2n+1)^{1/2}\zeta_n(x), \tag{3.50}$$

with $x = \epsilon/2\pi k_B T$ and:

$$\pi \int dx \frac{\zeta_n(x)\zeta_{n'}(x)}{\cosh^2 \pi x} = \delta_{nn'}. \tag{3.51}$$

A few solutions were proposed [226, 47] but in the end the lowest order polynomials were worked out as:

$$\zeta_0(x) = 1, \quad \zeta_1(x) = 2x, \quad \zeta_2(x) = 3x^2 - \frac{1}{4}, \tag{3.52}$$

and a recursive solution for the leading coefficient has been found [9], which was only verified numerically:

$$\zeta_n(x) = [2^n(2n-1)!!/(n!)2]x^2 + \ldots. \tag{3.53}$$

In practice, we will only use the zeroth and first order in n, so the only two functions we need are:

$$\sigma_0 = 1, \quad \text{and} \quad \sigma_1(\epsilon_{\boldsymbol{k}}) = \frac{\sqrt{3}}{\pi k_B T}\epsilon_{\boldsymbol{k}}. \tag{3.54}$$

Biorthonormal basis sets

Two complete sets of biorthogonal basis function are introduced based on FSH [9]:

$$\chi_{Jn}(k) = \frac{\psi_J(k)\sigma_n(\epsilon_{\boldsymbol{k}})}{N(\epsilon)v(\epsilon)}, \tag{3.55}$$

$$\xi_{Jn}(k) = \psi_J(k)\sigma_n(\epsilon_{\boldsymbol{k}})v(\epsilon) \left(\frac{-\partial f_k}{\partial \epsilon_{\boldsymbol{k}}} \right). \tag{3.56}$$

Any function of k can be expressed in either set. The first one is convenient for functions which are smooth in energy, while the second is more suitable for functions

peaked around the Fermi energy. The two functions are orthogonal both in the k and in the (J, n) spaces:

$$\sum_k \chi_{Jn}(k)\xi_{J'n'}(k) = \delta_{JJ'}\delta_{nn'}, \tag{3.57}$$

$$\sum_{Jn} \chi_{Jn}(k)\xi_{Jn}(k') = \delta_{kk'}. \tag{3.58}$$

Scattering operators

FSH properties (Eqs.(3.48)) allows us to rewrite a generic scattering operator $Q_{kk'}$ and coefficients ϕ_k in the two basis Eq.(3.55):

$$Q_{kk'} = \sum_{Jn,J'n'} \xi_{Jn}(k)Q_{Jn,J'n'}\xi_{J'n'}(k'), \tag{3.59a}$$

$$\phi_k = \sum_{Jn} \phi_{Jn}\chi_{Jn}(k). \tag{3.59b}$$

The inverse relations read:

$$Q_{Jn,J'n'} = \sum_{kk'} \chi_{Jn}(k)Q_{k,k'}\chi_{J'n'}(k'), \tag{3.59c}$$

$$\phi_{Jn} = \sum_k \xi_{Jn}(k)\phi_k. \tag{3.59d}$$

The elastic scattering operator from k' to k discussed in Sec. 3.2 can be decomposed into scattering "in" and "out" transition probability $P_{kk'}$:

$$Q_{kk'} = \frac{1}{k_B T}\left(\delta_{kk'}\sum_{k''} P_{k''k} - P_{kk'}\right), \tag{3.60}$$

Explicit transition probability for elastic scattering from a phonon bath in thermal equilibrium have the form of Eqs. (3.31). Considering that $P_{kk'}$ is symmetric in kk' yields:

$$Q_{Jn,J'n'} = (2k_B T)^{-1}\sum_{kk'} P_{kk'}\left(\chi_{Jn}(k) - \chi_{Jn}(k')\right)\times \\ \times\left(\chi_{J'n'}(k) - \chi_{J'n'}(k')\right). \tag{3.61}$$

3.6 Lowest Order Variational Approximation

The x component of the left hand side of Eq.(3.45) can be expressed in terms of $\xi_{Jn}(k)$ as follows:

$$eE\xi_{X0} + \frac{\pi k_B}{\sqrt{3}}\nabla T\xi_{X1}, \tag{3.62}$$

since:

$$\xi_{X0} = v_{\boldsymbol{k}x}\sigma_0(\epsilon_{\boldsymbol{k}})\left(-\frac{\partial f_k}{\partial \epsilon_{\boldsymbol{k}}}\right) = v_{\boldsymbol{k}x}\left(-\frac{\partial f_k}{\partial \epsilon_{\boldsymbol{k}}}\right), \tag{3.63}$$

and:

$$\xi_{X1} = v_{\boldsymbol{k}x}\sigma_1(\epsilon_{\boldsymbol{k}})\left(-\frac{\partial f_k}{\partial \epsilon_{\boldsymbol{k}}}\right) = \frac{\sqrt{3}}{\pi k_B T}\epsilon_{\boldsymbol{k}} v_{\boldsymbol{k}x}\left(-\frac{\partial f_k}{\partial \epsilon_{\boldsymbol{k}}}\right). \tag{3.64}$$

Multiplying χ_{Jn} and summing over k:

$$\begin{aligned} -\left(eE\delta_{n0} + \frac{\pi k_B}{\sqrt{3}}\nabla T\delta_{n1}\right)\delta_{JX} &= \sum_{kk'}\chi_{Jn}(k)Q_{kk'}\phi_{k'} \\ &= \sum_{Jn,J'n'} Q_{Jn,J'n'}\phi_{J'n'}, \end{aligned} \tag{3.65}$$

where eqs.(3.59b) and biorthonormality relations (3.57) have been used in the last equality.
The integration over k in Eq. (3.45) has now been transformed into a matrix equation. Due to its construction, the expansion in (Jn) should converge quickly.

3.6.1 Currents

The electrical and thermal current densities introduced in Eq. (1.2) can be expressed using the distribution function [278] into discrete form:

$$\boldsymbol{j}_e = -2\int e\mathbf{v}_{\boldsymbol{k}} f_{\boldsymbol{k}} d\boldsymbol{k} = -2e\sum_{\boldsymbol{k}} \mathbf{v}_{\boldsymbol{k}}\phi_{\boldsymbol{k}}\left(-\frac{\partial f_k}{\partial \epsilon_{\boldsymbol{k}}}\right), \tag{3.66a}$$

$$\boldsymbol{j}_Q = 2\int \epsilon_{\boldsymbol{k}}\mathbf{v}_{\boldsymbol{k}} f_{\boldsymbol{k}} d\boldsymbol{k} = 2\sum_{\boldsymbol{k}} \epsilon_{\boldsymbol{k}}\mathbf{v}_{\boldsymbol{k}}\phi_{\boldsymbol{k}}\left(-\frac{\partial f_k}{\partial \epsilon_{\boldsymbol{k}}}\right), \tag{3.66b}$$

where we considered the spin degeneration and Eq. (3.33).
Using (3.59b) and (3.55) the first of Eqs. (3.66) becomes:

$$\begin{aligned} \boldsymbol{j}_e &= -2e\sum_{\boldsymbol{k}}\mathbf{v}_{\boldsymbol{k}}\sum_{Jn}\phi_{Jn}\chi_{Jn}(k)\left(-\frac{\partial f_k}{\partial \epsilon_{\boldsymbol{k}}}\right) \\ &= -2e\sum_{\boldsymbol{k}}\mathbf{v}_{\boldsymbol{k}}\sum_{Jn}\phi_{Jn}\frac{\psi_J(k)\sigma_n(\epsilon_{\boldsymbol{k}})}{N(\epsilon)v(\epsilon)}\left(-\frac{\partial f_k}{\partial \epsilon_{\boldsymbol{k}}}\right). \end{aligned} \tag{3.67}$$

We now consider the property of Dirac delta function $g(\epsilon) = \int d\epsilon' g(\epsilon')\delta(\epsilon - \epsilon')$ and the orthonormality relation (3.49) with $\sigma_0(\epsilon) = 1$:

$$\boldsymbol{j}_e = -2e \int d\epsilon \sum_{\boldsymbol{k}} \mathbf{v}_{\boldsymbol{k}} \sum_{Jn} \phi_{Jn} \frac{\psi_J(k)\sigma_n(\epsilon)}{N(\epsilon)v(\epsilon)} \left(-\frac{\partial f_k}{\partial \epsilon_{\boldsymbol{k}}}\right) = \tag{3.68}$$

$$= -2e \sum_{\boldsymbol{k}} \mathbf{v}_{\boldsymbol{k}} \sum_{Jn} \phi_{Jn} \frac{\psi_J(k)}{N(\epsilon)v(\epsilon)} \delta_{n0}\,. \tag{3.69}$$

We now take the projection along $\hat{\boldsymbol{x}}$ direction:

$$\begin{aligned}\boldsymbol{j}_{xe} =& -2e\phi_{J0} \sum_{J,\boldsymbol{k}} v_{\boldsymbol{k}x} \frac{\psi_J(k)}{N(\epsilon)v(\epsilon)} = -2e\phi_{J0} \sum_{J,\boldsymbol{k}} \frac{v_{\boldsymbol{k}x}^2}{N(\epsilon)v^2(\epsilon)} \\ =& -2e\phi_{X0}\,.\end{aligned} \tag{3.70}$$

In the last equality we exploited the orthonormal property of FSH, so in the sum over J only the x term survived and the property (3.47d).
Thermal current can be obtained in the same way, just considering that $\sigma_1(\epsilon)$ from Eq. (3.54) is proportional to ϵ. Then:

$$\begin{aligned}\boldsymbol{j}_Q =& 2\sum_{\boldsymbol{k}} \epsilon_{\boldsymbol{k}} \mathbf{v}_{\boldsymbol{k}} \sum_{Jn} \phi_{Jn}\chi_{Jn}(k) \left(-\frac{\partial f_k}{\partial \epsilon_{\boldsymbol{k}}}\right) \\ =& 2\int d\epsilon \sum_{\boldsymbol{k}} \epsilon \mathbf{v}_{\boldsymbol{k}} \sum_{Jn} \phi_{Jn} \frac{\psi_J(k)\sigma_n(\epsilon)}{N(\epsilon)v(\epsilon)} \left(-\frac{\partial f_k}{\partial \epsilon_{\boldsymbol{k}}}\right) \\ =& 2\frac{\pi k_B T}{\sqrt{3}} \int d\epsilon \sum_{\boldsymbol{k}} \mathbf{v}_{\boldsymbol{k}} \sum_{Jn} \phi_{Jn} \frac{\psi_J(k)\sigma_n(\epsilon)\sigma_1(\epsilon)}{N(\epsilon)v(\epsilon)} \left(-\frac{\partial f_k}{\partial \epsilon_{\boldsymbol{k}}}\right) \\ =& 2\frac{\pi k_B T}{\sqrt{3}} \sum_{\boldsymbol{k}} \mathbf{v}_{\boldsymbol{k}} \sum_{J} \phi_{J1} \frac{\psi_J(k)}{N(\epsilon)v(\epsilon)}.\end{aligned} \tag{3.71}$$

Taking now the projection along $\hat{\boldsymbol{x}}$, and using (3.47d), we get:

$$\boldsymbol{j}_Q = \left(\frac{2\pi k_B T}{\sqrt{3}}\right) \phi_{X1}. \tag{3.72}$$

3.6.2 Transport coefficients

Macroscopic transport coefficients introduced in Sec. 1.1.1 can be expressed in terms of FSH. Extracting the term $\{Jn\} = \{X0\}$ from Eq. (3.65) yields:

$$-eE = \sum_{J'n'} Q_{X0,J'n'} \phi_{J'n'}. \tag{3.73}$$

Multiplying both sides by $(Q^{-1})_{XO,Jn}$ and summing over Jn yields:

$$-eE = Q_{X0,X0}\phi_{X0}. \tag{3.74}$$

Plugging Eqs. (3.70) and (3.72)in the previous relation we obtain for conductivity (Eq. (3.3)):

$$\sigma = 2e^2 \left(Q^{-1}\right)_{X0,X0}. \tag{3.75}$$

It can be shown that [9]:

$$S = -\frac{\pi k_B T}{\sqrt{3}e} \frac{(Q^{-1})_{X0,X1}}{(Q^{-1})_{X0,X0}}, \tag{3.76}$$

$$\kappa = \frac{2}{3}\pi^2 k_B^2 T \left[\left(Q^{-1}\right)_{X1,X1} - \frac{\left|(Q^{-1})_{X0,X1}\right|^2}{.}\left(Q^{-1}\right)_{X0,X0}\right]. \tag{3.77}$$

3.6.3 Resistivity

Eq. (3.75) can be inverted to obtain the expression of resistivity from FSH:

$$\rho = 1/2e^2 \left(Q^{-1}\right)_{X0,X0}. \tag{3.78}$$

It is possible to avoid the matrix inversion and expand this equation in a perturbative way. Considering the *rigid shift* ansatz, chooseing $\boldsymbol{E}$ along the $\hat{\boldsymbol{x}}$ direction is equivalent to say that the *real* solution of the variational problem (Φ in Eq. (3.33)) is in the same direction. It makes sense to conclude that only the $\{X0\}$ element of the trial functions basis set $\{\phi_{Jn}\}$ is large. This means that the off-diagonal elements of the $Q_{Jn,J'n'}$ matrix are small and it can be treated perturbatively:

$$\rho \approx \frac{1}{2e^2}\Big(Q_{X0,X0} - {\sum_{\alpha}}' \frac{Q_{X0,\alpha}Q_{\alpha,X0}}{Q_{\alpha,\alpha}} + \\ + {\sum_{\alpha,\beta}}' \frac{Q_{X0,\alpha}Q_{X0,\alpha}Q_{\alpha,\beta}Q_{\beta,X0}}{Q_{\alpha,\alpha}Q_{\beta,\beta}} \dots\Big), \tag{3.79}$$

where ${\sum_{\alpha}}'$ is the sum of over all index $Jn \neq X0$, ${\sum_{\alpha,\alpha}}'$ sums of over all index $J'n' \neq X0$ and $J'n' \neq Jn$, and so on.
This means practically that the calculation of just one term of the $Q_{Jn,J'n'}$ matrix gives us a first estimation of the value of resistivity. Higher order terms will correct this first estimation.
We will refer to the results as the Lowest Order Variational Approximation (LOVA), with LOVA0 (meaning that no $Q_{Jn,J'n'}$ is calculated), LOVA1 (only $Q_{J0,J'0}$ is calculated), LOVA2 (elements with $n = 1$ and $n' = 1$ or viceversa are calculated) etc.

3.6.4 Relaxation times

From Eqs. (3.3) and (3.8) true the resistivity reads:

$$\rho = \left[\left(\frac{n}{m}\right)_{\text{eff}} e^2\right]^{-1} \left(\frac{1}{\tau_{\text{imp}}} + \frac{1}{\tau_{\text{ph}}} + \dots\right). \tag{3.80}$$

Equation (3.80) is the generalization of Eq. (3.6) to metals with non-Debye phonon spectra and non-spherical Fermi Surface.
To the lowest order in the LOVA expansion (3.79), the relaxation time relative to the scattering event a can be obtained by equaling the right hand sides of Eq. (3.80) and (3.79):

$$\frac{1}{\tau_a^0} = \frac{1}{2}\left(\frac{n}{m}\right)_{\text{eff}} Q^a_{X0,X0} \tag{3.81}$$

$$= \frac{1}{4k_BT}\left(\frac{n}{m}\right)_{\text{eff}} \sum_{kk'} \left(\chi_{X0}(k) - \chi_{X0}(k')\right)^2 P^a_{kk'}, \tag{3.82}$$

where (3.61) has been used. The 0 superscript indicates that this is at the zeroth LOVA order. The explicit value of $\chi_{X0}(k)$ can be obtained from the definition (3.55), (3.54) and properties (3.47d):

$$\chi_{X0}(k) = 2\left(\frac{n}{m}\right)^{-1}_{\text{eff}} v_{\boldsymbol{k}x}\,. \tag{3.83}$$

We finally obtain:

$$\frac{1}{\tau_a^0} = \left[\left(\frac{n}{m}\right)_{\text{eff}} k_BT\right]^{-1} \sum_{kk'} (v_{\boldsymbol{k}x} - v_{\boldsymbol{k}x'})^2 P^a_{kk'}\,. \tag{3.84}$$

The scattering rate is then obtained from the scattering operators.

Impurities

For impurities, the elastic scattering matrix element from k to k' is:

$$P^{imp}_{kk'} = \frac{2\pi n_i}{\hbar} |T_{kk'}|^2 f_k(1-f_{k'})\delta(\epsilon_{\boldsymbol{k}} - \epsilon_{\boldsymbol{k'}}), \tag{3.85}$$

where n_i is the impurity density and T is the matrix for impurity scattering.
In the elastic approximation, $\epsilon_{\boldsymbol{k}} = \epsilon_{\boldsymbol{k'}}$, so:

$$f_k(1-f_{k'}) = f_k(1-f_k) \simeq k_BT\left(-\frac{\partial f_k}{\partial \epsilon_{\boldsymbol{k}}}\right) \simeq k_BT\delta(\epsilon_{\boldsymbol{k}})\,. \tag{3.86}$$

The term $\delta(\epsilon_{\boldsymbol{k}})$ is non zero only when $\epsilon_{\boldsymbol{k}} = 0$, likewise, $\delta(\epsilon_{\boldsymbol{k}} - \epsilon_{\boldsymbol{k'}})$ will be non null only for $\epsilon_{\boldsymbol{k}} = \epsilon_{\boldsymbol{k'}} = 0$ and can be rewritten as $\delta(\epsilon_{\boldsymbol{k'}})$. Moreover, we again use (3.47d) to write:

$$\frac{1}{\tau^0_{\text{imp}}} = \frac{2\pi n_i}{\hbar} N(0) \frac{\sum_{kk'} (v_{\boldsymbol{k}x} - v_{\boldsymbol{k}x'})^2 |V_{kk'}|^2 \delta(\epsilon_{\boldsymbol{k}}) \delta(\epsilon_{\boldsymbol{k'}})}{2 \sum_{pp'} v_{px}^2 \delta(\epsilon_p) \delta(\epsilon_{p'})} \,. \tag{3.87}$$

Phonons

The electron-phonon elastic scattering matrix element from k to k' has been given in (3.25) and the relative scattering rates in (3.31). The four components in Eqs. (3.31) can be rewritten as a single term if we consider that i) the EPC matrix terms are symmetric in kk' ii) substituting $\boldsymbol{q}$ to $-\boldsymbol{q}$ and iii) writing $\boldsymbol{k'}$ instead of $\boldsymbol{k} + \boldsymbol{q}$.

$$\begin{aligned} \frac{1}{\tau^0_{\text{ph}}} = &- \frac{2\pi}{\hbar} \frac{N(0)}{k_B T} \frac{1}{2 \sum_{pp'} v_{px}^2 \delta(\epsilon_p) \delta(\epsilon_{p'})} \sum_{kk'} (v_{\boldsymbol{k}x} - v_{\boldsymbol{k}x'})^2 |g_{kk'}|^2 \\ & F_{\boldsymbol{k}} \left(1 - F_{\boldsymbol{k'}}\right) \left\{ \left[N(\omega_{\boldsymbol{q}}) + 1 \right] \delta(\epsilon_{\boldsymbol{k}} - \epsilon_{\boldsymbol{k'}} - \hbar\omega_{\boldsymbol{q}}) + N(\omega_{\boldsymbol{q}}) \delta(\epsilon - \epsilon' + \omega_{\boldsymbol{q}}) \right\} \,. \end{aligned} \tag{3.88}$$

Furthermore, we can introduce three delta functions over ϵ, ϵ' and ω:

$$\begin{aligned} \frac{1}{\tau^0_{\text{ph}}} = &- \frac{2\pi}{\hbar} \frac{N(0)}{k_B T} \int d\epsilon \int d\epsilon' \int d\omega \frac{1}{2 \sum_{pp'} v_{px}^2 \delta(\epsilon_p) \delta(\epsilon_{p'})} \\ & \sum_{kk'} (v_{\boldsymbol{k}x} - v_{\boldsymbol{k}x'})^2 |g_{kk'}|^2 \delta(\epsilon - \epsilon_{\boldsymbol{k}}) \delta(\epsilon' - \epsilon_{\boldsymbol{k'}}) \delta(\omega - \omega_{\boldsymbol{q}}) \\ & F_{\boldsymbol{k}} \left(1 - F_{\boldsymbol{k'}}\right) \left\{ \left[N(\omega_{\boldsymbol{q}}) + 1 \right] \delta(\epsilon_{\boldsymbol{k}} - \epsilon_{\boldsymbol{k'}} - \hbar\omega_{\boldsymbol{q}}) + N(\omega_{\boldsymbol{q}}) \delta(\epsilon - \epsilon' + \hbar\omega_{\boldsymbol{q}}) \right\} \,. \end{aligned} \tag{3.89}$$

Note that this expression has been derived without the elastic approximation. Moreover, this relation differs from (3.32) for the squared velocity terms introduced with the FSH.

3.7 Transport Spectral Functions

A class of electron-phonon spectral functions can be introduced for the EPC scattering, depending on a weighting function $w(k, k')$:

$$\alpha^2_w F(\omega) \equiv N(0) \frac{\sum_{kk'} |g_{\boldsymbol{kk'}}|^2 w(k, k') \delta(\epsilon_k) \delta(\epsilon'_k) \delta(\omega - \omega_{\boldsymbol{q}})}{\sum_{kk'} w(k, k') \delta(\epsilon_k) \delta(\epsilon_{k'})}, \tag{3.90}$$

with $\boldsymbol{q} = \boldsymbol{k} - \boldsymbol{k'}$ and relative coupling constant λ_w:

$$\lambda_w = 2 \int_0^\infty d\omega \frac{\alpha^2_w F(\omega)}{\omega} \,. \tag{3.91}$$

For $w = 1$ the Migdal-Eliashberg theory [63, 199, 44] is recovered. Eqs. (3.90) and (3.91) reduce respectively to (3.26) and (3.30).
For transport quantities, the dependence on group velocity is acheived by choosing $w(k, k') = (v_{\boldsymbol{k}x} - v_{\boldsymbol{k}'x})^2$:

$$\alpha^2_{\mathrm{tr}}F(\omega) \equiv N(0)\frac{\sum_{kk'}|g_{\boldsymbol{k}\boldsymbol{k}'}|^2(v_{\boldsymbol{k}x} - v_{\boldsymbol{k}'x})^2\delta(\epsilon_k)\delta(\epsilon'_k)\delta(\omega - \omega_{\boldsymbol{q}})}{\sum_{kk'}(v_{\boldsymbol{k}x} - v_{\boldsymbol{k}'x})^2\delta(\epsilon_k)\delta(\epsilon_{k'})}, \tag{3.92}$$

The transport spectral function $\alpha^2_{\mathrm{tr}}F$ is analogous to the Eliashberg spectral function for superconductivity, but weighted by contributions from electron velocities. In Fig. 3.3 the PDOS and Eliashberg spectral function (3.26) already shown in Fig. 3.1 are compared to the transport spectral function $\alpha^2 F_{\mathrm{tr}}(\omega)$ introduced with Eq.(3.92). We can see that the phonons frequencies with more weight in the interaction are not always the same.

It is useful to factorize the angular and the energy components of Eq. (3.61). The

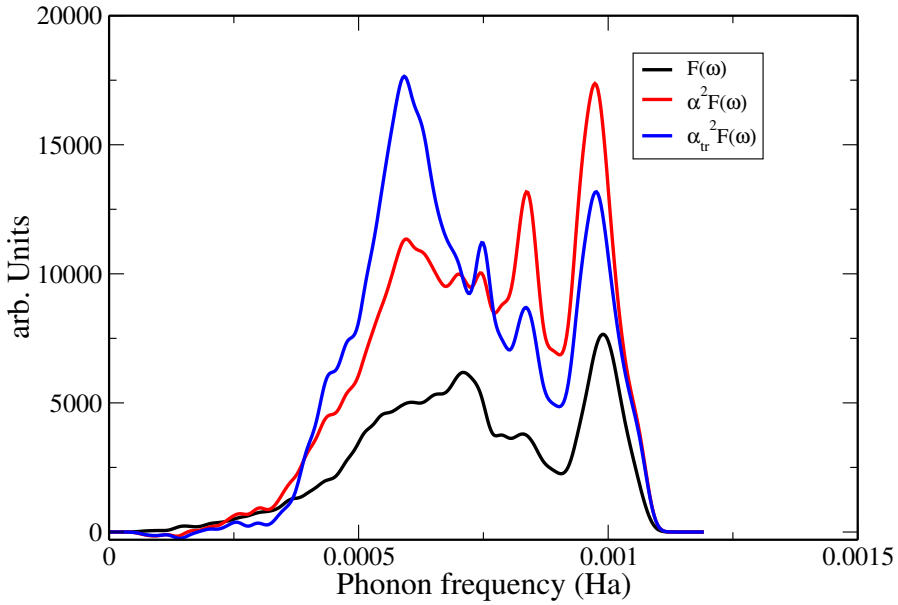

Figure 3.3: Spectral functions for Copper. Black: PDOS from Eq. (3.29), Red: Eliashberg spectral function from Eq.(3.26), Blue: transport spectral function from Eq.(3.92).

following identity holds:

$$\begin{aligned}&\left(\chi_{Jn}(k)-\chi_{Jn}(k')\right)\left(\chi_{J'n'}(k)-\chi_{J'n'}(k')\right)=\\&=\frac{1}{4}\sum_{s,s'=\pm1}\left[\psi_J(k)-s\psi_J(k')\right]\left[\psi_{J'}(k)-s'\psi_{J'}(k')\right]\\&\left[\frac{\sigma_n(\epsilon)}{N(\epsilon)v(\epsilon)}+s\frac{\sigma_n(\epsilon')}{N(\epsilon')v(\epsilon')}\right]\left[\frac{\sigma_{n'}(\epsilon)}{N(\epsilon)v(\epsilon)}+s'\frac{\sigma_{n'}(\epsilon')}{N(\epsilon')v(\epsilon')}\right].\end{aligned}\tag{3.93}$$

We introduce the joint polinomial $\mathcal{J}(s,s',n,n',\epsilon,\epsilon')$ and the generalized spectral function $\alpha^2_{\rm gen}(s,s',J,J',\epsilon,\epsilon')F(\omega)$ functions in order to factorize the angular (JJ') and the energetic part (nn'):

$$\begin{aligned}\mathcal{J}(s,s',n,n',\epsilon,\epsilon')=\frac{1}{4}&\left[\frac{\sigma_n(\epsilon)}{N(\epsilon)v(\epsilon)}+\frac{s\sigma_n(\epsilon')}{N(\epsilon')v(\epsilon')}\right]\\&\left[\frac{\sigma_{n'}(\epsilon)}{N(\epsilon)v(\epsilon)}+\frac{s'\sigma_{n'}(\epsilon')}{N(\epsilon')v(\epsilon')}\right],\end{aligned}\tag{3.94a}$$

$$\begin{aligned}\alpha^2_{\rm gen}(s,s',J,J',\epsilon,\epsilon')F(\omega)=&\frac{1}{2N(0)}\sum_{\boldsymbol{kk'}}|g_{\boldsymbol{kk'}}|^2\delta(\epsilon_{\boldsymbol{k}}-\epsilon)\delta(\epsilon_{\boldsymbol{k'}}-\epsilon')\delta(\omega-\omega_{\boldsymbol{q}})\\&\left[\psi_J(k)-s\psi_J(k')\right]\left[\psi_{J'}(k)-s'\psi_{J'}(k')\right].\end{aligned}\tag{3.94b}$$

In terms of these two functions. it is possible to explicitly write the exact result for the scattering operator due to phonons:

$$\begin{aligned}Q^{ph}_{Jn,J'n'}=&\frac{2\pi N}{\hbar k_{\rm B}T}\int d\epsilon\int d\epsilon'\int d\omega\sum_{s,s'=\pm1}\alpha^2_{\rm gen}(s,s',J,J',\epsilon,\epsilon')F(\omega)\times\\&\mathcal{J}(s,s',n,n',\epsilon,\epsilon')F\left(1-F'\right)\times\\&\left\{\left[N(\omega)+1\right]\delta(\epsilon-\epsilon'-\hbar\omega)+N(\omega)\delta(\epsilon-\epsilon'+\hbar\omega)\right\}.\end{aligned}\tag{3.95}$$

More generally, for a generic spectral function w:

$$1/\tau_w=\frac{4\pi k_BT}{\hbar}\int_0^\infty\frac{d\omega}{\omega}\alpha^2_wF(\omega)\left[\frac{\hbar\omega/2k_BT}{\sinh(\hbar\omega/2k_BT)}\right]^2.\tag{3.96}$$

3.7.1 Elastic LOVA

Some important simplification can be introduced if the energy dependence is analyzed. In Eq. (3.95) the dependence on electronic energy has mainly two contributions: i) from electronic band structure ($N(\epsilon)$, $v(\epsilon)$, and $\alpha^2_{\rm gen}$), which can vary from a few tenths to a few eV; ii) terms linked to the energy conservation ($\delta(\epsilon-\epsilon'\pm\hbar\omega)$ and $f(1-f')$) which vary on a much faster scale (ω and k_BT).

The temperature of the system has then an important role and can determine which contribution is dominant. At low temperature, the terms (i) are less important and can be neglected to the lowest order in n. It is in general true that $\alpha^2_{\rm tr}F(\omega)$ depends weakly on ϵ, ϵ' and this dependence can be dropped.
On the other hand, when T is high enough ($k_BT >> \omega_D$) then the electronic structure variations cannot be neglected. It makes sense to treat phonon scattering as elastic, setting then $\omega = 0$ in the δ functions of (3.95). There is no more energy exchange in the scattering and different electronic bands are no more coupled.
We now assume that the Fermi smearing effects (i.e. the rapid oscillations of electronic properties at high temperature) can be neglected. We set $\epsilon = \epsilon' = 0$ in $\alpha^2_{\rm gen}$ and $\mathcal{J}$ introduced with (3.94). The $N(\epsilon)v(\epsilon)$ terms in Eq. (3.94a) are now identical and can be put to $N(0)v(0)$. The joint polynomials become:

$$\mathcal{J}(s,s',n,n',\epsilon,\epsilon') = \frac{1}{4}\frac{1}{N(0)v(0)}\left[\sigma_n(\epsilon) + s\sigma_n(\epsilon')\right] \left[\sigma_{n'}(\epsilon) + s'\sigma_{n'}(\epsilon')\right] . \tag{3.97}$$

$\mathcal{J}$ is now even (odd) with respect to the exchange of ϵ and ϵ' when $s = s'$ ($s = -s'$). The same parity occurs for the $\alpha^2_{\rm gen}(s,s',J,J',\epsilon,\epsilon')F(\omega)$ function, thus we can keep the even terms only ($s = s'$). We further modify the notation to $\mathcal{J}_{\rm elas}(n,n',\epsilon,\epsilon')$ and $\alpha^2_{\rm elas}(s,JJ')F(\omega)$ (Only one s is kept since $s = -s'$ gives no contribution).

Zero$^{\rm th}$ order

We have already dropped the dependence on ϵ, ϵ' in Eqs. (3.94). If we take $n = 0$, then also the dependences on J, J' and s can be dropped in $\alpha^2_{\rm elas}(s,JJ')F(\omega)$ and $\mathcal{J}_{\rm elas}(n,n',\epsilon,\epsilon') = 1$. We can then just explicitly rewrite $\alpha^2_{\rm tr}F(\omega)$ in the previous Eq. (3.89):

$$\frac{1}{\tau^0_{\rm ph,\ elas}} = \frac{4\pi k_BT}{\hbar}\int_0^\infty \frac{d\omega}{\omega}\alpha^2_{\rm tr}F(\omega)I\left(\frac{\omega}{2k_BT}\right) , \tag{3.98}$$

where the two integration over ϵ and ϵ' have been included into the I function

$$I\left(\frac{\omega}{2k_BT}\right) \equiv \frac{\omega}{2k_B^2T^2}\int_{-\infty}^{\infty}d\epsilon\int_{-\infty}^{\infty}d\epsilon' f(\epsilon)\left[1-f(\epsilon')\right] \left\{\left[N(\omega)+1\right]\delta(\epsilon-\epsilon'-\omega) + N(\omega)\delta(\epsilon-\epsilon'+\omega)\right\} . \tag{3.99}$$

It is possible to show that $I(x)$ integrates to $(x/\sinh(x))^2$.
For low temperatures, $\alpha^2_{\rm tr}F(\omega)$ gives the highest contribution. For high temperatures, $I(x)$ approaches to unity, so we have:

$$\frac{1}{\tau^{0,HT}_{\rm ph,elas}} = \frac{2\pi}{\hbar}k_BT\lambda_{\rm tr}, \tag{3.100}$$

with $\lambda_{\rm tr} = 2\int_0^\infty d\omega/\omega \alpha^2_{\rm tr}F(\omega)$ from Eq. (3.91).
This is an *ab-initio* expression for the transport coupling. It differs from the superconducting λ only for the term proportional to $(v_{\boldsymbol{k}x} - v_{\boldsymbol{k'}x})^2$. This term modifies the dependence on ω of $\alpha^2_{\rm tr}F(\omega)$ to ω^4 (while $\alpha^2_{\rm El}F(\omega) \sim \omega^2$). By inserting Eqs. (3.102) in expressions (3.80) we finally obtain:

$$\rho_{\alpha\beta} = \frac{2\pi V_{cell} k_B T}{e^2 \hbar N(\epsilon_F) v_\alpha(\epsilon_F) v_\beta(\epsilon_F)} \int_0^\infty \frac{d\omega}{\omega} \frac{x^2}{\sinh^2 x} \alpha^2_{\rm tr}F(\omega)\,, \tag{3.101}$$

which gives the expected T^5 behavior for ρ (Eq. (3.6)).

Higher orders

The relaxation time and scattering operators reads:

$$\begin{aligned} \frac{1}{\tau_{\rm ph,elas}} = \frac{4\pi k_B T}{\hbar} \sum_{\pm 1} \int_0^\infty \frac{d\omega}{\omega} \alpha^2(s, J, J') F(\omega) \times \\ \times \left(\frac{\omega/2k_BT}{\sinh(\omega/2k_BT)} \right)^2 I^s_{n,n'}(\omega/2k_BT)\,, \end{aligned} \tag{3.102a}$$

$$Q^{\rm ph,elas}_{Jn,J'n'} \simeq 2\left[\left(\frac{n}{m} \right)_{\rm eff} \tau^0_{\rm ph,elas} \right]\,. \tag{3.102b}$$

The $I^s_{n,n'}(\omega/2k_BT)$ functions can be derived for some specific cases only. It can be shown that they vanish for odd $n + n'$. Thus $Q^{\rm ph,elas}_{Jn,J'n'}$ is non zero if n, n' are both even or odd, and all matrix elements which do not fall into this case are zero.
These relations are much easier to solve numerically. The integration over all the $\boldsymbol{k}$ points is simply avoided. Unfortunately this approach results into a vanishing Seebeck coefficient due to the block diagonal property of $Q^{\rm ph,elas}_{Jn,J'n'}$.
On the other side, being the $\{X0, X1\}$ element null, it is straightforward to estimate the thermal resistivity $W = \kappa^{-1}$:

$$W^{(0)}_{\rm elas} = \frac{3}{2\pi^2 k_B^2 T} Q_{X1,X1}\,. \tag{3.103}$$

As shown in Ref. [198], by inserting Eqs. (3.102) in (3.103) we finally obtain:

$$\begin{aligned} w_{\alpha\beta} = \frac{6V_{cell}}{\pi\hbar k_B N(\epsilon_F) v_\alpha(\epsilon_F) v_\beta(\epsilon_F)} \int_0^\infty \frac{d\omega}{\omega} \frac{x^2}{\sinh^2 x} \\ \times \left[\alpha^2_{\rm tr}F(\omega) + \frac{4x^2}{\pi^2} \alpha^2_{out} F(\omega) + \frac{2x^2}{\pi^2} \alpha^2_{in} F(\omega) \right]\,. \end{aligned} \tag{3.104}$$

3.7.2 Full Inelastic LOVA

To calculate the Seebeck coefficient we need to go beyond the Elastic LOVA introduced just before and consider all dependencies in $\alpha^2_{\rm gen}F(\omega)$ and $\mathcal{J}$. The same argument used to obtain the expansion for resistivity in Sec.3.6.2 can be used to express the thermal conductivity and the Seebeck coefficient (3.77) and (3.76):

$$\kappa_{\alpha\beta} = \frac{2}{3}\pi^2 k_B^2 T \left[(Q_{11}^{-1})_{\alpha\beta} - \frac{(Q_{01}^{-1})^2_{\alpha\beta}}{(Q_{00}^{-1})_{\alpha\beta}} \right] \approx \frac{2}{3}\pi^2 k_B^2 T \frac{1}{(Q_{11})_{\alpha\beta}}\,, \tag{3.105}$$

$$S_{\alpha\beta} = -\frac{\pi k_B}{\sqrt{3}e}\frac{(Q_{01}^{-1})_{\alpha\beta}}{(Q_{00}^{-1})_{\alpha\beta}} \approx \frac{\pi k_{\rm B}}{\sqrt{3}e}\sum_{\gamma}(Q_{01})_{\alpha\gamma}(Q_{11}^{-1})_{\gamma\beta}\,. \tag{3.106}$$

Cartesian components have been explicitly written out in previous relations. These equations fully consider the "Fermi smearing" effect, e.g. the dependence of $\alpha^2_{\rm tr}F$ on ϵ and ϵ'.

Copper

The Seebeck coefficient from Eq.(3.106) is shown in Fig.3.6. The black lines represent experimental data from Ref.[103]. The two curves represent the Seebeck coefficient temperature dependence for Gaussian integration (Red) and for tetrahedron integration (Blue). For Gaussian integration a smearing factor of 0.1 mHa was used.
The resistivity of Copper is shown in Fig. 3.4. Three curves are displayed: $\rho_1(T)$ (black) and $\rho_2(T)$ (red) compared to experimental results (blue with closed squares) from Ref.[103]. The difference in the two curves is the spectral function used in the integration. When the fully energy dependent $\alpha(s,s',J,J',\epsilon,\epsilon')^2F(\omega)$ is used (3.94b) inelastic scattering is considered (red curve) while for the black curve the elastic $\alpha^2_{\rm elas}(s,JJ')F(\omega)$ is employed. The red curve actually contains a correction to the black one. I will refer to these results as (elastic or inelastic) LOVA (Lowest Order Variational Approximation).
In figures with theoretical results, if not stated other wise, the subscripts 0,1 and 2 indicates the Eliashberg coefficients, elastic LOVA and inelastic LOVA approximation respectively.

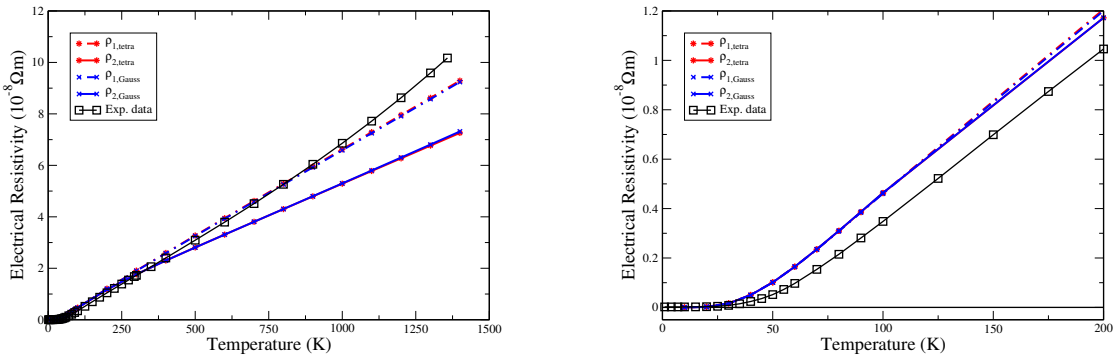

(a) High Temperatures **(b)** Low Temperatures

Figure 3.4: Resistivity of Copper vs. Temperature. Left: High temperatures, right: low temperatures. Black dashed line with open squares: experimental results from Ref.[103]. Red lines: Tetrahedron integration, blue lines: Gaussian integration (electronic smearing of 0.1 mHa). Dot-dashed lines: elastic approximation (LOVA1), full lines: inelastic approximation (LOVA2). More details for the calculations are given in the main text.

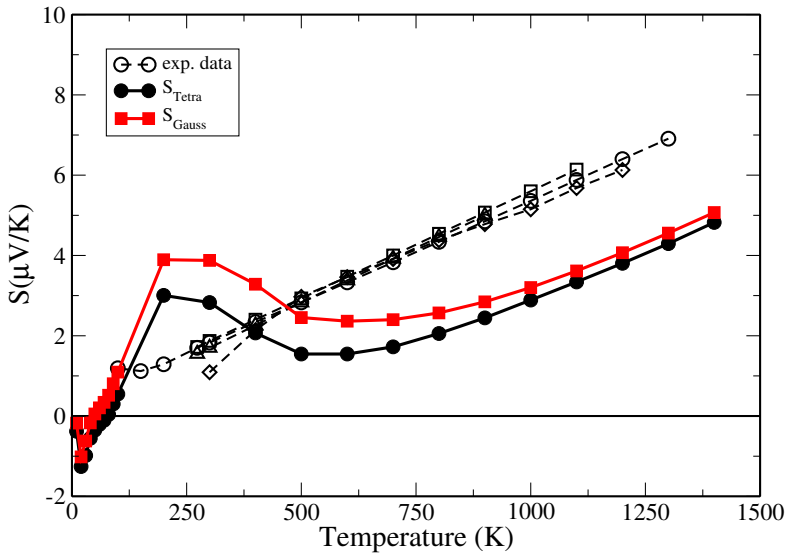

Figure 3.5: Seebeck coefficient of copper vs. temperature. Black dashed lines with open symbols: experimental results from Ref.[103]. Full lines: Seebeck coefficient calculated from inelastic LOVA. Black curve: tetrahedron integration in the reciprocal space. Red: Gaussian integration with Temperature smearing of 0.1 mHa. More details regarding the calculation in the main text.

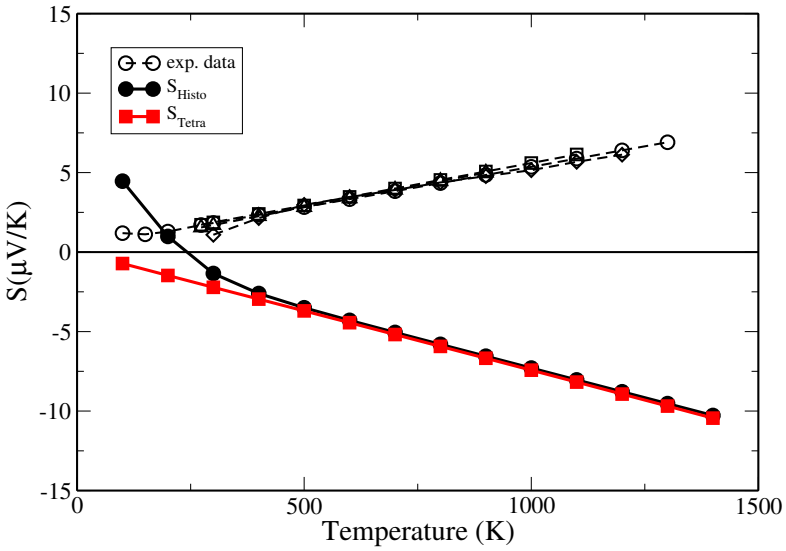

Figure 3.6: Seebeck coefficient of copper vs. temperature. Black dashed lines with open symbols: experimental results from Ref.[103]. Full lines: Seebeck coefficient calculated with RTA. Black curve: tetrahedron integration. Red: Gaussian integration. More details regarding the calculation in the main text.

Chapter 4

Seebeck and spin dependent Seebeck calculations

This Chapter contains transport calculations for several materials which are interesting for Spintronics applications, i.e. either spin polarized metals or ones with elevated SOC.
Bandstructures and densities of states for electrons and phonons are calculated with *Abinit* and shown for each material. Spectral functions and LOVA transport results for electronic resistivity and Seebeck effects are presented as well. RTA calculations carried out using *BolzTraP* on top of *ab-initio* DFT calculations are compared to LOVA results.
For spin polarized materials, the SDSE coefficient introduced in Sec 1.3.1 is predicted. Thermal expansion of the unit cell is also taken into account as a correction in Sec. 4.3.
Unless explicitly stated, a grid of 24^3 irreducible reciprocal points for electronic calculations and a grid of 12^3 reciprocal points for phonon calculations were used. The smearing of the Fermi-Dirac distribution was set to 0.1 mHa and the ground state wavefunction was converged to a tolerance of at least 10^{-9}. Both LOVA and RTA transport calculations are carried out on top of the same EPC matrix elements calcualted from DFPT. Different integration schemes over the FSF were compared for the two methods (tetrahedron and Gaussian for LOVA, tetrahedron and histogram for RTA).
The interpolation of the discrete results is performed with two *Abinit* utilities: *mrgddb* which generates the database containing the IFC data and *mrggkk* which merges all the elements of the EPC matrix.

4.1 Spin polarized metals

Spin-polarized materials owe their magnetic moment to the occupation of their d-orbitals and eventually f-orbitals. These orbitals are filled only for one of the two spin channels, and if they satisfy the Stoner criterion they will have non zero spin polarization.
The spin polarization splits the EBS and of the EDOS. Also the electron-phonon coupling now is spin dependent and phonons couple more or less strongly to spin-up/spin-down electrons. The assumptions made in Sec. 3.5 are not satisfied since the FSF is composed by more than one sheet. We treat the two spin channels separately neglecting all sorts of spin dynamics and try to validate our method *a posteriori*.

Spin-flip contribution to resistivity

If the two spin channels are independent, the total resistivity can be calculated as the resistivity of two parallel channels:

$$\rho_{\mathrm{FM}} = \frac{\rho_{\uparrow}\rho_{\downarrow}}{\rho_{\uparrow} + \rho_{\downarrow}}, \tag{4.1}$$

Spin-flip mixes the two channels, and introduces a new source of scattering to introduce in Eq. (3.8) for a correct estimation of resistivity. The spin-flip contribution to the resistivity can be calculated as [69]:

$$\rho_{\mathrm{FM}} = \frac{\rho_{\uparrow}\rho_{\downarrow} + \rho_{\uparrow\downarrow}(\rho_{\uparrow} + \rho_{\downarrow})}{\rho_{\uparrow} + \rho_{\downarrow} + 4\rho_{\uparrow\downarrow}}. \tag{4.2}$$

In this work, we neglect spin flip. This induces to a systematic error in our calculations, since one term is neglected. On the other hand, if scattering mechanisms other than phonons are negligible (e.g. highly pure magnets), this calculation offers a valid estimation of the spin-flip contribution to resistivity as the difference with the full value, which can be measured or calculated otherwise [225, 69].

4.1.1 Iron

Electrical properties of Iron have been already been presented in Sec.2.3.2. Here we present vibrational and transport calculations. Iron's phase diagram presents several phase transitions at high temperature and pressure [263, 181, 189]. At about 1043 K, the the iron passes from the low temperature α phase, aka *ferrite* which is ferromagnetic, to the β phase which is paramagnetic, aka *beta-ferrite*. No structural change happens and the structure is bcc up to about 1185 K, where the crystal symmetry becomes fcc. This phase is called the γ phase or *austenite*.

Above 1800 K or for high pressure ($>$ 10 GPa) other phases are present: the δ phase (bcc, paramagnetic) and the ϵ phase (hpc, antiferromagnetic).
Here we analyse α Fe which is magnetic with a relaxed lattice parameter of 2.467$\mathring{A}$ and magnetic moment of 2.332 μ_B. The results shown in this paragraph were produced with the same pseudopotential used to generate Fig. 2.4 (FHI with 50 Ha of energy cutoff, 32^3 kpt and 8^3 qpt for DFPT). The wavefunction was converged to a tolerance of 10^{-11}. A Gaussian smearing of 4 mHa was used for integration over the FSF. Iron FSF for spin up and spin down electrons have been already shown in Fig.2.5. Due to the difference in the two surfaces, transport properties for spin up and down can be extremely different. Theoretical PBS obtained from DFPT is compared to experimental data in Fig. 4.1 (left). On the right side of the same figure the PDOS calculated with Eq. (3.29). The DFPT results are close to experimental results.

Fig. 4.2 shows the spin dependent spectral functions $\alpha^2_{El}F(\omega)$ and $\alpha^2_{tr}F(\omega)$ calcu-

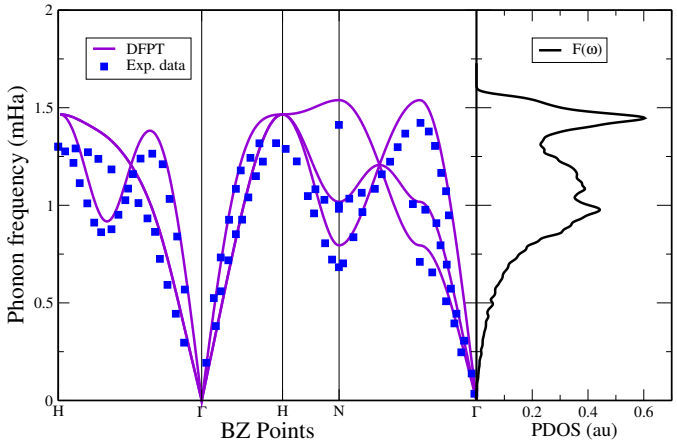

Figure 4.1: Vibrational properties of Iron. Left: PBS from DFPT compared to experimental results from [39]. Right: PDOS (3.29). More details on the calculations are given in the main text.

lated with Eqs. (3.28b) and (3.92) respectively, compared to the PDOS already shown in Fig.4.1. The spectral functions are similar, and we observe a sharp peak around 1.44 mHa which is sharper for spin down electrons (purple lines).

Electronic resistivity from elastic and inelastic LOVA are compared to experimental results in Figs.4.4. The two explicit spin contributions are shown in Fig. 4.3 for elastic (red) and inelastic (blue) LOVA. Spin down electrons have a higher resistivity.
The FM-PM phase transition is recognizable from a change of slope in experimental points (black) at T_c. Just before the FM-PM phase transition, the number of magnons increases considerably, leading to a high scattering form magnons. The

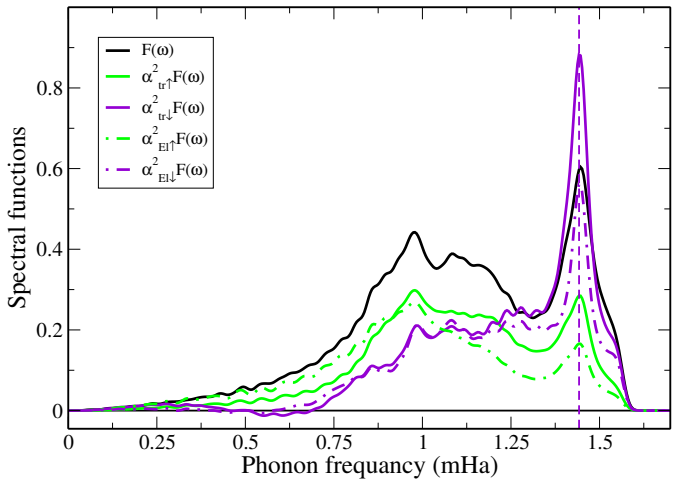

Figure 4.2: Spin dependent spectral functions for Fe. Black line: PDOS from Eq. (3.29). Full lines: generalized transport spectral functions from Eq. (3.92). Dash-dotted lines: Eliashberg spectral functions from Eq. (3.28b). Green lines spin-up electrons. Purple lines: spin-down electrons. The vertical dashed line corresponds to peaks for the two transport spectral functions.

EPC contribution to resistivity is of about 10%. At lower temperatures (Fig. 4.4b), experimental results still show a quadratic behavior, while LOVA results are linear and still underestimate experiments, but with a smaller difference. Assuming that the only source of scattering we are neglecting is the electon-magnon scattering, we can conclude that this contribute to the resistivity for about the 80%. However, for T lower than 50 K, though, quantum effect should be taken into account.
Iron Seebeck coefficient results are shown in Fig. 4.5. $S_\uparrow$ and $S_\downarrow$ are obtained by plugging the spin dependent transport spectral function into Eq. (3.106). As discussed in Sec. 3.7, the spectral functions do not vary with temperature. So the difference is entirely due to the $\mathcal{J}$ term in Eq. (3.95).
The experimental ferromagnetic Seebeck coefficient for Fe is positive up to room temperature, with a peak of about $10\mu V/K$ at around 200 K, then it becomes negative with a negative peak of around -20$\mu V/K$ at 400 K and saturates close to zero when the temperature approaches the Curie temperature T_c. The positive peak is an effect of the magnon-drag mechanism on electrons [25]. Experimental results (black dashed lines with open symbols) should be compared to the red curve which represents $\langle S \rangle_\sigma$ from Eq. (1.21). The blue curve with closed square is instead ΔS from Eq. (1.23). The other two curves are the explicit spin up and down contributions (green up triangles and purple down triangles). LOVA results are calculated with DFPT on top of harmonic calculations, so all effects due to anharmonicity are neglected. The calculated ΔS has an asymptotic behavior with

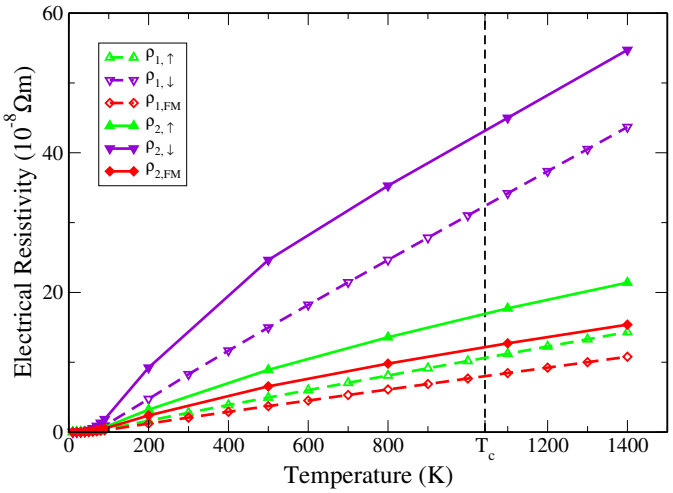

Figure 4.3: Electronic resistivity of Iron vs temperature. Green lines with up triangles: spin up electrons. Purple lines with down triangles: spin downs electrons. Red lines: ρ_{FM} from Eq. (4.1). Dashes lines with open symbols: elastic LOVA. Full lines with full symbols: inelastic LOVA. The vertical dashed line represents the Curie temperature.

a limit value of -60$\mu V/K$ close to the Curie temperature. Afterwards the system becomes paramagnetic.
Seebeck results from RTA calculations are showed in Fig. 4.5b. *BolzTraP* calculations were performed on the same *ab-initio* calculations used to produce Fig. 4.5a. 100 planewaves per energy band were used (LPFAC) with an energy resolution of 0.1 mRy. Note that *BolzTraP* returns the ratio of σ over τ, thus the red curve represents:

$$\langle S' \rangle_\sigma = \frac{\sigma_\uparrow/\tau_\uparrow S_\uparrow + \sigma_\downarrow/\tau_\downarrow S_\downarrow}{\sigma_\uparrow/\tau_\uparrow + \sigma_\downarrow/\tau_\downarrow} \tag{4.3}$$

It should be noted that the RTA assumes a free electron model, thus no EPC is considered. Thus, for example $S_\uparrow$ and $S_\downarrow$ are quite similar in Fig. 4.5b, so their average is also similar and their difference is almost null, while LOVA predicts a more complex structure, with spin up and down channels having different sign for S. According to these results, spin up electrons behave as in a N-doped metal, while spin down electrons behave as if they were in a P-doped metal, giving rise to a considerable ΔS.

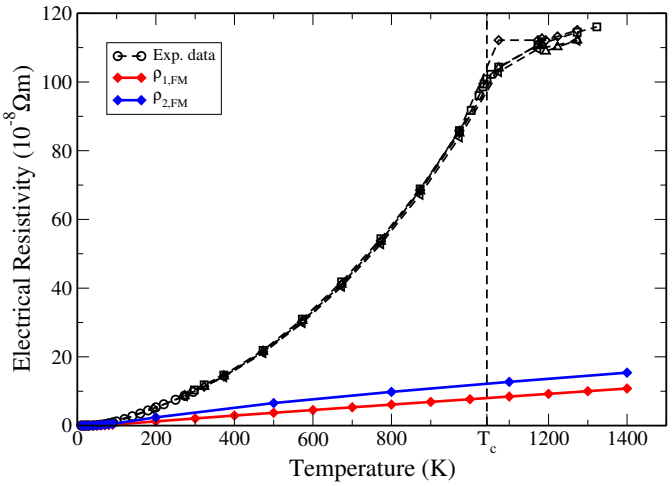

(a) High temperatures

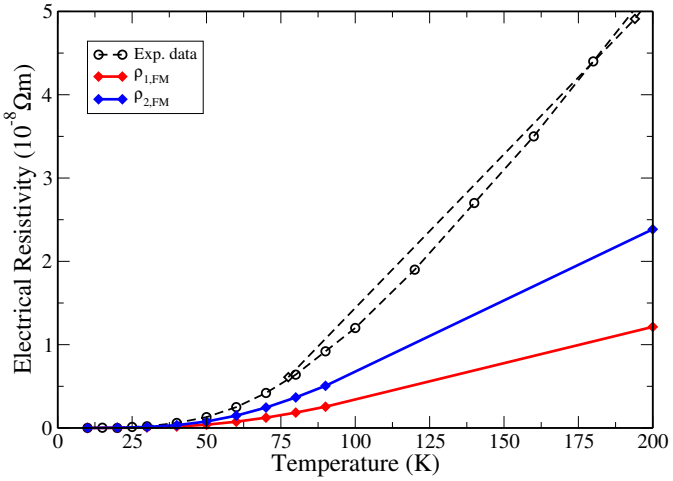

(b) Low temperatures.

Figure 4.4: Electronic resistivity of Iron vs temperature. Red: elastic LOVA. Blue line: Inelastic LOVA. Black dashed lines with open symbols: experimental data from [103]. Dashed vertical line: Curie temperature.

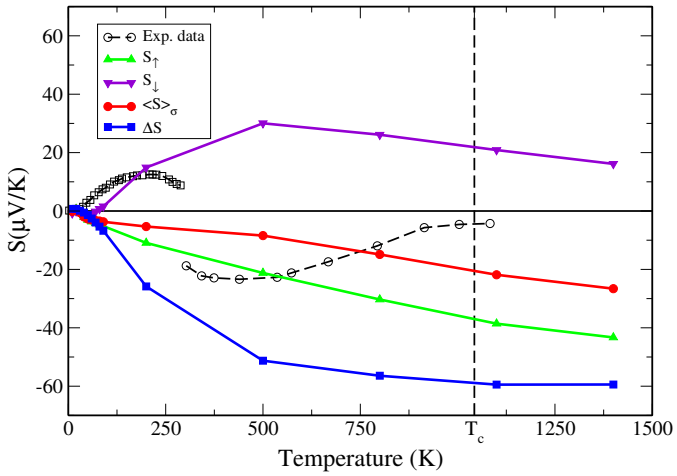

(a) Inelastic LOVA.

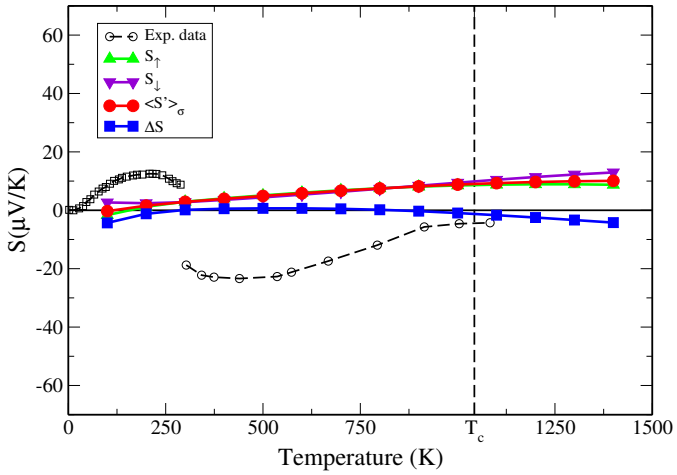

(b) RTA.

Figure 4.5: Iron Seebeck coefficient vs. temperature. Black dashed lines with open symbols: experimental data from [103]. Green up triangles: spin up contribution. Purple down triangles: spin down contribution. Red curve with closed circles: ferromagnetic Seebeck coefficient (Eq. (1.21)). Blue curve with closed squares: spin dependent Seebeck coefficient (Eq. (1.23)). Black dashed vertical line: Curie temperature.

4.1.2 Nickel

Ni is a transition metal like Iron. It presents a fcc symmetry with lattice parameter of about 7.59 a_0 for the cubic cell. Its magnetic momentum is of 0.625 μ_B and its Curie temperature of 628.5 K [188]. I used a LDA-FHI pseudopoential with 32^2 kpt for GS calculations and 4^3 qpt for DFPT. The GS wavefunction was converged up to 10^{-9} and the electronic smearing was set to 0.1 mHa.
EBS and EDOS are shown in Fig. 4.6, FSF for spin up and spin down electrons are represented in Fig. 4.7. Spin polarization has the same splitting effect on the EBS, electronic DOS and spectral functions as for Iron. The FSF are quite different for the two spin channels. Spin up have a pretty easy FSF, quite similar to the one of Copper (Fig. 2.2), with only one sheet almost spherical. Spin down instead show four sheets: one inner polyhedral (red) surface, a pretty complex blue sheet (transparent) plus several disconnected parts. It is then possible that spin up electrons will be much easier to treat with respect to spin down electrons.
Vibrational properties and spectral functions are shown respectively in Figs.4.8 and 4.9. Phonons from DFPT agree with experiments from Ref. [24]. From Fig. 4.9 we observe that in the case of Nickel, the spectral functions for spin down electrons have higher peaks (at around 1 mHa and 1.31 mHa). This is unfortunate since transport properties will depend a lot on spin down electrons, which, as already mentioned, have a FSF pretty difficult to parametrize within FSH formalisms.
Nickel resistivity is shown in Figs. 4.10 and 4.11. The first one shows the explicit contributions from spin up and down electrons to the resistivity. Also in this case, spin down electrons have a higher resistivity than spin up electrons. Similar comments with respect to the Iron case can be made relatively to the comparison of the ρ_{FM} calculated from Eq.(4.1).
Seebeck coefficients from LOVA and RTA are shown respectively in Fig. 4.12a and Fig. 4.12b. The experimental Seebeck coefficient is always negative, with a negative peak around 500 K and a positive one corresponding to the Curie temperature. A Gaussian integration with smearing of 4 mHa was used for LOVA calculations while *BolzTraP* calculations were performed with 100 planewaves per energy band (LPFAC) with an energy resolution of 0.1 mRy on top of the same *ab-initio* calculations used to produce Fig. 4.12a.

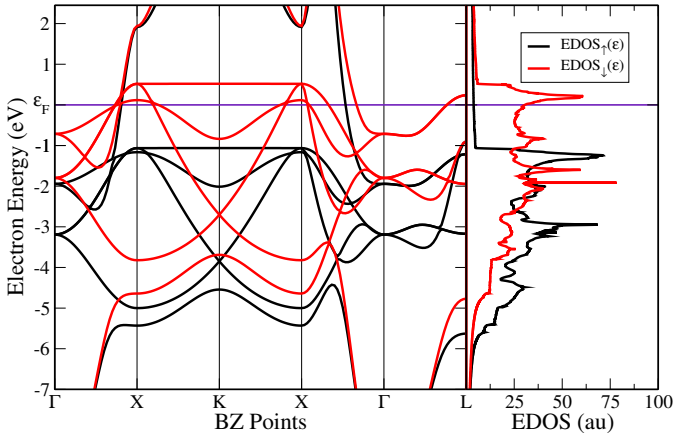

Figure 4.6: Electronic GS properties for Nickel from DFT. Left: EBS. Right: EDOS. Black lines: spin up electrons. Red: spin down electrons.

(a) Spin up Fermi surface

(b) Spin down Fermi surface

Figure 4.7: Nickel Fermi surface for spin up (left) and spin down (right) inside the first BZ (white lines).

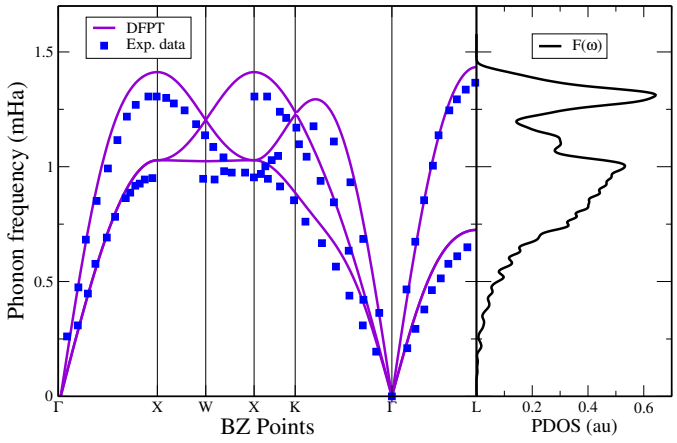

Figure 4.8: Vibrational properties of Nickel. Left: PBS from DFPT compared to experimental results from [24]. Right: PDOS (3.29).

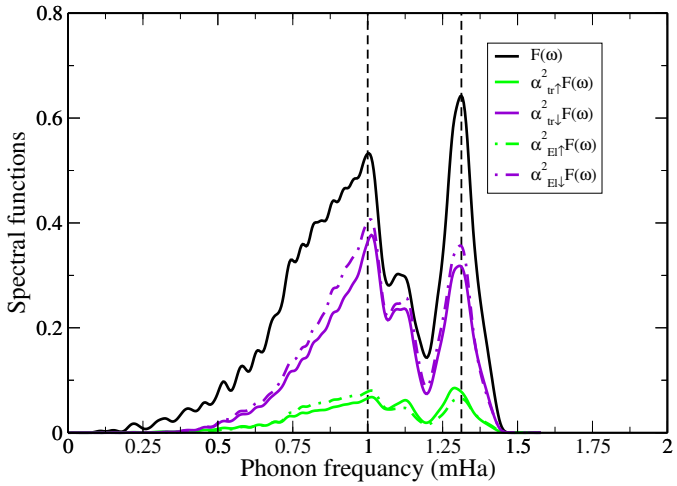

Figure 4.9: Spin dependent spectral functions for Ni. Black line: PDOS from Eq. (3.29). Full lines: generalized transport spectral functions from Eq. (3.92). Dash-dotted lines: Eliashberg spectral functions from Eq. (3.28b). Green lines spin-up electrons. Purple lines: spin-down electrons. The vertical dashed line corresponds to peaks for the two transport spectral functions.

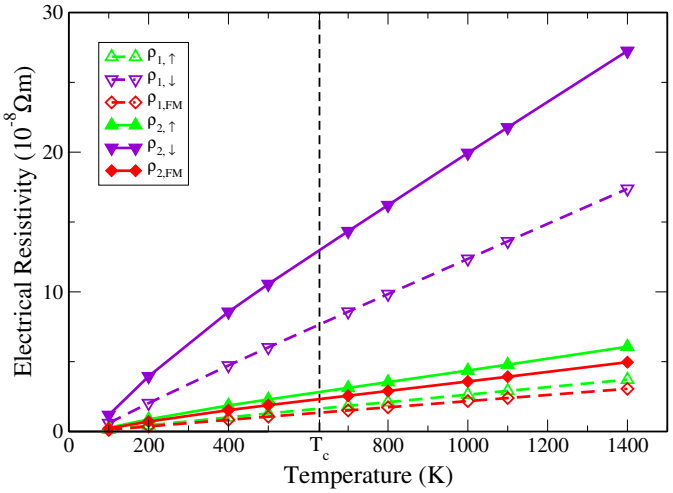

Figure 4.10: Electronic resistivity of Nickel vs temperature. Explicit spin up (green lines up triangles) and down (purple lines down triangles) components. Red lines: ρ_{FM} from Eq. (4.1). Dashes lines with open symbols: elastic LOVA. Full lines with full symbols: inelastic LOVA. The vertical dashed line represents the Curie temperature.

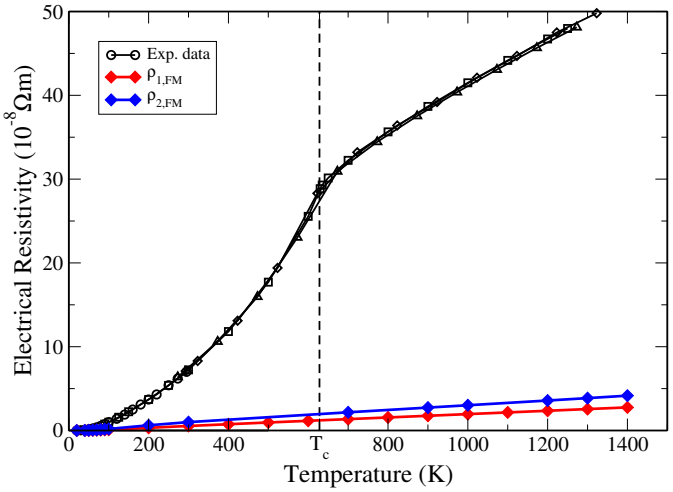

(a) High temperatures

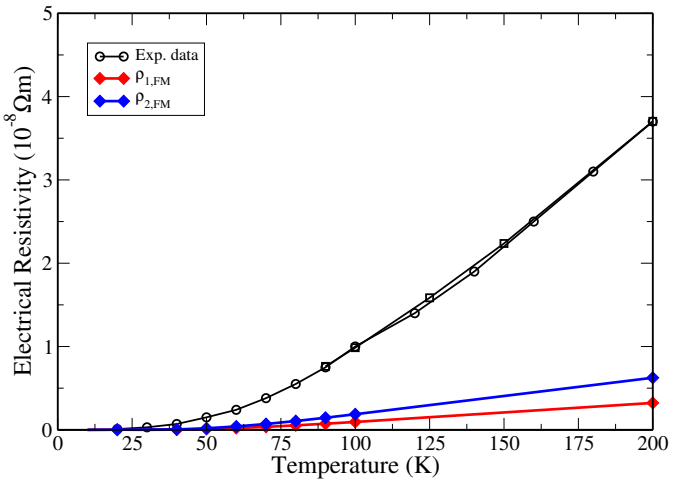

(b) Low temperatures.

Figure 4.11: Electronic resistivity of Nickel vs temperature. Red: elastic LOVA. Blue line: Inelastic LOVA. Black dashed lines with open symbols: experimental data from [103]. Dashed vertical line: Curie temperature.

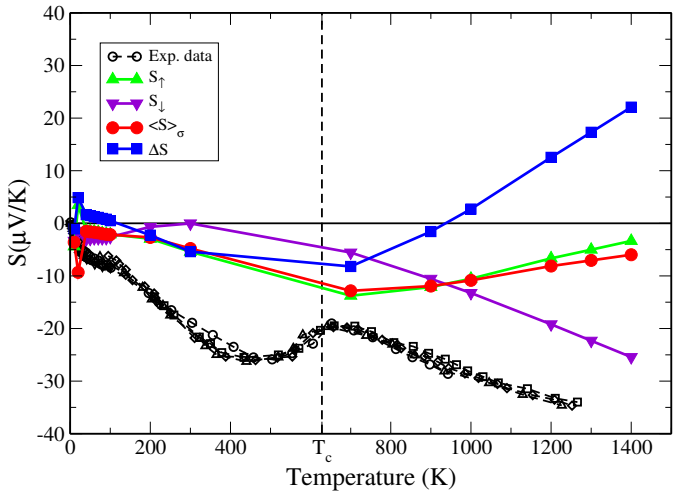

(a) Inelastic LOVA.

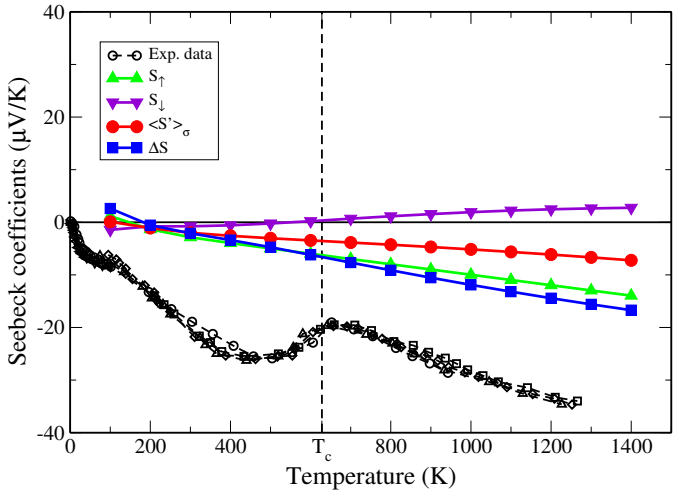

(b) RTA.

Figure 4.12: Nickel Seebeck coefficient vs. temperature. Black dashed lines with open symbols: experimental data from [103]. Green up triangles: spin up contribution. Purple down triangles: spin down contribution. Red curve with closed circles: ferromagnetic Seebeck coefficient (Eq. (1.21)). Blue curve with closed squares: spin dependent Seebeck coefficient (Eq. (1.23)). Black dashed vertical line: Curie temperature.

4.2 Spin-orbit coupled metals

Platinum is a heavy metal, which means that relativistic effects, such as spin orbit coupling, are not negligible. Heavy metals are extremely important for applications in Spintronics, since the SHE allows the mutual transformation of an electrical current into a spin current (Sec. 1.4.2).
Here I present transport property calculations for Pt. Pt presents a fcc structure with lattice cubic parameter of 7.5 a_0 and paramagnetic order [189]. As for the previous cases, I present ground state electronic properties from DFT, vibrational properties from DFPT and LOVA transport quantities compared to available experimental results. These calculations were carried out using a Hartwigsen-Goedecker-Hutter pseudopotential [97] with 18 valence electrons. 30 Ha were used for the plane wave cut off. SOC is included explicitly in the calculation of the wavefunction [257], which was converged up to 10^{-20}.
EBS and EDOS are shown in Fig. 4.13. A zoom along the ΓX direction (100) is shown in Fig. 4.13. The SOC splits the 5d band into the $5d_{3/2}$ and $5d_{5/2}$, with a difference in energy of electronic levels of about 1 eV [228]. It is remarkable the presence of two hole-like bands which intersect the Fermi energy around the X and the L points. This will have consequences for transport calculations.
The FSF (with and without SOC) are shown in Fig 4.14. FSF for Pt shows a main free-electron band and some more complex bands. SOC does not change the FSF severely. PBS and PDOS are shown in Fig. 4.15. The agreement with experiment is good, apart from an overestimation of phonon frequencies a the W point [257]. The Eliashberg and transport spectral functions are shown in Fig.4.16 in relation to the PDOS. $\alpha^2_{\mathrm{El}}F$ and $\alpha^2_{\mathrm{tr}}F$ are extremely similar. Transport properties are nicely predicted by LOVA. Fig. 4.17 shows the resistivity of Pt. Theoretical curves represent the calculated resistivity within the elastic and inelastic LOVA and with Gaussian or Tetrahedron integration. The elastic LOVA gives a better prediction than the inelastic one for resistivity, while the contrary happened for the Nickel and Iron case. This depends on the sign of the off diagonal Q elements in Eq. (3.79). A smearing of 6 mHa was used for the Gaussian integrations.
Fig. 4.18 shows the Seebeck coefficient calculated with the LOVA (4.18a) and with the RTA (4.18b) methods. LOVA prediction is quite accurate, apart from a positive maximum below 100 K probably due to electon-phonon drag, which we neglect. On the other side, the S calculated with *BolzTraP* shown in Fig. 4.18b has the right order of magnitude but wrong sign. This is due to the presence of the hole-like bands in the EBS (Fig. 4.13). The sign of the Seebeck coefficient is important to determine if a metal is of the N or P type, and as already observed for Lithium in [271], electron-free like models do not always give good predictions since the EPC is not taken into account.

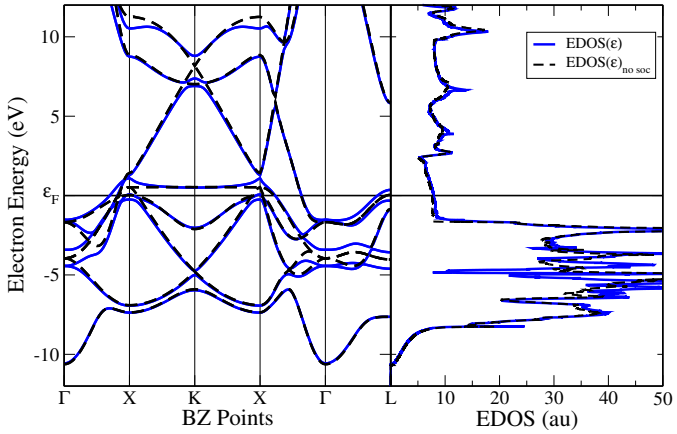

(a) GS properties for Platinum.

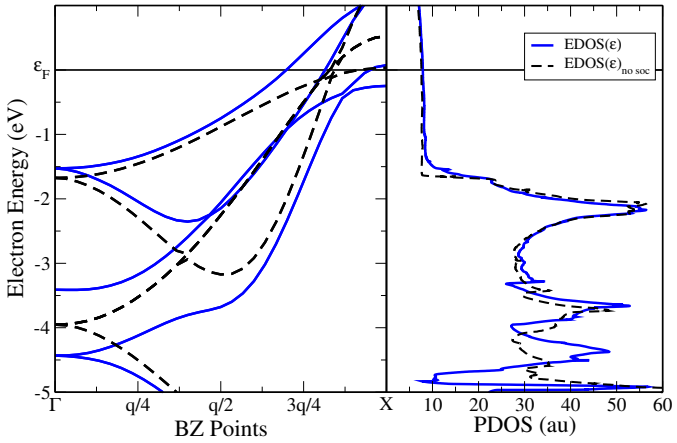

(b) Zoom along the ΓX direction.

Figure 4.13: Electronic GS properties for Platinum from DFT. Left: EBS. Right: EDOS. Blue full lines: calculations with SOC. Black dashed lines: no SOC.

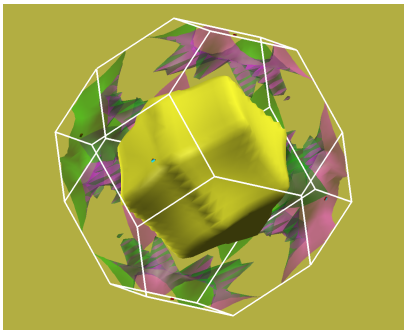

(a) FSF of Platinum including SOC.

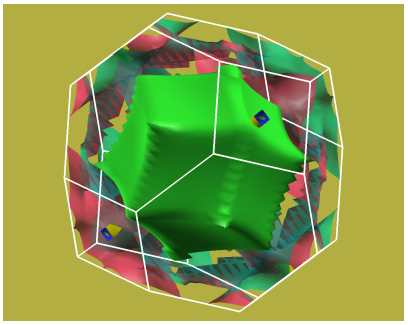

(b) FSF of Platinum without SOC.

Figure 4.14: FSF of Platinum in the first BZ.

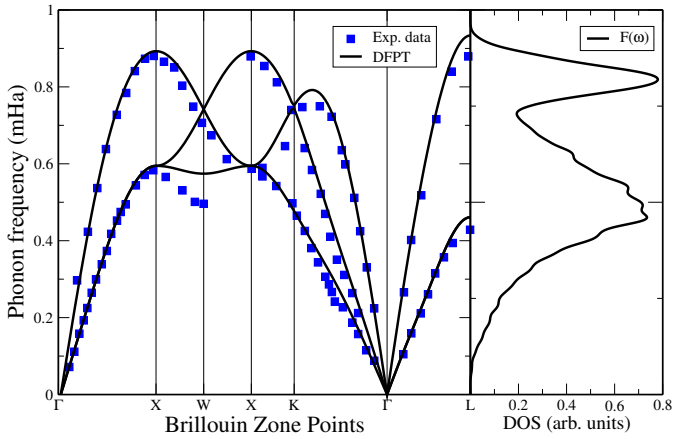

Figure 4.15: Vibrational properties of Platinum. Left: PBS from DFPT compared to experimental results from [56]. Right: PDOS.

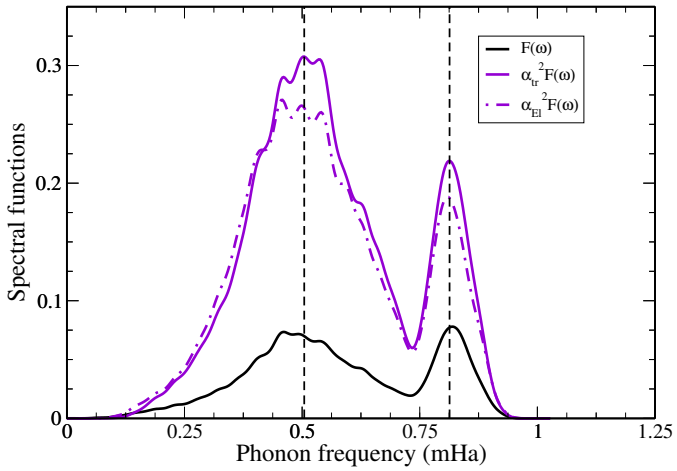

Figure 4.16: Spectral functions for Pt. Black line: PDOS from Eq. (3.29). Full line: generalized transport spectral functions from Eq. (3.92). Dash-dotted lines: Eliashberg spectral functions from Eq. (3.28b). Vertical dashed lines correspond to peaks for the two transport spectral functions.

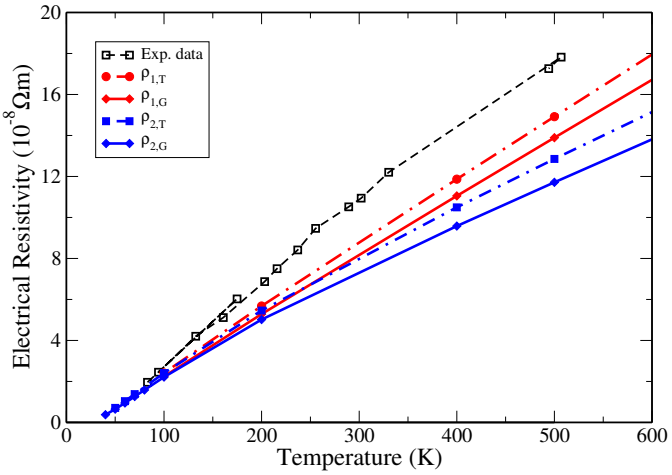

Figure 4.17: Resistivity of Platinum vs. temperature. Black dashed line with open symbols: experimental data from [184]. Red curves: elastic LOVA. Blue curves: inelastic LOVA. Dot-dashed lines: Tetrahedron integration. Full lines: Gaussian integration.

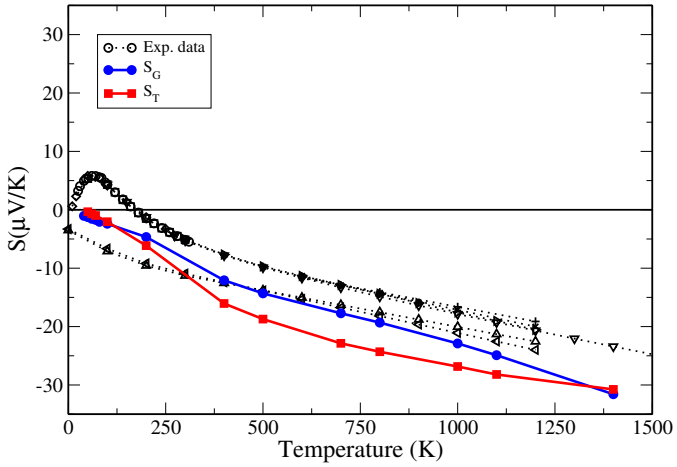

(a) Inelastic LOVA.

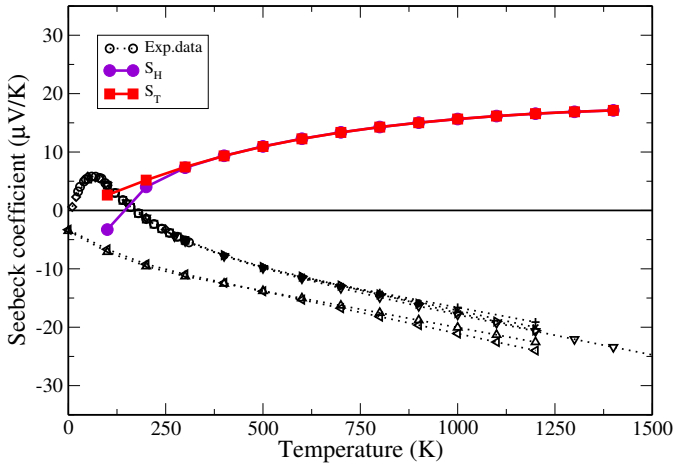

(b) RTA.

Figure 4.18: Platinum Seebeck coefficient vs. temperature. Black dashed lines with open symbols: experimental data from [103]. Full lines with closed circles: Seebeck for Tetrahedron (red), Gaussian (blue) and Histogram (Purple) integration.

4.3 Disordered metals

For disordered materials the scattering from impurities becomes extremely important. Several approaches have been proposed for dealing with disorder in first principles calculations:

1. The Virtual crystal approximation (VCA) [170],
2. Average of large supercells calculations with different configurations,
3. The Coherent potential approximation (CPA) [219],

The VCA approximation

In the VCA, a binary disordered alloy $A_{x_A}B_{x_B}$ is replaced by an uniform medium composed by a fictitious element with atomic number $\bar{Z} = x_A Z_A + x_B Z_B$. In practice, the pseudopotential of the two species are averaged to the desired ration, leading to some nonlocal effects. This technique offers a simple and computationally light approach, since the Bloch symmetry is restored. On the other hand, all short range interactions are neglected. The scattering from impurity is totally removed, so we expect the resistivity will be underestimated even more than within the LOVA approximation.

Supercell approximation

Several standard *ab-initio* calculations for a large, non primitive, unit cell with fixed composition are realized. The position of impurities in the cell is varied between different cells and the result is averaged over all configurations.
This approach is computationally expensive and with limited applicability, but it can be more realistic than VCA if the cells and the number of configurations are large enough since short range interaction are taken into account.

The CPA-KKR approximation

The CPA method approximates a random alloy with an effective ordered medium that is determined self-consistently from the condition of stationary scattering. The space is decomposed into isolated atomic scattering sites embedded into a free electron environment. Within the single atomic sites then, one can seek exact numerical solution, while, in the interstitial space a multiple scattering problem has to be solved.
Within the KKR method, GF can be used to represent a binary disordered alloy $A_{x_A}B_{x_B}$ using a weighted t-matrix of the form $\underline{t}^{ATA} = x_A \underline{t}^A + x_B \underline{t}^B$ [62].

In principle, this method has an accuracy which is intermediate between the VCA and the supercell methods.

4.3.1 Permalloy

Permalloy (Py) has already been introduced in Chap. 1 as one of the most promising materials for Spintronics applications. It is a nickel-iron magnetic alloy invented at Bell Telephone Laboratories in 1914 [14] and since then widely used as a spin injector in nanomagnetic experiments such as non local spin valves [65, 157] and lateral spin valves [210, 255, 258, 114, 157] as well as for domain wall motion [153, 165] and has been suggested for applications in spintronic devices [174] due to its advantagious properties which can be summarized in its low magnetic anisotropy, high Curie temperature, and significant spin-dependent scattering that yields a highly spin-polarized current within a few nanometers [166]. In many SSE experiments with metals a $Ni_{81}Fe_{19}$ alloy was used to generate the spin current [248]. Permalloy presents a fcc crystal structure in which atomic positions are randomly occupied by one of the Ni or Fe species. The VCA method has been used to simulate disorder: two GGA-FHI potentials were mixed at the exact 81-19 proportion. Our LOVA approach does not consider disorder, even in principle. One way of integrating this scattering would be to calculate the impurity density in a big cell and match the boundary conditions with a bulk calculation. The relaxed cubic cell parameter is of about 6.836 a_0. The plane wave cut off was set to 40 Ha. Convergence tests showed that 32^3 points are needed for the sampling of the BZ and 4^3 qpt are enough for DFPT. The GS wavefunction was converged up to 10^{-10}.
The EBS and EDOS are shown in Fig. 4.19. The FSF for spin up and spin down electrons are shown in Fig. 4.20. Spin up electrons have a quite regular FS, with a few "necks", which reminds of the copper FSF (Fig 2.2). Spin down electrons have a more complicated FSF structure, with three different sheets.
The PBS and relative PDOS is shown in Fig. 4.21. VCA offers quite a good agreement with experimental results. The PDOS and spin dependent spectral functions are shown in Fig. 4.22. The spectral functions are similar with a well defined peak at around 1.19 mHa (dashed vertical line). Phonons which transport spin up electrons belong to a lower energy band with respect to phonons which couple to spin up.
Resistivity calculations are more complicated in the Py case. Since the system is disordered, we expect that the scattering from impurities matters in Eq. (3.8), and that the resistivity is much higher than Ni or Fe. Our treatment of the disorder goes in the opposite direction and treats the alloy as if it was a crystal. Actually, experimental results lie between Ni and Fe. The two explicit spin contributions are presented in Fig. 4.23. Elastic and inelastic LOVA, with the two usual integration methods are shown. The spin down channel shows a resistivity almost two order of

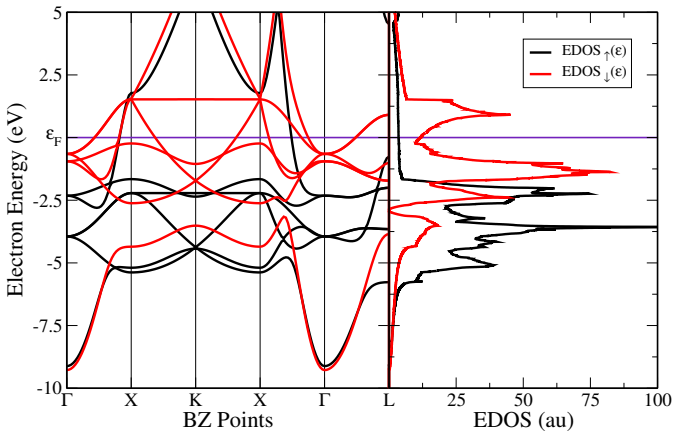

Figure 4.19: Electronic band structure (left) and electronic density of states (right) for Py. More details about the calculations can be found in the main text.

magnitude larger than the spin up electrons, which will then be more important in the $\langle S \rangle_\sigma$ calculation.
In Fig. 4.24 instead the ferromagnetic resistivity from Eq. (4.1) is shown, always for the elastic and the inelastic cases with the two integrations. (with electronic smearing of 4 mHa for the Gaussian integration). Experimental data for Py, Fe and Ni are shown for comparison [103]. Note that the underestimation done in Eq. (4.1) is the same for the two spin channels. Neither spin flip nor disorder are considered.
Fig. 4.25 shows the Seebeck coefficients for Permalloy, calculated with inelastic LOVA (Fig. 4.25a) and RTA (Fig. 4.25b) on top of the same DFPT data obtained from *Abinit*. In the LOVA case, both spin channels return a negative Seebeck coefficient. The $\langle S \rangle_\sigma$ curve is extremely close to $S_\uparrow$ since spin up have higher conductivity, as can be observed in the resistivity (Fig. 4.23). On the contrary, for SDSE coefficient $\Delta S = S_\uparrow - S_\downarrow$, the two spin channels have the same weight, and for high temperatures, while $S_\uparrow$ becomes small, $S_\downarrow$ becomes more and more important. The RTA returns both channels with negative Seebeck coefficients, and varying almost linearly with the temperature.

4.4 Thermal Expansion

DFT is exact only for ground state properties calculations. Phonon calculations are based on the harmonic approximation presented in Sec. 2.4. In practice, in this picture, all ions vibrate with constant amplitude and frequency around their equilibrium position and IFC calculations are easily done. In DFPT, due to the

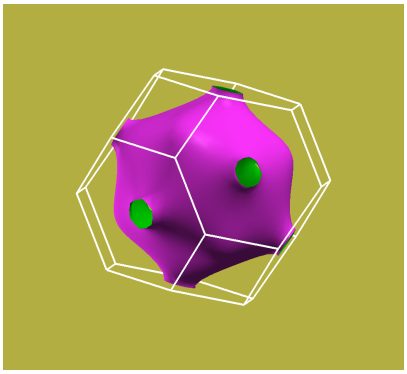

(a) FSF of permalloy for spin up electrons.

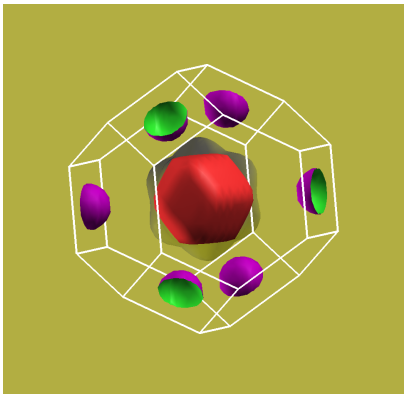

(b) FSF of permalloy for spin down electrons.

Figure 4.20: FSF of permalloy in the first BZ. Spin down electrons (right) have three sheets. One is transparent.

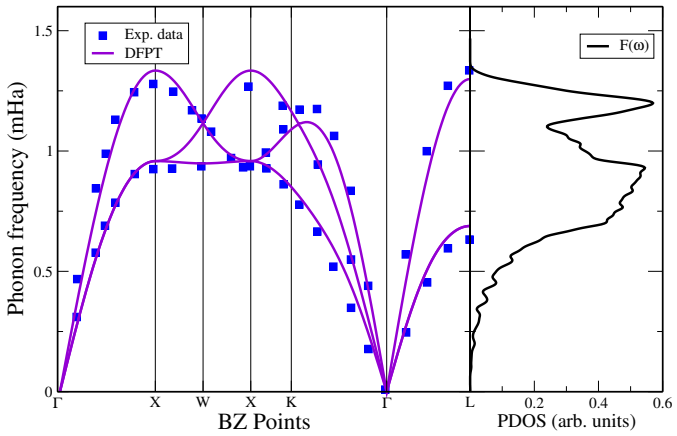

Figure 4.21: Vibrational properties of permalloy. Left: PBS from DFPT compared to experimental results from [95]. Right: PDOS (3.29). More details about the calculations can be found in the main text.

adiabatic approximation, the response of the electronic density to this vibration is negligible, being the former on a time scale much longer than the latter. With increasing temperature, vibrations are no longer harmonic, phonons start to interact, and higher order anharmonic terms contribute to the transport.
The quasi-harmonic approximation (QHA) is often employed to include anharmonicities related to the thermal expansion of the crystal lattice. Phonon frequencies are still calculated in the harmonic approximation, but for different cell volumes. Other sources of anharmonicities are neglected.
This picture is in principle valid when phonons interact weakly, for example at low

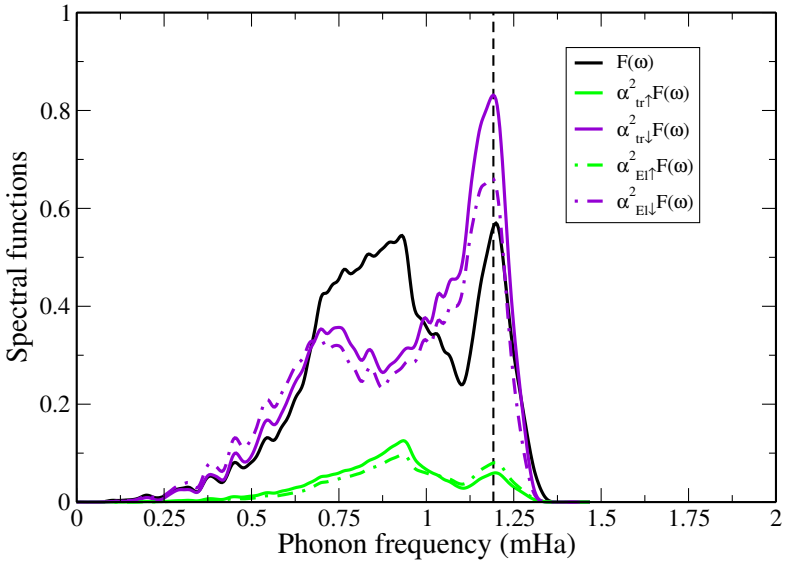

Figure 4.22: Spectral functions for Py. Black line: PDOS (3.29). Full lines: generalized transport spectral functions (3.92). Dash-dotted lines: Eliashberg spectral functions (3.28b). Green lines spin-up electrons. Purple lines: spin-down electrons. Vertical dashed line: peaks for the two transport spectral functions. More details about the calculations can be found in the main text.

T, and the residual phonon scattering beyond the QHA is small. However, when the temperature increases, phonons undergo mutual scattering, which corresponds to the anharmonic vibrations of atoms. Anharmonicity is in general weak [142] and usually hardens unstable phonon frequencies, as the restoring forces which keep atoms in the vicinity of their equilibrium positions become progressively larger with temperature. Explicit anharmonic contributions can be sometimes key to obtain correct vibrational spectra [52].

Thermal expansion corrections can sometimes be important for transport quantities. I performed QHA calculations for Fe and Ni separately and for the mixed VCA Py. Results are shown in Figs. 4.26, 4.27 and 4.28 for the three systems respectively. The harmonic results presented above are represented with the same colors and dashed lines with open symbols.

For Iron the spin up component $S_\uparrow$ almost goes to zero, while the spin down component changes drastically (Fig. 4.26c). This modifies the $\langle S\rangle_\sigma$ and ΔS in Fig. 4.26d. Now $\langle S\rangle_\sigma$ shows a behavior which reproduces experiments at high temperature, while at low T, the magnon-phonon drag is still missing. The predicted ΔS has a maximum at about room temperature and change sign at about 750 K.

Nickel...

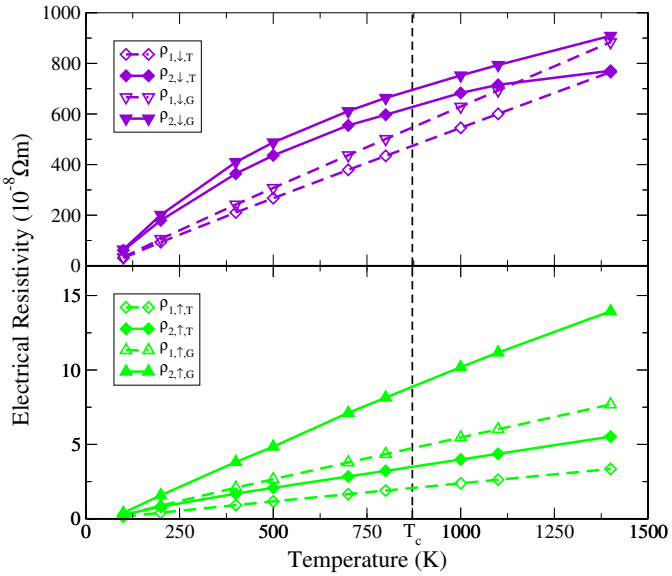

Figure 4.23: Electronic resistivity of Permalloy vs temperature. Explicit spin up (Bottom: green lines) and down (Top: purple lines) components. Dashes lines with open symbols: Elastic LOVA. Full lines with full symbols: Inelastic LOVA. Lines with diamond: Tetrahedron integration. Lines with triangles: Gaussian integration. The vertical dashed line represents the Curie temperature.

For permalloy there is no big modification due to thermal expansion: Almost all the coefficients have the same behavior, with $\langle S \rangle_\sigma$ which gets closer to the experimental results and ΔS which is higher at low T.

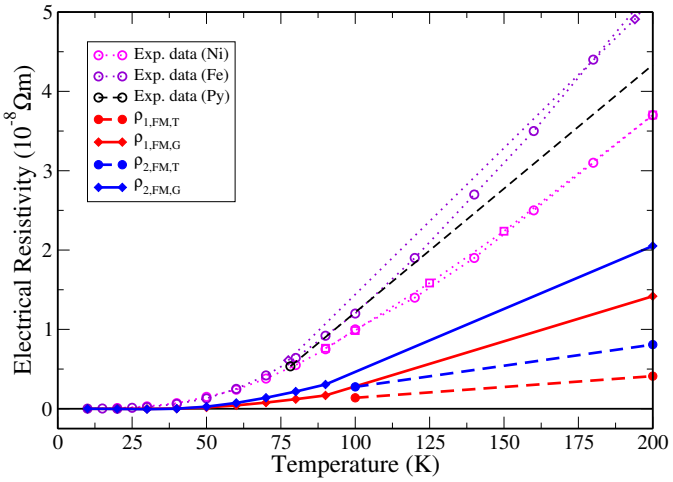

(a) Low temperature limit.

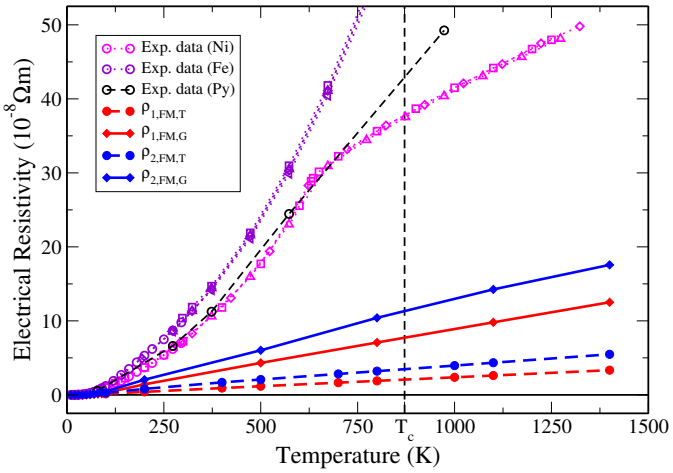

(b) High temperature limit.

Figure 4.24: Spin dependent resistivity from LOVA vs. temperature for Permalloy. Dotted lines with open symbols: experimental results for Ni (pink), Fe (purple) and Py (black) from [103]. Red: elastic LOVA. Blue: inelastic LOVA. Dashed lines with full symbols: tetrahedron integration (T). Full lines with full symbols: Gaussian integration. More details about the calculations can be found in the main text.

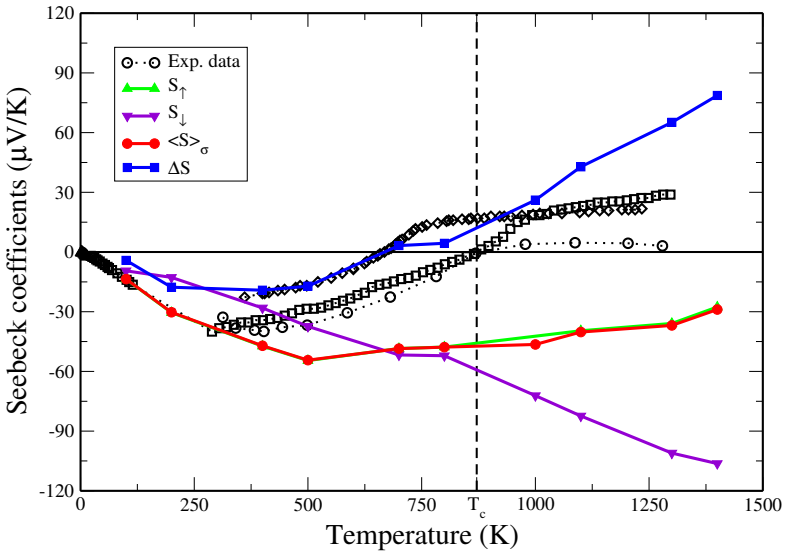

(a) Inelastic LOVA.

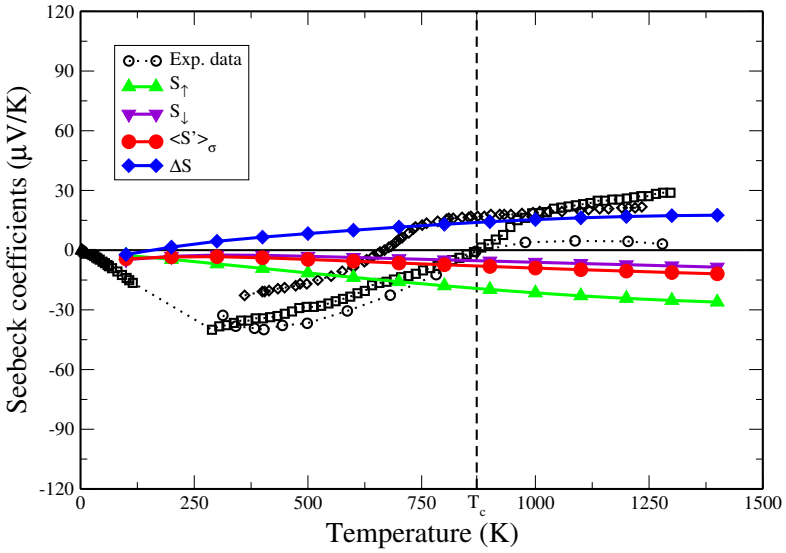

(b) RTA.

Figure 4.25: Permalloy Seebeck coefficient vs. temperature. Black dashed lines with open symbols: experimental data from [103]. Green up triangles: spin up contribution. Purple down triangles: spin down contribution. Red curve with closed circles: ferromagnetic Seebeck coefficient (Eq. (1.21)). Blue curve with closed squares: spin dependent Seebeck coefficient (Eq. (1.23)). Black dashed vertical line: Curie temperature. More details about the calculations can be found in the main text.

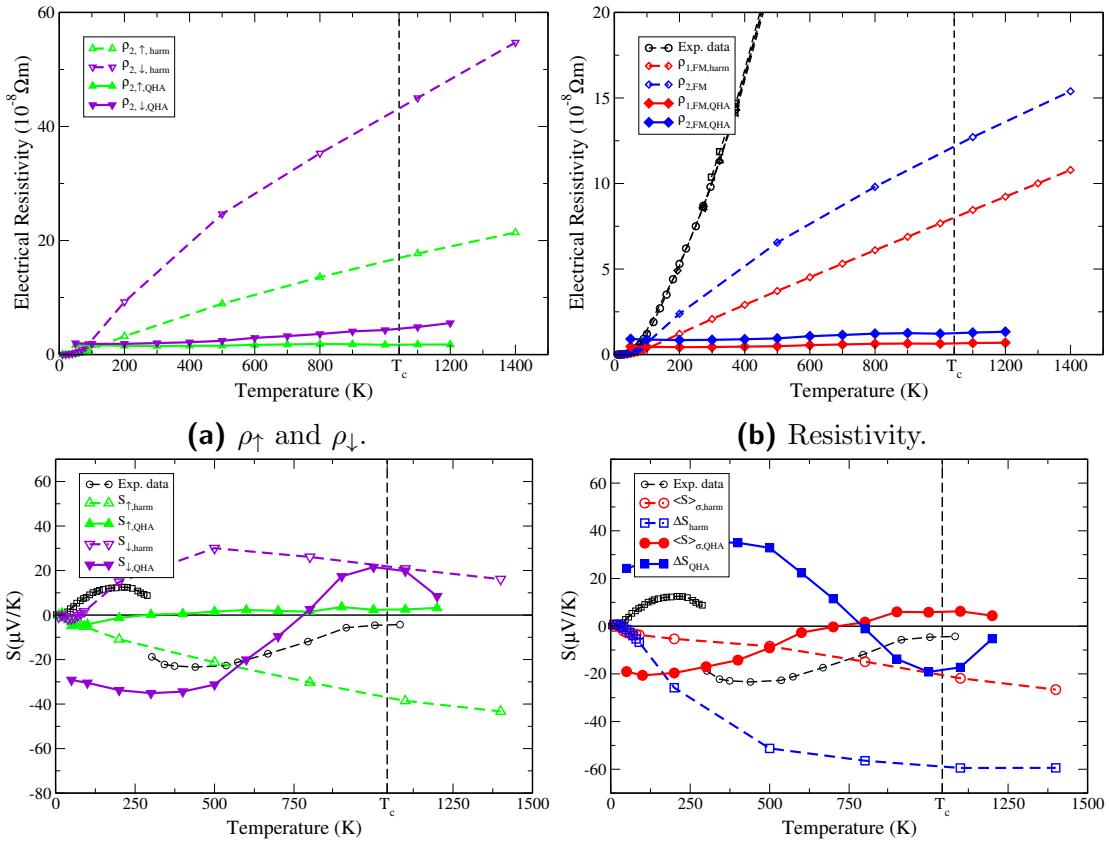

(a) $\rho_\uparrow$ and $\rho_\downarrow$.

(b) Resistivity.

(c) $S_\uparrow$ and $S_\downarrow$.

(d) $\langle S\rangle_\sigma$ and SDSE coefficients.

Figure 4.26: Transport coefficient vs. temperature for Iron within QHA. Top: resistivity. Bottom: Seebeck coefficients. Left: explicit spin channels contributions. Right: macroscopic coefficients. Full lines with closed symbols are QHA results. Dashed lines with open symbols are harmonic results (same as in Fig. 4.12a.). Black dashed lines with open symbols: experimental data from [103]. Green up triangles: spin up contribution. Purple down triangles: spin down contribution. Red with circles: ferromagnetic resistivity (Eq. (4.1)) and Seebeck coefficient (Eq. (1.21)). Blue with squares: spin dependent Seebeck coefficient (Eq. (1.23)). Black dashed vertical line: Curie temperature.

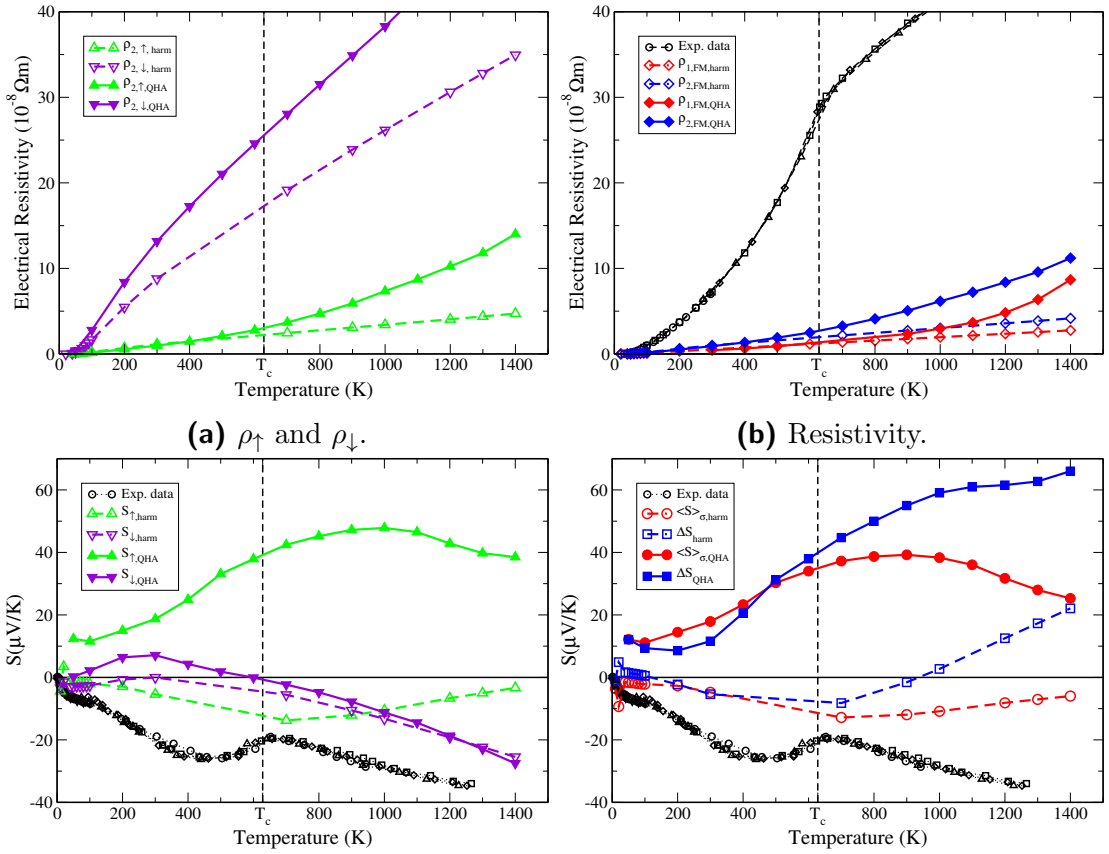

(a) $\rho_\uparrow$ and $\rho_\downarrow$.

(b) Resistivity.

(c) $S_\uparrow$ and $S_\downarrow$.

(d) $\langle S\rangle_\sigma$ and SDSE coefficients.

Figure 4.27: Transport coefficient vs. temperature for Nickel within QHA. Top: resistivity. Bottom: Seebeck coefficients. Left: explicit spin channels contributions. Right: macroscopic coefficients. Full lines with closed symbols are QHA results. Dashed lines with open symbols are harmonic results (same as in Fig. 4.12a.). Black dashed lines with open symbols: experimental data from [103]. Green up triangles: spin up contribution. Purple down triangles: spin down contribution. Red with circles: ferromagnetic resistivity (Eq. (4.1)) and Seebeck coefficient (Eq. (1.21)). Blue with squares: spin dependent Seebeck coefficient (Eq. (1.23)). Black dashed vertical line: Curie temperature.

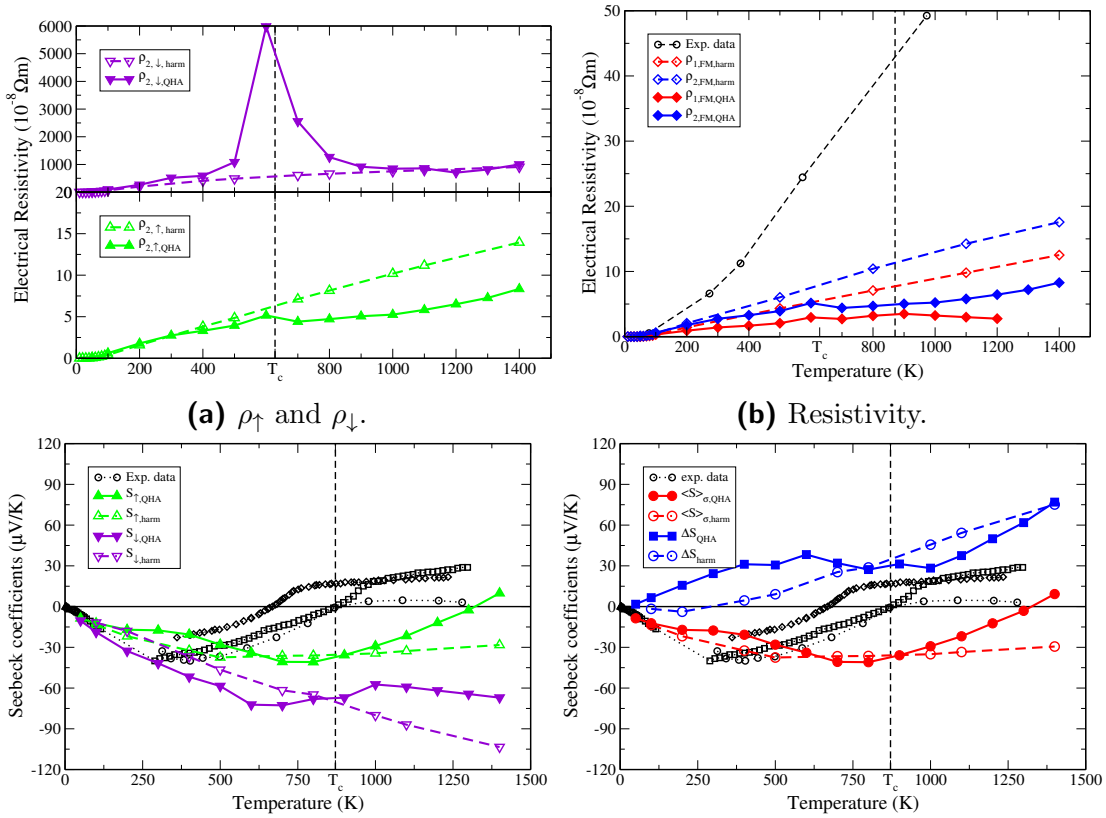

(a) $\rho_\uparrow$ and $\rho_\downarrow$. **(b)** Resistivity.

(c) $S_\uparrow$ and $S_\downarrow$. **(d)** $\langle S\rangle_\sigma$ and SDSE coefficients.

Figure 4.28: Transport coefficient vs. temperature for Permalloy within QHA. Top: resistivity. Bottom: Seebeck coefficients. Left: explicit spin channels contributions. Right: macroscopic coefficients. Full lines with closed symbols are QHA results. Dashed lines with open symbols are harmonic results (same as in Fig. 4.25a.). Black dashed lines with open symbols: experimental data from [103]. Green up triangles: spin up contribution. Purple down triangles: spin down contribution. Red with circles: ferromagnetic resistivity (Eq. (4.1)) and Seebeck coefficient (Eq. (1.21)). Blue with squares: spin dependent Seebeck coefficient (Eq. (1.23)). Black dashed vertical line: Curie temperature.

4.5 Conclusion and Perspectives

I presented calculations carried out within the LOVA method presented in Chapter 3 for spin-polarized, spin-orbit coupled and disordered materials. Scattering form magnons is important for the calculation of resistivity in spin polarized materials and is the predominant contribution before the PM-FM phase transition. At low temperature, as expected, the EPC gives a reasonable estimation of experimental values, with inelastic contributions providing a correction.
The electron-magnon scattering affects spin up and spin down electrons to the same extent, so in the calculation of $\langle S \rangle_\sigma$ this effect is averaged out go to a good approximation. Spin-orbit coupling and disorder are on the other hand not an obstacle to our calculations.
Contrary to what we expected, the QHA introduces some important corrections, especially in the Fe case, where the contribution to $\langle S \rangle_\sigma$ from spin up is almost suppressed, and in Ni, where $S_\uparrow$ changes sign.

Material	PP	Exc	Ecut	kpt	qpt	GSM (mHa)
Cu	FHI	GGA	40	24	12	0.1
Fe	FHI	GGA	50	32	8	0.4
Ni	FHI	LDA	40	32	8	0.4
Pt	HGH	GGA	30	24	12	0.6
Py	FHI	GGA	40	32	12	0.4
Fe (QHA)	FHI	GGA	50	24	12	0.4
Ni (QHA)	FHI	LDA	40	24	12	0.4
Py (QHA)	FHI	GGA	40	32	4	0.4

Table 4.1: Details of calculation for each material: pseudopotential (pp), Exchange-correlation functional (Exc), cut off for the plane wave expansion (Ecut), number of points in the irreducible BZ for DFT (kpt) and DFPT calculations (qpt), energy smearing for the Gaussian integration in EPC calculations (Gsm).

Chapter 5

Thermomagnetic excitations

Phonons and Magnons have been introduced in Chapter 2. For both excitations, the band structure can be calculated *ab-initio* within linear response or from finite differences (Secs. 2.4.1 and 2.6).
In this Chapter, I will focus the Magnon-Phonon coupling in magnetic systems. After a brief review paragraph (Sec. 5.1), I will show the calculation of ground state exchange integrals for a few magnetic systems within the KKR method in Sec. 5.2. Subsequently, I will present our strategy to extrapolate temperature dependent exchange integrals from their ground state value together with thermal displacement calculations (Sec. 2.4.1). These values will then be used to calculate Curie temperature within the Mean Field Approximation (Sec 5.4) and Magnon Band Structures at finite temperature with the Atomistic Spin Dynamics (Sec 5.5) and estimate the influence of magnon-phonon coupling on these calculations.

5.1 Magnon Phonon Coupling

Like Electron-Phonon Coupling (Sec. 3.3), Magnon-Phonon Coupling (MPC) is a fascinating problem which carries many fundamental questions and opens a fertile terrain for technological applications (e.g. Spin-Calortronics, Sec 1.4).
MPC is pivotal for the correct description of thermodynamical properties of magnetic materials [254]. The energy, time and length scale which characterize this interaction are nevertheless poorly known.
Magnons contribute to thermal transport [193]. Experimental evidence of heat transport by magnons at low temperature has been found in for example Refs. [196, 76, 149, 53, 187], and theoretical analysis have been carried out in [22, 262]. Nevertheless, as reviewed in Ref. [193], not all magnetic materials show evidence of thermal conductivity for magnons. Magnons can be scattered by phonons or by magnetic impurities, which lowers the magnon conductivity [42, 43]. The MPC

strength is maximum when spin waves and elastic waves of the same frequency have the same wave number, e.g. when there is a crossing in the two dispersion curves [128]. At the point of intersection, the excitation is neither a magnon or a phonon, it is rather a magneto-elastic excitation. Away from this crossover point the strength of the interaction decreases as the inverse of the difference in wave vector [193].
On the other hand, while phonons generally do not affect the magnetic properties of lattices [190], there are a few cases in which systems close to magnetic or structural instability show a modification of their magnetic properties due to phonons. For example, rare earths-iron compounds can present a modification of their Curie temperature of several hundreds of Kelvin for a small volume expansion [223].
SSE experiments renewed the interest of scientists towards the MCP, since the theoretical explanation requires a strong MPC in the magnetic sample for the SSE to happen (Sec. 1.5.4). To understand if the MPC can explain the SSE alone, it is necessary to know how this interaction modifies phonon lifetime and consequently, their characteristic length. Recent experimental studies in Refs. [5, 239] showed that the coupling is strong at the middle of the sample and weak at the boundaries. The MPC relaxation time τ_{mp} was studied phenomenologically in Refs. [6, 180, 130, 128, 120] and by first principles [206] for various materials. Specifically, it was estimated to be of the order of 10^{-6} s for YIG and 10^{-7} s for Py [220, 51]. These seem to be the right order of magnitude for YIG, while too short for Py [269]. Yet more robust results are needed, with a proper temperature dependent theory for specific heats and bulk thermal conductivities for both subsystems.

5.2 Ground state Exchange Integrals

Ab-initio exchange integrals for the ground state of a few magnetic materials important for Spintronics are presented in this Section. Spin-polarized relativistic calculations were carried out within the *SPRKKR* [61] by Mr. José Alonso López Miranda at CINVESTAV (Mx). The KKR method, as well results for bcc-Fe have been presented in Sec. 2.5.1. For all SCF calculations, a PBE pseudopotential [176] with a tolerance of 10^{-4} and 500 k-points in the BZ were used.

Nickel

Exchange integrals for a Ni atom in a fcc cell are shown in Fig. 5.1. The interactions with the three nearest neighbors (NN) in the primitive fcc cell (e.g. the cell with lattice parameters $\boldsymbol{a}_1 = \frac{a}{2}(\hat{\boldsymbol{y}} + \hat{\boldsymbol{z}}), \boldsymbol{a}_2 = \frac{a}{2}(\hat{\boldsymbol{z}} + \hat{\boldsymbol{x}})$ and $\boldsymbol{a}_3 = \frac{a}{2}(\hat{\boldsymbol{x}} + \hat{\boldsymbol{y}})$) and with their replicas in the adjacent cells are shown (red, blue and green curves), as

well as the interaction of the atom in the origin with its symmetric replicas in the origin of the adjacent cells (black curve). The exchange relative to the primitive NN (Ni_2, Ni_3 and Ni_4) are degenerate since the system is symmetric in the three directions. Conventional cubic and primitive fcc cells are sketched in Fig. 5.2. The exchange in Fig. 5.1 is ferromagnetic, with an amplitude of about 3 meV for the primitive NN and a weak antiferromagnetic exchange ($|J_{ij}| < 0.5$ meV) for the first replica. All exchanges decay quite quickly with the distance.
Note that for bcc-Fe (Fig. 2.9), there is only one NN atom in the primitive cell and both interactions (primitive NN and the origin replica) are ferromagnetic with amplitude of more than 10 meV.

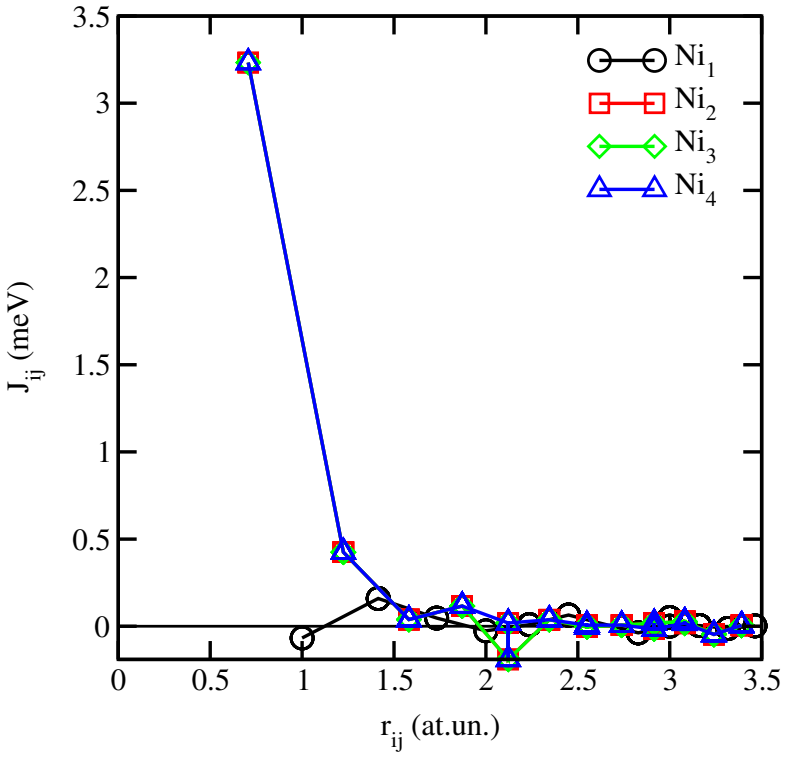

Figure 5.1: Exchange integrals $\mathcal{J}_{ij}$ vs. interatomic distance for Ni-fcc cell. Black line with open circles: replicas of the atom at the origin of the conventional unit cell. Red, green and blue lines: NN in the primitive unit cell and their replicas in the adjacent cells. The distance is given in units of cell parameter. Courtesy of J. Miranda.

Ni_3Fe

Let us consider a ordered Ni_3Fe crystal. Fig. 5.2 represents the Ni_3Fe cell. The black cube is the cubic conventional cell, while primitive fcc cell is drawn in cyan.

The atomic sites 1,2, and 3 are occupied by Ni atoms (blue) and the atomic site 4 is occupied by a Fe atom (pink). The exchange integrals are represented with red arrows.
The exchange integrals for the fcc Ni_3Fe crystal system are shown in Fig. 5.3. With two species in the cell, we shall differentiate among exchange between atoms of the same species and of different species. We will label this *homo-interaction* and *hetero-interaction* respectively.
In Fig. 5.3a, the cell is centered over the Fe atom. All primitive NN and their replicas are Ni atoms (black, red and green curve) while all replicas of the origin in adjacent cells are Fe atoms (blue). We observe that the replicas of the Fe atom in the first adjacent cell have ferromagnetic exchange, while the second is AFM with a non negligible amplitude (∼3 meV). Fig. 5.3a represents the exchange in the cell centered over a Ni atom. The primitive NN atoms are two Ni (red and green, degenerate for symmetry reason) and Fe atom (blue). The black curve is the replica of the central Ni atom in the adjacent cell, which is always a Ni atom. The exchange interaction quickly decays after a few atomic distances.

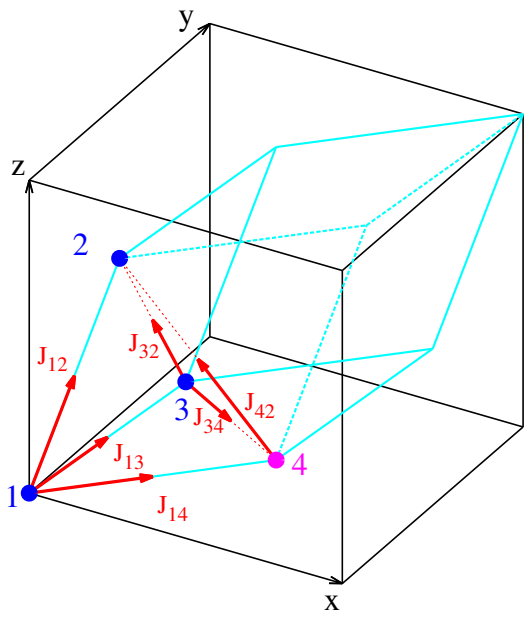

Figure 5.2: Fcc cell cubic (black) and primitive (cyan) cell. The atomic sites 1,2 and 3 are occupied by a Ni atom (blue) while the atomic site 4 is occupied by a Fe (pink). The exchange vectors between atoms are shown in red.

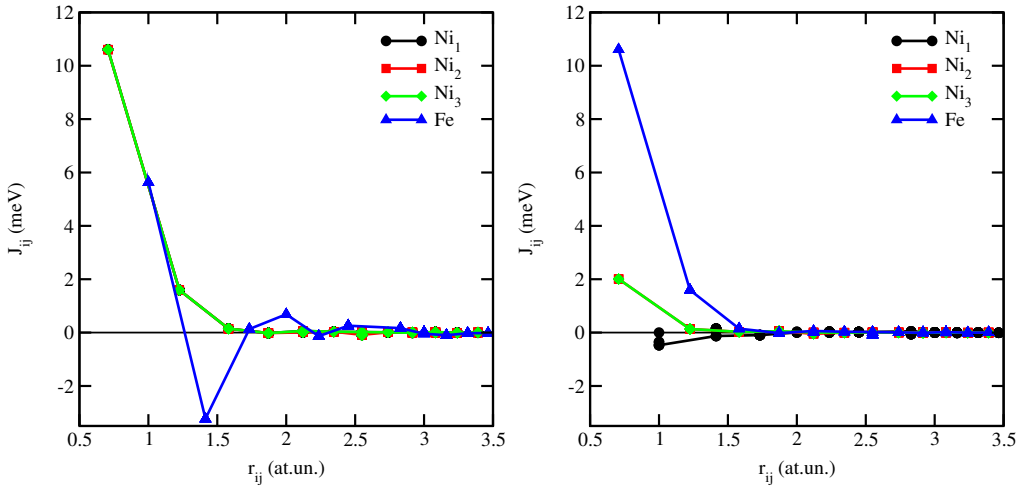

(a) Fe in the middle of the cell. **(b)** Ni in the middle of the cell.

Figure 5.3: Exchange integrals $\mathcal{J}_{ij}$ vs. interatomic distance for Ni_3Fe-fcc cell. Black, red and green lines: exchange integrals with NN Ni atoms and their replicas. Blue line: exchange integrals with the Fe atom. Left: the cell is centered over the Fe atom. Right: the cell is centered over a Ni atom. The distance is given in units of cell parameter. Note that replicas of one atom are of the same specie. Courtesy of J. Miranda.

Permalloy

Permalloy has been introduced in Sec. 4.3, alongside with the simulation tools which we can use to simulate disorder properties. While electronic transport properties were calculated using the VCA method, exchange integrals have been calculated using the CPA method, which, contrary to VCA approximation, keeps the specificities of the single atom and averages the surrounding medium. So we can study the exchange integrals between each couple of atoms explicitly.
The Permalloy exchange integrals are shown in two plots (Figs. 5.4), relative to the cell centered over a Fe atom (Fig. 5.4a) and over a Ni atom (Fig. 5.4b).
Due to disorder, the replica of an atom into an adjacent cell is not necessarly of the same species, but can be different. Thus, we shall consider two exchange integrals between each couple of sites, a homo-exchange and a hetero-exchange.
In Figs. 5.4 four lines are shown. The black and red curves represent the exchange of the atom at the origin with the replica of the origin in the first adjacent cell. This replica can be either a Ni atom (black line) or a Fe atom (red). The green and blue lines represent instead the exchange of the atom at the origin with the NN in the primitive cell (only one line is shown since they are degenerate) for the case of Ni and Fe respectively.

We observe that, for the Fe case in Py (Fig. 5.4a), homo and hetero-interaction have the same magnitude in the primitive cell (green and blue), while the homo-interaction with the first replica is much larger than the hetero-interaction (red and black). On the other hand, for the Ni case in Py (Fig. 5.4b), the primitive hetero-interaction (blue) is much larger than all other interactions.

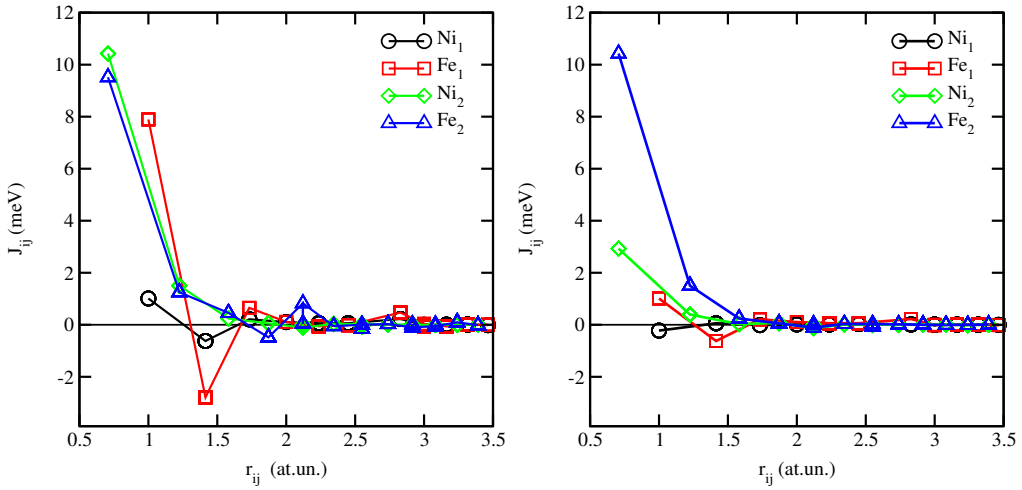

(a) Fe in the middle of the cell. **(b)** Ni in the center of the cell.

Figure 5.4: Exchange integrals $\mathcal{J}_{ij}$ vs. interatomic distance for Py-fcc cell. Black and red lines: exchange with the replica at the origin of the adjacent cells. Green and blue: exchange with the primitive cell NN (and their replicas). Note that the replica of one atom in an adjacent cell is not necessarily of the same species due to disorder. The distance is given in units of cell parameter. Courtesy of J. Miranda.

5.3 Temperature dependent exchange field

In the previous Section, GS calculations for exchange integrals realized by Mr. Miranda were shown. In this Section, I will explain how I managed to extrapolate temperature dependent exchange integrals from these values.
We consider the previously introduced Eqs. (2.38) and (2.62) with a slightly modified notation. The MPC Hamiltonian reads:

$$\begin{aligned}\mathcal{H}_{MP} = &\frac{1}{2}\sum_{ij}\mathcal{V}_{ij}^{(2)}(\boldsymbol{R}_i,\boldsymbol{R}'_j)u_i(\boldsymbol{R}_i)u_j(\boldsymbol{R}_j)\\ &+\sum_{ij}\mathcal{J}_{ij}(\boldsymbol{R}_i,\boldsymbol{R}_j)\boldsymbol{s}_i(\boldsymbol{R}_i)\boldsymbol{s}_j(\boldsymbol{R}_j),\end{aligned} \tag{5.1}$$

where $\boldsymbol{R}$ and $\boldsymbol{R'}$ represent the atomic position, u is the displacement of the atom respect to its equilibrium position, $\mathcal{V}^{(2)}$ is the second derivative of the ionic potential. The local spin on site i is denoted with $\boldsymbol{s}_i(\boldsymbol{R})$.
We adopt a slight generalization of the approach used in Ref. [190], assuming that the exchange parameter $\mathcal{J}_{ij}$ depends only on the distance between the atoms:

$$\mathcal{J}_{ij}(\boldsymbol{R}_i, \boldsymbol{R}_j) = \mathcal{J}_{ij}(\boldsymbol{R}_i - \boldsymbol{R}_j) \equiv \mathcal{J}_{ij}(\boldsymbol{R}). \tag{5.2}$$

For small deviations δR from the equilibrium position, a Taylor expansion of the exchange integral for a variation of the position vector $\boldsymbol{R}$ can be assumed:

$$\mathcal{J}_{ij}(\boldsymbol{R}) = \mathcal{J}_{ij}^{(0)} + \mathcal{J}_{ij}^{\alpha}\delta R_\alpha + \frac{1}{2}\delta R_\alpha \mathcal{J}_{ij}^{\alpha\beta}\delta R_\beta + O\left(\delta R^3\right), \tag{5.3}$$

with α, β Cartesian indices. In Eq. (5.3) the zeroth order unperturbed term is given by the formula (2.50). The Cartesian components of the first and second order derivative of the exchange integral read:

$$\mathcal{J}_{ij}^{\alpha} \equiv \frac{\partial \mathcal{J}_{ij}(\boldsymbol{R})}{\partial x_\alpha}, \tag{5.4a}$$

$$\mathcal{J}_{ij}^{\alpha\beta} \equiv \frac{\partial^2 \mathcal{J}_{ij}(\boldsymbol{R})}{\partial x_\alpha \partial x_\beta}. \tag{5.4b}$$

We estimate these components by finite displacement of the atoms in the unit cell. Two coupled equations per one atom and one unit cell read [190]:

$$\begin{aligned} \omega^2 e(q) &= \sum D(q) e(q), \\ E_q \theta(q) &= \sum \mathcal{J}(q)\theta(q), \end{aligned} \tag{5.5}$$

with $e(q)$ and ω eigenvector and eigenvalue for phonons and $\theta(q)$ and E_q eigenvector and eigenvalue for magnons.

5.3.1 Thermal displacement

Due to thermal excitations (Sec. 2.4.1), atoms oscillate around their equilibrium position of with a temperature dependent amplitude $\sqrt{\langle u^2(T)\rangle}$. It makes sense then to assume that this induces a change in the exchange integral between two atoms. We assume it is possible to factorize the second order term as:

$$\frac{1}{2}\sqrt{\langle u^2\rangle}_\alpha \mathcal{J}_{ij}^{\alpha\beta}\sqrt{\langle u^2\rangle}_\beta = \frac{1}{2} tr[\mathcal{J}_{ij}^{\alpha\beta}] * \langle u^2\rangle. \tag{5.6}$$

Since we can calculate quantitatively the thermal displacement amplitude $\sqrt{\langle u^2\rangle}$, we can substitute it to the δR in Eq. (5.3) and obtain in this way an expression for

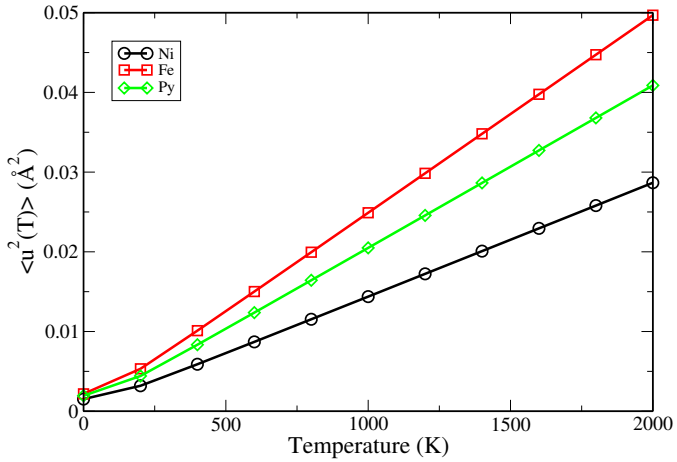

Figure 5.5: Expectation value of the squared atomic displacement vs. temperature. Black with open circles: Nickel. Red with open squares: Iron. Green with open diamonds: Permalloy. More calculation details are given in the main text.

$\mathcal{J}_{ij}(\boldsymbol{T})$. This value can than be used to correct the Curie temperature from MFA (Eqs. (2.63)) or MBS provided by ASD in Eq. (2.66).
Ab-initio thermal displacement calculations have been presented in Sec. 2.4.1 and shown for Cu and Fe in Fig. 2.7. The same calculation has been carried out on Ni and Py. The crystal structure was relaxed with *Abinit*. A LDA-FHI set of pseudopotential was used, with energy cutoff of 40 Ha, 24^3 points in the BZ for WF calculation, which was converged to at least 10^{-9} for all the systems. An electronic smearing of 1 mHa was used in all cases. Thermal displacement amplitudes calculated with *phonopy* are shown in Fig. 5.5.

5.3.2 Temperature Fit

We consider a set of finite displacements $\{\Delta x_n\}$ of the atom at the center of the cell the along the $\hat{\boldsymbol{x}}$ axis. Exchange integrals are calculated for each configuration. The values $\mathcal{J}_{11}(\Delta x_n)$ of the exchange integral for a homo-interaction with a NN primitive atom are shown for bcc-Fe and fcc-Ni as a function of Δx in Figs. 5.6a and 5.6b respectively (black points). We then interpolate the points obtained with a quadratic function and obtain a displacement dependent exchange integral which we define as $\mathcal{J}_{ij}^{(fit)}(\Delta x)$. The fitting function are shown in red in Fig. 5.6.
We observe that in the Ni case, increasing the distance between two neighbors decrease the exchange, while for Fe the behavior is opposite. This effect probably depends on the different symmetries of the systems.
Here the Δx is an independent variable. We will substitute it with the thermal

displacement $\langle u^2(T)\rangle$ calculated with Eq. (2.43), so we will in the end have a consistent expression for the temperature dependent exchange integrals:

$$\mathcal{J}_{ij}(T) = \mathcal{J}_{ij}^{(\mathrm{fit})}(\Delta x)\Big|_{\Delta x=\sqrt{\langle u^2(T)\rangle}}, \tag{5.7}$$

from which we can calculate the Fourier transformed $\mathcal{J}_{ij}^{(\mathrm{fit})}(T,q)$ through Eq. (2.64) and use it as input in *UppASD* to produce temperature dependent MBS.
Note that i) in all previous equations, $\boldsymbol{R}$ refers to the interatomic distance while Δx refers to the finite displacement of the atom at the origin of the cell and ii) $\mathcal{J}_{ij}(T=0)$ is not necessary equal to the value calculated for the unperturbed cell from *SPRKKR* because of zero point motion. We will then distinguish unperturbed results (i.e. $\mathcal{J}_{ij}^{(\mathrm{fit})}(\Delta x=0) = \mathcal{J}_{ij}(\boldsymbol{R})$) from $\mathcal{J}_{ij}(T=0)$ results.
Eq. (5.7) provides an analytic expression for $\mathcal{J}_{ij}(T)$, from which we can obtain

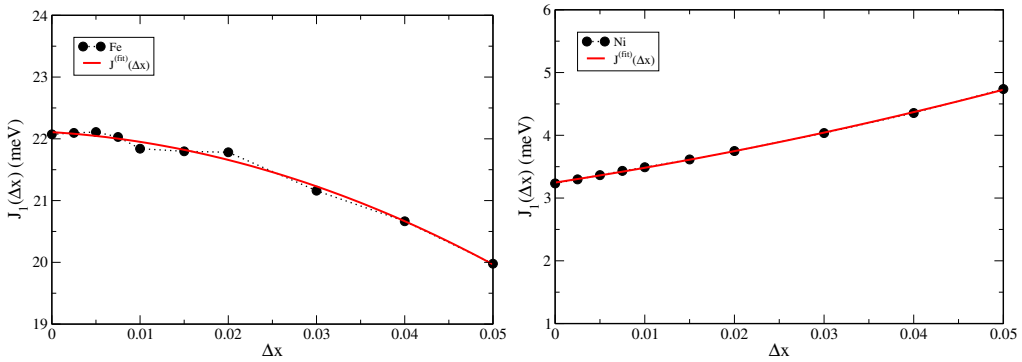

(a) Fe-Fe exchange in bcc geometry. **(b)** Ni-Ni interaction in fcc geometry.

Figure 5.6: NN homo-interaction exchange vs. distortion of the position of the atom at the origin of the cell. Black closed circles: NN exchange integral for homo-interaction. Red line: quadratic fit. $\mathcal{J}_{ij}^{(fit)}(\Delta x)$ fits well to a quadratic function of Δx in both cases. The displacement here is in relative coordinates. When the two Iron atoms are pushed apart, the exchange decreases for Fe and increases for Ni. Courtesy of J. Miranda.

the zeroth, first and second order coefficients. Actually, since the only displacement we performed was along the $\hat{\boldsymbol{x}}$ direction, the only terms we really have from the fitting procedure are $\mathcal{J}_{ij}^{x}$ and $\mathcal{J}_{ij}^{xx}$. Our aim is to get all the components of (5.4a) and (5.4b). For cubic cells with one atom per unit cell, we know that, due to the symmetry of the cell for rotations around one of the Cartesian axis and to the isotropy of the thermal displacements $\langle u^2(T)\rangle$, also matrices (5.4a) and (5.4b) have

the same properties:

$$\frac{\partial \mathcal{J}_{ij}^{(fit)}(\Delta x)}{\partial x_\alpha} = \frac{\partial \mathcal{J}_{ij}^{(fit)}(\Delta x)}{\partial x} \quad \forall \alpha, \tag{5.8a}$$

$$\frac{\partial^2 \mathcal{J}_{ij}^{(fit)}(\Delta x)}{\partial x_\alpha^2} = \frac{\partial^2 \mathcal{J}_{ij}^{(fit)}(\Delta x)}{\partial x^2} \quad \forall \alpha, \tag{5.8b}$$

$$\frac{\partial^2 \mathcal{J}_{ij}^{(fit)}(\Delta x)}{\partial x_\alpha \partial x_\beta} = 0 \text{ for } \alpha \neq \beta. \tag{5.8c}$$

In this way the full matrix in Eq. (5.7) is quickly reconstructed.
The effect of temperature on the exchange integrals for Fe and Ni are shown in Fig. 5.7a and 5.7b respectively. In both cases, $\mathcal{J}_{ij}(T)$ calculated from Eq. (5.7) at 0K, 500K and 1000K are compared to the unperturbed $\mathcal{J}_{ij}$ shown in Figs. 2.9 and 5.1. For Fe there is a slow decrease in the amplitude of the first $\mathcal{J}_{ij}$ while for Ni the variation is larger, of about 2 meV. Note that $\mathcal{J}_{ij}^{(\text{fit})}(0) \simeq \mathcal{J}_{ij}^{(0)}$ but is not identical due to the fitting operation.

5.3.3 Symmetrization of the Ni_3Fe cell

When two species are present in the cell, we should study the effect of thermal displacement of one species on both homo- and hetero-intraction. The symmetry considerations which lead to Eq. (5.8) are less strong since not all $\mathcal{J}_{ij}$ components are equivalent, but we will try to obtain all Cartesian components of Eqs. (5.4a) and (5.4b) from symmetry inversion.
Let us refer to Fig. 5.2, and let us choose the atom occupying position 4 as Fe, and all the others Ni. It is possible to transform the vector $\mathcal{J}_{12}$ into $\mathcal{J}_{13}$ with a rotation of 90°of the system around the $\hat{\boldsymbol{z}}$ axis, or equivalently by interchanging the $\hat{\boldsymbol{x}}$ and $\hat{\boldsymbol{y}}$ axes. This holds for all homo-interactions ($\mathcal{J}_{12}, \mathcal{J}_{23}$ and $\mathcal{J}_{13}$), which are equivalent among themselves by rotation around cubic axes.
Also, any hetero-interaction between the Fe atom and a Ni atom can be transformed into any other by cyclical permutation of $\hat{\boldsymbol{x}}$, $\hat{\boldsymbol{y}}$ and $\hat{\boldsymbol{z}}$. For example, always in Fig. 5.2, we can take $\mathcal{J}_{14}$, rotate the y axis of 90°towards the $\hat{\boldsymbol{z}}$ axis first, and then rotate the $\hat{\boldsymbol{x}}$ axis of 180°around the new $\hat{\boldsymbol{y}}$ axis, to obtain $\mathcal{J}_{42}$, which is equivalent to $\mathcal{J}_{24}$ because of the assumption (5.2).
To shorten the notation and differentiate homo- and hetero-interactions, let call them as follows:

$$\mathcal{J}_{14} = \mathcal{J}_{24} = \mathcal{J}_{34} \equiv \mathcal{F}\,, \tag{5.9a}$$

$$\mathcal{J}_{12} = \mathcal{J}_{23} = \mathcal{J}_{13} \equiv \mathcal{N}\,, \tag{5.9b}$$

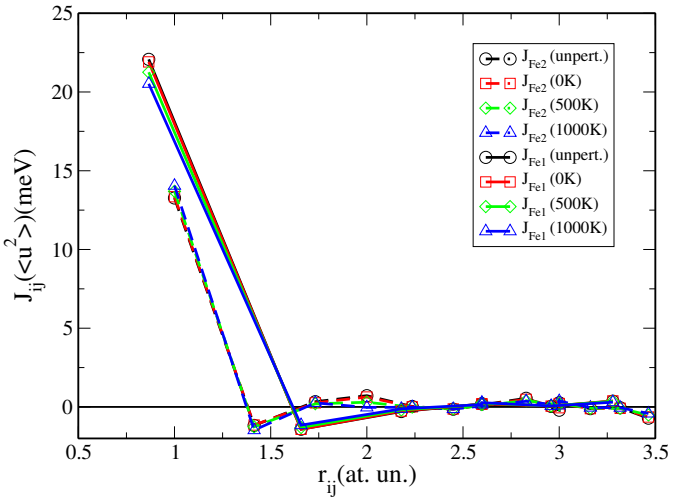

(a) Iron

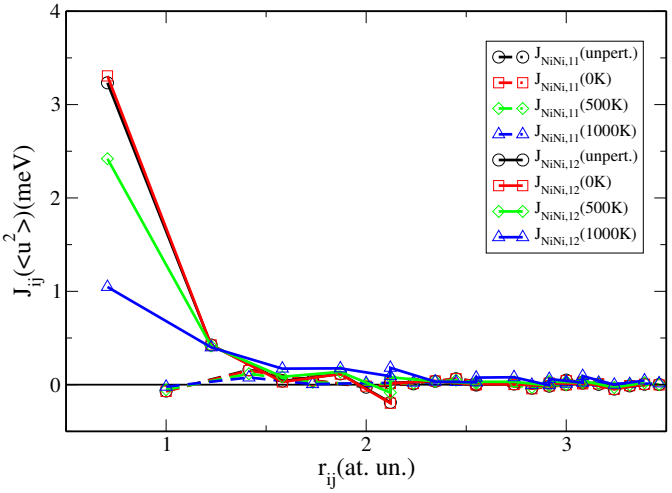

(b) Nickel

Figure 5.7: Temperature dependent exchange integral for bcc-Fe vs. interatomic distance. Full lines: NN in the primitive cell. Dashed lines: replica of the atom in the origin in the adjacent cells. Black: unperturbed value from *SPRKKR*. Red, green and blue: $\mathcal{J}_{ij}(T)$ form Eq. (5.7) 0 K, 500 K and 1000 K for respectively.

$\mathcal{J}_{14}$ is in the xy plane, so the displacement of the atom 1 along $\hat{\boldsymbol{x}}$ or $\hat{\boldsymbol{y}}$ will have an equivalent effect on $\mathcal{J}_{14}$. Similarly, a displacement of the atom 1 along $\hat{\boldsymbol{z}}$ will produce no effects on $\mathcal{J}_{14}$ being the displacement out of plane.

We define a new basis set $\{\hat{\boldsymbol{u}}, \hat{\boldsymbol{v}}\}$ such that:

$$\begin{pmatrix} \hat{\boldsymbol{x}} \\ \hat{\boldsymbol{y}} \end{pmatrix} = \begin{pmatrix} \sin\theta & -\cos\theta \\ \cos\theta & \sin\theta \end{pmatrix} \begin{pmatrix} \hat{\boldsymbol{u}} \\ \hat{\boldsymbol{v}} \end{pmatrix}, \tag{5.10}$$

where θ is the angle between $\mathcal{J}_{14}$ and the $\hat{\boldsymbol{x}}$ direction ($\theta = 45°$).
Let us now express $\mathcal{J}_{14}$ in the new basis set:

$$\begin{aligned} \mathcal{J}_{14} &= \sum_{\alpha} \mathcal{J}_{14,\alpha}\hat{\boldsymbol{x}}_{\alpha} = \mathcal{J}_{14,x}\hat{\boldsymbol{x}} + \mathcal{J}_{14,y}\hat{\boldsymbol{y}} + \mathcal{J}_{14,z}\hat{\boldsymbol{z}} \\ &= \frac{\mathcal{J}_{14,x} + \mathcal{J}_{14,y}}{\sqrt{2}}\hat{\boldsymbol{u}} + \frac{\mathcal{J}_{14,x} - \mathcal{J}_{14,y}}{\sqrt{2}}\hat{\boldsymbol{v}} + \mathcal{J}_{14,z}\hat{\boldsymbol{z}} \\ &\equiv \mathcal{J}_{\parallel}\hat{\boldsymbol{u}} + \mathcal{J}_{\perp}\hat{\boldsymbol{v}} + \mathcal{J}_{\perp}\hat{\boldsymbol{z}}, \end{aligned} \tag{5.11}$$

where $\mathcal{J}_{14,\alpha}$ is the component of the vector $\mathcal{J}_{14}$ along the $\hat{\boldsymbol{\alpha}}$ direction, and shall be differentiated from $\mathcal{J}_{14}^{\alpha}$, which is the derivative of $\mathcal{J}_{14}$ in the same direction. Considering the special case of cubic symmetry, the $\mathcal{J}_{\perp}$ term is zero, as well as the $\mathcal{J}_{14,z}$ component, we can generally write:

$$\mathcal{J}_{14} = \mathcal{J}_{\parallel}. \tag{5.12}$$

This is a general procedure, which can be applied to any $\mathcal{J}_{ij}$. In the following paragraph, I will present the calculations of the first and second derivative of the $\mathcal{J}_{ij}$ vector in the new basis set $\{\hat{\boldsymbol{u}}, \hat{\boldsymbol{v}}\}$.

First order derivative $\mathcal{J}_{ij}^{(1)}$

In the unperturbed cell, $\mathcal{J}_{14}$ has only projection along $\hat{\boldsymbol{u}}$. If we displace atom 1 of a quantity Δx in the $\hat{\boldsymbol{x}}$ direction, $\mathcal{J}_{14}$ will have non null component along $\hat{\boldsymbol{v}}$. We actually know the Cartesian component of this vector from Eq. (5.8a), thus we can write it in the new basis set:

$$\mathcal{J}_{14}^{x}\hat{\boldsymbol{x}} = \frac{1}{\sqrt{2}}\mathcal{J}_{14}^{x}\hat{\boldsymbol{u}} + \frac{1}{\sqrt{2}}\mathcal{J}_{14}^{x}\hat{\boldsymbol{v}} \equiv \mathcal{J}_{\parallel}\hat{\boldsymbol{u}} + \mathcal{J}_{\perp}\hat{\boldsymbol{v}}\,, \tag{5.13}$$

These are all hetero-interactions, so we can introduce $\mathcal{F}_{\perp}$ and $\mathcal{F}_{\parallel}$ to differentiate them from homo components $\mathcal{N}_{\perp}$ and $\mathcal{N}_{\parallel}$ for which the same symmetry considerations apply.
The system is invariant for exchange of x and y, so:

$$\mathcal{J}_{14}^{y}\hat{\boldsymbol{y}} = \mathcal{J}_{14}^{x}\hat{\boldsymbol{x}} \equiv \mathcal{F}_{\parallel}\hat{\boldsymbol{u}} + \mathcal{F}_{\perp}\hat{\boldsymbol{v}}\,, \tag{5.14}$$

$\mathcal{J}_{24}$ and $\mathcal{J}_{34}$ will have exactly the same expression in terms of $\{\hat{\boldsymbol{u}}, \hat{\boldsymbol{v}}\}$. Likewise, if we consider a displacement of atom 2 (3) in the $\hat{\boldsymbol{z}}$ ($\hat{\boldsymbol{y}}$) direction we will have:

$$\mathcal{J}_{24}^{z}\hat{\boldsymbol{y}} = \mathcal{J}_{34}^{y}\hat{\boldsymbol{z}} = \mathcal{J}_{24}^{x}\hat{\boldsymbol{y}} = \mathcal{J}_{34}^{z}\hat{\boldsymbol{z}} \equiv \mathcal{F}_{\parallel}\hat{\boldsymbol{u}} + \mathcal{F}_{\perp}\hat{\boldsymbol{v}}\,, \tag{5.15a}$$

Let us now consider the variation of $\mathcal{J}_{14}$ along of $\hat{\boldsymbol{z}}$ (or the two equivalent variations of $\mathcal{J}_{34}$ along $\hat{\boldsymbol{x}}$ and $\mathcal{J}_{24}$ along $\hat{\boldsymbol{y}}$). Being this perpendicular to the bond, we can assume:

$$\mathcal{J}_{14}^{z} = \mathcal{J}_{24}^{y} = \mathcal{J}_{34}^{x} \equiv \mathcal{F}_{\perp}. \tag{5.16}$$

For homo-interactions similar symmetry considerations apply. Let us start from $\mathcal{J}_{12}$ which lies in the yz plane, so it has no component along x, while its variation is all along x.

$$\mathcal{J}_{12}^{x} = \mathcal{J}_{13}^{y} = \mathcal{J}_{23}^{z} \equiv \mathcal{N}_{\perp}. \tag{5.17}$$

On the other side, all other first derivative terms are composed by a parallel and a perpendicular component:

$$\mathcal{J}_{12}^{z} = \mathcal{J}_{12}^{y} = \mathcal{J}_{23}^{x} = \mathcal{J}_{23}^{y} = \mathcal{J}_{13}^{x} = \mathcal{J}_{13}^{z} \equiv \frac{1}{\sqrt{2}}\mathcal{N}_{\perp} + \frac{1}{\sqrt{2}}\mathcal{N}_{\parallel}. \tag{5.18}$$

Explicit expression for $\mathcal{N}_{\parallel}$ can be obtained combining any two terms from Eqs. (5.19) and (5.18), e.g.:

$$\mathcal{N}_{\parallel} = \sqrt{2}\mathcal{J}_{12}^{z} - \mathcal{J}_{12}^{x} = \sqrt{2}\mathcal{J}_{23}^{x} - \mathcal{J}_{23}^{z} = \cdots \tag{5.19}$$

Second order $\mathcal{J}_{ij}^{(2)}$

Let us suppose we have two finite displacements now, always and only along $\hat{\boldsymbol{x}}$. Three possibilities are given:
i) both perturbations are in the same plane as the bond,
ii) both perturbations are in the plane orthogonal to the crystal plane spanned by the bond,
iii) one perturbation is in the plane parallel and the other one orthogonal.
However, as above, we have some projections of combinations of the $\mathcal{J}_{ij}$. If we suppose the general $\mathcal{J}_{ij}^{(2)}$ derivative can be decomposed as a derivative along the bond and a (isotropic) derivative perpendicular to it, we are able to write: The totally parallel (case i) or totally perpendicular (case ii) ones can be easily derived:

$$\mathcal{J}_{12}^{xx} = \mathcal{J}_{13}^{yy} = \mathcal{J}_{23}^{zz} = \mathcal{N}_{\perp}^{(2)}, \tag{5.20a}$$
$$\mathcal{J}_{12}^{yz} = \mathcal{J}_{13}^{xz} = \mathcal{J}_{23}^{xy} = \mathcal{N}_{\parallel}^{(2)}, \tag{5.20b}$$
$$\mathcal{J}_{14}^{zz} = \mathcal{J}_{24}^{yy} = \mathcal{J}_{34}^{xx} = \mathcal{F}_{\perp}^{(2)}, \tag{5.20c}$$
$$\mathcal{J}_{14}^{xy} = \mathcal{J}_{24}^{xz} = \mathcal{J}_{34}^{yz} = \mathcal{F}_{\parallel}^{(2)}, \tag{5.20d}$$

we do not have explicit access to the latter xy derivative yet.
Let us call Δu and Δv the finite displacements in the new basis due to a finite

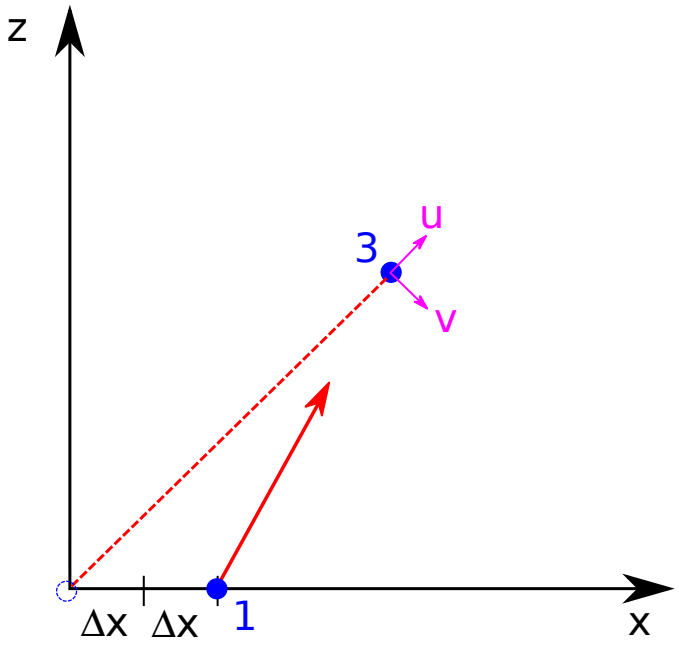

Figure 5.8: Cartoon representing the modification of $\mathcal{J}_{13}$ after two consecutive Δx displacements. The element of the basis $\{\hat{\boldsymbol{u}}, \hat{\boldsymbol{v}}\}$ are shown in purple.

displacement Δx, with:

$$\Delta u^2 = \Delta v^2 = \frac{\Delta x^2}{2},$$

for construction. Two identical finite displacement of atom 1 along $\hat{\boldsymbol{x}}$ will generate a perturbation in the exchange integrals which can be written as:

$$\mathcal{J}_{14}^{xx}\Delta x^2 = \mathcal{F}_{\perp}^{(2)}\Delta v^2 + \mathcal{F}_{\parallel}^{(2)}\Delta u^2 = (\mathcal{F}_{\perp}^{(2)} + \mathcal{F}_{\parallel}^{(2)})\frac{\Delta x^2}{2}, \tag{5.21a}$$

$$\mathcal{J}_{13}^{xx}\Delta x^2 = \mathcal{N}_{\perp}^{(2)}\Delta v^2 + \mathcal{N}_{\parallel}^{(2)}\Delta u^2 = (\mathcal{N}_{\perp}^{(2)} + \mathcal{N}_{\parallel}^{(2)})\frac{\Delta x^2}{2}, \tag{5.21b}$$

Inserting Eq. (5.20a) into Eq. (5.21b) we obtain:

$$\mathcal{N}_{\parallel}^{(2)} = 2\mathcal{J}_{13}^{xx} - \mathcal{J}_{12}^{xx}. \tag{5.21c}$$

The effect of two finite displacements along $\hat{\boldsymbol{x}}$ on $\mathcal{J}_{13}$ is sketched in Fig. 5.8. Eqs. (5.21) are general relations for homo- and hetero-interactions and yield the following symmetry relations:

$$\mathcal{J}_{34}^{yy} = \mathcal{J}_{34}^{zz} = \mathcal{J}_{24}^{xx} = \mathcal{J}_{24}^{zz} = \mathcal{J}_{14}^{xx} = \mathcal{J}_{14}^{yy} = \frac{\mathcal{F}_{\perp}^{(2)} + \mathcal{F}_{\parallel}^{(2)}}{2}, \tag{5.22a}$$

$$\mathcal{J}_{12}^{yy} = \mathcal{J}_{12}^{zz} = \mathcal{J}_{13}^{xx} = \mathcal{J}_{13}^{zz} = \mathcal{J}_{23}^{xx} = \mathcal{J}_{23}^{yy} = \frac{\mathcal{N}_{\perp}^{(2)} + \mathcal{N}_{\parallel}^{(2)}}{2}, \tag{5.22b}$$

The cross derivatives (case iii) can be obtained if we consider that the primitive axes are inclined at 60°, thus:

$$\Delta u^2 = \frac{3}{4}\Delta x^2\,, \tag{5.23a}$$

$$\Delta v^2 = \frac{1}{4}\Delta x^2\,, \tag{5.23b}$$

and, for example:

$$\mathcal{J}_{12}^{xy}\Delta x^2 = \mathcal{N}_{\perp}^{(2)}\Delta v^2 + \mathcal{N}_{\parallel}^{(2)}\Delta u^2 = (\mathcal{N}_{\perp}^{(2)}\frac{3}{4} + \mathcal{N}_{\parallel}^{(2)}\frac{1}{4})\Delta x^2\,, \tag{5.24a}$$

$$\mathcal{J}_{14}^{xz}\Delta x^2 = \mathcal{F}_{\perp}^{(2)}\Delta v^2 + \mathcal{F}_{\parallel}^{(2)}\Delta u^2 = (\mathcal{F}_{\perp}^{(2)}\frac{3}{4} + \mathcal{F}_{\parallel}^{(2)}\frac{1}{4})\Delta x^2\,, \tag{5.24b}$$

which yields:

$$\mathcal{N}_{\parallel}^{(2)} = \frac{1}{3}(4\mathcal{J}_{12}^{xy} - \mathcal{J}_{12}^{xx})\,. \tag{5.25}$$

Unfortunately we do not dispose of the cross derivatives at this stage. From these 2 fundamentals all the element of the tensor $\mathcal{J}_{ij}^{(2)}$ for the nearest neighbors can be obtained:

$$\mathcal{J}_{12}^{xy} = \mathcal{J}_{12}^{xz} = \mathcal{J}_{13}^{xy} = \mathcal{J}_{13}^{yz} = \mathcal{J}_{23}^{xz} = \mathcal{J}_{23}^{yz} = \frac{3\mathcal{N}_{\perp}^{(2)} + \mathcal{N}_{\parallel}^{(2)}}{4}\,, \tag{5.26a}$$

$$\mathcal{J}_{34}^{xy} = \mathcal{J}_{34}^{xz} = \mathcal{J}_{24}^{xy} = \mathcal{J}_{24}^{yz} = \mathcal{J}_{14}^{xz} = \mathcal{J}_{14}^{yz} = \frac{3\mathcal{F}_{\perp}^{(2)} + \mathcal{F}_{\parallel}^{(2)}}{4}\,. \tag{5.26b}$$

By symmetry upon interchange of the 2 atoms the $\mathcal{J}_{ij}$ matrix is symmetric:

$$\mathcal{J}_{ij}^{\alpha\beta} \;=\; \mathcal{J}_{ji}^{\alpha\beta}\,. \tag{5.27}$$

This holds for the unperturbed systems, while for the derivative components, similar expression can be obtained considering the specific direction of ij with respect to α and β.

5.4 Curie Temperature

We can use the temperature dependent integrals derived in the previous Section to estimate the how the MFA theoretical Curie Temperature (Sec. 2.6.1) varies with temperature. Results are reported in Fig. 5.9 for Fe and Ni. A clear decrease of the calculated T_c for Iron can be observed, which goes in the right direction (the

experimental value is not shown in the figure, but is of 1043 K). For Ni instead, a oscillating behaviour is present. Thus MFA overestimates the real values for Fe and underestimate it for Ni, and temperature corrections appear to improve the agreement in the first case but not in the second. We can think that the reason of this difference is in the different crystal structure and that Fe has a slight AFM interaction at longer distance.

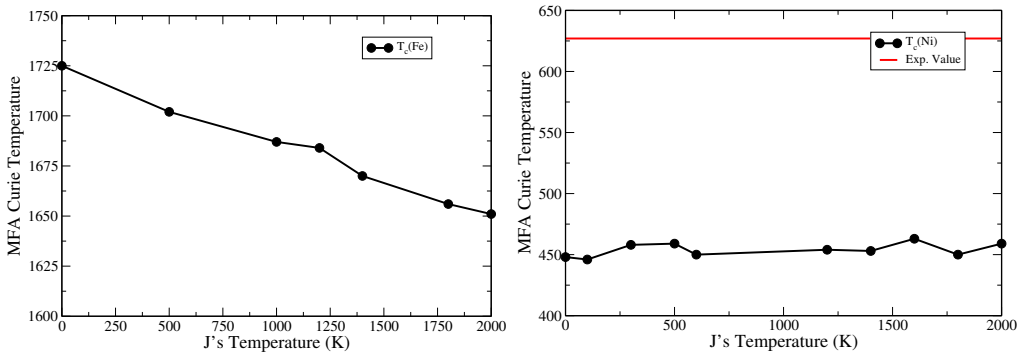

(a) Iron **(b)** Nickel

Figure 5.9: MFA Curie Temperature vs. temperature. T_c was calculated from Eqs. 2.63 on top of temperature dependent exchange integrals calculated in Sec. 5.3.

5.5 Magnon Band Structure

Magnon Band Structures (MBS) from ASD calculated on top of the *ab-initio* exchange integrals calculated in Sec. 5.3 are shown along the [100] direction in the BZ in Figs. 5.10 and 5.11 for Iron and Nickel respectively. MBS for unperturbed $\mathcal{J}_{ij}$s are shown alongside with magnons obtained from thermally perturbed $\mathcal{J}_{ij}$ for $T = 0, 500$ and $1000\ K$. In both cases we observe a small effect. $\mathcal{J}_{ij}$ variation with temperature is of about 1 meV for both systems. Variation of the magnon dispersion is on a similar order of magnitude. In the Fe case, the position of the peak in the MBS is shifted from about 5/8 to 3/4 in the ΓX direction. Also in the Ni case, there is a shift in the position of the peak towards the X direction, with the dispersion which becomes almost linear between $X/4$ and $X/2$.

5.6 Conclusion and Perspectives

We proposed a microscopic method to calculate temperature dependent exchange integrals and estimate the influence of MPC on the Curie temperature (within the

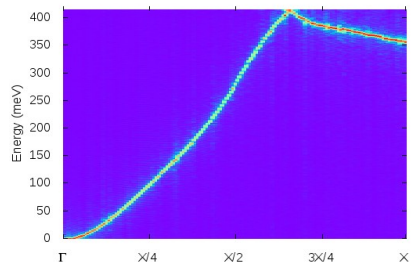

(a) Magnon from unperturbed $\mathcal{J}_{ij}$s.

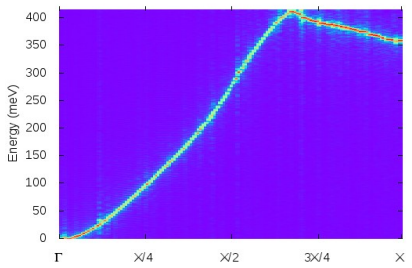

(b) Magnon from $\mathcal{J}(0\ K)$.

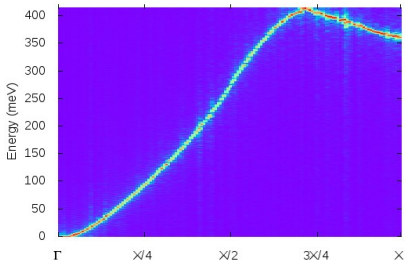

(c) Magnon from $\mathcal{J}(500\ K)$.

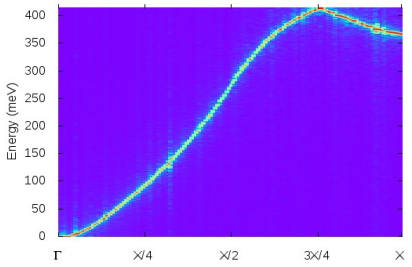

(d) Magnon from $\mathcal{J}(1000\ K)$.

Figure 5.10: MBS for Iron along the [100] direction in the BZ. **(a)**: magnons from unperturbed $\mathcal{J}_{ij}$. **(b)**: magnons for T=0 K, **(c)**: magnons for T=500 K, **(d)**: magnons for T=1000 K. Courtesy of J. Miranda.

MFA) and MBS. We only considered finite displacements of one atom in the [100] Cartesian direction. The method can be improved by considering the displacement in other directions ([110] and [111] for example). Also the displacement in two different directions can give access to the cross derivative in Eqs. (5.26). Moreover, the mutual displacement of two atoms at the same time can give higher order corrections.

We have found some important difference between Ni and Fe. These can be attributed to in part the difference in their crystal structure (bcc has 8 NN while fcc has 12 NN). Thus, also tests with other cubic materials (e.g. high pressure fcc Co) can be useful.

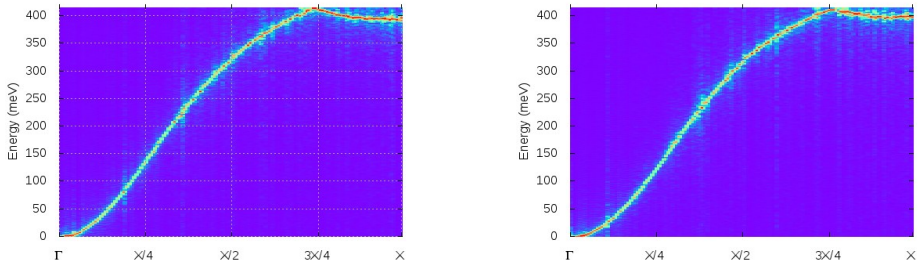

(a) Magnon from unperturbed $\mathcal{J}_{ij}$s.

(b) Magnon from $\mathcal{J}(0\ K)$.

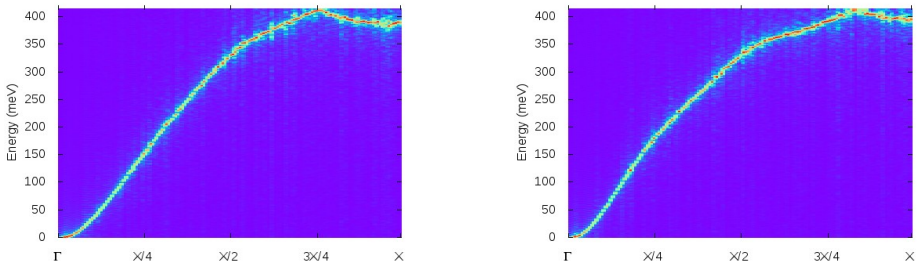

(c) Magnon from $\mathcal{J}(500\ K)$.

(d) Magnon from $\mathcal{J}(1000\ K)$.

Figure 5.11: MBS for Nickel along the [100] direction in the BZ. **(a)**: magnons from unperturbed $\mathcal{J}_{ij}$. **(b)**: magnons for T=0 K, **(c)**: magnons for T=500 K, **(d)**: magnons for T=1000 K. Courtesy of J. Miranda.

Chapter 6

On the proximity effect in the NiPt interface

In this Chapter, I focus on the effects which appear across an interface between a spin polarized metal (Ni) and a heavy metal (Pt, Au, Ta). An overview on the role of interfaces is presented in Sec. 6.1. The Spin-Orbit-Coupling and the Dzyaloshinskii-Moriya interactions are formally introduced. Finally, the magnetization density for a set of interfaces is presented.
The results shown are an exploration and offer a strategy of investigation.

6.1 Interfaces and Spintronics

The main novelty about nanotechnologies is that, when the dimensions shrinks to the nanoscale, the physics we used to know changes drastically and new effects which are macroscopically irrelevant become important.
As explained in Chapter 1, one example is the interplay between spin torque and spin pumping, which at the macroscale would not happen. It is always true that an electrical current passing through a ferromagnet becomes spin polarized because of the exchange field. The opposite phenpomena (i.e. a polarized current which locally modifies the magnetization of a system, or spin torque) has a limited effect at the macroscale, while at the nanoscale, this can eventually change the magnetization of a magnet.
The interplay of these effects is largely used in Spintronics. The more basic Spintronic device is a Spin Valve (Sec. 1.2) in which the current passes through a PM-FM interface and according to the magnetization direction, the global resistance is modified (GMR). One can think to the PM-FM interface in Spintronics as equivalent to the p-n junction or a Schottky barrier in traditional Electronics.
In the case described above, the current flows in direction a perpendicular to the

plane spanned by the interface between the two layers (CPP configuration). More complex effect can happen if, for example, the current flows in the same direction as the magnetization direction (CIP configuration), since the inversion symmetry is broken.
If then, the normal material is substituted with a heavy metal (HM), even more complex physics can happen due to the appearance of SOC-dependent effects, like e.g. the SHE presented in Sec. 1.4.2. At a FM-HM interface, beside the inversion symmetry, the time reversal symmetry is broken, due to the presence of SOC. When both these two symmetry breakings are present, the Dzyaloshinskii-Moriya interaction arises. Let us introduce formally these two quantities.

6.1.1 Spin orbit coupling

The SOC is a relativistic effect due to the relative motion of an electron with spin $\vec{\sigma}$ into a potential $V(\mathbf{r})$. Without going in many details, the Hamiltonian can be written as:

$$\mathcal{H}_{SOC} = [\vec{\nabla} V(\mathbf{r}) \times \vec{p}] \cdot \vec{\sigma}. \tag{6.1}$$

SOC causes the so-called fine structure splitting of atomic energy levels due to electromagnetic interaction between the electron's spin and the magnetic field generated by the electron's orbit around the nucleus. The time reversal symmetry of the Hamiltonian is broken due to the linear dependence on $\vec{p}$. All materials show SOC, but only for a few of them the SOC is observable.

6.1.2 Dzyaloshinskii-Moriya interaction

The Dzyaloshinskii-Moriya interaction (DMI) is the asymmetric contribution to the exchange interaction between two adjacent spins [60, 160]. It is induced by the SOC in magnetic materials with broken spatial inversion symmetry (surfaces, interfaces...). It plays in fact a central role in the creation of topologically complexes textures at the ferromagnet-heavy metal interfaces [70, 162, 275, 100] since it favors spatially rotating magnetic structures with a specific rotational direction. DMI could eventually be so strong as to overcome other kinds of interactions such as the symmetric exchange interactions, leading to a spatially rotating magnetic ground state. It can be derived from an extended Heisenberg model:

$$\mathcal{H} = -\sum_{i,j} \mathbf{s_i}^T \mathcal{V}_{ij} \mathbf{s_j}, \tag{6.2}$$

where $\mathcal{V}_{ij}$ can be decomposed into a symmetric and an antisymmetric part (with respect to the Cartesian indices):

$$\mathcal{V}_{ij} = \underbrace{V_{ij}^{S}}_{symmetric} + \underbrace{V_{ij}^{A}}_{antisymmetric} = \underbrace{(V_{ij}^{S} - \mathcal{J}_{ij} I)}_{traceless} + \mathcal{J}_{ij} I + V_{ij}^{A}. \tag{6.3}$$

The trace is over the space components. The extended Heisenberg Hamiltonian can be rewritten as:

$$\mathcal{H} = -\sum_{i,j} [\underbrace{\mathcal{J}_{ij} \cdot \mathbf{S_j^T} \cdot \mathbf{S_i}}_{\substack{symmetric \\ isotropic}} + \underbrace{\mathbf{S_j^T} \cdot \mathbf{K_i} \cdot \mathbf{S_i} \cdot \delta_{ij}}_{anis} + \underbrace{\mathbf{D_{ij}} \cdot (\mathbf{S_i} \times \mathbf{S_j})}_{DMI}], \tag{6.4}$$

with:

$$\mathcal{J}_{ij} = \frac{1}{3} tr[V_{ij}^{S}], \tag{6.5a}$$

$$\boldsymbol{s}_i^T \cdot (V_{ij}^{S} - \mathcal{J}_{ij} I) \cdot \boldsymbol{s}_j \sim \boldsymbol{s}_i^T \cdot \boldsymbol{K}_i \cdot \boldsymbol{s}_i \cdot \delta_{ij}, \tag{6.5b}$$

$$[V_{ij}^{A}]_{nn'} = \sum_{l} [D_{ij}]_l \cdot \epsilon_{lnn'}, \tag{6.5c}$$

and with "anis" referring to the anisotropy energy introduced with Eq.(2.59) in Sec. 2.5.2. The symmetric isotropic term is the Heisenberg model (eq. 2.45). An *ab-initio* calculation of DMI at the Co-Pt interface can be found in Ref. [272].

6.2 The NiPt interface

Nickel and Platinum are transition metals belonging respectively to the 3^{rd} and 5^{th} row of the Periodic table. Their electronic, vibrational and transport properties have been analyzed in Sec.4.2 and 4.1.2 respectively.
Due to its 3d-type electronic configuration, Ni is a ferromagnet at room temperature and can be used as a spin polarizer for electrical currents. The effect of spin polarization is a splitting of all the electronic bands that without spin would be degenerate. The effect of SOC is a splitting of the valence bands with consecutive electronic rearrangement. For Pt it happens that after including SOC the 5d bands splits into $5d_{\frac{3}{2}}$ and $5d_{\frac{5}{2}}$ so that the highest occupied state is the $5d_{\frac{5}{2}}$ [228].
Due to its remarkable SOC, Pt is exploited in Spintronics to transform electrical currents in spin currents and *viceversa* via the SHE and the ISHE (Sec. 1.4.2). Proximity effects have been demonstrated to exist in Pt when deposited on a FM [106]. This gave rise to an acute discussion about the authenticity of the SSE in the longitudinal configuration (Sec. 1.5.2).

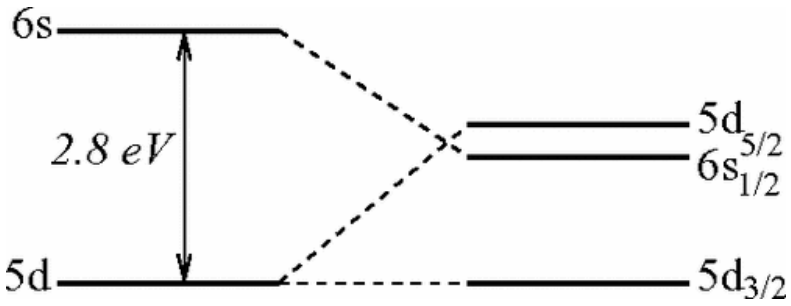

Figure 6.1: Schematic representation of the splitting due to spin-orbit interaction in Platinum. From Ref. [228].

6.2.1 The ferromagnetic instability of Heavy Metals

Platinum is not the only HM used for Spintronics applications. Gold and Tantalum are also used [125, 146] due to their SOC properties, thus it is interesting to make a comparison between these materials and study how their physical properties vary in an unusual situation at an interface.
It is well known that Pt at room conditions is close to the FM instability [107]. Also superconducting Tantalum shows magnetic properties [35] at low temperatures.
In the SSE experiments, the Pt strip is sputtered on top of the magnetic Py strip, so at least for the former crystal planes, Pt atoms assume the same positions as the atom on top of the Py surface (relaxed lattice parameter for Py is 1.011 times larger than Ni, so we consider Ni as a reference in this paragraph). In Fig. 6.2 the atomic magnetization of Ni (black), Pt (blue), Ta (red) and Au (green) are plotted vs. the cell parameter (primitive and cubic). The dashed vertical lines represent the relaxed value for the four materials. Ni has the smallest cubic cell, while Pt, Ta and Au are closer.
For these calculations, a set of GGA-PBE-JTH pseudopotentials [119] were used, with a cutoff of 20 Ha for the plane wave expansion. The GS was calculated with 24^3 kpt and an electronic smearing of 1 mHa. The wavefunction was converged up to 10^{-20} for Ni and Pt and up to 10^{-10} for Au and Ta.
While Nickel is always spin polarized, all of the three HM studied show rising magnetization for large values of the lattice parameter, which means none of them is actually "safe" from magnetic spurious effects. On the other hand, if we imagine to sputter them on a Ni surface, they will assume a shorter lattice parameter, where there is no magnetization.
Note that, to compute the atomic magnetization, a spin collinear calculation is carried out, i.e. the wavefunction for the two spin channels are treated as independent scalar quantities. This produces a difference in the relaxation of the lattice, and for example, Pt (pink lines in Fig. 6.2) results to be spin polarized at

ambient conditions, where it should be still paramagnetic. A correct relativistic treatment requires a spinorial treatment of the wavefunction. The goal of this study is qualitative, so what is interesting to note is the presence of a non null magnetization at high pressure.

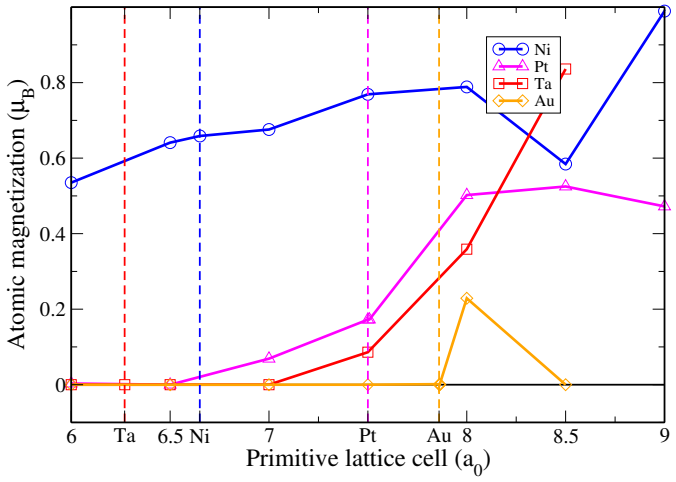

(a) Primitive cell parameter.

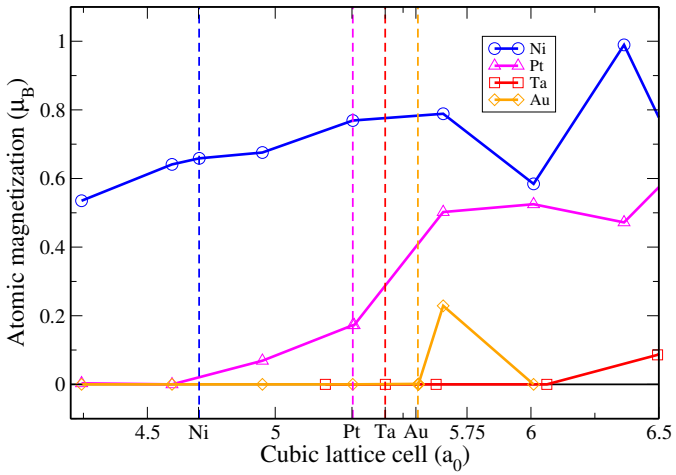

(b) Cubic cell parameter.

Figure 6.2: Atomic magnetization of bulk metals vs. lattice parameter. Black: fcc-Nickel. Red: bcc-Tantalum. Green: fcc-Gold. Blue: fcc-Platinum. Vertical dashed lines represent the relaxed lattice cell for each material. Top: primitive cell parameter. Bottom: cubic cell parameter.

6.3 FM-HM Interfaces

In this section I present *ab-initio* calculation of magnetization density in HM surfaces and HM-FM interfaces. In Ref. [66], a Pt monolayer on top of Iron was studied, but only exchange interaction was considered. Here I consider six-layers slabs of Pt, Au and Ta, and interfaces of these three materials with Ni (three Ni layers on top of three HM layers). For each HM-Ni interface I consider the effect of the lattice, taking into account the structure calculated at the relaxed lattice parameter of the HM.
Calculation details are the same as for Fig.6.2, but this time a spinorial wavefunction including SOC has been used. The slab has a fcc structure along the [1,1,1] direction with six metal layers and six vacuum layers.
In the two Tables 6.1 and 6.2 the explicit magnetization for the six atoms in the z direction (perpendicular to the interface) are reported, for the single-atom slabs and for the Ni-HM interfaces respectively. All values are in μ_B. In the single atomic case, Ni has a considerable magnetization in the center of the slab, while at the external surfaces, the magnetization is close to the bulk value. Pt, Au and Ta systems have a much weaker magnetization.
In the interfaces instead, almost all the magnetization is concentrated on Ni atoms (1,2 and three), with a magnetization transfer in the NiPt and NiTa case.

These results can be seen in Figs. 6.3, 6.5 and 6.4 for NiPt, NiAu and NiTa

	Ni	Pt	Au	Ta
1	0.629	-0.117	0.007	-0.671
2	-0.652	-0.087	-0.005	0.157
3	1.975	0.002	-0.004	0.003
4	1.959	0.003	-0.004	0.003
5	-0.666	-0.083	-0.005	0.159
6	-0.855	-0.124	0.012	-0.679

Table 6.1: Atomic magnetization in the z direction for the Ni, Pt, Au and Ta slabs.

respectively. All the figures were realized with *XCrysDen* [135]. Ni, Pt, Au and Ta atoms are represented in gray, pink, yellow and purple respectively. Red and blue shapes represent the magnetization isosurfaces ($\mu = 0.004\mu_B$) for spin up and down respectively. The color scale is the same in all cases and shown on the left side of the two figures. In the figure on the left, the slabs composed by HM atoms only is shown. On the right side, the Ni-HM interface is shown. We notice that inserting the Ni layers pushes the negative spin magnetization (red) on the external surfaces of the HM slabs, while all positive magnetization density (purple) is concentrated around the Ni layers.

	NiPt	NiAu	NiTa
1	0.647	0.976	1.162
2	1.342	1.294	1.295
3	1.538	1.241	0.830
4	-0.354	-0.053	0.136
5	-0.315	0.010	0.090
6	-0.281	-0.009	-0.481

Table 6.2: Atomic magnetization in the z direction for NiPt, NiAu and NiTa interface systems.

6.4 Conclusion and Perspectives

We can deduce some qualitative conclusion from the analysis of these data. We observe two effects in our calculation: magnetic migration from Ni to the HM and an asymmetry in the magnetization density related to DMI. The magnetization proximity effect is quite large in Pt and Ta, while Au seems to be less responsive to the presence of Ni. A check of the EDOS would help clarifying the charge transfer among atoms. From our preliminary analysis, we conclude that Pt may not be the best HM to be used in Spintronics applications.
In the Ta case, being the system bcc, it would be interesting to do the same calculation on a Fe substrate, instead of Ni. This would help clarify the effect of lattice geometry.
The DMI on the contrary, being a geometric effect is present in all cases. A quantitative analysis can be done calculating the energy for different spin configurations (magnetic anisotropy energy), considering for example different orientation of the Ni exchange field, or explicit spin spirals, with periodicity of a few atoms as proposed in [272].

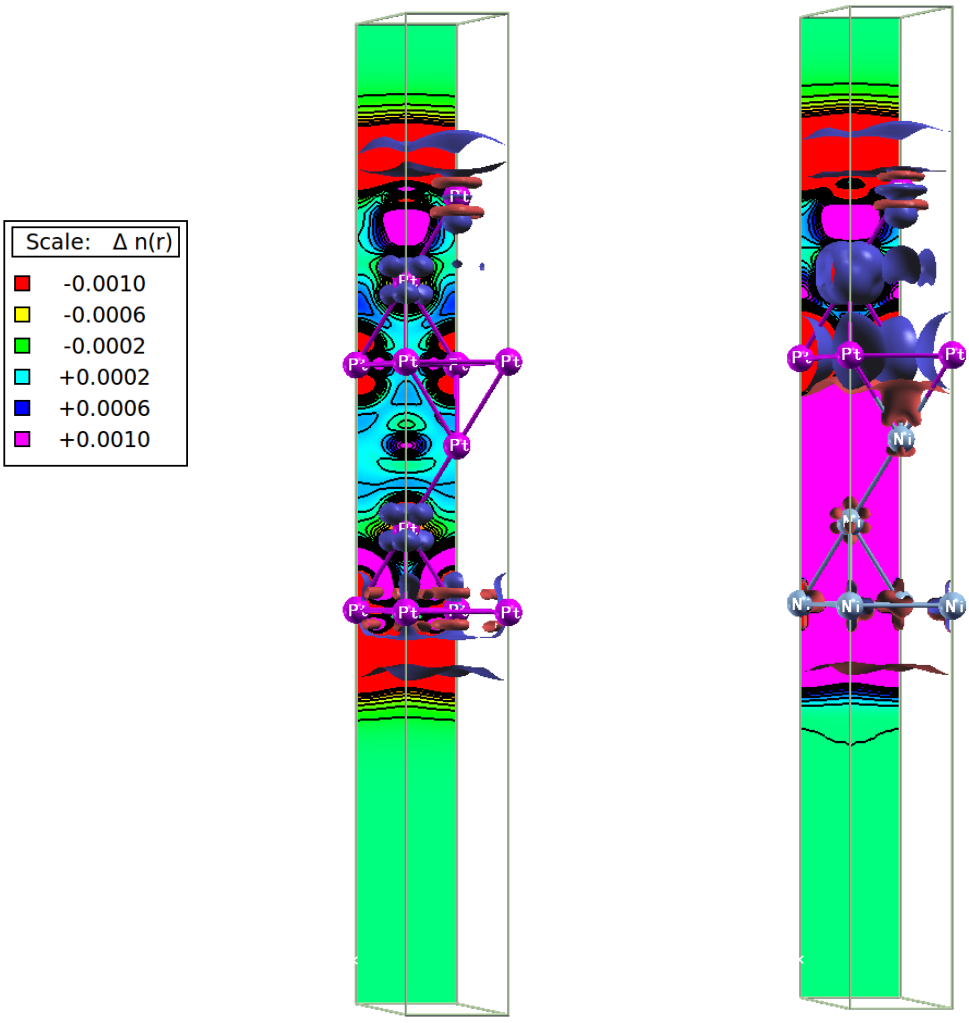

(a) Pt slab in vacuum. **(b)** Pt-Ni interface in vacuum.

Figure 6.3: Pt slab and Pt-Ni interface in vacuum with magnetization density for spin up (red curves) and spin down (blue curves).

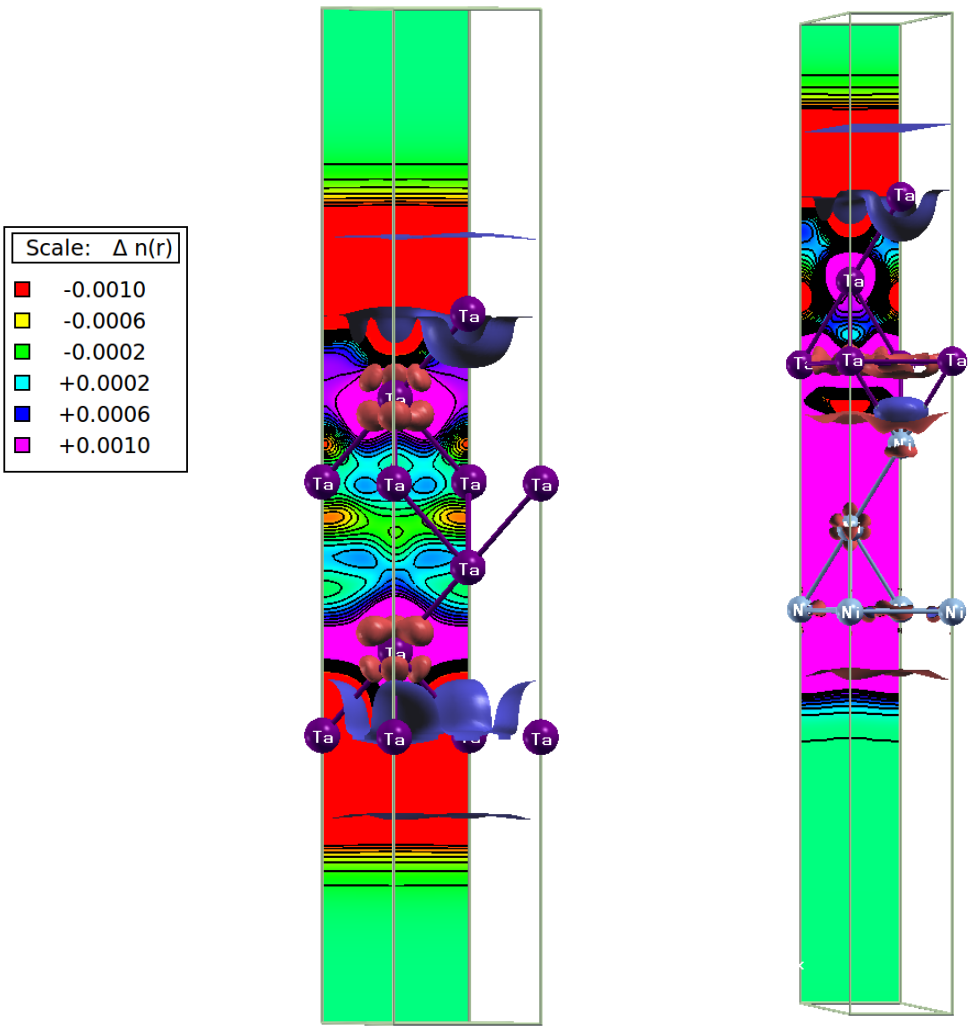

(a) Ta slab in vacuum. **(b)** Ta-Ni interface in vacuum.

Figure 6.4: Ta slab and Ta-Ni interface in vacuum with magnetization density for spin up (red curves) and spin down (blue curves).

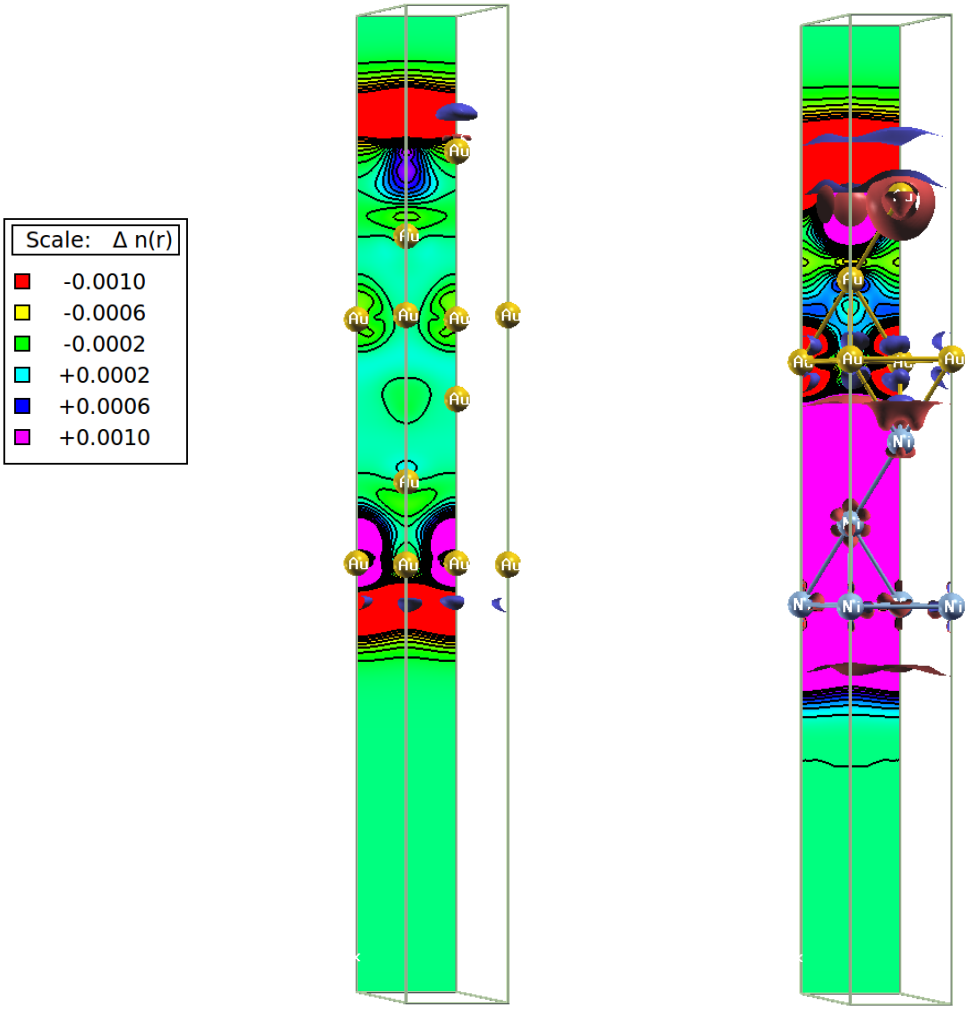

(a) Au slab in vacuum. **(b)** Au-Ni interface in vacuum.

Figure 6.5: Au slab and Pt-Au interface in vacuum with magnetization density for spin up (red curves) and spin down (blue curves).

Conclusions and Perspectives

The *ab-initio* methods presented in this Thesis seem to have succeed in their initial goal, i.e. to predict properties of materials.
Roughly speaking, we wanted to see what happens when we put electrons, magnons and phonons into a pot and we set the temperature of the system to a certain value. Our analysis showed that each of the three ingredients is responsible for some behavior in the the final recipe.
The ECP is certainly a good basis to study resistivity in metals. We showed that the LOVA method is extremely accurate in predicting transport coefficients for non-magnetic metals, also with quite complex FSF. The inclusion of inelastic scattering provides, albeit at a high computational cost, also a good prediction for Seebeck coefficient. The accuracy of our approach in predicting electrical resistivity drastically decreases for magnetic materials in the middle and high temperature window, where the electon-magnon scattering contribution dominates the resistivity. The Seebeck coefficient does not seem to depend much on this, since the value of S is averaged over σ, and both spin channels conductivities are, in general, equally overestimated. Also disorder does not seem to play a determinant role in the transport quantities that we analyzed, even though it will certainly provide a very real correction.
The calculation of electrical thermal conductivity is only outlined, and no data are shown, even though EPC matrix element seem good. This will certainly be an additional benchmark for the method if the lattice contribution can be extracted separately.
We also provided a prediction of spin dependent quantities which are nowadays difficult to measure, and we surprisingly find that strong thermally induced spin current can be just behind the corner. Unfortunately, SDSE experiment are difficult to realize at high temperature. We nevertheless hope to stimulate the curiosity of experimentalists in the near future.
We hope this work could generate more interest on the subject both from theorists and from experimentalists, and could in turn help to design new materials for green technologies.

The MPC is a key ingredient to explain several effects, first and foremost the

SSE. We have shown that lattice vibrations can have different effects on different materials, depending on their crystal structure and on the ferromagnetic elements involved.

The interfaces I presented show some extremely interesting features. My preliminary analysis shows that the special configuration of the FM-HM interface is extremely sensitive to the lattice parameter and to the specific HM used. Several improvements can be done on this calculation: the convergence of the magnetization dynamics with the thickness of the slab in the first place. We expect that the magnetization migration concerns only the first atomic layers. Actually a large supercell is needed to simulate also the modification of the crystal lattice far from the interface (we assumed that all atoms are disposed according to the same pattern, while all species have different cell parameters).
Moreover we studied only the magnetization in the direction perpendicular to the interface. One can study, for example, the case (probably not interesting) of the exchange field of the FM parallel to the interface, or the case (probably really interesting) of some easy magnetic texture, with the exchanges of the FM orientated in such a way to create a discrete spin wave with a periodicity of a few atomic sites. The DMI will probably give a difference in energy between clockwise and anticlockwise configurations which in turn can generate a strong Magnetic Anisotropy Effect.
The energies in play here are so small, that probably only DFT will give a realistic prediction and other methods with better scalability (e.g. Tight Binding) will probably not be helpful.

What I resumed in this Thesis is the result of a draining period of computation, comparison to available results (experimental in the first place), check, test, debug and finally computation again (over and over). I can say now that I am pretty confident with the results produced, and the predictions done on the Spin dependent Seebeck coefficient of magnetic metals are credible.

List of Publications

- Marco Di Gennaro, Srijan Kumar Saha and Matthieu J. Verstraete: The role of anharmonicity in the ab-initio phase diagram of calcium - Phys. Rev. Lett. 111, 025503 (2013).

- Marco Di Gennaro and Matthieu J. Verstraete: *Ab-initio* calculation of the spin dependent Seebeck effect in Permalloy. - In preparation.

- Marco Di Gennaro, Bin Xu and Matthieu J. Verstraete: *Ab-initio* calculation of electronic transport properties in Spintronics materials: Pt, Ni, Fe and Co. - In preparation.

- Marco Di Gennaro, José Alonso López Miranda, Aldo Romero and Matthieu J. Verstraete: *Ab-initio* calculation of temperature dependent exchange integrals in spin polarized metals. - In preparation.

- Bin Xu, Marco Di Gennaro, Brahim Belhadji and Matthieu J. Verstraete: The implementation of the Lowest Order Variational Approximation in *Abinit*. Application to Cu, Au, Ag, K, Na and Li. - In preparation.

- Marco Di Gennaro, Allen MacDonald, Henrique Miranda and Matthieu J. Verstraete: *Ab-initio* study of proximity effects at the Ferromagnetic-Heavy Metal interfaces. - In preparation.

Bibliography

[1] H. Adachi, J. ichiro Ohe, S. Takahashi, and S. Maekawa. Linear-response theory of spin seebeck effect in ferromagnetic insulators. *Phys. Rev. B*, 83:094410, Mar 2011.

[2] H. Adachi and S. Maekawa. Linear-response theory of the longitudinal spin seebeck effect. *Journal of the Korean Physical Society*, 62(12):1753–1758, 2013.

[3] H. Adachi, K. Uchida, E. Saitoh, and S. Maekawa. Theory of the spin seebeck effect. *Reports on Progress in Physics*, 76(3):036501, 2013.

[4] H. Adachi, K. Uchida, E. Saitoh, J.-i. Ohe, S. Takahashi, and S. Maekawa. Gigantic enhancement of spin seebeck effect by phonon drag. *Applied Physics Letters*, 97(25):–, 2010.

[5] M. Agrawal, V. I. Vasyuchka, A. A. Serga, A. D. Karenowska, G. A. Melkov, and H. Burkard. Magnon-phonon coupling unmasked: a direct measurement of magnon temperature. *arXiv:1209.3405*, 2012.

[6] A. Akhiezer. *J. Phys. (U.S.S.R.)*, 10:217, 1946.

[7] P. Allen. Chapter 6 electron transport. In S. G. Louie and M. L. Cohen, editors, *Conceptual Foundations of Materials A Standard Model for Ground- and Excited-State Properties*, volume 2 of *Contemporary Concepts of Condensed Matter Science*, pages 165 – 218. Elsevier, 2006.

[8] P. B. Allen. Fermi-surface harmonics: A general method for nonspherical problems. application to boltzmann and eliashberg equations. *Phys. Rev. B*, 13:1416–1427, Feb 1976.

[9] P. B. Allen. New method for solving boltzmann's equation for electrons in metals. *Phys. Rev. B*, 17:3725–3734, May 1978.

[10] P. B. Allen. *Quantum Theory of Real Metals*. Kluwer, 1996.

[11] P. B. Allen. *Contemporary Concepts of Condensed Matter Science*, volume Conceptual Foundations of Materials A Standard Model for Ground- and Excited-State Properties. Elsevier B.V., 2006.

[12] Z. An, F. Q. Liu, Y. Lin, and C. Liu. The universal definition of spin current. *Sci. Rep.*, 2.

[13] P. Anderson. *Theory of Magnetic Exchange Interactions: Exchange in Insulators and Semiconductors*, volume 14. Academic Press, New York.

[14] H. Arnold and G. Elmen. Permalloy, a new magnetic material of very high permeability. *Bell System Technical Journal*, 2(3):101–111, 1923.

[15] N. Ashcroft and N. Mermin. *Solid State Physics*. Saunders College, Philadelphia, 1976.

[16] M. N. Baibich, J. M. Broto, A. Fert, F. N. Van Dau, F. Petroff, P. Etienne, G. Creuzet, A. Friederich, and J. Chazelas. Giant magnetoresistance of (001)fe/(001)cr magnetic superlattices. *Phys. Rev. Lett.*, 61:2472–2475, Nov 1988.

[17] F. L. Bakker, A. Slachter, J.-P. Adam, and B. J. van Wees. Interplay of peltier and seebeck effects in nanoscale nonlocal spin valves. *Phys. Rev. Lett.*, 105:136601, Sep 2010.

[18] R. D. Barnard. *Thermoelectricity in Metals and Alloys*. Taylor and Francis Ltd, 1972.

[19] S. Baroni, S. de Gironcoli, A. Dal Corso, and P. Giannozzi. Phonons and related crystal properties from density-functional perturbation theory. *Rev. Mod. Phys.*, 73:515–562, Jul 2001.

[20] L. E. Bell. Cooling, heating, generating power, and recovering waste heat with thermoelectric systems. *Science*, 321(5895):1457–1461, 2008.

[21] L. Berger. Emission of spin waves by a magnetic multilayer traversed by a current. *Phys. Rev. B*, 54:9353–9358, Oct 1996.

[22] C. M. Bhandari and G. S. Verma. Scattering of magnons and phonons in the thermal conductivity of yttrium iron garnet. *Phys. Rev.*, 152:731–736, Dec 1966.

[23] G. Binasch, P. Grünberg, F. Saurenbach, and W. Zinn. Enhanced magnetoresistance in layered magnetic structures with antiferromagnetic interlayer exchange. *Phys. Rev. B*, 39:4828–4830, Mar 1989.

[24] R. J. Birgeneau, J. Cordes, G. Dolling, and A. D. B. Woods. Normal modes of vibration in nickel. *Phys. Rev.*, 136:A1359–A1365, Nov 1964.

[25] F. J. Blatt, D. J. Flood, V. Rowe, P. A. Schroeder, and J. E. Cox. Magnon-drag thermopower in iron. *Phys. Rev. Lett.*, 18:395–396, Mar 1967.

[26] F. J. Blatt, P. A. Schroeder, C. L. Foiles, and D. Greig. *Thermoelectric Power of Metals*. New York: Plenum, 1976.

[27] F. Bloch. über die quantenmechanik der elektronen in kristallgittern. *Zeitschrift f ur Physik*, 52(7-8):555–600, 1929.

[28] F. Bloch. Zum elektrischen widerstandsgesetz bei tiefen temperaturen. *Zeitschrift für Physik*, 59(3-4):208–214, 1930.

[29] S. Blügel, H. N., V. Meden, D. Wortmann, and (Eds.). *45^{th} IFF Spring School 2014. Computing solids. Models, ab-initio methods and supercomputing.* Forschungszentrum Jülich GmbH, IAS, PGI, JCNS, ICS, 2014.

[30] M. Bockstedte, A. Kley, J. Neugebauer, and M. Scheffler. *Comput. Phys. Commun.*, 107:187, 1997.

[31] L. Boltzmann. *Wien. Ber.*, 66:273, 1872.

[32] S. R. Boona, R. C. Myers, and J. P. Heremans. Spin caloritronics. *Energy Environ. Sci.*, 7:885–910, 2014.

[33] M. Born and R. Oppenheimer. Zur Quantentheorie der Molekeln. *Annalen der Physik*, 389:457–484, 1927.

[34] S. Bosu, Y. Sakuraba, K. Uchida, K. Saito, T. Ota, E. Saitoh, and K. Takanashi. Spin seebeck effect in thin films of the heusler compound co_2mnsi. *Phys. Rev. B*, 83:224401, Jun 2011.

[35] G. Bots, J. Pals, B. Blaisse, L. D. Jong, and P. V. Engelen. Magnetic properties of superconducting tantalum. *Physica*, 31(7):1113 – 1123, 1965.

[36] A. Brataas, G. E. Bauer, and P. J. Kelly. Non-collinear magnetoelectronics. *Physics Reports*, 427(4):157 – 255, 2006.

[37] A. Brataas, A. D. Kent, and H. Ohno. Current-induced torques in magnetic materials. *Nat Mater*, 11(5):372–381, 05 2012.

[38] A. Brataas, Y. V. Nazarov, and G. E. W. Bauer. Finite-element theory of transport in ferromagnet˘normal metal systems. *Phys. Rev. Lett.*, 84:2481–2484, Mar 2000.

[39] B. Brockhouse, H. Abou-Helal, and E. Hallman. Lattice vibrations in iron at 296 °k. *Solid State Communications*, 5(4):211 – 216, 1967.

[40] M. Brooks and B. Johansson. *Handbook of Magnetic Materials*. Elsevier Science, New York, 1993.

[41] C. Burrowes, B. Heinrich, B. Kardasz, E. A. Montoya, E. Girt, Y. Sun, Y.-Y. Song, and M. Wu. Enhanced spin pumping at yttrium iron garnet/au interfaces. *Applied Physics Letters*, 100(9):–, 2012.

[42] J. Callaway. Scattering of spin waves by magnetic defects. *Phys. Rev.*, 132:2003–2009, Dec 1963.

[43] J. Callaway and R. Boyd. Scattering of spin waves by magnetic defects. *Phys. Rev.*, 134:A1655–A1662, Jun 1964.

[44] J. P. Carbotte. Properties of boson-exchange superconductors. *Rev. Mod. Phys.*, 62:1027–1157, Oct 1990.

[45] D. Ceperley and B. Alder. Ground state of the electron gas by a stochastic method. *Phys. Rev. Lett.*, 45:566–569, Aug 1980.

[46] D. Chadi and R. Martin. Calculation of lattice dynamical properties from electronic energies: Application to c, si and ge. *Solid State Communications*, 19(7):643 – 646, 1976.

[47] S. Chapman and T. G. Cowling. *The Mathematical Theory of Non-Univorm Gases*. Cambridge U.P., 1970.

[48] K. Chen and S. Zhang. Spin pumping in the presence of spin-orbit coupling. *Phys. Rev. Lett.*, 114:126602, Mar 2015.

[49] J.-H. Cho and M. Scheffler. *Ab initio* pseudopotential study of fe, co, and ni employing the spin-polarized lapw approach. *Phys. Rev. B*, 53:10685–10689, Apr 1996.

[50] L. Chotorlishvili, Z. Toklikishvili, V. K. Dugaev, J. Barnaś, S. Trimper, and J. Berakdar. Fokker-planck approach to the theory of the magnon-driven spin seebeck effect. *Phys. Rev. B*, 88:144429, Oct 2013.

[51] B.-E. condensation of quasi-equilibrium magnons at room temperature under pumping. *Nature*, 433:430–433, 2006.

[52] M. Di Gennaro, S. K. Saha, and M. J. Verstraete. Role of dynamical instability in the *Ab Initio* phase diagram of calcium. *Phys. Rev. Lett.*, 111:025503, Jul 2013.

[53] R. L. Douglass. Heat transport by spin waves in yttrium iron garnet. *Phys. Rev.*, 129:1132–1135, Feb 1963.

[54] P. Drude. Zur elektronentheorie der metalle. *Annalen der Physik*, 306(3):566–613, 1900.

[55] P. Drude. Zur elektronentheorie der metalle; ii. teil. galvanomagnetische und thermomagnetische effecte. *Annalen der Physik*, 308(11):369–402, 1900.

[56] D. H. Dutton, B. N. Brockhouse, and A. P. Miiller. Crystal dynamics of platinum by inelastic neutron scattering. *Canadian Journal of Physics*, 50(23):2915–2927, 1972.

[57] M. Dyakonov and V. Perel. *Pis. Z. Eksp. Teor. Fiz.*, 13:657, 1971.

[58] M. Dyakonov and V. Perel. Current-induced spin orientation of electrons in semiconductors. *Physics Letters A*, 35(6):459 – 460, 1971.

[59] A. Dyrdał and J. Barnaś. Intrinsic contribution to spin hall and spin nernst effects in a bilayer graphene. *Journal of Physics: Condensed Matter*, 24(27):275302, 2012.

[60] I. E. Dzyaloshinskii. Thermodynamic theory of weak ferromagnetism in antiferromagnetic substances. *Sov. Phys. JETP*, 5(6):1259–1272, 1957.

[61] H. Ebert, B. Drittler, and H. Akai. Spin-polarized relativistic electronic structure calculations for disordered alloys using the cpa: application to fexco1-x and coxpt1-x. *Journal of Magnetism and Magnetic Materials*, 104-107, Part 1(0):733 – 734, 1992.

[62] H. Ebert, D. Ködderitzsch, and J. Minár. Calculating condensed matter properties using the kkr-green's function method recent developments and applications. *Reports on Progress in Physics*, 74(9):096501, 2011.

[63] G. Eliashberg. Interactions between electrons and lattice vibrations in a superconductor. *Soviet Phys. JETP*, 11:696, 1960.

[64] H.-A. Engel, B. I. Halperin, and E. I. Rashba. Theory of spin hall conductivity in n-doped gaas. *Phys. Rev. Lett.*, 95:166605, Oct 2005.

[65] M. Erekhinsky, F. Casanova, I. K. Schuller, and A. Sharoni. Spin-dependent seebeck effect in non-local spin valve devices. *Applied Physics Letters*, 100(21):212401, 2012.

[66] M. C. S. Escaño, T. Q. Nguyen, and H. Kasai. Molecular oxygen adsorption on ferromagnetic platinum. *Chemical Physics Letters*, 555:125 – 130, 2013.

[67] C. Etz, L. Bergqvist, A. Bergman, A. Taroni, and O. Eriksson. Atomistic spin dynamics and surface magnons. *Journal of Physics: Condensed Matter*, 27(24):243202, 2015.

[68] A. Fert and I. A. Campbell. Two-current conduction in nickel. *Phys. Rev. Lett.*, 21:1190–1192, Oct 1968.

[69] A. Fert and I. A. Campbell. Electrical resistivity of ferromagnetic nickel and iron based alloys. *Journal of Physics F: Metal Physics*, 6(5):849, 1976.

[70] A. Fert and P. M. Levy. Role of anisotropic exchange interactions in determining the properties of spin-glasses. *Phys. Rev. Lett.*, 44:1538–1541, Jun 1980.

[71] R. P. Feynman. Forces in molecules. *Phys. Rev.*, 56:340–343, Aug 1939.

[72] B. L. Fielek. The phonon dispersion curves of copper. *Journal of Physics F: Metal Physics*, 5(8):1451, 1975.

[73] C. Fiolhais, F. Nogueira, and M. Marques. *A Primer in Density Functional Theory*. Springer, Berlin [etc.], 2003.

[74] FlipseJ., B. L., SlachterA., D. K., and van WeesB. J. Direct observation of the spin-dependent peltier effect. *Nat Nano*, 7(3):166–168, 03 2012.

[75] J. Foros, A. Brataas, Y. Tserkovnyak, and G. E. W. Bauer. Magnetization noise in magnetoelectronic nanostructures. *Phys. Rev. Lett.*, 95:016601, Jun 2005.

[76] S. Friedberg and E. Harris. *Proceedings of the Eighth International Conference on Low Temperature Physics*. Butterworths, London, 1962.

[77] M. Fuchs and M. Scheffler. Ab initio pseudopotentials for electronic structure calculations of poly-atomic systems using density-functional theory. *Computer Physics Communications*, 119(1):67 – 98, 1999.

[78] M. Gajek, J. J. Nowak, J. Z. Sun, P. L. Trouilloud, E. J. O'Sullivan, D. W. Abraham, M. C. Gaidis, G. Hu, S. Brown, Y. Zhu, R. P. Robertazzi, W. J. Gallagher, and D. C. Worledge. Spin torque switching of 20 nm magnetic tunnel junctions with perpendicular anisotropy. *Applied Physics Letters*, 100(13):–, 2012.

[79] V. Gantmakher and Y. Levinson. *Carrier Scattering in Metals and Semiconductors*. North-Holland, 1987.

[80] R. Gebauer and S. Baroni. Magnons in real materials from density-functional theory. *Phys. Rev. B*, 61:R6459–R6462, Mar 2000.

[81] M. Gell-Mann and K. Brueckner. Correlation energy of an electron gas at high density. *Phys. Rev.*, 106:364–368, Apr 1957.

[82] T. Gerrits, H. A. M. van den Berg, J. Hohlfeld, L. Bar, and T. Rasing. Ultrafast precessional magnetization reversal by picosecond magnetic field pulse shaping. *Nature*, 418:509–512, 2002.

[83] T. L. Gilbert. *Phys. Rev.*, 100:1243, 1955.

[84] X. Gonze, B. Amadon, P.-M. Anglade, J.-M. Beuken, F. Bottin, P. Boulanger, F. Bruneval, D. Caliste, R. Caracas, M. Côté, T. Deutsch, L. Genovese, P. Ghosez, M. Giantomassi, S. Goedecker, D. Hamann, P. Hermet, F. Jollet, G. Jomard, S. Leroux, M. Mancini, S. Mazevet, M. Oliveira, G. Onida, Y. Pouillon, T. Rangel, G.-M. Rignanese, D. Sangalli, R. Shaltaf, M. Torrent, M. Verstraete, G. Zerah, and J. Zwanziger. Abinit: First-principles approach to material and nanosystem properties. *Computer Physics Communications*, 180(12):2582 – 2615, 2009.

[85] X. Gonze, J.-M. Beuken, R. Caracas, F. Detraux, M. Fuchs, G.-M. Rignanese, L. Sindic, M. Verstraete, G. Zerah, F. Jollet, M. Torrent, A. Roy, M. Mikami, P. Ghosez, J.-Y. Raty, and D. Allan. First-principles computation of material properties: the abinit software project. *Computational Materials Science*, 25(3):478 – 492, 2002.

[86] X. Gonze, G. Rignanese, and R. Caracas. First-principle studies of the lattice dynamics of crystals, and related properties. *Zeitschrift für Kristallographie*, 220:458–472, 2005.

[87] X. Gonze, G.-M. Rignanese, M. Verstraete, J.-M. Beuken, Y. Pouillon, R. Caracas, F. Jollet, M. Torrent, G. Zerah, M. Mikami, P. Ghosez, M. Veithen, J.-Y. Raty, V. Olevano, F. Bruneval, L. Reining, R. Godby, G. Onida, D. Hamann, and D. Allan. A brief introduction to the abinit software package. *Zeit. Kristallogr.*, 220:558–562, 2005.

[88] X. Gonze, R. Stumpf, and M. Scheffler. Analysis of separable potentials. *Phys. Rev. B*, 44:8503–8513, Oct 1991.

[89] X. Gonze and J.-P. Vigneron. Density-functional approach to nonlinear-response coefficients of solids. *Phys. Rev. B*, 39:13120–13128, Jun 1989.

[90] G. Grimvall. *The Electron-Phonon Interaction in Metals, Selected Topics in Solid State Physics*, volume 16. North-Holland, Amsterdam, 1981.

[91] E. Grüneisen. Die abhängigkeit des elektrischen widerstandes reiner metalle von der temperatur. *Ann. Phys. (Leipzig)*, 4:530–540, 1933.

[92] S. V. Halilov, H. Eschrig, A. Y. Perlov, and P. M. Oppeneer. Adiabatic spin dynamics from spin-density-functional theory: Application to fe, co, and ni. *Phys. Rev. B*, 58:293–302, Jul 1998.

[93] E. H. Hall. *Am. J. Math.*, 2(287), 1879.

[94] E. H. Hall. *Philos. Mag.*, 12(157), 1881.

[95] E. Hallaman and B. Brockhouse. Crystal dynamics of nickel-iron and copper-zinc alloys. *Canadian Journal of Physics*, 47:1117, 1969.

[96] D. R. Hamann. Generalized norm-conserving pseudopotentials. *Phys. Rev. B*, 40:2980–2987, Aug 1989.

[97] C. Hartwigsen, S. Goedecker, and J. Hutter. Relativistic separable dual-space gaussian pseudopotentials from h to rn. *Phys. Rev. B*, 58:3641–3662, Aug 1998.

[98] M. Hatami, G. E. Bauer, S. Takahashi, and S. Maekawa. Thermoelectric spin diffusion in a ferromagnetic metal. *Solid State Communications*, 150(11-12):480 – 484, 2010. Spin Caloritronics.

[99] M. Hatami, G. E. W. Bauer, Q. Zhang, and P. J. Kelly. Thermal spin-transfer torque in magnetoelectronic devices. *Phys. Rev. Lett.*, 99:066603, Aug 2007.

[100] S. Heinze, K. von Bergmann, M. Menzel, J. Brede, A. Kubetzka, R. Wiesendanger, G. Bihlmayer, and S. Blugel. Spontaneous atomic-scale magnetic skyrmion lattice in two dimensions. *Nat Phys*, 7(9):713–718, 09 2011.

[101] W. Heisenberg. *Z. Phys.*, 49:619, 1928.

[102] H. Hellmann. *Einführung in die Quantumchemie*. Deuticke, Leipzig, Leipzig, 1937.

[103] K.-H. Hellwege and J. O. (Eds.). *Electrical Resistivity, Thermoelectrical Power and Optical Properties*, volume 15b. Springer Berlin Heidelberg, 1985.

[104] J. E. Hirsch. Spin hall effect. *Phys. Rev. Lett.*, 83(9):1834–1837, Aug 1999.

[105] P. Hohenberg and W. Kohn. Inhomogeneous electron gas. *Phys. Rev.*, 136:B864–B871, Nov 1964.

[106] S. Y. Huang, X. Fan, D. Qu, Y. P. Chen, W. G. Wang, J. Wu, T. Y. Chen, J. Q. Xiao, and C. L. Chien. Transport magnetic proximity effects in platinum. *Phys. Rev. Lett.*, 109:107204, Sep 2012.

[107] S. Y. Huang, W. G. Wang, S. F. Lee, J. Kwo, and C. L. Chien. Intrinsic spin-dependent thermal transport. *Phys. Rev. Lett.*, 107:216604, Nov 2011.

[108] I. Žutić, J. Fabian, and S. Das Sarma. Spintronics: Fundamentals and applications. *Rev. Mod. Phys.*, 76:323–410, Apr 2004.

[109] E. Şaşıoğlu, L. M. Sandratskii, and P. Bruno. First-principles calculation of the intersublattice exchange interactions and curie temperatures of the full heusler alloys ni_2Mnx ($x = \mathrm{Ga}, \mathrm{In}, \mathrm{Sn}, \mathrm{Sb}$). *Phys. Rev. B*, 70:024427, Jul 2004.

[110] C. Jaworski, R. Myers, E. Johnston-Halperin, and J. Heremans. Giant spin seebeck effect in a non-magnetic material. *Nature*, 487, 2012.

[111] C. M. Jaworski, J. Yang, S. Mack, D. D. Awschalom, J. P. Heremans, and R. C. Myers. Observation of the spin-seebeck effect in a ferromagnetic semiconductor. *Nat Mater*, 9(11):898–903, 11 2010.

[112] C. M. Jaworski, J. Yang, S. Mack, D. D. Awschalom, R. C. Myers, and J. P. Heremans. Spin-seebeck effect: A phonon driven spin distribution. *Phys. Rev. Lett.*, 106:186601, May 2011.

[113] F. J. Jedema, A. T. Filip, and B. J. van Wees. Electrical spin injection and accumulation at room temperature in an all-metal mesoscopic spin valve. *Nature*, 410(6826):345–348, Mar 2001.

[114] F. J. Jedema, A. T. Filip, and B. J. van Wees. Electrical spin injection and accumulation at room temperature in an all-metal mesoscopic spin valve. *Nature*, 410(6826):345–348, 03 2001.

[115] F. J. Jedema, H. B. Heersche, A. T. Filip, J. J. A. Baselmans, and B. J. van Wees. Electrical detection of spin precession in a metallic mesoscopic spin valve. *Nature*, 416(6882):713–716, 04 2002.

[116] X. Jia, K. Liu, K. Xia, and G. E. W. Bauer. Spin transfer torque on magnetic insulators. *EPL (Europhysics Letters)*, 96(1):17005, 2011.

[117] M. Johnson and R. H. Silsbee. Interfacial charge-spin coupling: Injection and detection of spin magnetization in metals. *Phys. Rev. Lett.*, 55:1790–1793, Oct 1985.

[118] M. Johnson and R. H. Silsbee. Thermodynamic analysis of interfacial transport and of the thermomagnetoelectric system. *Phys. Rev. B*, 35:4959–4972, Apr 1987.

[119] F. Jollet, M. Torrent, and N. Holzwarth. Generation of projector augmented-wave atomic data: A 71 element validated table in the {XML} format. *Computer Physics Communications*, 185(4):1246 – 1254, 2014.

[120] M. Kaganov and V. M. Tsukernik. *J. Exptl. Theoret. Phys. (U.S.S.R.)*, 36:224, 1959.

[121] Y. Kajiwara, K. Harii, S. Takahashi, J. Ohe, K. Uchida, M. Mizuguchi, H. Umezawa, H. Kawai, K. Ando, K. Takanashi, S. Maekawa, and E. Saitoh. Transmission of electrical signals by spin-wave interconversion in a magnetic insulator. *Nature*, 464(7286):262–266, Mar 2010.

[122] Y. Kajiwara, K. Harii, S. Takahashi, J. Ohe, K. Uchida, M. Mizuguchi, H. Umezawa, H. Kawai, K. Ando, K. Takanashi, S. Maekawa, and E. Saitoh. Transmission of electrical signals by spin-wave interconversion in a magnetic insulator. *Nature*, 464:262–266, 2010.

[123] R. Karplus and J. M. Luttinger. Hall effect in ferromagnetics. *Phys. Rev.*, 95:1154–1160, Sep 1954.

[124] Y. K. Kato, R. C. Myers, A. C. Gossard, and D. D. Awschalom. Observation of the spin hall effect in semiconductors. *Science*, 306(5703):1910–1913, 2004.

[125] T. Kikkawa, K. Uchida, Y. Shiomi, Z. Qiu, D. Hou, D. Tian, H. Nakayama, X.-F. Jin, and E. Saitoh. Longitudinal spin seebeck effect free from the proximity nernst effect. *Phys. Rev. Lett.*, 110:067207, Feb 2013.

[126] T. Kimura and Y. Otani. Large spin accumulation in a permalloy-silver lateral spin valve. *Phys. Rev. Lett.*, 99:196604, Nov 2007.

[127] T. Kimura, Y. Otani, T. Sato, S. Takahashi, and S. Maekawa. Room-temperature reversible spin hall effect. *Phys. Rev. Lett.*, 98:156601, Apr 2007.

[128] C. Kittel. Interaction of spin waves and ultrasonic waves in ferromagnetic crystals. *Phys. Rev.*, 110:836–841, May 1958.

[129] C. Kittel. *Introduction to solid state physics, 7th Ed.* Wiley, 1996.

[130] C. Kittel and E. Abrahams. Relaxation process in ferromagnetism. *Rev. Mod. Phys.*, 25:233–238, Jan 1953.

[131] M. Kohler. *Z. Phys.*, 124(772), 1948.

[132] M. Kohler. *Z. Phys.*, 125(679), 1949.

[133] W. Kohn and N. Rostoker. Solution of the schrödinger equation in periodic lattices with an application to metallic lithium. *Phys. Rev.*, 94:1111–1120, Jun 1954.

[134] W. Kohn and L. J. Sham. Self-consistent equations including exchange and correlation effects. *Phys. Rev.*, 140:A1133–A1138, Nov 1965.

[135] A. Kokalj. Computer graphics and graphical user interfaces as tools in simulations of matter at the atomic scale. *Computational Materials Science*, 28(2):155 – 168, 2003. Proceedings of the Symposium on Software Development for Process and Materials Design.

[136] J. Korringa. On the calculation of the energy of a bloch wave in a metal. *Physica*, 13(6–7):392–400, 1947.

[137] J. Kubler, K. H. Hock, J. Sticht, and A. R. Williams. Density functional theory of non-collinear magnetism. *Journal of Physics F: Metal Physics*, 18(3):469, 1988.

[138] H. Kuttruff. *Acoustics: An Introduction.* Taylor & Francis, New York, 2007.

[139] G. L. *Zh. Eksp. Teor. Fiz.*, 16:193, 1946.

[140] L. Landau. Oscillations in a fermi liquid. *J. Exp. Theor. Phys.*, 30:1058, 1956.

[141] L. Landau, E. M. Lifshitz, and L. P. Pitaevski. *Statistical Physics, Part 2, 3rd ed.* Pergamon, Oxford, 1980.

[142] L. D. Landau and E. Lifshitz. *Statistical Physics, Third Edition, Part 1: Volume 5.* Elsevier, 1980.

[143] A. Liechtenstein, M. Katsnelson, V. Antropov, and V. Gubanov. *J. Magn. Magn. Mater.*, 67:65–74, 1987.

[144] A. I. Liechtenstein, M. I. Katsnelson, and V. A. Gubanov. Exchange interactions and spin-wave stiffness in ferromagnetic metals. *Journal of Physics F: Metal Physics*, 14(7):L125, 1984.

[145] E. M. Lifshitz and L. P. Pitaevskii. *Physical Kinetics*. New York: Plenum, 1982.

[146] L. Liu, C.-F. Pai, Y. Li, H. W. Tseng, D. C. Ralph, and R. A. Buhrman. Spin-torque switching with the giant spin hall effect of tantalum. *Science*, 336(6081):555–558, 2012.

[147] N. Locatelli, V. Cros, and J. Grollier. Spin-torque building blocks. *Nat Mater*, 13:11–20, 2014.

[148] M. Lundstrom. *Foundamentals of carrier transport*. Cambridge University Press, 1990.

[149] B. Lüthi. *J. Phys. Chem. Solids*, 23:35, 1962.

[150] G. K. Madsen and D. J. Singh. Boltztrap. a code for calculating band-structure dependent quantities. *Computer Physics Communications*, 175(1):67 – 71, 2006.

[151] M. A. Marques, M. J. Oliveira, and T. Burnus. Libxc: A library of exchange and correlation functionals for density functional theory. *Computer Physics Communications*, 183(10):2272 – 2281, 2012.

[152] R. M. Martin. *Electronic Structure. Basic theory and practical methods*. Cambridge University Press, 2004.

[153] G. Meier, M. Bolte, R. Eiselt, B. Krüger, D.-H. Kim, and P. Fischer. Direct imaging of stochastic domain-wall motion driven by nanosecond current pulses. *Phys. Rev. Lett.*, 98:187202, May 2007.

[154] M. Meinert, J.-M. Schmalhorst, and G. Reiss. Ab initio prediction of ferrimagnetism, exchange interactions and curie temperatures in mn 2 tiz heusler compounds. *Journal of Physics: Condensed Matter*, 23(3):036001, 2011.

[155] M. C. Michelini, R. Pis Diez, and A. H. Jubert. A density functional study of small nickel clusters. *International Journal of Quantum Chemistry*, 70(4-5):693–701, 1998.

[156] I. Mihai Miron, G. Gaudin, S. Auffret, B. Rodmacq, A. Schuhl, S. Pizzini, J. Vogel, and P. Gambardella. Current-driven spin torque induced by the rashba effect in a ferromagnetic metal layer. *Nat Mater*, 9:230–234, Sep 2010.

[157] K. Miura, S. Kasai, K. Kobayashi, and T. Ono. Non local spin detection in ferromagnet/superconductor/ferromagnet spin-valve device with double-tunnel junctions. *Japanese Journal of Applied Physics*, 45(4R):2888, 2006.

[158] T. Miyasato, N. Abe, T. Fujii, A. Asamitsu, S. Onoda, Y. Onose, N. Nagaosa, and Y. Tokura. Crossover behavior of the anomalous hall effect and anomalous nernst effect in itinerant ferromagnets. *Phys. Rev. Lett.*, 99:086602, Aug 2007.

[159] H. J. Monkhorst and J. D. Pack. Special points for brillouin-zone integrations. *Phys. Rev. B*, 13:5188–5192, Jun 1976.

[160] T. Moriya. Anisotropic superexchange interaction and weak ferromagnetism. *Phys. Rev.*, 120:91–98, Oct 1960.

[161] V. L. Moruzzi and P. Marcus. *Handbook of Magnetic Materials*. Elsevier Science, New York, 1993.

[162] S. Mühlbauer, B. Binz, F. Jonietz, C. Pfleiderer, A. Rosch, A. Neubauer, R. Georgii, and P. Böni. Skyrmion lattice in a chiral magnet. *Science*, 323(5916):915–919, 2009.

[163] S. Murakami, N. Nagaosa, and S.-C. Zhang. Dissipationless quantum spin current at room temperature. *Science*, 301(5638):1348–1351, 2003.

[164] N. Nagaosa, J. Sinova, S. Onoda, A. H. MacDonald, and N. P. Ong. Anomalous hall effect. *Rev. Mod. Phys.*, 82:1539–1592, May 2010.

[165] G. Nahrwold, L. Bocklage, J. M. Scholtyssek, T. Matsuyama, B. Krüger, U. Merkt, and G. Meier. Current-induced domain-wall depinning in curved permalloy nanowires. *Journal of Applied Physics*, 105(7), 2009.

[166] G. Nahrwold, J. M. Scholtyssek, S. Motl-Ziegler, O. Albrecht, U. Merkt, and G. Meier. Structural, magnetic, and transport properties of permalloy for spintronic experiments. *Journal of Applied Physics*, 108(1), 2010.

[167] P. Nemec, E. Rozkotova, N. Tesarova, F. Trojanek, E. De Ranieri, K. Olejnik, J. Zemen, V. Novak, M. Cukr, P. Maly, and T. Jungwirth. Experimental observation of the optical spin transfer torque. *Nat Phys*, 8:411–415, Aug 2012.

[168] B. K. Nikolić, L. P. Zârbo, and S. Souma. Imaging mesoscopic spin hall flow: Spatial distribution of local spin currents and spin densities in and out of multiterminal spin-orbit coupled semiconductor nanostructures. *Phys. Rev. B*, 73:075303, Feb 2006.

[169] Q. Niu and L. Kleinman. Spin-wave dynamics in real crystals. *Phys. Rev. Lett.*, 80:2205–2208, Mar 1998.

[170] L. Nordheim. *Ann. Phys. (Leipzig)*, 9:607, 1931.

[171] T. S. Nunner and F. von Oppen. Quasilinear spin-voltage profiles in spin thermoelectrics. *Phys. Rev. B*, 84:020405, Jul 2011.

[172] J.-i. Ohe, H. Adachi, S. Takahashi, and S. Maekawa. Numerical study on the spin seebeck effect. *Phys. Rev. B*, 83:115118, Mar 2011.

[173] G. L. Oliver and J. P. Perdew. Spin-density gradient expansion for the kinetic energy. *Phys. Rev. A*, 20:397–403, Aug 1979.

[174] S. S. P. Parkin, M. Hayashi, and L. Thomas. Magnetic domain-wall racetrack memory. *Science*, 320(5873):190–194, 2008.

[175] K. Parlinski, Z. Q. Li, and Y. Kawazoe. First-principles determination of the soft mode in cubic zro_2. *Phys. Rev. Lett.*, 78:4063–4066, May 1997.

[176] J. P. Perdew, K. Burke, and M. Ernzerhof. Generalized gradient approximation made simple. *Phys. Rev. Lett.*, 77:3865–3868, Oct 1996.

[177] C. Petitjean, X. Waintal, M. Chshiev, and J. Miltat. Mesoscopic current-in-plane giant magneto-resistance. *ArXiv*, cond-mat/1109.3602v1, 2011.

[178] R. M. Pick, M. H. Cohen, and R. M. Martin. Microscopic theory of force constants in the adiabatic approximation. *Phys. Rev. B*, 1:910–920, Jan 1970.

[179] N. A. Pike and D. Stroud. Model for the spin-dependent seebeck coefficient of insb in a magnetic field. *Phys. Rev. B*, 90:174435, Nov 2014.

[180] D. Polder. *Phil. Mag.*, 40(99), 1949.

[181] H. Pollack. *Materials Science and Metallurgy (4th Edition)*. Prentice Hall, 1988.

[182] G. A. Prinz. Magnetoelectronics. *Science*, 282(5394):1660–1663, 1998.

[183] Y. Pu, D. Chiba, F. Matsukura, H. Ohno, and J. Shi. Mott relation for anomalous hall and nernst effects in $ga_{1-x}mn_xAs$ ferromagnetic semiconductors. *Phys. Rev. Lett.*, 101:117208, Sep 2008.

[184] R. R. W. Powell, R. Tye, and M. Woodman. Thermal conductivities and electrical resistivities of the platinum metals. *Platinum Metals Rev.*, 6:138–143, 1962.

[185] D. Ralph and M. Stiles. Spin transfer torques. *Journal of Magnetism and Magnetic Materials*, 320(7):1190–1216, 2008.

[186] E. I. Rashba. Spin currents in thermodynamic equilibrium: The challenge of discerning transport currents. *Phys. Rev. B*, 68:241315, Dec 2003.

[187] J. Rives. Thermal conductivity in magnetic insulators. *Physics Letters A*, 36(4):327 – 328, 1971.

[188] S. J. Rosenberg. *Nickel and its alloys*. National Bureau of Standards, 1986.

[189] R. Ross. *Metallic Materials Specification Handbook*. Springer, 1992.

[190] R. F. Sabiryanov and S. S. Jaswal. Magnons and magnon-phonon interactions in iron. *Phys. Rev. Lett.*, 83:2062–2064, Sep 1999.

[191] E. Saitoh, G. E. W. Bauer, and B. J. van Wees. Spin caloritronics. *Nature Materials*, 11:391–399, 2012.

[192] E. Saitoh, M. Ueda, H. Miyajima, and G. Tatara. Conversion of spin current into charge current at room temperature: Inverse spin-hall effect. *Applied Physics Letters*, 88(18):182509, 2006.

[193] D. J. Sanders and D. Walton. Effect of magnon-phonon thermal relaxation on heat transport by magnons. *Phys. Rev. B*, 15:1489–1494, Feb 1977.

[194] L. M. Sandratskii. Energy band structure calculations for crystals with spiral magnetic structure. *physica status solidi (b)*, 136(1):167–180, 1986.

[195] C. W. Sandweg, Y. Kajiwara, A. V. Chumak, A. A. Serga, V. I. Vasyuchka, M. B. Jungfleisch, E. Saitoh, and B. Hillebrands. Spin pumping by parametrically excited exchange magnons. *Phys. Rev. Lett.*, 106:216601, May 2011.

[196] H. Sato. *Prog. Theor. Phys.*, 13:119, 1955.

[197] S. Y. Savrasov. Linear response calculations of spin fluctuations. *Phys. Rev. Lett.*, 81:2570–2573, Sep 1998.

[198] S. Y. Savrasov and D. Y. Savrasov. Electron-phonon interactions and related physical properties of metals from linear-response theory. *Phys. Rev. B*, 54:16487–16501, 1996.

[199] D. J. Scalapino, J. R. Schrieffer, and J. W. Wilkins. Strong-coupling superconductivity. i. *Phys. Rev.*, 148:263–279, Aug 1966.

[200] T. Seebeck. *Repts. Prussian Acad. Sci.*, 1823.

[201] T. Seebeck. Magnetische polarisation der metalle und erze durch temperaturdifferenz. *Abhandlungen der Königlichen Akademie der Wissenschaften zu Berlin*, page 265, 1825.

[202] W. Setyawan and S. Curtarolo. High-throughput electronic band structure calculations: Challenges and tools. *Computational Materials Science*, 49(2):299 – 312, 2010.

[203] L. J. SHAM. Electronic contribution to lattice dynamics in insulating crystals. *Phys. Rev.*, 188:1431–1439, Dec 1969.

[204] J. Shi, P. Zhang, D. Xiao, and Q. Niu. Proper definition of spin current in spin-orbit coupled systems. *Phys. Rev. Lett.*, 96:076604, Feb 2006.

[205] G. Shirane, R. Nathans, O. Steinsvoll, H. A. Alperin, and S. J. Pickart. Measurement of the magnon dispersion relation of iron. *Phys. Rev. Lett.*, 15:146–148, Jul 1965.

[206] K. P. Sinha and U. N. Upadhyaya. Phonon-magnon interaction in magnetic crystals. *Phys. Rev.*, 127:432–439, Jul 1962.

[207] J. Sinova. Spin seebeck effect: Thinks globally but acts locally. *Nat Mater*, 9, May 2010.

[208] J. Sinova, D. Culcer, Q. Niu, N. A. Sinitsyn, T. Jungwirth, and A. H. MacDonald. Universal intrinsic spin hall effect. *Phys. Rev. Lett.*, 92:126603, Mar 2004.

[209] B. Skubic, J. Hellsvik, L. Nordström, and O. Eriksson. A method for atomistic spin dynamics simulations: implementation and examples. *Journal of Physics: Condensed Matter*, 20(31):315203, 2008.

[210] A. Slachter, F. L. Bakker, J.-P. Adam, and B. J. van Wees. Thermally driven spin injection from a ferromagnet into a non-magnetic metal. *Nat Phys*, 6(11):879–882, 11 2010.

[211] A. Slachter, F. L. Bakker, and B. J. van Wees. Anomalous nernst and anisotropic magnetoresistive heating in a lateral spin valve. *Phys. Rev. B*, 84:020412, Jul 2011.

[212] G. A. Slack and D. W. Oliver. Thermal conductivity of garnets and phonon scattering by rare-earth ions. *Phys. Rev. B*, 4:592–609, Jul 1971.

[213] J. Slonczewski. Current-driven excitation of magnetic multilayers. *Journal of Magnetism and Magnetic Materials*, 159(1–2):L1 – L7, 1996.

[214] J. C. Slonczewski. Conductance and exchange coupling of two ferromagnets separated by a tunneling barrier. *Phys. Rev. B*, 39:6995–7002, Apr 1989.

[215] J. C. Slonczewski. Initiation of spin-transfer torque by thermal transport from magnons. *Phys. Rev. B*, 82:054403, Aug 2010.

[216] A. Sommerfeld. Zur elektronentheorie der metalle auf grund der fermischen statistik. *Zeits. and Physik*, 47:1–32 and 43–60, 1928.

[217] A. Sommerfeld and H. Bethe. Elektronentheorie der metalle. *Handbook Phys.*, 24/2:1–290, 1932.

[218] E. H. Sondheimer. The theory of the transport phenomena in metals. *Proceedings of the Royal Society of London A: Mathematical, Physical and Engineering Sciences*, 203(1072):75–98, 1950.

[219] P. Soven. Coherent-potential model of substitutional disordered alloys. *Phys. Rev.*, 156:809–813, Apr 1967.

[220] E. G. Spencer and R. C. LeCraw. Spin-lattice relaxation in yttrium iron garnet. *Phys. Rev. Lett.*, 4:130–131, Feb 1960.

[221] D. D. Stancil and A. Prabhakar. *Spin Waves Theory and Applications*. Springer, 2009.

[222] R. M. Sternheimer. Electronic polarizabilities of ions from the hartree-fock wave functions. *Phys. Rev.*, 96:951–968, Nov 1954.

[223] H. Sun, J. M. D. Coey, Y. Otani, and D. P. R. Hurley. *J. Phys. Condens. Matter*, 2:6465, 1990.

[224] Q.-f. Sun and X. C. Xie. Definition of the spin current: The angular spin current and its physical consequences. *Phys. Rev. B*, 72:245305, Dec 2005.

[225] H. Swantje. *Effect of spin-orbit scattering on transport properties of low-dimensional dilute alloys*. PhD thesis, RWTH Aachen University, May 2011.

[226] J. Sykes and G. A. Brooker. *Ann. Phys. (N. Y.)*, 56, 1970.

[227] S. Takahashi and S. Maekawa. Spin current in metals and superconductors. *Journal of the Physical Society of Japan*, 77(3):031009, 2008.

[228] A. Tchernatinsky and J. W. Halley. Relativistic tight-binding model: Application to pt surfaces. *Phys. Rev. B*, 83:205431, May 2011.

[229] M. Tessarotto, C. Cremaschini, and M. Tessarotto. On the conditions of validity of the boltzmann equation and boltzmann h-theorem. *The European Physical Journal Plus*, 128(3), 2013.

[230] K. S. Tikhonov, J. Sinova, and A. M. Finkel'stein. Spectral non-uniform temperature and non-local heat transfer in the spin seebeck effect. *Nat Commun*, 4, 2013.

[231] A. Togo, F. Oba, and I. Tanaka. First-principles calculations of the ferroelastic transition between rutile-type and cacl2-type sio2 at high pressures. *Phys. rev. B*, 78:134106, Oct 2008.

[232] Y. S. Touloukian. *Thermophysical Properties of Matter*. IFI, New York, 1970.

[233] N. Troullier and J. L. Martins. Efficient pseudopotentials for plane-wave calculation. *Phys. Rev. B*, 43:1993, 1991.

[234] W.-K. Tse and S. Das Sarma. Spin hall effect in doped semiconductor structures. *Phys. Rev. Lett.*, 96:056601, Feb 2006.

[235] Y. Tserkovnyak, A. Brataas, and G. E. W. Bauer. Enhanced gilbert damping in thin ferromagnetic films. *Phys. Rev. Lett.*, 88:117601, Feb 2002.

[236] Y. Tserkovnyak, A. Brataas, G. E. W. Bauer, and B. I. Halperin. Nonlocal magnetization dynamics in ferromagnetic heterostructures. *Rev. Mod. Phys.*, 77:1375–1421, Dec 2005.

[237] I. Tudosa, C. Stamm, A. B. Kashuba, F. King, H. C. Siegmann, J. Stohr, G. Ju, B. Lu, and D. Weller. The ultimate speed of magnetic switching in granular recording media. *Nature*, 428:831–833, 2004.

[238] A. Tulapurkar and Y. Suzuki. *Solid State Communications*, 150:466 – 470, 2010. Spin Caloritronics.

[239] K. Uchida, H. Adachi, T. An, T. Ota, M. Toda, B. Hillebrands, S. Maekawa, and E. Saitoh. Long-range spin seebeck effect and acoustic spin pumping. *Nat Mater*, 10, 2011.

[240] K. Uchida, H. Adachi, T. Ota, H. Nakayama, S. Maekawa, and E. Saitoh. Observation of longitudinal spin-seebeck effect in magnetic insulators. *Applied Physics Letters*, 97(17):–, 2010.

[241] K. Uchida, H. Adachi, T. Ota, H. Nakayama, S. Maekawa, and E. Saitoh. Observation of longitudinal spin-seebeck effect sintered polycrystalline (mn,zn) fe_2o_4. *Applied Physics Letters*, 97, 2010.

[242] K. Uchida, M. Ishida, T. Kikkawa, A. Kirihara, T. Murakami, and E. Saitoh. Longitudinal spin seebeck effect: from fundamentals to applications. *Journal of Physics: Condensed Matter*, 26(34):343202, 2014.

[243] K. Uchida, T. Nonaka, T. Ota, and E. Saitoh. Longitudinal spin-seebeck effect in sintered polycrystalline (mn,zn)fe_2o_4. *Applied Physics Letters*, 97(26), 2010.

[244] K. Uchida, T. Nonaka, T. Ota, and E. Saitoh. Longitudinal spin-seebeck effect in sintered polycrystalline (mn,zn)fe2o4. *Applied Physics Letters*, 97(26):–, 2010.

[245] K. Uchida, T. Ota, H. Adachi, J. Xiao, T. Nonaka, Y. Kajiwara, G. E. W. Bauer, S. Maekawa, and E. Saitoh. Thermal spin pumping and magnon-phonon-mediated spin-seebeck effect. *Journal of Applied Physics*, 111(10):–, 2012.

[246] K. Uchida, T. Ota, K. Harii, S. Takahashi, S. Maekawa, Y. Fujikawa, and E. Saitoh. Spin-seebeck effects in films. *Solid State Communications*, 150(11-12):524 – 528, 2010. Spin Caloritronics.

[247] K. Uchida, T. Ota, Y. Kajiwara, H. Umezawa, H. Kawai, and E. Saitoh. Electric detection of the spin-seebeck effect in magnetic insulator in the presence of interface barrier. *Journal of Physics: Conference Series*, 303(1):012096, 2011.

[248] K. Uchida, S. Takahashi, K. Harii, J. Ieda, W. Koshibae, K. Ando, S. Maekawa, and E. Saitoh. Observation of the spin seebeck effect. *Nature*, 455(7214):778–781, 10 2008.

[249] K. Uchida, S. Takahashi, J. Ieda, K. Harii, K. Ikeda, W. Koshibae, S. Maekawa, and E. Saitoh. Phenomenological analysis for spin-seebeck effect in metallic magnets. *Journal of Applied Physics*, 105(7), 2009.

[250] K. Uchida, J. Xiao, H. Adachi, J. Ohe, S. Takahashi, J. Ieda, T. Ota, Y. Kajiwara, H. Umezawa, H. Kawai, G. E. W. Bauer, S. Maekawa, and E. Saitoh. Spin seebeck insulator. *Nature Materials*, 9:894–897, 2010.

[251] R. Urban, G. Woltersdorf, and B. Heinrich. Gilbert damping in single and multilayer ultrathin films: Role of interfaces in nonlocal spin dynamics. *Phys. Rev. Lett.*, 87:217204, Nov 2001.

[252] S. O. Valenzuela and M. Tinkham. Direct electronic measurement of the spin hall effect. *Nature*, 442(7099):176–179, Jul 2006.

[253] T. Valet and A. Fert. Theory of the perpendicular magnetoresistance in magnetic multilayers. *Phys. Rev. B*, 48:7099–7113, Sep 1993.

[254] J. VAN KRANENDONK and J. H. VAN VLECK. Spin waves. *Rev. Mod. Phys.*, 30:1–23, Jan 1958.

[255] A. van Staa, J. Wulfhorst, A. Vogel, U. Merkt, and G. Meier. Spin precession in lateral all-metal spin valves: Experimental observation and theoretical description. *Phys. Rev. B*, 77:214416, Jun 2008.

[256] M. Verstraete and X. Gonze. Smearing scheme for finite-temperature electronic-structure calculations. *Phys. Rev. B*, 65:035111, Dec 2001.

[257] M. J. Verstraete, M. Torrent, F. m. c. Jollet, G. Zérah, and X. Gonze. Density functional perturbation theory with spin-orbit coupling: Phonon band structure of lead. *Phys. Rev. B*, 78:045119, Jul 2008.

[258] A. Vogel, J. Wulfhorst, and G. Meier. Enhanced spin injection and detection in spin valves with integrated tunnel barriers. *Applied Physics Letters*, 94(12):–, 2009.

[259] U. von Barth. Basic density-functional theory - an overview. *Physica Scripta*, 2004(T109):9, 2004.

[260] X. Waintal, E. B. Myers, P. W. Brouwer, and D. C. Ralph. Role of spin-dependent interface scattering in generating current-induced torques in magnetic multilayers. *Phys. Rev. B*, 62:12317–12327, Nov 2000.

[261] D. C. Wallace. *Thermodynamics of Crystals*. John Wiley and Sons, Inc., 1972.

[262] D. Walton, J. E. Rives, and Q. Khalid. Thermal transport by coupled magnons and phonons in yttrium iron garnet at low temperatures. *Phys. Rev. B*, 8:1210–1216, Aug 1973.

[263] E. Wasserman, L. Stixrude, and R. E. Cohen. Thermal properties of iron at high pressures and temperatures. *Phys. Rev. B*, 53:8296–8309, Apr 1996.

[264] H. Wendel and R. M. Martin. Theory of structural properties of covalent semiconductors. *Phys. Rev. B*, 19:5251–5264, May 1979.

[265] R. White. *Quantum Theory of Magnetism*. McGraw-Hill, 1970.

[266] E. Wigner. On the interaction of electrons in metals. *Phys. Rev.*, 46:1002–1011, Dec 1934.

[267] Wikipedia. Resistor model of spin-valve giant magnetoresistance effect. [Online; accessed 29-July-2015].

[268] S. A. Wolf, D. D. Awschalom, R. A. Buhrman, J. M. Daughton, S. von Molnár, M. L. Roukes, A. Y. Chtchelkanova, and D. M. Treger. Spintronics: A spin-based electronics vision for the future. *Science*, 294(5546):1488–1495, 2001.

[269] J. Xiao, G. Bauer, K. Uchida, E. Saitoh, and S. Maekawa. Theory of magnon-driven spin seebeck effect. *Phys. Rev. B*, 81(21):214418, Jun 2010.

[270] J. Xiao, G. E. W. Bauer, S. Maekawa, and A. Brataas. Charge pumping and the colored thermal voltage noise in spin valves. *Phys. Rev. B*, 79:174415, May 2009.

[271] B. Xu and M. J. Verstraete. First principles explanation of the positive seebeck coefficient of lithium. *Phys. Rev. Lett.*, 112:196603, May 2014.

[272] H. Yang, A. Thiaville, S. Rohart, A. Fert, and M. Chshiev. Anatomy of dzyaloshinskii-moriya interaction at co/pt interfaces. *ArXiv*, cond-mat/1501.05511v1, 2015.

[273] M. T. Yin and M. L. Cohen. Theory of lattice-dynamical properties of solids: Application to si and ge. *Phys. Rev. B*, 26:3259–3272, Sep 1982.

[274] H. Yu, S. Granville, D. P. Yu, and J.-P. Ansermet. Evidence for thermal spin-transfer torque. *Phys. Rev. Lett.*, 104:146601, Apr 2010.

[275] X. Z. Yu, Y. Onose, N. Kanazawa, J. H. Park, J. H. Han, Y. Matsui, N. Nagaosa, and Y. Tokura. Real-space observation of a two-dimensional skyrmion crystal. *Nature*, 465(7300):901–904, 06 2010.

[276] M. Zaffalon and B. J. van Wees. Zero-dimensional spin accumulation and spin dynamics in a mesoscopic metal island. *Phys. Rev. Lett.*, 91:186601, Oct 2003.

[277] S. Zhang. Spin hall effect in the presence of spin diffusion. *Phys. Rev. Lett.*, 85:393–396, Jul 2000.

[278] J. M. Ziman. *Electrons and phonons: the theory of transport phenomena in solids*. International series of monographs on physics. Clarendon Press, Oxford, 1960.